Physical analysis of percolating silver nanowire networks used as transparent electrodes for flexible applications

Mélanie Lagrange

UNIVERSITÉ GRENOBLE ALPES

THÈSE

Pour obtenir le grade de

DOCTEUR DE L'UNIVERSITÉ GRENOBLE ALPES

Spécialité : **Ingénierie - Matériaux, mécanique, énergétique, environnement, procédés, production**

Arrêté ministériel : 7 août 2006

Présentée par

Mélanie LAGRANGE

Thèse dirigée par **Daniel Bellet** et
codirigée par **Yves Bréchet**

préparée au sein du **Laboratoire des Matériaux et du Génie Physique**
dans **l'École Doctorale I-MEP2**

Physical analysis of percolating silver nanowire networks as transparent electrodes for flexible applications

Thèse soutenue publiquement le **12 Octobre 2015,**
devant le jury composé de :

Jonathan COLEMAN
Professeur, CRANN, Trinity College Dublin, Président
Karine MASENELLI-VARLOT
Professeur, MATEIS, INSA Lyon, Rapporteur
Mona TREGUER-DELAPIERRE
Maître de Conférences, ICMCB-CNRS, Univ. de Bordeaux, Rapporteur
Ngoc Duy NGUYEN
Professeur, SPIN, Univ. de Liège, Examinateur
Jean-Pierre SIMONATO
Ingénieur de Recherche, CEA-LITEN, Examinateur
Daniel BELLET
Professeur, LMGP, Grenoble INP-CNRS, Directeur de thèse
Yves BRECHET
Professeur, SIMaP, Grenoble INP-CNRS, Co-directeur de thèse

Acknowledgements

These three years spent at the LMGP have been the occasion to meet and work with unforgettable people. Each of them contributed to this thesis work with their advices, their scientific or technical skills and their friendship.

First of all, I would like to thank my supervisor Daniel Bellet, for all his advices that helped me to improve, and for his constant friendliness. This thesis was greatly conducted thanks to his unwavering commitment to his PhD students. Thanks to you I developed numerous skills to become a good scientist, and I improved my chocolate cake cooking style.

Thanks also to my co-supervisor Yves Bréchet, for the gainful discussions throughout this thesis that helped us progressing in the topic, and for the amusing anecdotes.

I would like to thank the other members of the jury: Karine Masenelli-Varlot and Mona Tréguer-Delapierre for accepting to review this manuscript. Thanks to Jonathan Coleman for accepting to be president of the jury, and for the interesting discussion we had in Dublin. I want to thank Ngoc Duy Nguyen for accepting to be part of the jury, and for the discussions we had at the LMGP when he visited us. Thanks to Jean-Pierre Simonato to examine this thesis and to have shared his knowledge with us during the numerous meetings with the CEA-Liten team.

I want to thank all the people from the silver nanowire team that worked by my sides during these three years. First Gaël, for being always available for discussions, and for his contagious cheerfulness. Thanks to Thomas for the numerous discussions about surprising results, and for his friendliness. Good luck for the next two years! I would also like to thank all the “stagiaires” that worked with us and brought new perspectives on the topic: Rachael, Eric, Thomas, Amit, Maud, Benoit and Mallory.

The last but not the least: a big thank you to Dan, who has been more than my co-doctorant: an awesome friend. It was great to work with you, thanks for supporting me and advising me when it was needed.

I would like to thank the director of the LMGP, Franz Bruckert and his co-director Carmen Jimenez. Thank you Carmen for always being available when technical problems arised. Many thanks also for your involvement in the discussions about the topic.

I want to thank David Muñoz-Rojas for all his help, the gainful discussions, and for the time he spent working with us, at the PTA or at the LMGP, always bringing useful literature contents.

Thanks to Odette Chaix, Béatrice Doisneau, Mikhail Anikin, Dominique de Barros, Laetitia Rapenne, Matthieu Jouvert and Hervé Roussel from LMGP for their contribution to the acquisition of results in the silver nanowire topic, and for their valuable advices.

I also thank Alexandre Niembro, Tan Phu Vuong and Philippe Ferrari from IMEP-LAHC for dedicating some of their time to the antennas and EM shielding topic the last few months. Thanks to Julian Reindl, and Stefano Boscarino for their involvement in the Eurotop project and for conducting sometimes lengthy experiments. Thanks to Caroline Celle and Céline Mayousse for their advices and for sharing their knowledge on the topic with our team.

I want to thank now all the “doctorants”, “post-docs” and “non-permanents”, or other people from LMGP with whom I shared either meals, office or crazy parties for the last three years. En particulier, je remercie Lucile pour toutes les soirées et confidences qu’on a pu partager, Sophie pour sa spontanéité, Renaud pour toutes nos discussions, Pauline pour sa jovialité, und my Freund Martin qui m’a mené la vie dure. Merci aussi à Jerôme, Lisi, Anne, Flora, Laure, Lijie, Sébastien, Claire, Thibaut, Shanting, Quentin, Vincent, Thomas, Yunji, Ionela, Raphaël, Fabien et tous les autres.

Un grand merci à mes parents pour leur soutien et leur patience qui m’ont permis d’arriver jusque-là.

Pour finir, un merci spécial à Louis, pour ton écoute et tes conseils, ton soutien sans faille, et pour tout ce que tu m’as apporté comme discussions et attentions depuis notre rencontre au LMGP.

Abstract

Transparent electrodes (TE) are used in a variety of optoelectrical devices. Among them, solar cells, flat panel displays, touch screens, OLEDs can be cited but also other applications such as transparent heaters. The physical properties of the TE influence the efficiency of these devices as a whole. Such electrodes are fabricated from transparent conducting materials (TCM) that have been undergoing development since the 1950s, initially from metallic oxides. Among these transparent conducting oxides (TCO), indium tin oxide (ITO) is the most commonly used in solar cells, and television or smartphone screens. However requirements such as cost reduction, flexibility and low cost/temperature fabrication techniques have oriented the researches toward emerging TCM, mostly using nanostructures. Among them, metallic nanowire networks, and in particular silver nanowires (AgNW), already present optical and electrical properties approaching those of ITO, *i.e.* a high electrical conductivity and a high transparency. These two properties are intrinsically linked to the network density, therefore a tradeoff has to be considered knowing that when conductivity increases, transparency decreases. Some post-deposition treatments do exist, allowing an increase of the TE electrical conductivity without changing the network density. Several of these optimization methods have been thoroughly studied during this thesis work, especially thermal annealing. This method have been investigated in details to understand the different thermally-induced mechanisms of conductivity improvement. In addition, the investigation of thermal effects raised the question of thermal instability of the nanowires, which is also addressed and discussed in this document. The key issue of density optimization, allowing the best tradeoff between transparency and conductivity, has been investigated for nanowires with different dimensions. Nanowire size has a strong impact on the network properties. Thus, electrical properties, within the framework of percolation theory, optical properties such as transmittance or haziness, and even thermal instability have been linked to the nanowires' dimensions and the network density by using simple physical models. Regarding the application of these emerging TE, studies were conducted on the application of AgNWs as transparent heaters, and the results are reported at the end of the document. Limitations arising from this application, like thermal and electrical stabilities, have also been addressed. To finish, preliminary studies conducted on new applications such as transparent antennas and transparent electromagnetic shielding using AgNW are presented.

Résumé

Les électrodes transparentes (ET) sont présentes dans de nombreux dispositifs optoélectroniques. Par exemple, on peut les trouver au sein de cellules solaires, d'écrans tactiles, d'OLEDs ou dans d'autres types d'applications telles que les films chauffants transparents. Les propriétés physiques de ces électrodes influencent l'efficacité de ces dispositifs. Les ET sont fabriquées à partir de matériaux transparents conducteurs (TCM) dont le développement a débuté dans les années 1950 notamment avec les oxydes métalliques. Parmi ces oxydes transparents conducteurs (TCO), l'oxyde d'étain-indium (ITO) est celui le plus communément utilisé dans les cellules solaires et les écrans de télévision ou de smartphones. Cependant, de nouvelles exigences telles qu'une réduction des coûts, la flexibilité et la fabrication à faible température et/ou faible coût, ont orienté les recherches vers de nouveaux TCM, notamment à base de nanostructures. Parmi ces matériaux émergents, les réseaux de nanofils métalliques, en particulier de nanofils d'argent, présentent déjà des propriétés optiques et électriques approchant celles de l'ITO, c'est-à-dire une conductivité électrique et une transparence élevées. Ces deux propriétés sont cependant intrinsèquement liées à la densité de nanofils constituant le réseau, et lorsque la conductivité augmente, la transparence diminue. Des traitements post-dépôt existent et permettent d'augmenter la conductivité électrique des ET sans changer la densité du réseau. Plusieurs de ces méthodes d'optimisation ont été étudiées pendant ce travail de thèse, en particulier le recuit thermique, analysé minutieusement afin de comprendre les différents mécanismes de réduction de la conductivité électrique induits par la température. L'examen des effets thermiques a soulevé la question de l'instabilité des nanofils en température, qui est aussi abordée et discutée dans ce document. Le paramètre clé de la densité de nanofils optimale menant au meilleur compromis entre transparence et conductivité a été recherché pour des nanofils de différentes dimensions. La taille des nanofils a en effet un fort impact sur les propriétés du réseau. Ainsi, les propriétés électriques, dans le cadre de la théorie de la percolation, les propriétés optiques comme la transmittance et le facteur de haze, et même l'instabilité thermique ont été reliées aux dimensions des nanofils ainsi qu'à la densité du réseau en utilisant des modèles physiques simples. En ce qui concerne les applications de ces ET émergentes, des études ont été menées sur l'application des réseaux de nanofils d'argent comme film chauffant transparent, et les résultats sont rapportés à la fin de ce document. Les limitations soulevées par cette application, comme les limites de stabilités électrique et thermique ont aussi été abordées. Pour finir, des études préliminaires menées sur de nouvelles applications comme des antennes transparentes ou le blindage électromagnétique transparent utilisant les nanofils d'argent sont présentées.

Table of contents

Introduction

The last decades have seen emerging an increasing interest towards nanotechnologies, in order to overcome technological barriers or reach higher standards. One of the most known illustration of this interest is the reduction of transistors size within microchips, to improve electronic devices capacities without increasing their size. Another example is the use of nanostructures in solar cells. Considering the struggle surrounding fossil fuels, sustainable energies development has become a strategical field. Nanostructures can for example increase the specific surface of a material within the cell, allowing the use of an extremely thin absorber (ETA). Compared to standard solar cells, ETA technology limits the recombination of the photogenerated carriers[1,2] and enables to use a low amount of material. Nanostructured materials are also used in energy storage technologies,[3] which is a key issue for a better development of sustainable energies. Finally, within the topic studied during the present thesis, *i.e.* silver nanowire- (AgNW-) based transparent electrodes (TE), the use of a nanostructured film enables to obtain a final electrode which is transparent while it would have been opaque using the same mass of bulk material.[4]

Nanomaterials present numerous advantages interesting to exploit for many applications since they are placed at the intersection between material science, physics, chemistry, but also biology and medicine.[5] However, reducing the dimensions of a material often implies some changes in its physical properties, as well as in its fabrication processes, and can lead to the appearance of instability problems. Integrated circuits with nanoconnectors suffer for example from electromigration, limiting their lifetime.[6] The process of choosing a material for a specific application therefore implies tradeoffs between the fabrication processes and the material constraints, but also between the different required physical properties.[7,8] Transparent conducting materials (TCM) are no exception, the main tradeoff of interest in this thesis being between transparency and conductivity. This document will show that other tradeoffs also rise from the different applications of the material.

TCM are a key component in a variety of optoelectronic devices, such as solar cells, flat panel displays, LED or transparent heaters. The need for TCM is increasing as the market of electronic devices is constantly growing, with an increasing number of devices varieties. Portable personal electronic devices are booming, as well as large flat panel displays that need transparent electrodes. The use of TCM is also primary in solar cells as they enable the collection of the electrons photogenerated within the cell, while allowing a large amount of photons to reach it, thanks to the optical transparency. The widely commercialized TCM these days in touch screens, solar cells and most of the optoelectronic devices cited above is indium tin oxide (ITO). But considering the increasing demand in personal electronics, sustainable energy (solar cells), LCD displays, and the appearance of devices which need additional

requirements such as flexibility, ITO tends to reach some limits, considering its brittle nature, its fabrication methods and the scarcity of indium, inducing an increase of costs.

In material science, new requirements induce a whole reconsideration of the materials used for an intended application. Therefore in the TCM field, the need for flexibility has opened the door to emerging TCM fulfilling this requirement, like conductive polymer, or nanomaterials such as metallic nanowires networks, carbon nanotube (CNT) networks, graphene or metallic grids. Among these materials, metallic nanowire networks are promising because of the superior conductivity of metals, such as silver, and the free spaces between the nanowires responsible for the material transparency. Metallic nanowires, and especially AgNW, can be produced at large scale and deposited by wet chemistry techniques in ambient conditions, leading to a low cost fabrication. Although they have been studied only during the last ten years, AgNW-based TE already reach the market requirements in terms of transparency and conductivity. Silver being the most conducting element existing, AgNW networks can be seen as a model system to validate metallic nanowire-based TCM in general. The use of other metals will then be required to reduce materials cost since the price of silver is rather high considering its relative scarcity. However the required amount of silver for a TE made with AgNW is rather low, around 0.1 g per square meter. Studies on less rare materials, in particular copper nanowires, have started in the past few years. Metallic nanowire however suffer from instability, coming either from temperature, atmospheric corrosion or electrical current flow. These drawbacks need to be overcome and are the subjects of an increasing number of studies,[9–14] in order to enable the integration of metallic nanowires into devices.[15]

This thesis work is therefore dedicated to the study of AgNW networks used as transparent electrodes, through investigations of density and nanowire dimensions effects on the physical properties, as well as the improvement of these properties by using post-deposition treatments such as thermal annealing. The studies have been conducted by a systematic approach, during which only one or two parameters varied: either the network density, or the nanowire length and diameter. Then simple physical models were used in order to relate these parameters to the networks physical properties. The use of AgNW in different applications was also investigated. This document is therefore divided into five chapters. In the first one, a bibliographical study of TCMs in general and AgNW-based transparent electrodes in particular is reported. The physical properties of TCM are described as well as the potential integration of AgNW networks into various devices. The second chapter is dedicated to the experimental methods used during the present thesis work to fabricate, characterize and study AgNW networks. The third chapter is an in-depth investigation of the thermal annealing effects on the AgNW networks physical properties, including resistance reduction but also thermal instability. In addition, this chapter presents alternative post-deposition treatments

to improve AgNW networks physical properties. Chapter four discusses the impact of the nanowires dimensions on the different networks physical properties and on the network stability through simple physical models. To finish with, the application of AgNW networks as transparent heaters is reported in chapter five, while preliminary tests for their application in transparent electromagnetic shielding and transparent antennas are presented. This chapter also discusses instability problems that arise from the use of AgNW networks as transparent heaters, such as electrical failure, partially caused by electromigration.

The present thesis work has been conducted in parallel with another thesis, codirected by Daniel Bellet at the LMGP and Ngoc Duy Nguyen at University of Liège, in the framework of an IDS FunMat international program. The thesis was conducted by Daniel Langley and was focused mainly on electrical percolation within AgNW networks, taking into account network density and nanowire dimensions through Monte-Carlo simulations study,[16] but also started experiments on thermal annealing effects. It has been defended in October 2014. Another PhD student, Thomas Sannicolo, supervised by Daniel Bellet and Jean-Pierre Simonato at the CEA-Leti in Grenoble has started his thesis in October 2014, focused on the experimental study of electrical percolation and more generally on the fabrication of AgNW networks, from the nanowire synthesis to the integration into devices (electromagnetic shielding and RF antennas). Technical and scientific discussions have accompanied these three thesis works, and provided an interesting emulation.

We believe the field of metallic nanowire-based TCM is of main interest now and will certainly grow in the future, as it has in the last few years. This work is therefore a contribution to the understanding of this material physical properties, in order to assist the expansion of this field.

References

[1] Grätzel M 2001 Photoelectrochemical cells *Nature* **414** 338–44

[2] Michallon J, Bucci D, Morand A, Zanuccoli M, Consonni V and Kaminski-Cachopo A 2014 Light trapping in ZnO nanowire arrays covered with an absorbing shell for solar cells *Opt. Express* **22** A1174

[3] Aricò A S, Bruce P, Scrosati B, Tarascon J-M and van Schalkwijk W 2005 Nanostructured materials for advanced energy conversion and storage devices *Nat. Mater.* **4** 366–77

[4] De S, Higgins T M, Lyons P E, Doherty E M, Nirmalraj P N, Blau W J, Boland J J and Coleman J N 2009 Silver Nanowire Networks as Flexible, Transparent, Conducting Films: Extremely High DC to Optical Conductivity Ratios *ACS Nano* **3** 1767–74

[5] D. Vollath 2008 *Nanomaterials: an introduction to synthesis, properties and applications* (Weinheim: Wiley-VCH Verlag GmbH & Co. KGaA)

[6] Murr L E 2015 Failure of Integrated Circuits *Handbook of Materials Structures, Properties, Processing and Performance* (Springer International Publishing) pp 999–1007

[7] Yves Bréchet Le choix des matériaux et des procédés: l'art du compromis http://www.college-de-france.fr/site/yves-brechet/course-2013-02-01-10h00.htm

[8] Ashby M F, Bréchet Y J M, Cebon D and Salvo L 2004 Selection strategies for materials and processes *Mater. Des.* **25** 51–67

[9] Elechiguerra J L, Larios-Lopez L, Liu C, Garcia-Gutierrez D, Camacho-Bragado A and Yacaman M J 2005 Corrosion at the Nanoscale:□ The Case of Silver Nanowires and Nanoparticles *Chem. Mater.* **17** 6042–52

[10] Karim S, Toimil-Molares M E, Balogh A G, Ensinger W, Cornelius T W, Khan E U and Neumann R 2006 Morphological evolution of Au nanowires controlled by Rayleigh instability *Nanotechnology* **17** 5954–9

[11] Toimil Molares M E, Balogh A G, Cornelius T W, Neumann R and Trautmann C 2004 Fragmentation of nanowires driven by Rayleigh instability *Appl. Phys. Lett.* **85** 5337–9

[12] Khaligh H H and Goldthorpe I A 2013 Failure of silver nanowire transparent electrodes under current flow *Nanoscale Res. Lett.* **8** 1–6

[13] Ahn Y, Jeong Y and Lee Y 2012 Improved Thermal Oxidation Stability of Solution-Processable Silver Nanowire Transparent Electrode by Reduced Graphene Oxide *ACS Appl. Mater. Interfaces* **4** 6410–4

[14] Li H, Biser J M, Perkins J T, Dutta S, Vinci R P and Chan H M 2008 Thermal stability of Cu nanowires on a sapphire substrate *J. Appl. Phys.* **103** 024315–23

[15] Langley D, Giusti G, Mayousse C, Celle C, Bellet D and Simonato J-P 2013 Flexible transparent conductive materials based on silver nanowire networks: a review *Nanotechnology* **24** 452001

[16] Daniel Langley 2014 *Silver nanowire networks: Effects of percolation and thermal annealing on physical properties* (PhD thesis: Université de Grenoble, Université de Liège)

Chapter 1 : Transparent conducting materials properties, issues and application

Transparent electrodes (TE) are fabricated from transparent conducting materials (TCM) that have started to be studied in the 1950s. These electrodes are crucial in a variety of optoelectrical devices, increasingly produced in different domains such as energy, lighting, screens, heating or more recently electromagnetic shielding or RF antennas. TCM main requirements for improving the efficiency of the optoelectrical devices just mentioned, are a high transparency coupled with a high conductivity. For example in a solar cell, a high transparency would allow a maximum of photons to enter the cell, while a high conductivity will facilitate the extraction of the photogenerated charge carriers. In transparent heaters, for vehicle windows defrosting for instance, the conductivity (both electrical and thermal) needs to be efficient enough to induce heating using a low voltage, while the high transparency is mandatory when the transparent heater is used on a windscreen.

This first chapter aims at introducing the physical properties of TCM as well as their main issues, in particular coming from thermal treatments, electrical or mechanical stress. Then the focus will be on the study of one of the most promising emerging TCM intended for flexible TE: silver nanowire (AgNW) networks. The different steps of fabrication to obtain such TE will be detailed, starting from the nanowire synthesis, then the deposition techniques and the network properties optimization by different post-deposition treatments. To finish with, an overview of the various applications of AgNW-based TE will be presented through a bibliographical study.

1.1 Introduction to TCM

TCM are used in a variety of optoelectronic devices, such as solar cells, OLED, flat panel displays or transparent heaters. The TCM family comprises transparent conducting oxides (TCO) which have been extensively studied and improved during several decades, especially indium tin oxide (ITO) which is now largely commercialized, as well as aluminum doped zinc oxide (AZO) and fluorine tin oxide (FTO). Emerging TCM like graphene, CNT or metallic nanowires networks, metallic grids, or conducting polymers have been more recently investigated. This section is a short introduction to the different existing TCO, with their properties and limitations. It then extends to an overview of the different families of emerging TCM, including AgNW networks.

1.1.1 TCO and the special case of ITO

ITO has been dominating the TCM market for decades. This material is still the subject of research studies[1,2] but the scientific community is increasingly looking for other materials

suitable as transparent electrodes for the following reasons. Firstly, ITO is composed at 90% of indium oxide, and indium is a material suffering from scarcity. There are no mines of indium across the world: indium is extracted only in small amounts as a by-product from zinc mines. Its price is therefore quite high and fluctuating, especially since ITO is used at large industrial scale. ITO is used in majority in LCD displays, according to a report made in 2012 by the Belgian group Nyrstar,[3] from which Figure 1-1a and b have been extracted. Moreover, zinc mines are situated mostly in China, which is the first zinc producer worldwide. The country produces around 50% of the world's primary indium from around 15 different plants (see Figure 1-1b). Indium is a critical resource and its extensive use has become a geopolitical issue. Fortunately indium-free TCO have also been developed, such as AZO[4,5] or FTO for instance.[6–10] Secondly, ITO and more generally TCO are brittle materials. Under mechanical stress, they would break and lose their conductive nature[11]. That drawback prevents them from being integrated into flexible devices, which is quite problematic considering the increasing demand in flexible or stretchable applications.[12] To finish with, the most used method for ITO deposition is sputtering, that is performed under vacuum and at relatively high temperatures, leading to a high cost of ITO. For example ITO-based transparent electrode represents 12% of the final material price of a silicon heterojunction solar cell (from Labfab, CEA-INES).

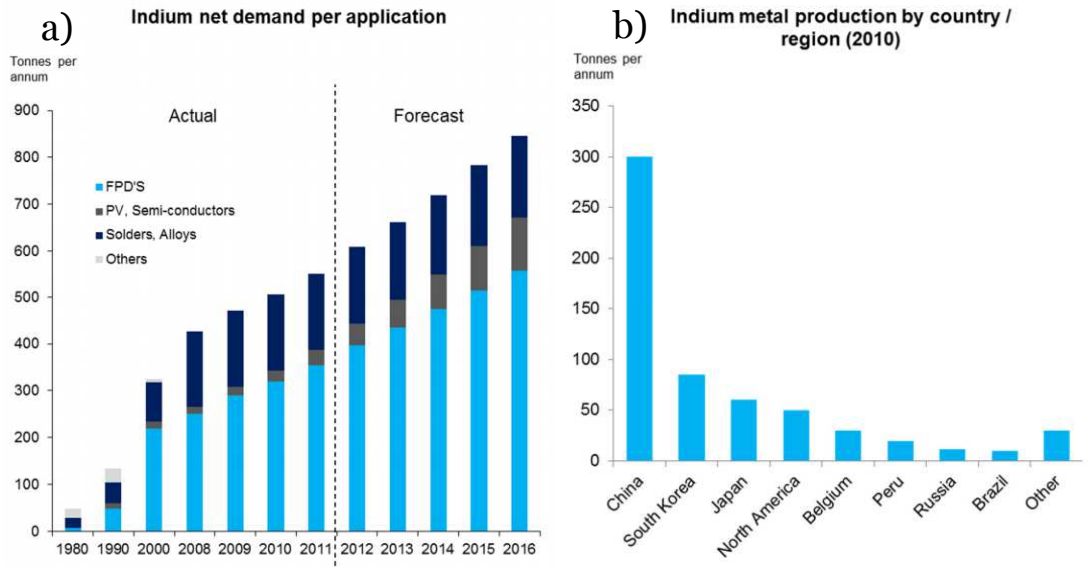

Figure 1-1: a) Indium demand per application (2012) and b) indium production by country in 2010, reported by Nyrstar.[3] FPD stands for flat panel displays and PV for photovoltaics.

To overcome these drawbacks and propose flexible transparent electrodes that can be fabricated at low price, new TCM have been developed and are detailed in the following section.

1.1.2 Emerging TCM

Different families of TCM have been developed over the last two decades to overcome ITO limitations like brittleness, scarcity of indium and high cost fabrication. The main ones are summarized in Figure 1-2a and the emerging materials can be divided in two main categories: conducting polymers, such as PEDOT:PSS, and nanomaterials. Among the nanomaterials, some are carbon-based while other are metal-based. Regarding the TCM based on nanomaterials, graphene[13–15] (Figure 1-2b) and CNT[16–19] (Figure 1-2c) based TE have been widely studied and can be very transparent considering their low thickness. However these TCM suffer so far from rather poor conductivity[20]. To improve the conductivity, the amount of material should be increased, but it would have a detrimental effect on the transparency. These carbon-based materials however present other interesting properties such as flexibility or low surface roughness. Graphene also presents advantages in transparent nanocomposites, and can be used as a layer to protect metallic nanowires against chemical instability[21] that also improves their adhesion.[22] Metallic grids[23,24] (Figure 1-2d) are very efficient considering that the sparseness and lines width can be chosen during the lithography processes to optimize the tradeoff between transparency and conductivity. However this material suffers from low throughput fabrication which implies high costs due to the lithographical stages. Metallic nanowire-based transparent electrodes, mainly silver,[11,25–29] (Figure 1-2e) but increasingly copper[30–33], have good optical and electrical properties but need some additional material to protect them and improve their chemical, thermal and electrical stability. They also suffer from low adhesion. Therefore, hybrid materials have been developed[34–36] to overcome some of the weaknesses of these materials. For example, graphene sheets have been deposited on AgNW by Zhang *et al.*[22] in order to improve the thermal stability for transparent heaters application, while ensuring that the hybrid material is still transparent. Deng et al.[37] also encapsulated metal nanowires with graphene and observed that it limits corrosion and improves the adherence of the network on the substrate. Another TCM which can be seen as an intermediate material between metallic grids and metallic nanowire networks is metallic nanotrough (Figure 1-2f), which have been introduced by Wu *et al.*[38] They have been shown to achieve among the best optical and electrical properties of all the families of TCMs. On one hand they are highly flexible and can be deposited on a variety of substrates. One the other hand, the fabrication of the nanotrough was made by thermal evaporation, so in vacuum, which can induce lower fabrication throughput and high costs.

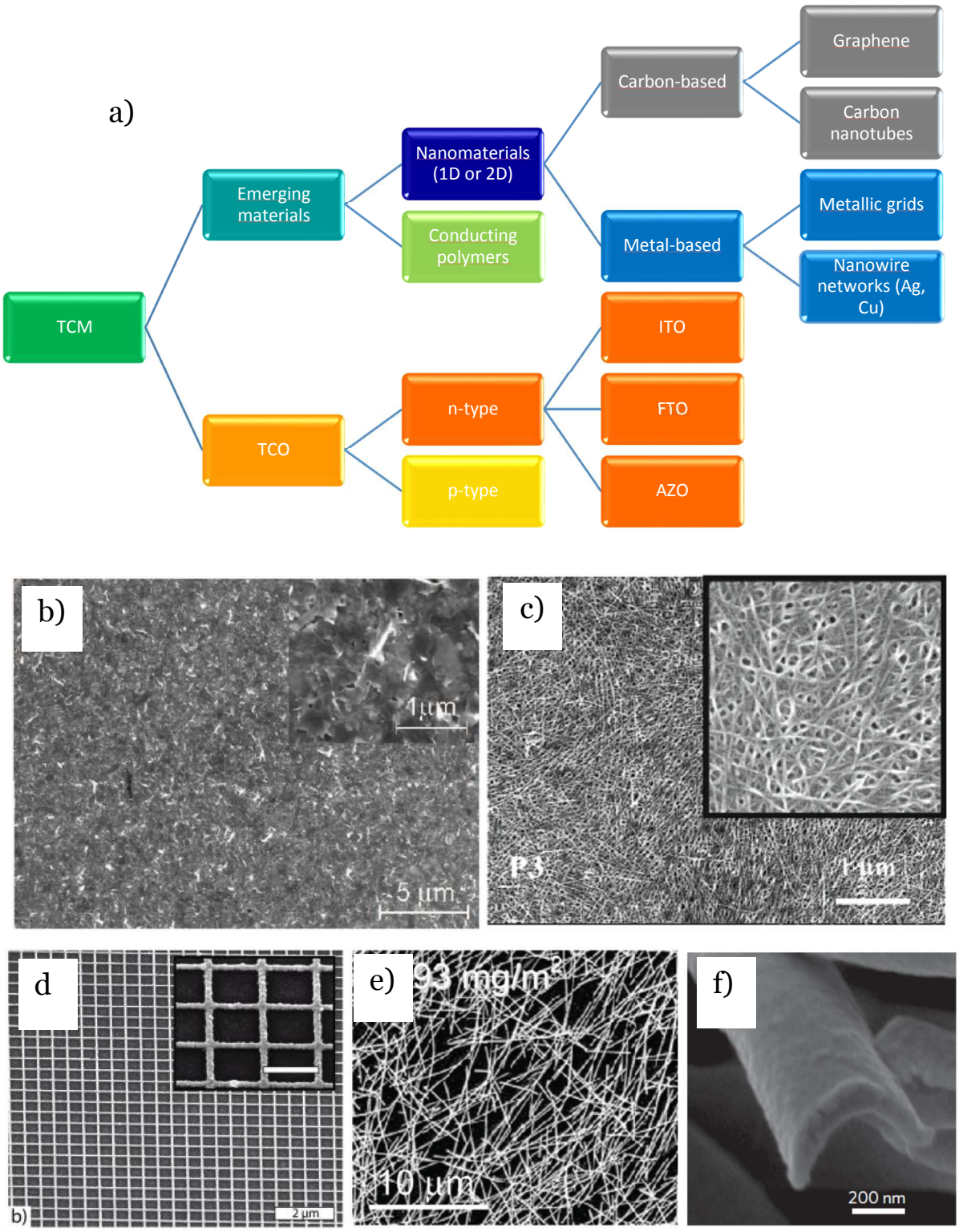

Figure 1-2: a) The main families of TCMs, and SEM images of the nanostructured ones: b) spray-coated thin film made of graphene obtained by chemical exfoliation,[39] c) CNT network,[40] d) metallic grid of silver fabricated by electron lithography of diameter 55 nm spaced of 500 nm. Large magnification inset scale bar is 500 nm,[23] e) AgNW film with mass density 93 mg.m^{-2},[25] f) cross-section of a single gold nanotrough.[38]

Among all the emerging TCM presented above, AgNW networks seem to be the most promising. They present already optical and electrical properties challenging those of ITO[20] whereas they have been studied for less than 10 years. This will be discussed later. One can therefore expect even further improvement of their properties in the near future.

1.2 AgNW networks for transparent electrodes

AgNW networks present many advantages that makes them promising as future flexible TE. Due to the malleability of silver, they can indeed be used in flexible devices, unlike TCO. Their method of synthesis the most used, the polyol process, is well mastered and has been extended to large scale production. Copper[30,31,41–43], gold[44,45] or cupronickel[46] nanowires have also been used for the fabrication of TE, but the most studied remain AgNW. Different low cost deposition methods at atmospheric pressure and/or at room temperature are available for depositing them on large and flexible surfaces. Low cost synthesis and deposition in ambient condition facilitate the development of AgNW networks at large scale, promising them shortly some industrial success. Therefore the focus of this section will be oriented towards the fabrication of AgNW networks, including the understanding of the method of nanowire synthesis, polyol process, and the different methods of nanowire deposition. The properties of AgNW-based TE will then be detailed and compared with those of other emerging TCM. Finally a bibliographical overview will detail their application in several devices.

1.2.1 Metallic nanowire synthesis by polyol process

Low-cost solution-based processes for the synthesis of metallic nanowires have been extensively developed in the past 20 years. The polyol process is a method of AgNW synthesis able to be extended to mass production. This method will be detailed here since it is the one used by the company Seashell Technology to fabricate the nanowire we used during this thesis work. Other methods of nanostructures synthesis exist such as hydrothermal method, microwave-assisted process, UV irradiation technique, template technique and electrochemical technique,[47,48] but none of them is as promising regarding simplicity, low-cost and ability to mass production as the polyol process.

The polyol method, firstly presented by the group of Xia,[49,50] is based on the reduction of metallic salts by a polyol, usually ethylene glycol because of its ability to solvate $AgNO_3$ and polyvinylpyrrolidone (PVP), and its high boiling point (196°C). A metal precursor, for example silver nitrate, is reduced by the glycol in the presence of a nucleating agent and a polymer: PVP. The reduction leads to the formation of multiply twinned nanoparticles having a five-fold symmetry,[51] as pictured in Figure 1-3a. The nanoparticle then evolves into a nanorod terminated by {111} facets and with side facets {100}. PVP strongly interacts with {100} facets,

leading to chemical adsorption, while the twin boundaries of the {111} facets, left bare, are active sides for silver atoms addition, allowing a uniaxial growth of the nanostructure as shown in Figure 1-3b. This method of nanowire synthesis and its understanding, especially of the role of PVP, have been extensively studied in the literature.[47,50,52–56] After synthesis, a thin layer of PVP remains on the AgNW walls, as can be seen in Figure 1-3c, with weak bonds.[53]

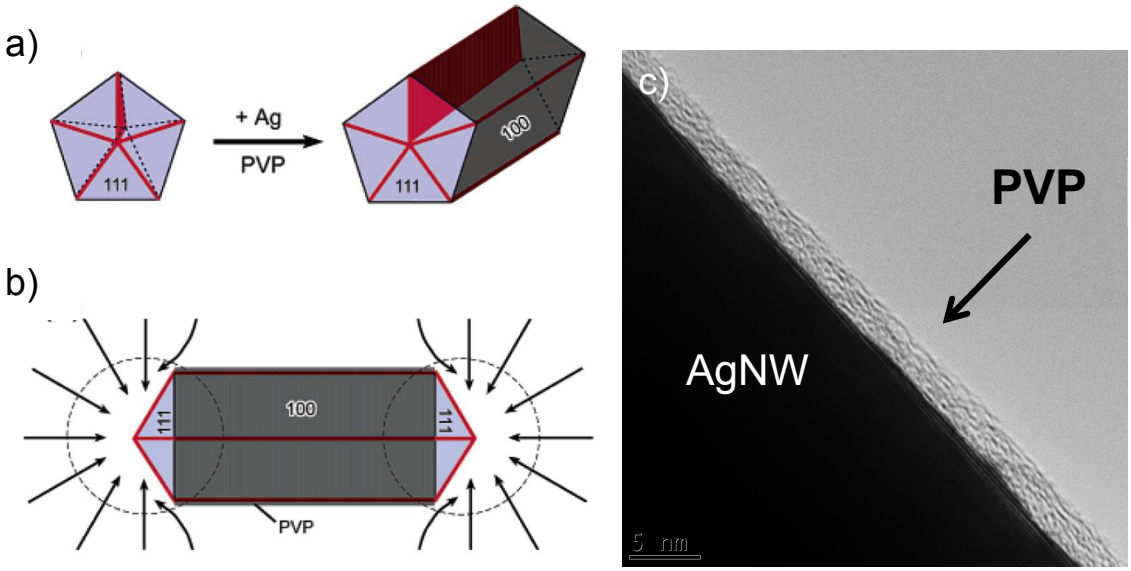

Figure 1-3: a) and b) Diagram of the process of AgNW growth by polyol process, from Sun et al.*[51] c) TEM image of the PVP layer left on AgNW walls after synthesis.*

1.2.2 Fabrication of metallic nanowire networks

Material deposition is a critical step in the fabrication of AgNW-based TE. In the case of networks of 1D nanostructures such as metallic nanowires or carbon nanotubes, the deposition must lead to randomly oriented nanostructures to favor the electrical conduction.[57] It is necessary to find a simple and reproducible method being also cost-efficient.

To fabricate thin films, several wet chemistry methods exist that were discussed by Pasquarelli et al.[58] and are displayed in Figure 1-4. There is a variety of methods available for depositing nanowires, all low cost and with relatively high throughput considering they are wet chemistry methods made in ambient conditions. In the case of 1D nanostructures, some methods can induce a preferential orientation such as spin coating and dip coating, and must be addressed carefully. The techniques most reported for AgNW deposition in the literature are spin coating, spray deposition, rod coating or simply drop casting. During this thesis work, several methods were tested. Some tests of doctor blading were performed at the LMGP but the resulting network properties were changing depending on the samples or on the operator. Therefore the mainly used methods for AgNW deposition during this thesis work were spin

coating and spray coating. The experimental conditions of these two deposition methods are detailed in Chapter 2.

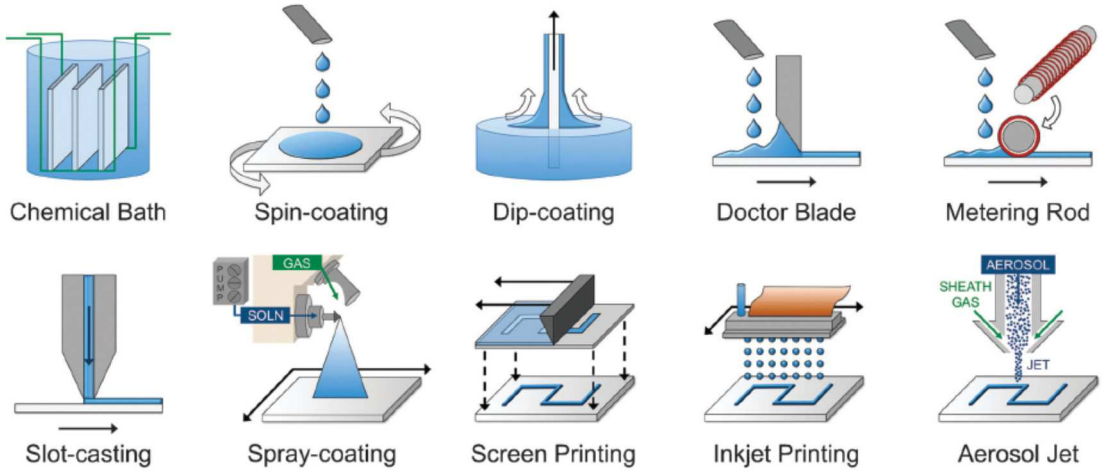

Figure 1-4: The different wet chemistry methods of deposition.[58]

1.2.3 TCM main properties

The tradeoff existing in TCM between electrical conductivity and optical transparency is critical in the fabrication of efficient transparent electrodes. However requirements for a material are generally application-dependent and secondary criteria such as flexibility, thermal stability or surface roughness can also be considered for TE. This section aims at defining the requirements of the major properties of AgNW networks and introducing the secondary properties that will also be addressed in this thesis regarding their integration into devices.

1.2.3.i Optical properties

Optical transmittance

Transparency is one of the two critical properties of TCM. In the case of screens or transparent heaters placed on windows, it is definitely a key criteria as the human eye must see through them. As previously noted, within solar cells the optical transmittance through the TCM is related to the amount of photons that could be absorbed by the cell and generate charge carriers. Therefore this application demands the most stringent requirements regarding TCM, *i.e.* an optical transmittance above 90%.[59] To compare transparencies of different materials or different samples, the optical transmittance value at the wavelength 550 nm is generally used, as the human eye maximum sensitivity stands close to this wavelength. However one has to keep in mind that there is interest in materials with high transmittance in the IR range, for

example in semi-transparent solar cells for which a majority of the solar spectrum entering the cell is appreciable (see section 1.2.6.i).

Transmittance regarding incident light wavelength has different behaviors depending on the material considered. For TCO and graphene, it is directly related to the film thickness. For 1D nanomaterials such as carbon nanotubes networks, metallic grids of metallic nanowire networks, it is related to the number of present nanostructures (the network density), their size and their chemical composition. Transmittance spectra of different TCM are presented in Figure 1-5. TCO, although being very conducting and transparent in the visible range have transmittances strongly decreasing at high wavelengths, mainly because of plasma absorption. Materials made of nanosticks such as AgNW network and CNT networks show however high transmittances on the whole range of wavelength considered during the measurement.

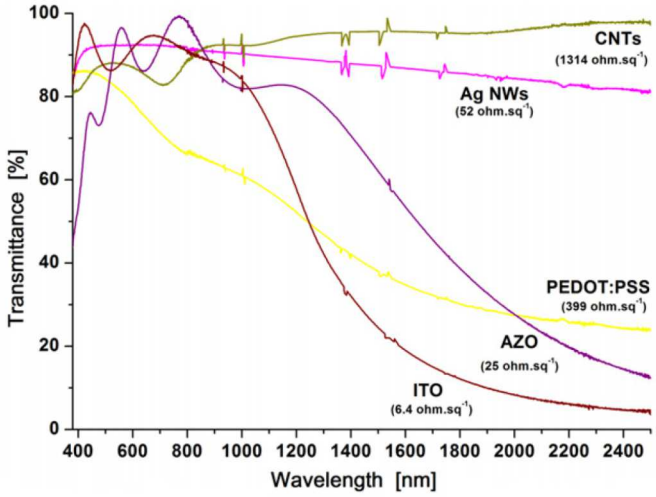

Figure 1-5: Optical transmittances of different TCMs with their corresponding sheet resistance.[11]

Haze factor

Another optical parameter that needs to be considered for TCM applications is the haze factor. The haze factor is a parameter that quantifies the amount of light scattered by the investigated material and is simply defined as the ratio between diffuse transmittance and total transmittance.

$$HF = \frac{T_{diffuse}}{T_{total}} \qquad (1\text{-}1)$$

The requirements regarding haziness are different depending on the TCM applications. For example touch panels and transparent heaters placed on windows would need a low haze factor to ensure comfort for the human eye and unblurred viewing, while solar cells performance would be enhanced by a high haze factor.[60,61] For instance Chih-Hung *et al.*[60] observed a clear improvement of dye-sensitized solar cells conversion efficiency by increasing the haziness of FTO layers used as top transparent electrodes, as displayed in Figure

1-6. This is why investigations have been lately focused on fabricating transparent electrodes with enhanced haziness (on TCO[10] but also AgNW networks[62]) since scattering light enhances the optical path length of photons in solar cells, increasing their probability to be absorbed by the active area of the cell to generate charge carriers.

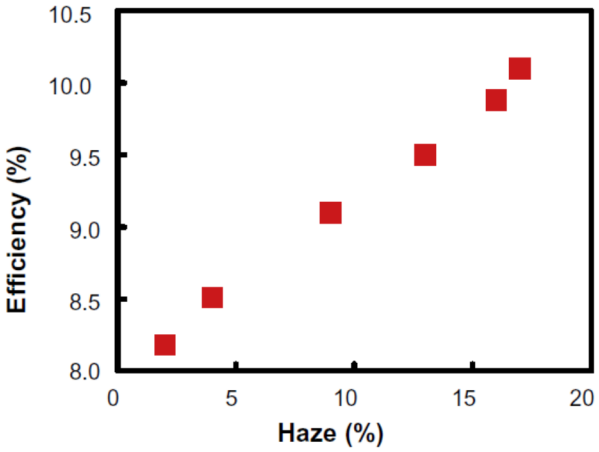

Figure 1-6: Effect of haze in FTO-based TE on dye-sensitized solar cells efficiency.[60]

1.2.3.ii Electrical properties

Electrical percolation

In order to increase the transparency of a material, one solution is to decrease its thickness, or, for the relevant materials, the network density. However this process usually results as well in a reduction of the materials conductivity. Regarding AgNW networks, or any material being conducting through connected stick-like structures, the decrease of network density leads eventually to a situation where the density of nanowires is not sufficiently high to create efficient electrical pathways across the whole sample. The network is then said to be non-percolating. Percolating and non-percolating networks are pictured in Figure 1-7, where red marked paths indicate the electrically percolating areas.

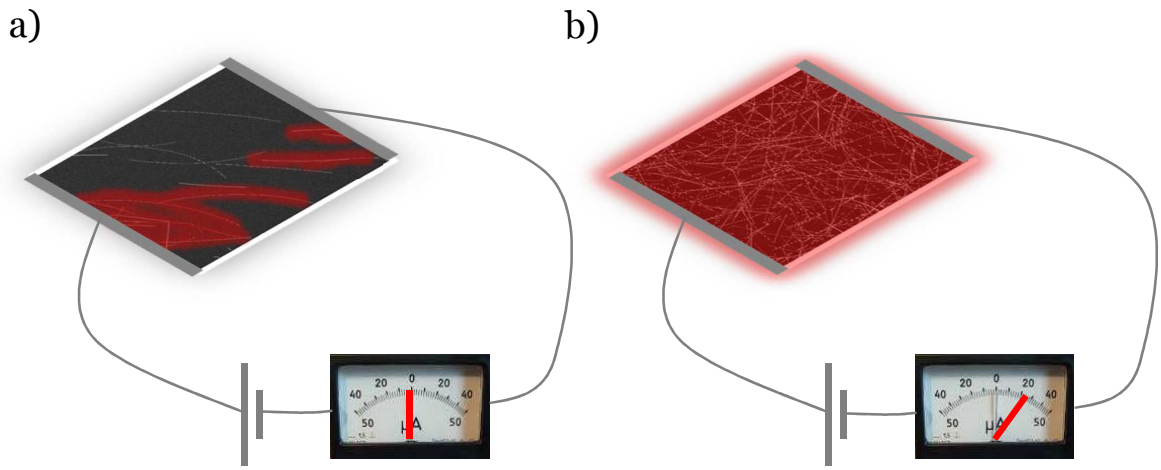

Figure 1-7: Diagram of a) non-percolating and b) percolating AgNW networks. The red marks indicate the electrical pathways connected to one or two of the contact electrodes.

Percolation theory has been already used to study AgNW network properties[63,64] and more generally 2D-stick networks[65,66] (that is the most suitable model for the material studied here). It relates the conductivity of the film to the density of sticks through the percolation conductivity scaling law which can be expressed as follows:[67]

$$\sigma \propto (n - n_c)^m \qquad (1\text{-}2)$$

Where σ is the network electrical conductivity, n is the network density (number of nanowires per unit area), n_c is the percolation threshold (or critical density) and is defined as the number of nanowires per unit area at which the network has the probability $\frac{1}{2}$ to be percolating, and m is the percolation exponent. Monte Carlo simulations show that for an infinite 2D system of percolating objects, the percolation exponent m is approximately equal to $\frac{4}{3}$.[67] The critical density n_c depends on the nanowire length, L_{NW}, and was determined from Monte Carlo simulations by Li and Zhang[65] to be:

$$n_c \cdot {L_{NW}}^2 = 5.637\ 26 \pm 0.000\ 02 \qquad (1\text{-}3)$$

Figure 1-8 shows an example of Monte-Carlo simulation results performed by Daniel Langley[68] at the LMGP, in collaboration with University of Liège, to determine the critical density of a network using a specific stick length of 37.5 µm. The black curve represents the probability of one nanowire, numbered i+1, to make a network with a density of i nanowires to be percolating for the first time. The critical density is directly found by looking at the nanowire density corresponding to the cumulative probability (blue curve in Figure 1-8) of 0.5.

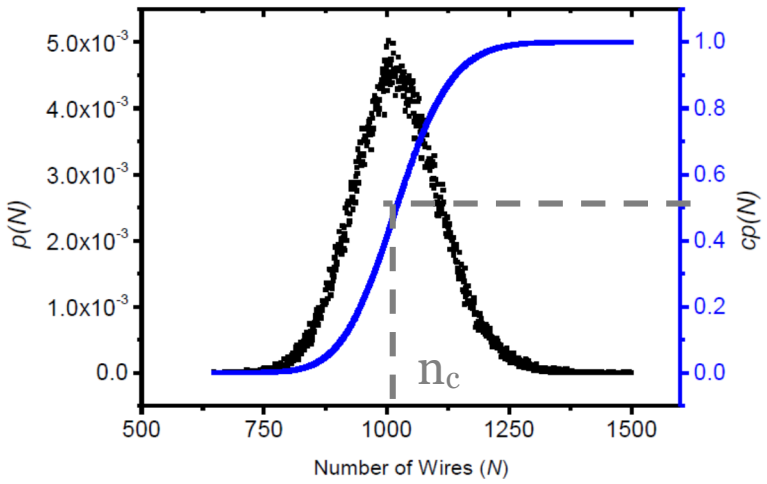

Figure 1-8: Results from Monte-Carlo simulations showing the probability of a network to become percolating for the first time when one supplementary stick is added (black, more information in reference[68]) as well as the cumulative probability, allowing to determine the critical density n_c (blue). The stick studied in this figure have a length of 37.5 µm and the studied system is a square of side 500 µm.

Additional simulation studies have been presented by Daniel Langley,[68] in order to investigate the impact of nanowire orientation, or nanowire curvature on the percolation properties within the system. He also studied the impact of a finite size space on the percolation occurrence.

Equation 1-3 is coherent with the intuitive idea that a network composed of longer AgNW is associated with a lower critical nanowire density. Nanowire dimensions have definitely an impact on the density needed to optimize the sample: the onset of percolation in the 2D stick system is determined predominantly by the length of the wire, which therefore governs the network sparseness at optimal density (and therefore its transmittance). One has however to be aware that the percolation threshold always increases with macroscopic anisotropy.[57] Therefore the random orientation of the nanowires is highly recommended to optimize percolation and avoid too high network density which could reduce the optical transmittance. Percolation dominates the electrical behavior of low density networks. This has been shown by De *et al.*[63] especially through the results presented in Figure 1-9. It shows that the resistance of 1D nanostructured TCM with low density (dashed lines) don't follow the expected bulk behavior (solid lines). This has to be taken into account regarding the tradeoff between transmittance and conductivity, strongly related to the stick density.

Although percolation occurrence is of great scientific interest, metallic nanowire networks optimized and designed to be integrated into devices have a network density about one order of magnitude larger than the critical density defined by Equation 1-3.

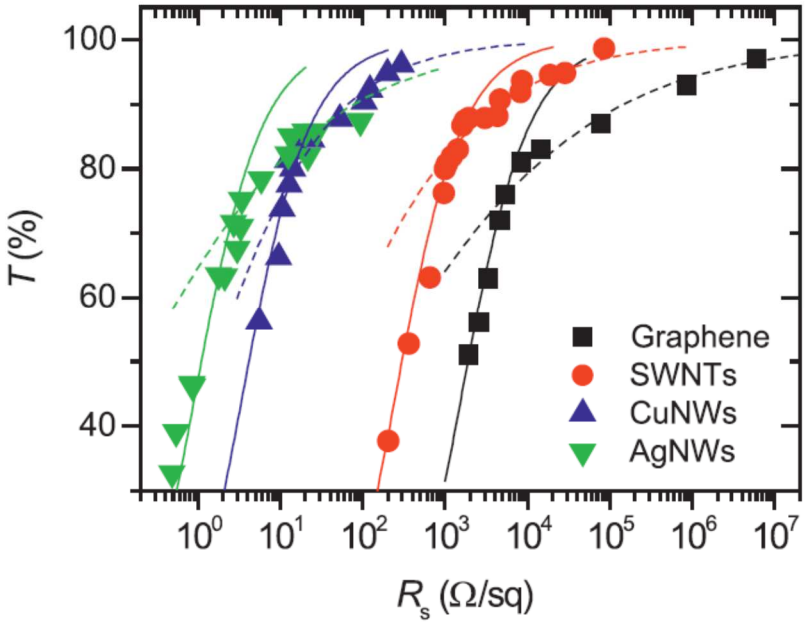

Figure 1-9: Experimental data showing the transmittance versus the sheet resistance of different TCM types associated to different layer thickness or network density. The lines are associated with different models: the bulk model (solid lines) or the percolation-based model (dashed lines) which exhibit different behavior depending on the graphene layer thickness or stick density.[63]

Sheet resistance

A local measure of the electrical resistance is of great interest to estimate the homogeneity of a sample and ensure its effectiveness when integrated into a device. This can be made by a four-point probes measurement allowing to know the sheet resistance of the material at a specific location. Sheet resistance is measured on thin films which are seen as two dimensional layers. Therefore the current flow during four point probes measurement, passing through two outer probes, is along the layer plane and not perpendicular to it. The voltage is then measured between two inner probes. The sheet resistance R_s is related to the sample resistivity ρ and thickness t with the following equation:

$$R_s \cong \frac{\rho}{t} \qquad (1\text{-}4)$$

The resistance of a material can be written as

$$R = \frac{\rho L}{A} = \frac{\rho L}{Wt} \qquad (1\text{-}5)$$

with L the sample length and A its area, also equals to the width W times the thickness t, as pictured in Figure 1-10. The resistance R is then related to the sheet resistance R_s with the following formula:

$$R \approx R_s \frac{L}{W} \qquad (1\text{-}6)$$

Sheet resistance are generally written in Ω/□ (Ohm per square) which is equivalent to Ω but is used only for sheet resistances in order to avoid confusion with bulk resistances. The name ohm per square comes from the fact that, in a square, $L = W$. According to Equation 1-

6, a material having a sheet resistance R_s of 2 Ω/□ will have a resistance R of 2 Ω, therefore they are equivalent but sheet resistance is independent of any geometrical dimension. Sheet resistance measurements are used in the TCM field to enable the comparison of samples made of different materials, sizes and geometries.

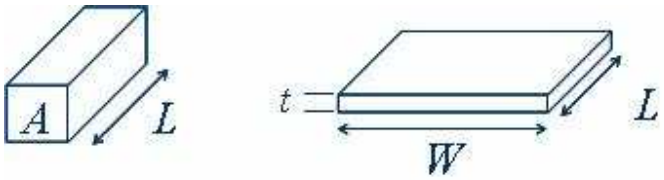

Figure 1-10: Diagram representing a bulk material (left) and a thin film (right).

Sheet resistance requirements in TCM depend on the intended application, as shown in Figure 1-11. The most stringent ones being for solar cells, for which the TE sheet resistance should be around or below 10 Ω/□.

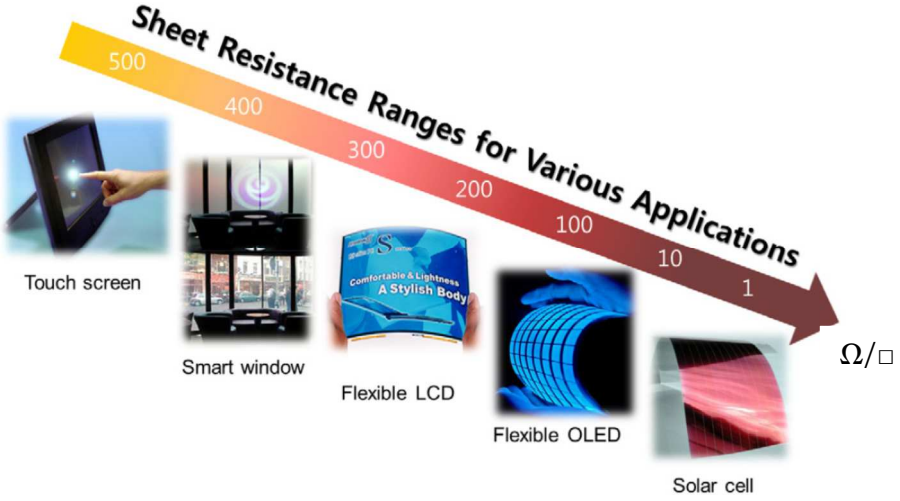

Figure 1-11: TE sheet resistance requirements depending on the application.[69]

Conductivity improvement by post-deposition treatments

As deposited AgNW networks are generally not as efficient as they could considering their density, mostly because of organic residues and bad electrical contact between nanowires, which increase the network resistance. Post-deposition treatments are therefore used to improve the conductivity of metallic nanowire networks without changing their density. Several treatments have been tested in the literature, the most used being thermal annealing. This technique has been shown to be efficient to significantly reduce the networks resistance[70], but has not been studied in details. A thorough experimental study of this process is proposed in Chapter 3, and some of the results we obtained have been published in

2014.[71] Other techniques of conductivity improvement have been developed to be efficient as well, such as acid treatment,[72] mechanical pressing[28] or illumination[73,74] or laser[75] sintering. Some of them will be presented in Chapter 3 as well.

1.2.4 Issues regarding material fabrication and lifetime

Optical and electrical properties are major criteria in the field of TCM. However other requirements arise from the way materials are fabricated and integrated into a device, requirements such as thermal and mechanical stability, and some other arise from the device lifetime improvement such as electrical and chemical stability. Several of these properties were discussed during this thesis work, therefore the present section aims at defining them.

1.2.4.i Thermal stability

One of the major drawback of metallic nanowires when compared with TCO is the thermal stability. Considering the nanoscale size of the NW, they are less stable at high temperature than an oxide layer. Cylindrical geometry instabilities were first observed by Plateau, and studied theoretically by Lord Rayleigh, who proposed an analysis of liquid jets under periodic perturbation.[76] Nichols and Mullins then extended this work to solids.[77] They made the statement that single crystals rods are expected to spheroidize during annealing and break into spheres due to surface diffusion driven by a reduction of surface energy, as pictured in Figure 1-12. Karim et al.[78] in particular addressed this issue for gold nanowires and observed spheroidization experimentally. Spheroidization leads to a loss of the electrical percolation within a network, therefore thermal treatment must be addressed carefully on AgNW networks to keep their conduction proprieties. The temperature of instability is highly dependent on the nanowire structure (presence of defects for instance) and on their diameter, as will be further discussed in Chapter 4.

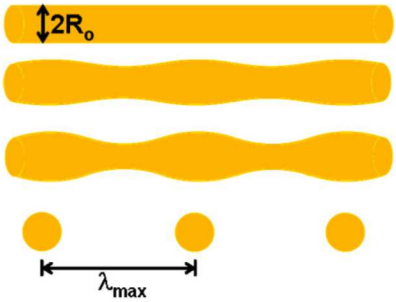

Figure 1-12: Schematic representation of thermally-induced instability in metallic nanowires.[78]

The problem of nanowires thermal instability has been addressed in the literature and several solutions have been proposed to overcome it, especially by coating the nanowires with

a TCO, which also increases the network adhesion. This has been tested with TiO_2,[79] ZnO[80,81] and more recently AZO[82] layers. The AZO-AgNW layer was then integrated in a solar cell and the AZO was observed to also increase the amount of collected electrons.[82]

1.2.4.ii Electrical stability

Electrical failure is also a key issue for nanowire-based electrodes considering the small diameter of these particles and the current density flowing, which can be high depending on the application. The networks must withstand the electrical load that they undergo. For example Khaligh and Goldthorpe[83] estimated that the current generated in an organic solar cell (around 10 $mA.cm^{-2}$) would correspond to a current density of $4x10^4$ $A.cm^{-2}$ flowing in a AgNW network with sheet resistance around 12 Ω/□. Therefore, according to these authors, the electrodes would fail in few days. The process of electrical breakdown in metallic nanowires is driven by electromigration.[84] Electrical instability of metallic nanowires will be further studied in Chapter 5 since it plays a key role in devices lifetime.

1.2.4.iii Mechanical stability

Mechanical stability is crucial when flexible applications are in focus. The TCM must be able to be deposited on flexible substrates without degrading it, and must resist when bending without losing its conductivity. TCO suffer from brittleness and the thin layers tend to crack under mechanical stress, as shown in the scanning electron microscopy (SEM) picture displayed as Figure 1-13a. The electrical conduction is altered and even, in most cases, lost on the whole sample. Studies are therefore currently done to improve TCO flexibility.[1,85] Unlike TCO, AgNW networks conductivity have been shown to be very stable under bending[11] as can be seen in Figure 1-13b. The malleable nature of metals of this size makes AgNW suitable for flexible applications. Some contacts might be damaged but the number of nanowire junctions on the sample makes the network fault tolerant, and the sample is still conducting even if few contacts are broken.

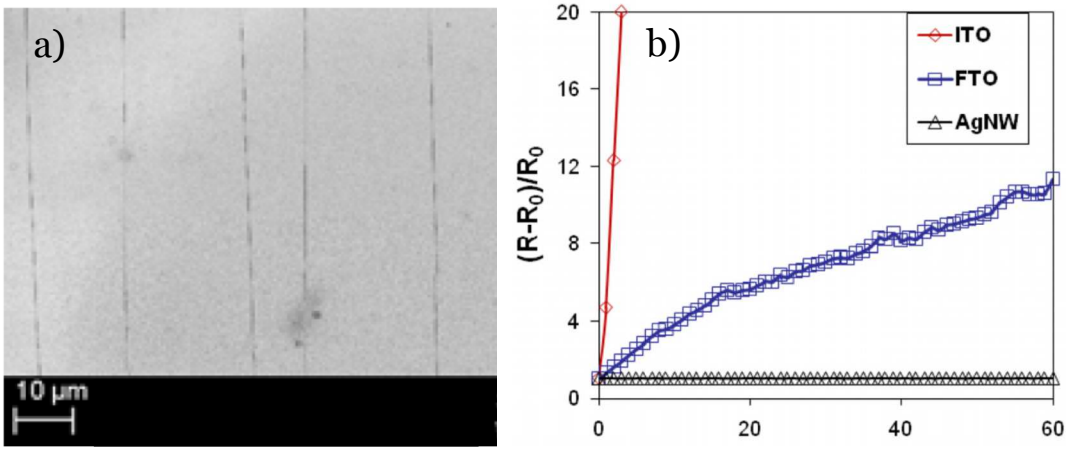

Figure 1-13: a) Image of cracked ITO after mechanical flexions b) measure of different TCM reduced electrical resistances versus the number of mechanical bending, associated to a radius of curvature of 5 mm.[11]

1.2.4.iv Problems of corrosion and adherence

AgNW-based TE have been seen in the literature to be sensitive to natural daylight and humidity.[86] Atmospheric conditions are strongly impacting AgNW, which is a problem of main importance for their integration into optoelectrical devices. Metals commonly suffer from atmospheric corrosion. In the case of silver, the blackish layer appearing on domestic silverware comes from the reaction of the metal with hydrogen sulfide (H_2S), coming from carbonyl sulfide (OCS) present in the atmosphere in small quantities. Hydrogen sulfide reaction with silver then forms silver sulfide (Ag_2S). The process follows these reaction equations:

$$OCS + H_2O \rightarrow H_2S + CO_2$$

$$2Ag + H_2S \rightarrow Ag_2S + H_2$$

The corrosion of AgNW in air by sulfur can be very rapid and a shell of Ag_2S surrounding the nanowires appears after few weeks, as shown in Figure 1-14. [87] This sulfur corrosion leads to a change in the resistance of the sample, and alters the nanowire morphology. To overcome this issue, several solutions have been proposed such as encapsulation with polymers,[88] graphene cover,[89] or coated metallic oxide.[81] In addition to the improvement of stability against atmospherical corrosion, these different methods allow to improve adhesion of the nanowires on the substrate.[37,90]

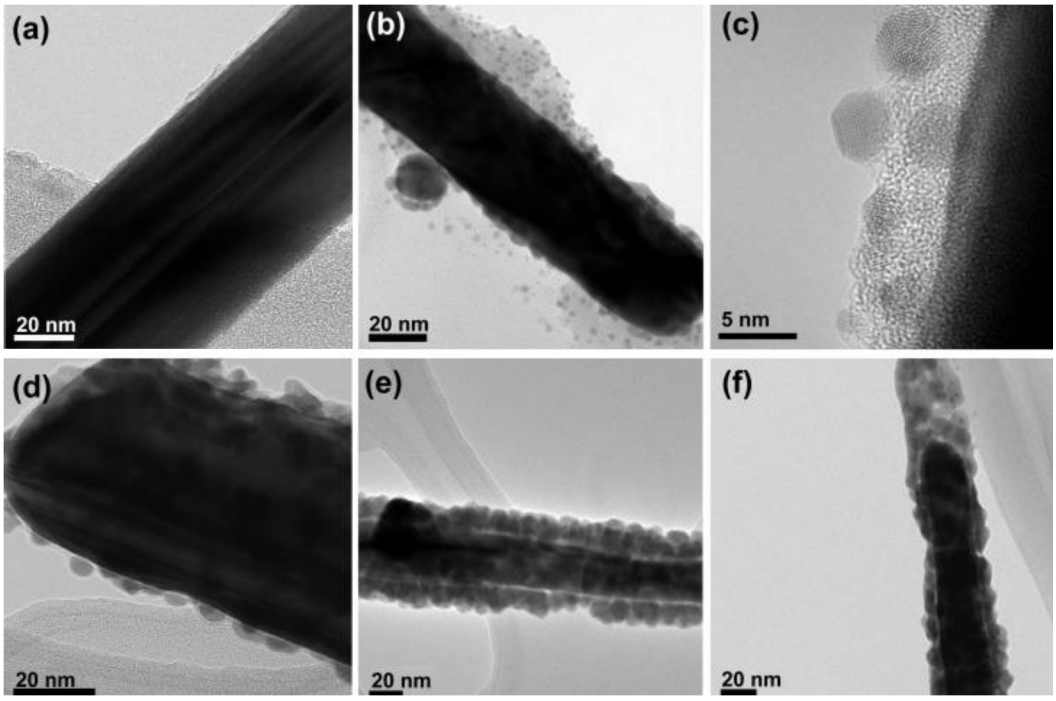

Figure 1-14: TEM images showing sulfur corrosion of AgNWs exposed to air in ambient conditions[87] a) as deposited, b and c) after 3 weeks, d) after 4 weeks, e) after 5 weeks and f) after 24 weeks.

1.2.5 TCM comparison

Depending on the application, the most relevant type of TCM to use, with the suitable properties can change. Several tools were developed in the TCM field in order to compare the different materials in terms of properties or fabrication processes and choose the most relevant one for a specific application. Few of them are presented in this section as well as the characteristics of different TCM.

Haacke figure of merit

Considering the tradeoff between electrical and optical properties that TE are subjected to, their optimization is a delicate challenge. We introduced the major criteria for TE comparison, *i.e.* high transmittance and low sheet resistance. In order to evaluate the potential of AgNW networks as TE and to compare them with other TCMs, the use of a figure of merit (FoM) is of great interest. Different FoM are used in the field of TEs. One well known was defined by Haacke in 1976,[91] and is related to transmittance T and sheet resistance R_S as follows:

$$FoM_{Haacke} = \frac{T^x}{R_S} \qquad (1\text{-}7)$$

The value of x depends on the properties aimed. For example, when x = 10, the maximum value of FoM is achieved for samples with a transmittance equals to 90%. If the goal is a transmittance of 99%, x must be equals to 100. That way, this figure of merit can be adapted

depending on the requirements of a specific application. Since a transmittance of 90% is often required in most applications, x is generally considered equal to 10. The major drawback of this FoM is that it doesn't take into account other parameters such as haziness, heat capacity, thermal and mechanical stability... these parameters can become critical depending on the application. One has to be aware that the efficient integration and use of a TCM in an optoelectronic device is not always guaranteed by a high FoM. Other features have to be taken into account, such as thermal, electrical and chemical stability, as well as band alignment.[92] However Haacke's FoM is a rather simple way to compare different materials using the two main requirements of any TCM application.

Sheet resistance versus transmittance diagram

To compare the performances of different TCM, their transmittance (at 550 nm) is generally plotted versus their sheet resistance (in logarithmic scale). One of these transmittance versus sheet resistance diagram is presented in Figure 1-15 with optical and electrical properties of ITO,[25,93] graphene,[14,93–95] CNT networks,[18,25,93] copper nanowires networks,[30,31,96,97] copper nanotrough,[38] AgNW networks[26–28,93,98] and LMGP-made FTO[10] (all data correspond to recent literature results published after 2009). The dashed lines correspond to different isovalues of Haackes FoM: 200, 100, 50, 10, 1 with units $10^{-3}\ \Omega^{-1}$.

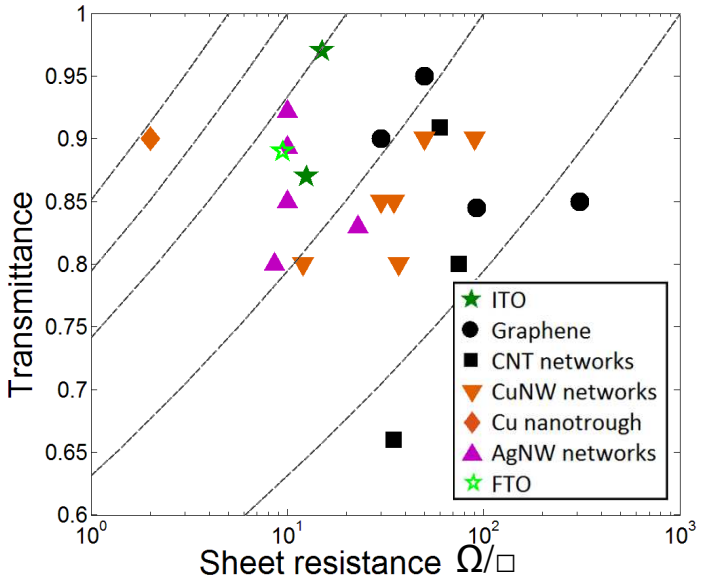

Figure 1-15: Transmittance versus sheet resistance diagram comparing the properties of different TCMs: ITO,[25,93] graphene,[14,93–95] carbon nanotube networks,[18,25,93] copper nanowires networks,[30,31,96,97] copper nanotrough,[38] silver nanowires networks[26–28,93,98] and LMGP-made FTO.[10]

As previously said, the properties of metallic, especially copper, nanotrough are the best on this diagram. However AgNW networks exhibit also excellent properties but need less fabrication steps. Carbon-based materials have lower conductivities but still lie within the range of resistances required for applications such as LCDs and touch screens (see Figure 1-11). However transparency and conductivity are not the only parameters to be considered. Fabrication process as well as other properties such as flexibility and stability are of great importance. Therefore Figure 1-16 displays a table which summarizes these different types of requirements for TE, and how the different TCMs respond to them.

Type	Material	Transparency[a] (%)	Sheet resistance[a] (Ω/□)	Compatibility with flexible substrate	Use as top electrode	Stability
Doped metal oxide	Indium-tin oxide	80 to 95	10 to 50	No	Difficult (sputtering damage, high temperature process)	Good
	ZnO:Al	80 to 95	10 to 100	No	Difficult (sputtering damage, high temperature process)	Poor stability when they are ultrathin
Thin metal layer	Thin metal layers	40 to 60	1 to 80	Yes	Yes	Depend on metal material
	Dielectric/metal/ dielectric multilayers	70 to 85	1 to 80	Yes	Yes	Unknown
	Metal grids	~80	6 to 50	Yes	Difficult (patterning issue)	Unknown
Transparent conductive polymer	Poly(3,4-ethylene dioxythiophene): polystyrene sulfonic acid	75 to 90	50 to 1000	Yes	Yes	Degrade under humidity, high temperature, and UV exposure
Nanoscale material	Graphene	60 to 95 90, 97.4	100 to 3000 30, 125	Yes	Difficult (complicated process)	Unknown
	Carbon nanotube	50 to 95	20 to 1000	Yes	Difficult (complicated process)	Unknown
	Ag nanowire	70 to 90	5 to 200	Yes	Yes	Corrode through chemical reaction, such as oxidation and suffixation

Figure 1-16 Comparison of the different TCM main properties: optical, electrical, mechanical, fabrication issues and stability.[99]

1.2.6 Applications of AgNW networks

AgNW networks used as transparent electrodes have been extensively studied the past few years and intended for a variety of applications that can be flexible. They have the ability to fit different requirements in terms of optical and electrical properties, through the variation of the network density and of the nanowire dimensions, as will be further discussed in Chapter 4. Therefore a lot of different applications have been intended for this material in several fields, and the main ones are discussed in this section through a brief bibliographical study.

1.2.6.i Solar cells

The development of solar cells is a popular topic since a large number of people feels concerned about the energy crisis, and the need for alternative and green energies. Fossil fuels are contributing to global warming and might be, sooner or later, limited by resources depletion. Photovoltaics, among other sustainable green energy technologies, has been and is still developed to offer an alternative to fossil fuel energy, with efforts devoted to fabrication costs reduction, efficiency improvement and the study of storage issues, in order to integrate solar cells in smart grids for instance.

Transparent electrodes constitute a key component of solar cells, directly related to the amount of photons entering the cell and to the number of photo-generated electrons collected, and is therefore contributing to the cell efficiency. This application of AgNW-based TE has been the most studied in literature especially in organic or dye-sensitized solar cells.

One of the topics of main interest recently is the development of flexible solar cells that use simple and low cost fabrication methods such as printing.[100,101] Another idea behind flexible solar cells is that they can be integrated on surfaces with complex shapes. Unlike the commonly used ITO, AgNW networks are flexible and keep their electrical properties intact when bending, as seen earlier. Andrés *et al.*[62] have recently synthesized high aspect ratio AgNW, observed to be a low-cost alternative to ITO in organic solar cells (OSC) whereas inducing only a small decrease in the power conversion efficiency. Guo *et al.*[100] obtained conversion efficiency up to 5.81 % by using AgNW as top electrode in tandem OSC. The use of AgNW could lead to the development of solar cells that can be entirely printed. This has been the focus of Angmo *et al.*[101] who could fabricate single and tandem cells almost entirely in ambient conditions with roll-to-roll method, an easily scaling up method of deposition on flexible substrates. Several other works have been performed which proved the efficiency of AgNW networks as transparent top electrode in OSC.[27,102,103] The networks show excellent capacities of bending within this application,[104,105] even at low radius of curvature, as displayed in Figure 1-17a. As mentioned earlier, some works have also been developed in the literature around the topic of the TE haziness.[60] The aim is to increase the solar cells

efficiency by increasing the photon pathways within the cell, allowing a higher probability of absorption

AgNW-based electrodes were also used to fabricate polymer solar cells that are semitransparent in the visible region[106,107] (for instance with a transmittance of 66% at 550 nm),[108] see Figure 1-17b. While transparent in the visible range, the cell is however highly absorbing in the IR range. As seen previously, AgNW networks, unlike other TCM like ITO, are highly transparent in this region, allowing the cell to be very efficient by absorbing in the IR while being transparent for the human eye. But one has to be careful that for the integration of such electrodes on windows, or any surface that needs to be seen through (like windscreens for instance), the haziness must remain low.

Fully printed solar cells induce an increase of fabrication throughput and a reduction of the cost. Another way to reduce even more the TE cost, and so the solar cell cost, would be to use another material, cheaper than silver. Some studies have therefore started on solar cells top transparent electrodes using copper nanowires.[109–111]

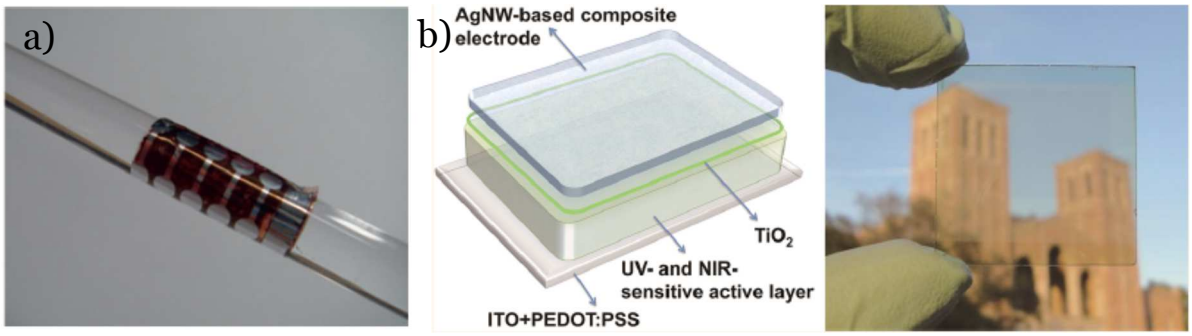

Figure 1-17: a) Flexible organic solar cell rolled around a rod of diameter around 1 or 2 cm,[104] b) transparent polymer solar cell with a transmittance of 66% at 550 nm.[108]

1.2.6.ii OLEDs and PLEDs

LED (Light-Emitting Diode) have an architecture similar to solar cells, except that instead of extracting the charge carriers, the TE conducts electrons and holes towards the active layer to allow them to recombine radiatively, leading to a photon emission. The need for a transparent electrode comes from the fact that the emitted light must be seen from the device. OLED (Organic LED) and PLEDs (Polymer LED) have been widely developed the past decade and find applications in displays and lighting.[112] Recently, flexibility and stretchability have been added as new requirements for TE in OLED in order to make their full fabrication compatible with solution process *i.e.* low-cost methods and enable new kind of applications such as foldable screens or rollable wallpaper-like lamps, for example.[113]

Transparent electrodes are a key component of OLED, and were fabricated with ITO up to now. However ITO is brittle which induces lower efficiency and lower brightness when

bending. In order to fabricate flexible OLED or PLED, researches are focused on emerging TCM. Some works have already been performed on graphene[95] or CNT[40] electrodes but the use of AgNW appears also very promising. AgNW networks have shown at least comparable, nay better results than ITO,[70,114–117] as shown in Figure 1-18a and b. AgNW networks have in addition been seen to enable high performance of OLED operating at low voltage[98,118]. This material also presents the ability to be stretched without decreasing the OLED brightness,[113] as demonstrated in Figure 1-18c. Gaynor *et al.*[117] presented very efficient white OLED made with AgNW, with stabilized viewing angle.

One major drawback of AgNW networks for integration in OLEDs (and solar cells) is however the high surface roughness increasing risks of short-circuit, considering that the different layers in an OLED are very thin. But this parameter has been diminished by using a polymeric layer, covering the AgNW network.[119,120]

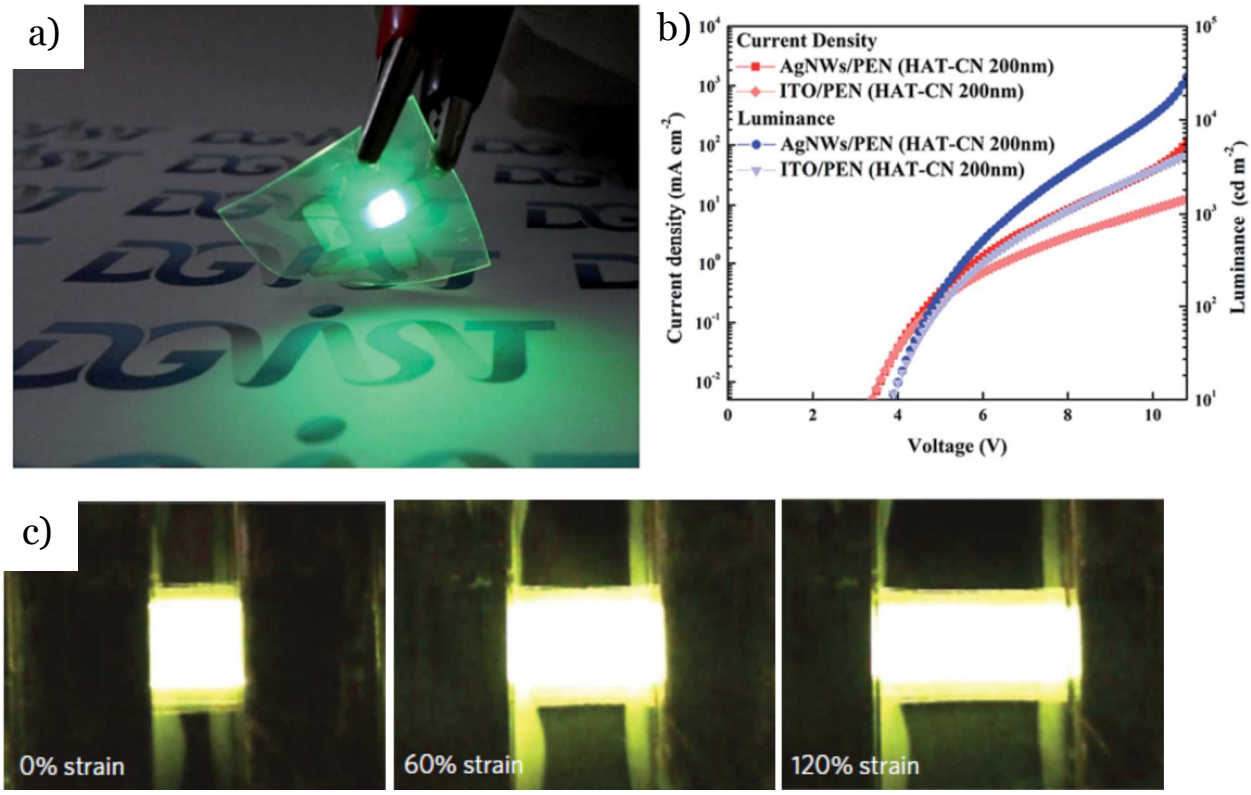

Figure 1-18: a) Photo of a flexible OLED with a TE made of AgNW[98] b) Current density and luminance characteristics comparison between AgNW and ITO-based TE in a flexible OLED [98] c) Stretchable OLED brightness under different tensile strains.[113]

1.2.6.iii Touch screens and sensors

Considering the increasing demand in personal electronics, the interest towards touch panels is growing. They can indeed be found in smartphone screens, tablets PCs but also in intelligent floors. Researches are orienting toward flexible touch screens and sensors to be

integrated onto complex or non-planar shapes, and to develop applications such as wearable sensors[121] or rollable touch screens. As for solar cells and LEDs, the main used TCM nowadays in touch panels is ITO but the use of AgNW network could help to develop flexible touch panels or sensors with low cost fabrication by printable processes. However the haziness induced by the use of AgNW networks is an issue for their application in touch screens and must be addressed carefully: low haze coupled with high transmittance is highly recommended in touch panels in order to avoid a blurred or distorted image from the display.

The most studied technologies of AgNW-based touch panels/sensors are resistive[75,122] and, more recently, capacitive[123,124], presented in Figure 1-19. Resistive touch panels are made with two electrodes separated by an insulating spacer. When a pressure is applied, the electrodes touch each other and an electrical contact is made. AgNW have been shown to be easily deposited on large surfaces,[122] and to be efficient in resistive technology. Regarding the capacitive technology, a conductive element like a finger approaching the electrode induces a change in the electrical field and therefore a change of the capacitance that can be measured and localized. The improvement of touch panel flexibility has been widely studied and the mechanical stability was improved by combining AgNW with other materials like polymer[124,125] or CNT.[126] A polymer layer also improves the adhesion of the material on the substrate, low adhesion being one of the main drawbacks of AgNW networks. More recently, works have been conducted on touch panels made with copper nanowires.[33]

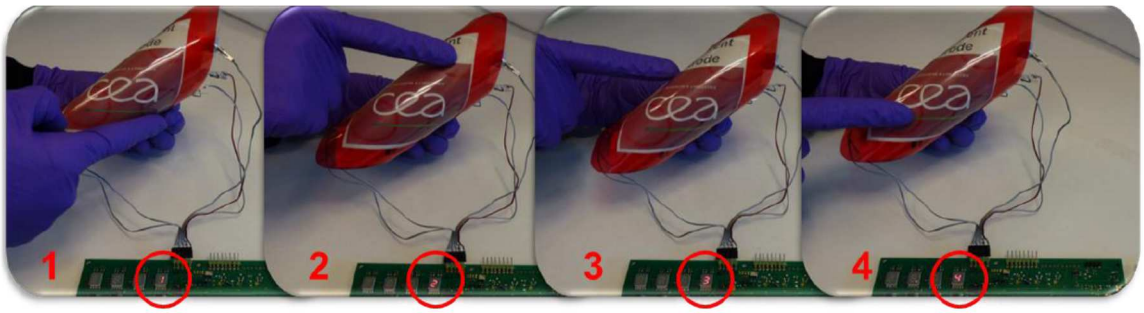

Figure 1-19: AgNW-based transparent capacitive sensor.[123] Recognition of different electrodes placed at different locations on the device (electrodes 1, 2, 3 and 4) while the sensor is bend.

1.2.6.iv Transparent heaters

Transparent heaters (TH) are transparent conducting films that can produce heat by Joule heating when a current is passing through the film. They have a variety of possible applications in defrosting or defogging vehicles windows, outdoor panel displays, or more generally devices exposed to high temperature variations. Historically, TH have been one of the first application thought for TCM in a patent describing their potential application for deicing aircraft windscreens in the late 1940s.[127] At that time, TCM were mostly represented by TCO. During the past few years, TH made from emerging TCMs such as metallic

nanowires[128,129] or carbon nanostructures[130,131] like graphene and CNT networks started to arise, as well as hybrids[22,35] for the same reasons as for other TE applications: reduction of fabrication costs, extension to large surface and increase of the flexibility, while still showing high transparency coupled with high conductivity. In the literature, the use of AgNW networks as TH was first proposed by Celle *et al.*,[128] and studied since then.[128,132,133] Studies have been especially focused on allowing high temperature elevation with low voltages.[132,133] Kim *et al.*[132] obtained excellent results with a network of R_s = 10 Ω/□, T ~ 90% and could increase the film temperature to 70°C with a voltage as low as 5V, as can be seen in Figure 1-20a. They optimized the sample properties by using clay platelets to improve the uniformity of the network on the substrate and by using thin (20-40 nm) and long (20-40 µm) nanowires. They were able to bend the AgNW-based TH (radius of curvature 10 mm) without conductivity (and so temperature elevation) degradation. Uniformity is important to obtain excellent electrical and optical properties, but also to prevent hot spots in TH. The clay platelets led as well to a better adhesion of the NW on the substrate: the samples could pass the "tape test", which is generally not the case for as deposited AgNW.

Limitations in the application of AgNW networks in TH like electrical failure and electromigration have been highlighted and research groups already started to work on overcoming these phenomena. For example, Li *et al.* created a composite made of AgNW and a heat-resistant composite to improve the thermal stability of the nanowires[134], as can be seen in Figure 1-20b where a temperature as high as 240°C can be observed without any nanowire degradation. Zhang *et al.* used graphene microsheets to improve the AgNW thermal stability and to protect them as well from oxidation [22].

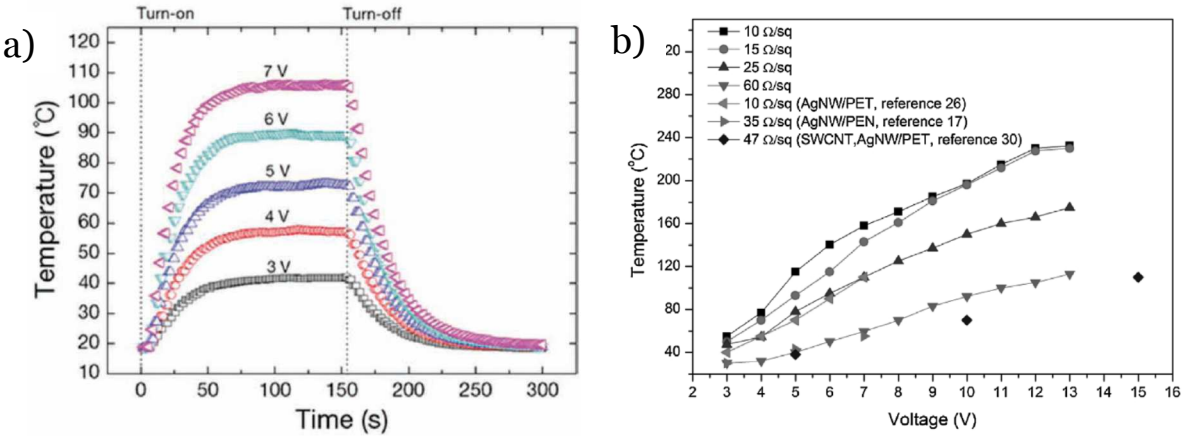

Figure 1-20: a) Temperature profile of a AgNW film with R_s ~ 10 Ω/□ versus time at different input voltages[132] b) saturation temperatures versus applied voltages for film heaters with various R_s and with heat resistant polymer composite.[134]

TH have been thoroughly studied and experimented during this thesis work. Therefore a more detailed investigation of the literature about AgNW-based TH is reported in Chapter 5, together with our experimental results.

1.2.6.v Antennas

Antennas are widely used in personal electronic devices such as laptop computer, smart phones where antenna components are essential for transmission and reception of information signals, but also for wireless network systems[135], automotive navigational systems, wearable motion detection systems, health monitoring[136] or RFID tags[137]. The application of AgNW networks as antennas has been developed quite recently, only during the past 5 years. To our knowledge, the first report of AgNW-based antennas has been made by Yang *et al.*[137] in the form of RFID tags. They could highlight the importance of the material resistance, especially in the read range (*i.e.* the distance at which the tag can be detected). They achieved a read range of 2.81 m with a RFID tag with a resistance of 63 Ω and observed that an increase of the resistance would lead to an inhibition of the read range.

Several studies have then been conducted in the development of flexible AgNW-based antennas[136,138], on flexible substrate such as PDMS but without being necessarily transparent. As PDMS is also stretchable, Song *et al.*[136] could see a variation of the resonant frequency of a microstrip patch with an applied tensile strain (see Figure 1-21). The resonant frequency of a radiating patch antenna, directly related to its length, is normally written as follows:

$$f_{res} = \frac{c}{2L\sqrt{\varepsilon_{reff}}} \qquad (1\text{-}8)$$

c is the speed of light in vacuum, L the length of the microstrip patch antenna and ε_{reff} the effective relative permittivity of the microstrip. An applied tensile strain will lead to a change of the microstrip dimensions. Therefore, f_{res} would be modified and become:

$$f'_{res} = \frac{c\sqrt{1+s}}{2L_0\sqrt{\varepsilon_{reff}}} \qquad (1\text{-}9a)$$

L_0 being the initial length and s the strain. For small strain $s \ll 1$, f'_{res} would be directly proportional to the applied strain:

$$f'_{res} = \frac{c}{2L_0\sqrt{\varepsilon_{reff}}}\left(1 + \frac{1}{2}s\right) \qquad (1\text{-}9b)$$

This behavior is of great interest for applications such as wireless strain sensing.

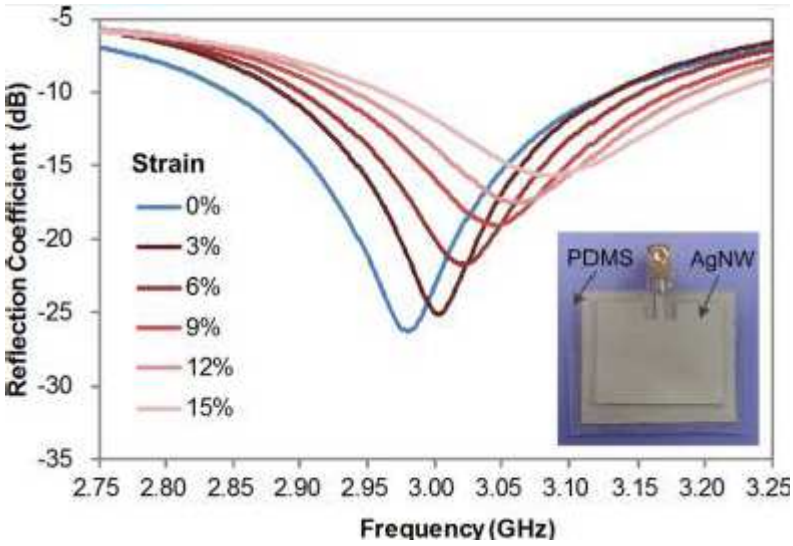

Figure 1-21: Change in the resonant frequency of a microstrip patch antenna based on AgNW and PDMS, as a function of the applied tensile strain.[136]

Beyond flexibility, Nogi *et al.*[139] tested the ability of AgNW-based antennas to be foldable. Antennas with high flexibility and foldability could improve device portability as they could be inserted into narrow spaces. Therefore the devices become lighter and smaller. Nogi *et al.*[139] identified a change in the antenna resonant frequency when folding (see Figure 1-22).

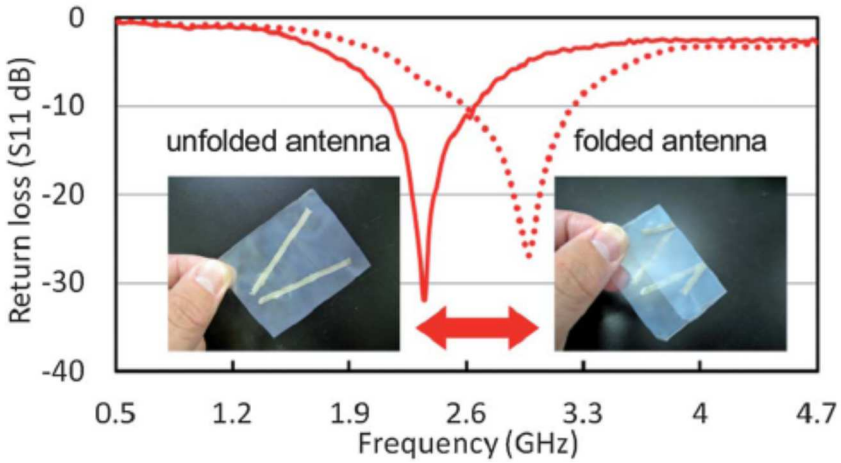

Figure 1-22: Change of the resonant frequency when folding an AgNW-based antenna.[139]

During this thesis work, tests with transparent antennas based on AgNW networks have been performed at the LMGP for the first time. Therefore additional state of the art on antennas, and especially on the importance of resistance and material roughness is displayed in Chapter 5 as well as some discussion about transparency, and experimental results.

1.2.6.vi Electromagnetic shielding

Electromagnetic (EM) shielding aims at minimizing electromagnetic interferences (EMI) emitted by electrical circuits that can cause noise signal and the malfunction of electronic devices. It can also be used to prevent EM waves to cross walls or windows (if transparent) for data protection purpose (preventing data hacking for instance) or creating electromagnetic wave-free areas like exams rooms or theaters for instance. The actual commercial target for shielding effectiveness (SE) is situated around 20 dB (99% of shielding).[88,140]

EM shielding has become an application for 1D nanoparticles first because the market wanted to orient toward ultralight materials, transparency was introduced later. Therefore CNT-based materials for EMI shielding were developed.[140–142] Huang *et al.*,[140] especially, could achieve EMI SE between 20-30 dB and highlighted the importance of the CNT aspect ratio regarding this phenomenon. From percolation theory, Huang *et al.* could indeed experimentally validate that a high aspect ratio of the CNT leads to a high conductivity and therefore increases EMI SE. Zhang *et al.*[142] found that for CNT networks, deposited on shape memory polymer, EMI SE is better at high frequencies (typically within the range 50 to 75 GHz) and increases with network density (see Figure 1-23), which can be explained by the amelioration of the material conductivity.

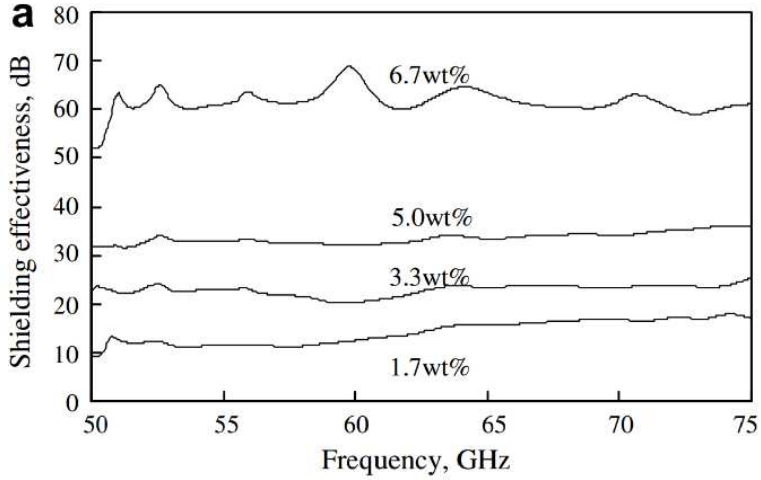

Figure 1-23: EMI SE of CNT network with different concentrations at high frequency.[142]

Different nanomaterials have then been tested such as graphite or graphene[143,144], copper nanowires[145,146] and AgNW[88,137,147,148]. For every material, the dependence of the EMI SE on the sample resistance was observed, most of the time through the increase of the EMI SE with the material content, allowed by the increase of EMI reflection by the material.[144,147,148] Yang *et al.*[137] first proposed to use AgNW as electromagnetic shielding, deposited them on a paper substrate (non-transparent) and tested the SE on a

smartphone. They could visibly decrease the electromagnetic wave coming from the phone, as depicted in Figure 1-24a. Yu *et al.*[147] could achieve very effective shielding (60 dB at 10.5 GHz) with AgNW blended with a polymer matrix (PVA), see Figure 1-24b. They compared the EMI SE of sample made from AgNW, and other from Ag nanoparticles (AgNP). AgNW were found to be more effective at low material content considering that lower resistances could be achieved with less amount of Ag (percolation theory). But they also found that samples with AgNP with lower resistances that AgNW samples achieved lower EMI SE. The resistance is a primary parameter in this application and needs to be low to increase shielding. However the AgNW density is primary as well and Yu *et al.*[147] found this parameter to be dominant over low resistance for shielding improvement due to the increase of reflections by the nanowires.

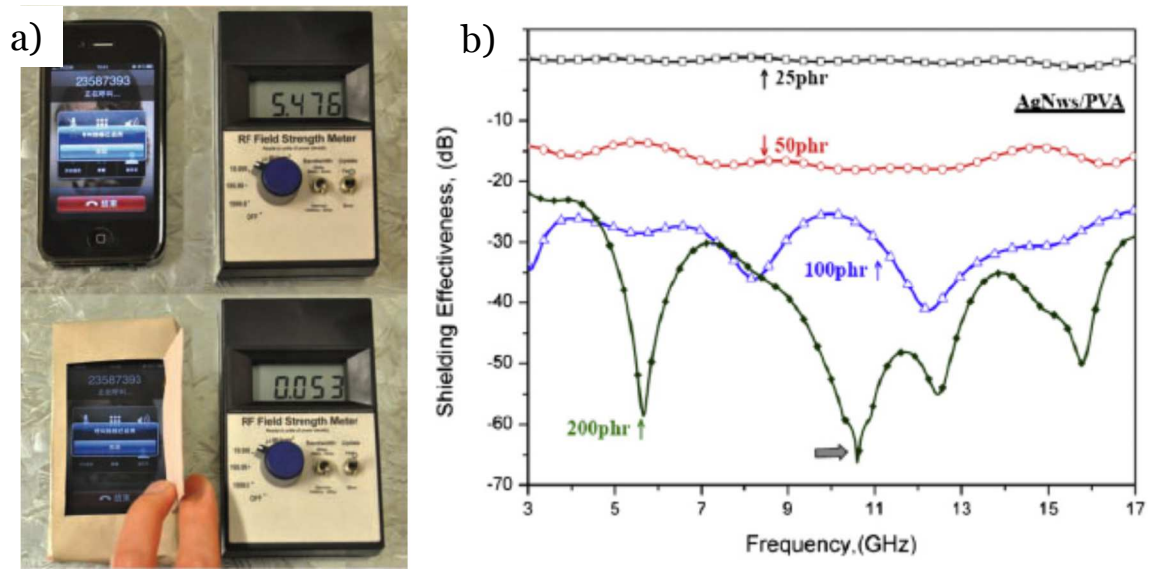

Figure 1-24: a) EM shielding of a smartphone signal with AgNW deposited on paper[137] b) SE of AgNW networks with a polymer matrix of PVA and different AgNW contents[147] (the y axis should be considered with positive values).

During this thesis, some work has been devoted to the development of a AgNW-based transparent film used for electromagnetic shielding. The preliminary results on this topic are reported in Chapter 5.

1.3 Thesis motivations and objectives

This chapter summarized some of the main problematics related to AgNW-based transparent electrodes through a study of their different properties and applications. This material has been shown to be very promising as a TCM and appears to be a good candidate to replace ITO for several applications.

The present thesis work is therefore devoted to the fabrication of efficient AgNW-based transparent electrodes, the comprehension of their physical properties, and their use in different applications. The first axis of research of this thesis was to develop a rapid and cheap method of fabrication, to deposit randomly oriented nanowires on large surfaces. Two techniques were largely used and optimized: spin coating and spray coating. Then an optimization of the network properties is of high interest, and was partly addressed through the use of a post-deposition method. This thesis focused on the method of thermal annealing which was thoroughly investigated. Combined with an efficient post-deposition method of optimization, the network density plays a key role in the TE efficiency, considering the tradeoff between conductivity and transparency directly related to the number of nanowires. An undoubted interest is in the search of an optimum density, allowing the best tradeoff. This was investigated in this document, with the help of a figure of merit. In addition, the size of a nanomaterial being of great importance regarding its physical properties, the investigation of the role of the nanowire diameter and length in the networks properties enabled to define the appreciable nanowire dimensions regarding the requirements associated with the different intended applications. This was developed by using simple physical models in order to relate directly the nanowires or networks properties (density, nanowire dimensions) to the network physical properties (resistance, transmittance, stability). Throughout the document, the problems of nanowire instability (electrical, thermal, mechanical…) were discussed. Some solutions to overcome these instabilities were proposed and tested. Finally the integration of AgNW in innovative applications such as transparent antennas and transparent electromagnetic shielding, as well as in a more traditional one, transparent heaters, was performed to validate the use of such material at the industrial level.

References

[1] Choi K-H, Jeong J-A, Kang J-W, Kim D-G, Kim J K, Na S-I, Kim D-Y, Kim S-S and Kim H-K 2009 Characteristics of flexible indium tin oxide electrode grown by continuous roll-to-roll sputtering process for flexible organic solar cells *Sol. Energy Mater. Sol. Cells* **93** 1248–55

[2] Socol G, Socol M, Stefan N, Axente E, Popescu-Pelin G, Craciun D, Duta L, Mihailescu C N, Mihailescu I N, Stanculescu A, Visan D, Sava V, Galca A C, Luculescu C R and Craciun V 2012 Pulsed laser deposition of transparent conductive oxide thin films on flexible substrates *Appl. Surf. Sci.* **260** 42–6

[3] Xavier Constant 2012 Indium facility at the Auby smelter http://www.nyrstar.com/investors/en/Nyr_Documents/English/Auby%20Indium%20Facility%2020092012%20FINAL.pdf

[4] Minami T 2005 Transparent conducting oxide semiconductors for transparent electrodes *Semicond. Sci. Technol.* **20** S35

[5] Guillén C, Montero J and Herrero J 2013 Transparent and conductive electrodes combining AZO and ATO thin films for enhanced light scattering and electrical performance *Appl. Surf. Sci.* **264** 448–52

[6] Kılıç Ç and Zunger A 2002 Origins of Coexistence of Conductivity and Transparency in SnO2 *Phys. Rev. Lett.* **88** 095501

[7] Peelaers H, Kioupakis E and Walle C G V de 2012 Fundamental limits on optical transparency of transparent conducting oxides: Free-carrier absorption in SnO2 *Appl. Phys. Lett.* **100** 011914

[8] Germain Rey 2012 *Etude d'oxydes métalliques nano-structurés (ZnO, SnO2) pour applications photovoltaïques* (PhD thesis: Université de Grenoble)

[9] Consonni V, Rey G, Roussel H, Doisneau B, Blanquet E and Bellet D 2013 Preferential orientation of fluorine-doped SnO2 thin films: The effects of growth temperature *Acta Mater.* **61** 22–31

[10] Giusti G, Consonni V, Puyoo E and Bellet D 2014 High Performance ZnO-SnO2:F Nanocomposite Transparent Electrodes for Energy Applications *ACS Appl. Mater. Interfaces* **6** 14096–107

[11] Langley D, Giusti G, Mayousse C, Celle C, Bellet D and Simonato J-P 2013 Flexible transparent conductive materials based on silver nanowire networks: a review *Nanotechnology* **24** 452001

[12] Yao S and Zhu Y 2015 Nanomaterial-Enabled Stretchable Conductors: Strategies, Materials and Devices *Adv. Mater.* **27** 1480–511

[13] Becerril H A, Mao J, Liu Z, Stoltenberg R M, Bao Z and Chen Y 2008 Evaluation of Solution-Processed Reduced Graphene Oxide Films as Transparent Conductors *ACS Nano* **2** 463–70

[14] Bae S, Kim H, Lee Y, Xu X, Park J-S, Zheng Y, Balakrishnan J, Lei T, Ri Kim H, Song Y I, Kim Y-J, Kim K S, Özyilmaz B, Ahn J-H, Hong B H and Iijima S 2010 Roll-to-roll

production of 30-inch graphene films for transparent electrodes *Nat. Nanotechnol.* **5** 574–8

[15] Eda G, Fanchini G and Chhowalla M 2008 Large-area ultrathin films of reduced graphene oxide as a transparent and flexible electronic material *Nat. Nanotechnol.* **3** 270–4

[16] Dan B, Irvin G C and Pasquali M 2009 Continuous and Scalable Fabrication of Transparent Conducting Carbon Nanotube Films *ACS Nano* **3** 835–43

[17] Gruner G 2006 Carbon nanotube films for transparent and plastic electronics *J. Mater. Chem.* **16** 3533

[18] Hecht D S, Heintz A M, Lee R, Hu L, Moore B, Cucksey C and Risser S 2011 High conductivity transparent carbon nanotube films deposited from superacid *Nanotechnology* **22** 075201–075201 – 5

[19] Doherty E M, De S, Lyons P E, Shmeliov A, Nirmalraj P N, Scardaci V, Joimel J, Blau W J, Boland J J and Coleman J N 2009 The spatial uniformity and electromechanical stability of transparent, conductive films of single walled nanotubes *Carbon* **47** 2466–73

[20] Guo C F and Ren Z 2015 Flexible transparent conductors based on metal nanowire networks *Mater. Today* **18** 143–54

[21] Zhu Z, Mankowski T, Balakrishnan K, Shikoh A S, Touati F, Benammar M A, Mansuripur M and Falco C M 2015 Ultra-high aspect ratio copper-nanowire-based hybrid transparent conductive electrodes with PEDOT:PSS and reduced Graphene Oxide exhibiting reduced surface roughness and improved stability *ACS Appl. Mater. Interfaces* **7** 16223–30

[22] Zhang X, Yan X, Chen J and Zhao J 2014 Large-size graphene microsheets as a protective layer for transparent conductive silver nanowire film heaters *Carbon* **69** 437–43

[23] van de Groep J, Spinelli P and Polman A 2012 Transparent Conducting Silver Nanowire Networks *Nano Lett* **12** 3138–44

[24] Catrysse P B and Fan S 2010 Nanopatterned Metallic Films for Use As Transparent Conductive Electrodes in Optoelectronic Devices *Nano Lett.* **10** 2944–9

[25] De S, Higgins T M, Lyons P E, Doherty E M, Nirmalraj P N, Blau W J, Boland J J and Coleman J N 2009 Silver Nanowire Networks as Flexible, Transparent, Conducting Films: Extremely High DC to Optical Conductivity Ratios *ACS Nano* **3** 1767–74

[26] Madaria A, Kumar A, Ishikawa F and Zhou C 2010 Uniform, highly conductive, and patterned transparent films of a percolating silver nanowire network on rigid and flexible substrates using a dry transfer technique *Nano Res.* **3** 564–73

[27] Leem D-S, Edwards A, Faist M, Nelson J, Bradley D D C and de Mello J C 2011 Efficient Organic Solar Cells with Solution-Processed Silver Nanowire Electrodes *Adv. Mater.* **23** 4371–5

[28] Tokuno T, Nogi M, Karakawa M, Jiu J, Nge T T, Aso Y and Suganuma K 2011 Fabrication of silver nanowire transparent electrodes at room temperature *Nano Res.* **4** 1215–22

[29] Araki T, Jiu J, Nogi M, Koga H, Nagao S, Sugahara T and Suganuma K 2014 Low haze transparent electrodes and highly conducting air dried films with ultra-long silver nanowires synthesized by one-step polyol method *Nano Res.* **7** 236–45

[30] Rathmell A R and Wiley B J 2011 The Synthesis and Coating of Long, Thin Copper Nanowires to Make Flexible, Transparent Conducting Films on Plastic Substrates *Adv. Mater.* **23** 4798–803

[31] Zhang D, Wang R, Wen M, Weng D, Cui X, Sun J, Li H and Lu Y 2012 Synthesis of Ultralong Copper Nanowires for High-Performance Transparent Electrodes *J. Am. Chem. Soc.* **134** 14283–6

[32] Hsu P-C, Wu H, Carney T J, McDowell M T, Yang Y, Garnett E C, Li M, Hu L and Cui Y 2012 Passivation Coating on Electrospun Copper Nanofibers for Stable Transparent Electrodes *ACS Nano* **6** 5150–6

[33] Mayousse C, Celle C, Carella A and Simonato J-P 2014 Synthesis and purification of long copper nanowires. Application to high performance flexible transparent electrodes with and without PEDOT:PSS *Nano Res.* **7** 315–24

[34] Ko Y-H, Lee J-W, Choi W-K and Kim S-R 2014 Ultrasonic Sprayed Graphene Oxide and Air Sprayed Ag Nanowire for the Preparation of Flexible Transparent Conductive Films *Chem. Lett.* **43** 1242–4

[35] Kim D, Zhu L, Jeong D-J, Chun K, Bang Y-Y, Kim S-R, Kim J-H and Oh S-K 2013 Transparent flexible heater based on hybrid of carbon nanotubes and silver nanowires *Carbon* **63** 530–6

[36] Lee M-S, Lee K, Kim S-Y, Lee H, Park J, Choi K-H, Kim H-K, Kim D-G, Lee D-Y, Nam S and Park J-U 2013 High-Performance, Transparent, and Stretchable Electrodes Using Graphene–Metal Nanowire Hybrid Structures *Nano Lett.* **13** 2814–21

[37] Deng B, Hsu P-C, Chen G, Chandrashekar B N, Liao L, Ayitimuda Z, Wu J, Guo Y, Lin L, Zhou Y, Aisijiang M, Xie Q, Cui Y, Liu Z and Peng H 2015 Roll-to-Roll Encapsulation of Metal Nanowires between Graphene and Plastic Substrate for High-Performance Flexible Transparent Electrodes *Nano Lett.* **15** 4206–13

[38] Wu H, Kong D, Ruan Z, Hsu P-C, Wang S, Yu Z, Carney T J, Hu L, Fan S and Cui Y 2013 A transparent electrode based on a metal nanotrough network *Nat. Nanotechnol.* **8** 421–5

[39] Blake P, Brimicombe P D, Nair R R, Booth T J, Jiang D, Schedin F, Ponomarenko L A, Morozov S V, Gleeson H F, Hill E W, Geim A K and Novoselov K S 2008 Graphene-Based Liquid Crystal Device *Nano Lett.* **8** 1704–8

[40] Zhang D, Ryu K, Liu X, Polikarpov E, Ly J, Tompson M E and Zhou C 2006 Transparent, Conductive, and Flexible Carbon Nanotube Films and Their Application in Organic Light-Emitting Diodes *Nano Lett.* **6** 1880–6

[41] Emmott C J M, Urbina A and Nelson J 2012 Environmental and economic assessment of ITO-free electrodes for organic solar cells *Sol. Energy Mater. Sol. Cells* **97** 14–21

[42] Rathmell A R, Bergin S M, Hua Y-L, Li Z-Y and Wiley B J 2010 The Growth Mechanism of Copper Nanowires and Their Properties in Flexible, Transparent Conducting Films *Adv. Mater.* **22** 3558–63

[43] Wu H, Hu L, Rowell M W, Kong D, Cha J J, McDonough J R, Zhu J, Yang Y, McGehee M D and Cui Y 2010 Electrospun Metal Nanofiber Webs as High-Performance Transparent Electrode *Nano Lett.* **10** 4242–8

[44] Lyons P E, De S, Elias J, Schamel M, Philippe L, Bellew A T, Boland J J and Coleman J N 2011 High-Performance Transparent Conductors from Networks of Gold Nanowires *J. Phys. Chem. Lett.* **2** 3058–62

[45] Sánchez-Iglesias A, Rivas-Murias B, Grzelczak M, Pérez-Juste J, Liz-Marzán L M, Rivadulla F and Correa-Duarte M A 2012 Highly Transparent and Conductive Films of Densely Aligned Ultrathin Au Nanowire Monolayers *Nano Lett.* **12** 6066–70

[46] Rathmell A R, Nguyen M, Chi M and Wiley B J 2012 Synthesis of Oxidation-Resistant Cupronickel Nanowires for Transparent Conducting Nanowire Networks *Nano Lett* **12** 3193–9

[47] Coskun S, Aksoy B and Unalan H E 2011 Polyol Synthesis of Silver Nanowires: An Extensive Parametric Study *Cryst. Growth Des.* **11** 4963–9

[48] Chen C, Wang L, Yu H, Wang J, Zhou J, Tan Q and Deng L 2007 Morphology-controlled synthesis of silver nanostructures via a seed catalysis process *Nanotechnology* **18** 115612

[49] Sun Y, Gates B, Mayers B and Xia Y 2002 Crystalline Silver Nanowires by Soft Solution Processing *Nano Lett.* **2** 165–8

[50] Sun Y and Xia Y 2002 Large-Scale Synthesis of Uniform Silver Nanowires Through a Soft, Self-Seeding, Polyol Process *Adv. Mater.* **14** 833–7

[51] Sun Y, Mayers B, Herricks T and Xia Y 2003 Polyol Synthesis of Uniform Silver Nanowires: A Plausible Growth Mechanism and the Supporting Evidence *Nano Lett.* **3** 955–60

[52] Gao Y, Jiang P, Song L, Liu L, Yan X, Zhou Z, Liu D, Wang J, Yuan H, Zhang Z, Zhao X, Dou X, Zhou W, Wang G and Xie S 2005 Growth mechanism of silver nanowires synthesized by polyvinylpyrrolidone-assisted polyol reduction *J. Phys. Appl. Phys.* **38** 1061–7

[53] Gao Y, Jiang P, Liu D F, Yuan H J, Yan X Q, Zhou Z P, Wang J X, Song L, Liu L F, Zhou W Y, Wang G, Wang C Y, Xie S S, Zhang J M and Shen D Y 2004 Evidence for the Monolayer Assembly of Poly(vinylpyrrolidone) on the Surfaces of Silver Nanowires *J. Phys. Chem. B* **108** 12877–81

[54] Gao Y, Jiang P, Liu D ., Yuan H ., Yan X ., Zhou Z ., Wang J ., Song L, Liu L ., Zhou W ., Wang G, Wang C . and Xie S . 2003 Synthesis, characterization and self-assembly of silver nanowires *Chem. Phys. Lett.* **380** 146–9

[55] Gou L, Chipara M and Zaleski J M 2007 Convenient, Rapid Synthesis of Ag Nanowires *Chem. Mater.* **19** 1755–60

[56] Lin J-Y, Hsueh Y-L and Huang J-J The concentration effect of capping agent for synthesis of silver nanowire by using the polyol method *J. Solid State Chem.* **214** 2–6

[57] Balberg I and Binenbaum N 1983 Computer study of the percolation threshold in a two-dimensional anisotropic system of conducting sticks *Phys. Rev. B* **28** 3799–812

[58] Pasquarelli R M, Ginley D S and O'Hayre R 2011 Solution processing of transparent conductors: from flask to film *Chem. Soc. Rev.* **40** 5406–41

[59] Rowell M W and McGehee M D 2011 Transparent electrode requirements for thin film solar cell modules *Energy Environ. Sci.* **4** 131

[60] Chih-Hung T, Sui-Ying H, Tsung-Wei H, Yu-Tang T, Yan-Fang C, Jhang Y H, Hsieh L, Chung-Chih W, Yen-Shan C, Chieh-Wei C and Chung-Chun L 2011 Influences of textures in fluorine-doped tin oxide on characteristics of dye-sensitized solar cells *Org. Electron.* **12** 2003–11

[61] Chiba Y, Islam A, Watanabe Y, Komiya R, Koide N and Han L 2006 Dye-Sensitized Solar Cells with Conversion Efficiency of 11.1% *Jpn. J. Appl. Phys.* **45** L638

[62] Andrés L J, Menéndez M F, Gómez D, Martínez A L, Bristow N, Kettle J P, Menéndez A and Ruiz B 2015 Rapid synthesis of ultra-long silver nanowires for tailor-made transparent conductive electrodes: proof of concept in organic solar cells *Nanotechnology* **26** 265201

[63] De S and Coleman J N 2011 The effects of percolation in nanostructured transparent conductors *MRS Bull.* **36** 774–81

[64] De S, King P J, Lyons P E, Khan U and Coleman J N 2010 Size Effects and the Problem with Percolation in Nanostructured Transparent Conductors *ACS Nano* **4** 7064–72

[65] Li J and Zhang S-L 2009 Finite-size scaling in stick percolation *Phys. Rev. E* **80** 040104–040104 – 4

[66] Žeželj M, Stanković I and Belić A 2012 Finite-size scaling in asymmetric systems of percolating sticks *Phys. Rev. E* **85** 021101–6

[67] Aharony A and Stauffer D 1991 *Introduction To Percolation Theory* (Taylor & Francis)

[68] Daniel Langley 2014 *Silver nanowire networks: Effects of percolation and thermal annealing on physical properties* (PhD thesis: Université de Grenoble, Université de Liège)

[69] Bae S, Kim S J, Shin D, Ahn J-H and Hong B H 2012 Towards industrial applications of graphene electrodes *Phys. Scr.* **2012** 014024

[70] Coskun S, Selen Ates E and Emrah Unalan H 2013 Optimization of silver nanowire networks for polymer light emitting diode electrodes *Nanotechnology* **24** 125202

[71] Langley D P, Lagrange M, Giusti G, Jiménez C, Bréchet Y, Nguyen N D and Bellet D 2014 Metallic nanowire networks: effects of thermal annealing on electrical resistance *Nanoscale* **6** 13535–43

[72] Céline Mayousse 2014 *Elaboration d'électrodes transparentes souples à base de nanofils métalliques* (PhD thesis: Université de Grenoble)

[73] Jiu J, Sugahara T, Nogi M, Araki T, Suganuma K, Uchida H and Shinozaki K 2013 High-intensity pulse light sintering of silver nanowire transparent films on polymer substrates: the effect of the thermal properties of substrates on the performance of silver films *Nanoscale* **5** 11820–8

[74] Garnett E C, Cai W, Cha J J, Mahmood F, Connor S T, Greyson Christoforo M, Cui Y, McGehee M D and Brongersma M L 2012 Self-limited plasmonic welding of silver nanowire junctions *Nat. Mater.* **11** 241–9

[75] Lee J, Lee P, Lee H, Lee D, Lee S S and Ko S H 2012 Very long Ag nanowire synthesis and its application in a highly transparent, conductive and flexible metal electrode touch panel *Nanoscale* **4** 6408–14

[76] Rayleigh L 1878 On The Instability Of Jets *Proc. Lond. Math. Soc.* **s1-10** 4–13

[77] Nichols F A and Mullins W M 1965 Surface- (Interface-) And Volume-Diffusion Contributions To Morphological Changes Driven By Capillarity *Trans. Metall. Soc. Aime* **233** 1840–8

[78] Karim S, Toimil-Molares M E, Balogh A G, Ensinger W, Cornelius T W, Khan E U and Neumann R 2006 Morphological evolution of Au nanowires controlled by Rayleigh instability *Nanotechnology* **17** 5954–9

[79] Ramasamy P, Seo D-M, Kim S-H and Kim J 2012 Effects of TiO2 shells on optical and thermal properties of silver nanowires *J. Mater. Chem.* **22** 11651–7

[80] Kim A, Won Y, Woo K, Kim C-H and Moon J 2013 Highly Transparent Low Resistance ZnO/Ag Nanowire/ZnO Composite Electrode for Thin Film Solar Cells *ACS Nano* **7** 1081–91

[81] Morgenstern F S F, Kabra D, Massip S, Brenner T J K, Lyons P E, Coleman J N and Friend R H 2011 Ag-nanowire films coated with ZnO nanoparticles as a transparent electrode for solar cells *Appl. Phys. Lett.* **4** 183307–183307 – 3

[82] Göbelt M, Keding R, Schmitt S W, Hoffmann B, Jäckle S, Latzel M, Radmilović V V, Radmilović V R, Spiecker E and Christiansen S 2015 Encapsulation of silver nanowire networks by atomic layer deposition for indium-free transparent electrodes *Nano Energy* **16** 196–206

[83] Khaligh H H and Goldthorpe I A 2013 Failure of silver nanowire transparent electrodes under current flow *Nanoscale Res. Lett.* **8** 1–6

[84] Zhao J, Sun H, Dai S, Wang Y and Zhu J 2011 Electrical breakdown of nanowires *Nano Lett.* **11** 4647–51

[85] Jeong J-A, Shin H-S, Choi K-H and Kim H-K 2010 Flexible Al-doped ZnO films grown on PET substrates using linear facing target sputtering for flexible OLEDs *J. Phys. Appl. Phys.* **43** 465403

[86] Jiu J, Wang J, Sugahara T, Nagao S, Nogi M, Koga H, Suganuma K, Hara M, Nakazawa E and Uchida H 2015 The effect of light and humidity on the stability of silver nanowire transparent electrodes *RSC Adv.* **5** 27657–64

[87] Elechiguerra J L, Larios-Lopez L, Liu C, Garcia-Gutierrez D, Camacho-Bragado A and Yacaman M J 2005 Corrosion at the Nanoscale: The Case of Silver Nanowires and Nanoparticles *Chem. Mater.* **17** 6042–52

[88] Hu M, Gao J, Dong Y, Li K, Shan G, Yang S and Li R K-Y 2012 Flexible Transparent PES/Silver Nanowires/PET Sandwich-Structured Film for High-Efficiency Electromagnetic Interference Shielding *Langmuir* **28** 7101–6

[89] Ahn Y, Jeong Y and Lee Y 2012 Improved Thermal Oxidation Stability of Solution-Processable Silver Nanowire Transparent Electrode by Reduced Graphene Oxide *ACS Appl. Mater. Interfaces* **4** 6410–4

[90] Zhu R, Chung C-H, Cha K C, Yang W, Zheng Y B, Zhou H, Song T-B, Chen C-C, Weiss P S, Li G and Yang Y 2011 Fused Silver Nanowires with Metal Oxide Nanoparticles and Organic Polymers for Highly Transparent Conductors *ACS Nano* **5** 9877–82

[91] Haacke G 1976 New figure of merit for transparent conductors *J. Appl. Phys.* **47** 4086–9

[92] Klein A 2001 Role of Surfaces and Interfaces for the Electronic Properties of Conducting Oxides *MRS Online Proc. Libr.* **666**

[93] Barnes T M, Reese M O, Bergeson J D, Larsen B A, Blackburn J L, Beard M C, Bult J and van de Lagemaat J 2012 Comparing the Fundamental Physics and Device Performance of Transparent, Conductive Nanostructured Networks with Conventional Transparent Conducting Oxides *Adv. Energy Mater.* **2** 353–60

[94] Kim U, Kang J, Lee C, Kwon H Y, Hwang S, Moon H, Koo J C, Nam J-D, Hong B H, Choi J-B and Choi H R 2013 A transparent and stretchable graphene-based actuator for tactile display *Nanotechnology* **24** 145501

[95] Sun T, Wang Z L, Shi Z J, Ran G Z, Xu W J, Wang Z Y, Li Y Z, Dai L and Qin G G 2010 Multilayered graphene used as anode of organic light emitting devices *Appl. Phys. Lett.* **96** 133301–3

[96] Han S, Hong S, Ham J, Yeo J, Lee J, Kang B, Lee P, Kwon J, Lee S S, Yang M-Y and Ko S H 2014 Fast Plasmonic Laser Nanowelding for a Cu-Nanowire Percolation Network for Flexible Transparent Conductors and Stretchable Electronics *Adv. Mater.* **26** 5808–14

[97] Hu L, Wu H and Cui Y 2011 Metal nanogrids, nanowires, and nanofibers for transparent electrodes *MRS Bull.* **36** 760–5

[98] Lee H, Lee D, Ahn Y, Lee E-W, Park L S and Lee Y 2014 Highly efficient and low voltage silver nanowire-based OLEDs employing a n-type hole injection layer *Nanoscale.* **6** 8565–70

[99] Cao W, Li J, Chen H and Xue J 2014 Transparent electrodes for organic optoelectronic devices: a review *J. Photonics Energy* **4** 040990–040990

[100] Guo F, Li N, Radmilović V V, Radmilović V R, Turbiez M, Spiecker E, Forberich K and Brabec C J 2015 Fully printed organic tandem solar cells using solution-processed silver nanowires and opaque silver as charge collecting electrodes *Energy Environ. Sci.* **8** 1690–7

[101] Angmo D, Andersen T R, Bentzen J J, Helgesen M, Søndergaard R R, Jørgensen M, Carlé J E, Bundgaard E and Krebs F C 2015 Roll-to-Roll Printed Silver Nanowire Semitransparent Electrodes for Fully Ambient Solution-Processed Tandem Polymer Solar Cells *Adv. Funct. Mater.* **25** 4539–4547

[102] Kang M-G, Xu T, Park H J, Luo X and Guo L J 2010 Efficiency Enhancement of Organic Solar Cells Using Transparent Plasmonic Ag Nanowire Electrodes *Adv. Mater.* **22** 4378–83

[103] Noh Y-J, Kim S-S, Kim T-W and Na S-I 2014 Cost-effective ITO-free organic solar cells with silver nanowire–PEDOT:PSS composite electrodes via a one-step spray deposition method *Sol. Energy Mater. Sol. Cells* **120, Part A** 226–30

[104] Lim J-W, Cho D-Y, Eun K, Choa S-H, Na S-I, Kim J and Kim H-K 2012 Mechanical integrity of flexible Ag nanowire network electrodes coated on colorless PI substrates for flexible organic solar cells *Sol. Energy Mater. Sol. Cells* **105** 69–76

[105] Yang L, Zhang T, Zhou H, Price S C, Wiley B J and You W 2011 Solution-Processed Flexible Polymer Solar Cells with Silver Nanowire Electrodes *ACS Appl Mater Interfaces* **3** 4075–84

[106] Yim J H, Joe S, Pang C, Lee K M, Jeong H, Park J-Y, Ahn Y H, de Mello J C and Lee S 2014 Fully Solution-Processed Semitransparent Organic Solar Cells with a Silver Nanowire Cathode and a Conducting Polymer Anode *ACS Nano* **8** 2857–63

[107] Lee J-Y, Connor S T, Cui Y and Peumans P 2010 Semitransparent Organic Photovoltaic Cells with Laminated Top Electrode *Nano Lett.* **10** 1276–9

[108] Chen C-C, Dou L, Zhu R, Chung C-H, Song T-B, Zheng Y B, Hawks S, Li G, Weiss P S and Yang Y 2012 Visibly Transparent Polymer Solar Cells Produced by Solution Processing *ACS Nano* **6** 7185–90

[109] Kang M-G, Joon Park H, Hyun Ahn S and Jay Guo L 2010 Transparent Cu nanowire mesh electrode on flexible substrates fabricated by transfer printing and its application in organic solar cells *Sol. Energy Mater. Sol. Cells* **94** 1179–84

[110] Stewart I E, Rathmell A R, Yan L, Ye S, Flowers P F, You W and Wiley B J 2014 Solution-processed copper–nickel nanowire anodes for organic solar cells *Nanoscale* **6** 5980–8

[111] Chen J, Zhou W, Chen J, Fan Y, Zhang Z, Huang Z, Feng X, Mi B, Ma Y and Huang W 2014 Solution-processed copper nanowire flexible transparent electrodes with PEDOT:PSS as binder, protector and oxide-layer scavenger for polymer solar cells *Nano Res.* **8** 1017–25

[112] Müllen K and Scherf U 2006 *Organic Light Emitting Devices: Synthesis, Properties and Applications* (Wiley-VCH Verlag GmbH & Co. KGaA)

[113] Liang J, Li L, Niu X, Yu Z and Pei Q 2013 Elastomeric polymer light-emitting devices and displays *Nat. Photonics* **7** 817–24

[114] Lee J-Y, Connor S T, Cui Y and Peumans P 2008 Solution-Processed Metal Nanowire Mesh Transparent Electrodes *Nano Lett* **8** 689–92

[115] Zeng X-Y, Zhang Q-K, Yu R-M and Lu C-Z 2010 A New Transparent Conductor: Silver Nanowire Film Buried at the Surface of a Transparent Polymer *Adv. Mater.* **22** 4484–8

[116] Li L, Yu Z, Hu W, Chang C, Chen Q and Pei Q 2011 Efficient Flexible Phosphorescent Polymer Light-Emitting Diodes Based on Silver Nanowire-Polymer Composite Electrode *Adv. Mater.* **23** 5563–7

[117] Gaynor W, Hofmann S, Christoforo M G, Sachse C, Mehra S, Salleo A, McGehee M D, Gather M C, Lüssem B, Müller-Meskamp L, Peumans P and Leo K 2013 Color in the Corners: ITO-Free White OLEDs with Angular Color Stability *Adv. Mater.* **25** 4006–13

[118] Yu Z, Zhang Q, Li L, Chen Q, Niu X, Liu J and Pei Q 2011 Highly Flexible Silver Nanowire Electrodes for Shape-Memory Polymer Light-Emitting Diodes *Adv. Mater.* **23** 664–8

[119] Duan Y-H, Duan Y, Wang X, Yang D, Yang Y-Q, Chen P, Sun F-B, Xue K-W and Zhao Y 2015 Highly flexible peeled-off silver nanowire transparent anode using in organic light-emitting devices *Appl. Surf. Sci.* **351** 445–50

[120] Yu Z, Li L, Zhang Q, Hu W and Pei Q 2011 Silver Nanowire-Polymer Composite Electrodes for Efficient Polymer Solar Cells *Adv. Mater.* **23** 4453–7

[121] Yao S and Zhu Y 2014 Wearable multifunctional sensors using printed stretchable conductors made of silver nanowires *Nanoscale* **6** 2345–52

[122] Madaria A R, Kumar A and Zhou C 2011 Large scale, highly conductive and patterned transparent films of silver nanowires on arbitrary substrates and their application in touch screens *Nanotechnology* **22** 245201

[123] Mayousse C, Celle C, Moreau E, Mainguet J-F, Carella A and Simonato J-P 2013 Improvements in Purification of Silver Nanowires by Decantation and Fabrication of Flexible Transparent Electrodes. Application to Capacitive Touch Sensors *Nanotechnology* **24** 215501

[124] Hu W, Niu X, Zhao R and Pei Q 2013 Elastomeric transparent capacitive sensors based on an interpenetrating composite of silver nanowires and polyurethane *Appl. Phys. Lett.* **102** 083303–083303 – 5

[125] Lee J, Lee P, Lee H B, Hong S, Lee I, Yeo J, Lee S S, Kim T-S, Lee D and Ko S H 2013 Room-Temperature Nanosoldering of a Very Long Metal Nanowire Network by Conducting-Polymer-Assisted Joining for a Flexible Touch-Panel Application *Adv. Funct. Mater.* **23** 4171–6

[126] Lee P, Ham J, Lee J, Hong S, Han S, Suh Y D, Lee S E, Yeo J, Lee S S, Lee D and Ko S H 2014 Highly Stretchable or Transparent Conductor Fabrication by a Hierarchical Multiscale Hybrid Nanocomposite *Adv. Funct. Mater.* **24** 5671–5678

[127] Harold A. Mcmaster 1947 Conductive coating for glass and method of application (patent)

[128] Celle C, Mayousse C, Moreau E, Basti H, Carella A and Simonato J-P 2012 Highly flexible transparent film heaters based on random networks of silver nanowires *Nano Res.* **5** 427–33

[129] Sorel S, Bellet D and Coleman J N 2014 Relationship between Material Properties and Transparent Heater Performance for Both Bulk-like and Percolative Nanostructured Networks *ACS Nano* **8** 4805–14

[130] Yoon Y-H, Song J-W, Kim D, Kim J, Park J-K, Oh S-K and Han C-S 2007 Transparent Film Heater Using Single-Walled Carbon Nanotubes *Adv. Mater.* **19** 4284–7

[131] Bae J J, Lim S C, Han G H, Jo Y W, Doung D L, Kim E S, Chae S J, Huy T Q, Van Luan N and Lee Y H 2012 Heat Dissipation of Transparent Graphene Defoggers *Adv. Funct. Mater.* **22** 4819–26

[132] Kim T, Kim Y W, Lee H S, Kim H, Yang W S and Suh K S 2013 Uniformly Interconnected Silver-Nanowire Networks for Transparent Film Heaters *Adv. Funct. Mater.* **23** 1250–5

[133] Wang S, Zhang X and Zhao W 2013 Flexible, Transparent, and Conductive Film Based on Random Networks of Ag Nanowires *J Nanomater.* **2013**

[134] Li J, Liang J, Jian X, Hu W, Li J and Pei Q 2014 A Flexible and Transparent Thin Film Heater Based on a Silver Nanowire/Heat-resistant Polymer Composite *Macromol. Mater. Eng.* **299** 1403–1409

[135] Inui T, Koga H, Nogi M, Komoda N and Suganuma K 2015 A Miniaturized Flexible Antenna Printed on a High Dielectric Constant Nanopaper Composite *Adv. Mater.* **27** 1112–6

[136] Song L, Myers A C, Adams J J and Zhu Y 2014 Stretchable and Reversibly Deformable Radio Frequency Antennas Based on Silver Nanowires *ACS Appl. Mater. Interfaces* **6** 4248–53

[137] Yang C, Gu H, Lin W, Yuen M M, Wong C P, Xiong M and Gao B 2011 Silver Nanowires: From Scalable Synthesis to Recyclable Foldable Electronics *Adv. Mater.* **23** 3052–6

[138] Rai T, Dantes P, Bahreyni B and Kim W S 2013 A Stretchable RF Antenna With Silver Nanowires *IEEE Electron Device Lett.* **34** 544–6

[139] Nogi M, Komoda N, Otsuka K and Suganuma K 2013 Foldable nanopaper antennas for origami electronics *Nanoscale* **5** 4395–9

[140] Huang Y, Li N, Ma Y, Du F, Li F, He X, Lin X, Gao H and Chen Y 2007 The influence of single-walled carbon nanotube structure on the electromagnetic interference shielding efficiency of its epoxy composites *Carbon* **45** 1614–21

[141] Xiang C, Pan Y and Guo J 2007 Electromagnetic interference shielding effectiveness of multiwalled carbon nanotube reinforced fused silica composites *Ceram. Int.* **33** 1293–7

[142] Zhang C-S, Ni Q-Q, Fu S-Y and Kurashiki K 2007 Electromagnetic interference shielding effect of nanocomposites with carbon nanotube and shape memory polymer *Compos. Sci. Technol.* **67** 2973–80

[143] Chung D D L 2012 Carbon materials for structural self-sensing, electromagnetic shielding and thermal interfacing *Carbon* **50** 3342–53

[144] Song W-L, Cao M-S, Lu M-M, Bi S, Wang C-Y, Liu J, Yuan J and Fan L-Z 2014 Flexible graphene/polymer composite films in sandwich structures for effective electromagnetic interference shielding *Carbon* **66** 67–76

[145] Al-Saleh M H, Gelves G A and Sundararaj U 2011 Copper nanowire/polystyrene nanocomposites: Lower percolation threshold and higher EMI shielding *Compos. Part Appl. Sci. Manuf.* **42** 92–7

[146] Gelves G A, Al-Saleh M H and Sundararaj U 2010 Highly electrically conductive and high performance EMI shielding nanowire/polymer nanocomposites by miscible mixing and precipitation *J. Mater. Chem.* **21** 829–36

[147] Yu Y-H, Ma C-C M, Teng C-C, Huang Y-L, Lee S-H, Wang I and Wei M-H 2012 Electrical, morphological, and electromagnetic interference shielding properties of silver nanowires and nanoparticles conductive composites *Mater. Chem. Phys.* **136** 334–40

[148] Ma J, Zhan M and Wang K 2014 Ultralightweight Silver Nanowires Hybrid Polyimide Composite Foams for High-Performance Electromagnetic Interference Shielding *ACS Appl. Mater. Interfaces* 7 563–76

Chapter 2 : AgNW networks fabrication and characterization of physical properties

The present chapter is a discussion related to the different techniques used during this thesis work to fabricate, improve and characterize AgNW-based transparent electrodes. The different steps of fabrication such as deposition and post-deposition treatments are detailed as well as a method to calculate the networks density. The methods of optical and electrical characterization are then detailed and discussed. A last section is dedicated to the presentation of homemade setups that have been of crucial interest to study *in situ* the AgNW networks properties under different stresses.

2.1 Fabrication of AgNW-based networks

The fabrication of AgNW networks has been an important part of this thesis work. Different types of nanowires were used in order to study the impact of length and diameter on the electrode properties. Then a variety of substrates were tested: first the work was focused on glass which presents a high transparency and high stability with temperature. But for the integration of the electrodes into flexible devices, flexible substrates were then investigated. Then, the deposition methods were of high importance to enable the fabrication of randomly oriented AgNW networks. Several methods were investigated, mainly spin coating. A spray coating setup was then built at the LMGP to allow deposition on large surfaces and was operational for the last year of this thesis. Optical and electrical properties of AgNW networks being directly related to the number of nanowires, a method of density calculation was developed using an image analysis software, and is described in this section.

2.1.1 Nanowires characteristics

Several types of nanowires were used during this thesis work. Their difference come from their dimensions: diameter and length. They were all provided by a company called Seashell Technology which synthesized them using the polyol process[1] discussed in Chapter 1. The AgNW provides were single crystalline. This was verified by TEM experiments. Their characteristics in term of dimensions are detailed in Table 2-1. The nanowires can present a distribution in size regarding their diameter and length. A precise value of these distributions is difficult to estimate in an accurate way during a reasonable time. We chose to estimate it from 1 or 2 SEM images (on ~100 nanowires) using the software Image J. The results are also displayed in Table 2-1. Histograms showing the distribution of the nanowires length and diameter measured are displayed in the Annexe.

	Ag26	Ag45	Ag55	Ag105	Ag117	Ag138
Average diameter given by Seashell (nm)	26	45	55	105	117	138
Estimated diameter distrib. with Image J (nm)	32±4	53±12	63±19	104±27	108±21	164±48
Average length given by Seashell (µm)	20.4	13.6	7.6	37.6	42.9	32.0
Estimated length distrib. with Image J (µm)	15.2±7.4	13.4±6.6	7.2±3.1	25.9±15.2	31.5±15.2	22.5±14.3

Table 2-1: Dimensions of the nanowires used during this thesis work

NB : the long nanowires (Ag26, Ag105, Ag117, Ag 138) length might be underestimated considering that a lot of them were longer that the SEM images used for the analysis and only those shorter than the image size could be measured.

The different nanowires are named after their diameter in this document. For example: we name Ag117 the nanowires with a diameter of 117 nm and a length of 42.9 µm. The nanowires used were all dispersed in isopropanol and, for some batches of Ag26 only, in water. The different dimensions of these nanowires allowed us to study the influence of both diameter and length on network physical properties. The results are presented in Chapter 4. Hereafter are displayed SEM images of AgNW networks made from nanowires with different dimensions.

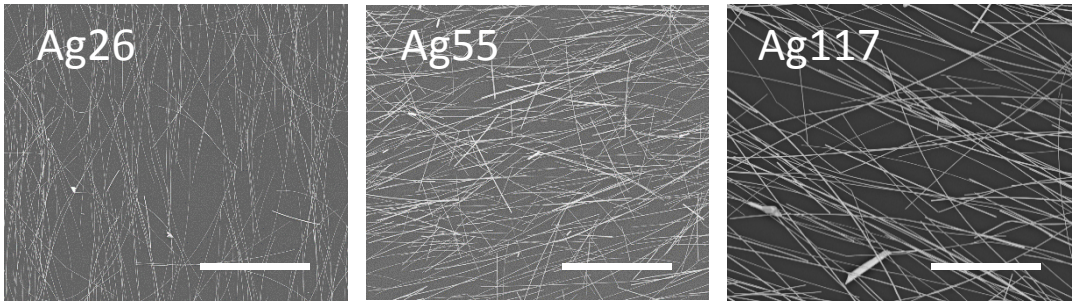

Figure 2-1: SEM images at the same magnification of AgNW networks with Ag26, Ag55 and Ag117 deposited by spin coating. The scale bars are 10 µm.

2.1.2 Substrates

During this thesis work, several transparent substrates were used. First, glass which has high transmittance and is stable at high temperatures. We used Corning glass (referenced C1737-S111) that have transmittances at 550 nm higher than 90%. It was a dedicated material to start with, as the first axis of research in this thesis work was to study the impact of thermal

annealing on the AgNW networks electrical properties. In particular, the stability of nanowires under heating was investigated, therefore the substrate must be stable under high temperature elevation, like glass is. Nanowires were also deposited on PEN (100 µm thick) that is flexible and rather transparent (87.6% at 550 nm). However this material starts to degrade at around 150°C, which is untoward as it is below the temperature of AgNW network optimization (typically around 200°C, as will be discussed in Chapter 3), and by extension to the temperature of instability that we want to study. However it was used to test the mechanical stability of the AgNW networks. Finally, we also used a transparent Kapton® (polyimide) as a substrate. This material was very flexible, stable at high temperature (up to 400°C according to Dupont™) and transparent (85% at 550 nm). It was the substrate we mainly used for the integration of optimized networks into flexible devices that undergo high temperature variations, such as flexible transparent heaters. However, it is the substrate the least transparent in the visible range, as displayed in Figure 2-2. Glass and Kapton were very transparent in the infrared range, which can be of great advantages in some applications such as solar cells where a maximum of light transmitted is appreciable.

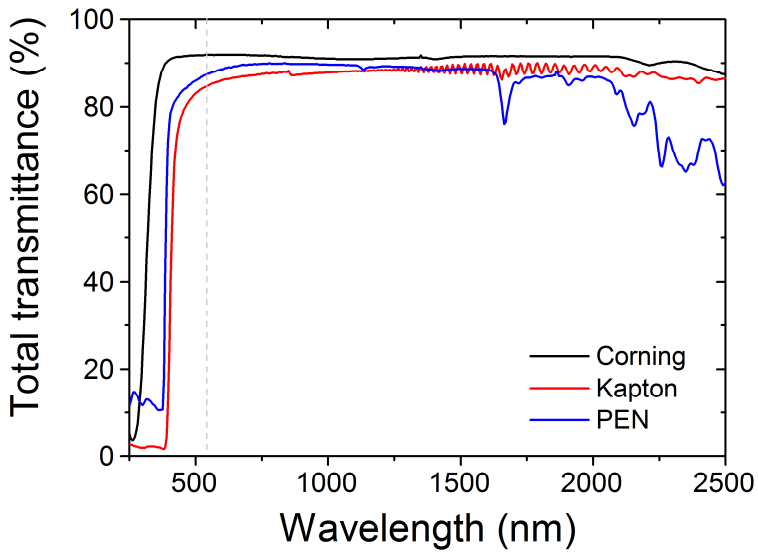

Figure 2-2: Total transmittance spectra of the different substrates used during this thesis.

Corning substrates cleaning

Corning glass substrates were cleaned before any AgNW deposition, to avoid NW aggregation or impurities within the networks. They were first immersed in acetone within an ultrasonic bath during 10 minutes in order to remove all the organic contaminants from the surface. Then the substrates were rinsed in a beaker of isopropanol heated at 150°C for several minutes. The glass slides were then dried using a nitrogen gun.

2.1.3 Nanowire deposition by wet chemistry for randomly oriented networks fabrication

To obtain efficient transparent electrodes, nanowires need to be deposited randomly and homogeneously.[2] Networks were fabricated first by using several techniques such as doctor blading or drop casting, but the techniques giving the best results and therefore the most used during the present thesis work were spin coating and spray coating. These two techniques have been introduced in Chapter 1 but the parameters used at LMGP to fabricate the samples are detailed in this section.

2.1.3.i Spin coating procedure

Spin coating is a rapid and cheap method enabling deposition at room temperature and atmospheric pressure. This technique is generally used, for instance in microelectronics, to fabricate thin films. Spin coating suffers however from a low ability to extend to large scale production as well as to large samples, yet it is an easy-access and rapid method of deposition at a laboratory scale. The apparatus used for this work, a SPS Spin 150, is displayed in Figure 2-3a. The substrate is placed on a rotating platform whose speed and acceleration can be controlled to spread a solution uniformly on the whole sample. These parameters also allow the control of the film thickness and depends on the solution viscosity. The nanowire used during this thesis work were dispersed in isopropanol which has a low viscosity, therefore the speed must be low to limit the ejection of the solution out of the sample. A limitation comes from the spin coating method: the nanowires tend to orientate radially from the center due to the centrifugal force induced by the platform rotation. A low speed is therefore also recommended to limit the radial orientation of the nanowires, by limiting the centrifugal force. However the speed has to be high enough to spread the film on the whole surface (usually 2.5 cm by 2.5 cm). Therefore a tradeoff has to be considered between sample full-coating and nanowires random orientation.

To address this issue, a specific deposition procedure was developed. Several speeds were tested and the one allowing the best deposition conditions (coverage of the entire substrate but with a limited nanowire radial orientation) was 1500 rpm (rotations per minute). To vary the density of deposited nanowires, we changed the AgNW concentration in the solution rather than the volume of solution deposited, which was kept constant. The volume used was 1 ml and was deposited in 2 coats of 0.5 ml, with a drying stage of 30 s in between (while the platform was still rotating). Each 0.5 ml was deposited using a micropipette, droplet by droplet (approximately 1 or 2 droplets per seconds for 20 seconds). This 'pulsed' deposition coupled with the drying step minimizes the amount of lost solution expulsed from the substrate, and leads to a homogeneous coating on the whole surface, as can be seen in Figure 2-3b.

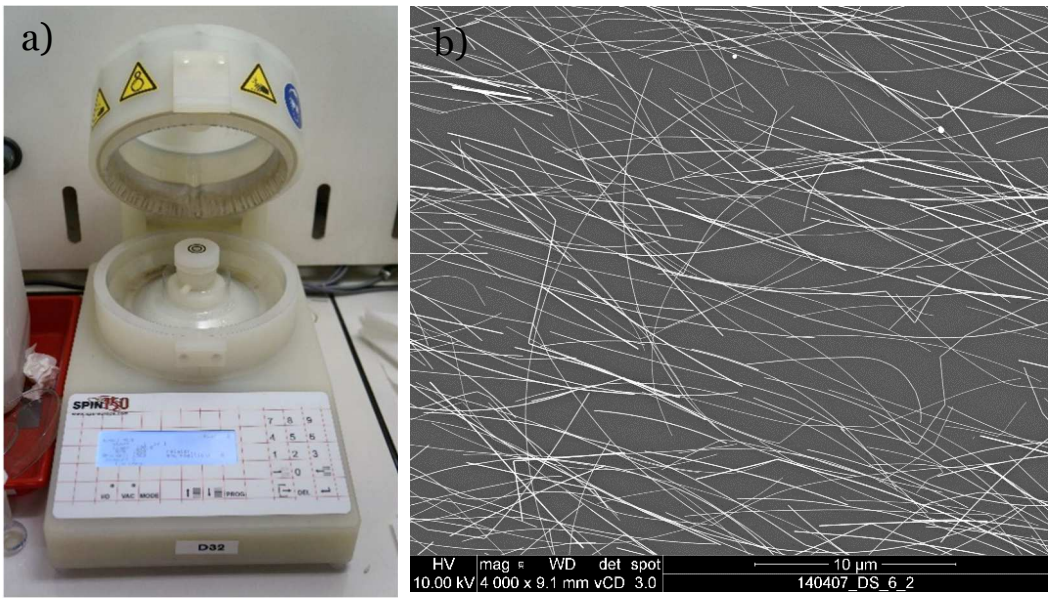

Figure 2-3 : a) Spin coater SPS Spin 150 b) SEM image of a Ag45 network deposited by spin coating 1 ml of solution of concentration 1 g.l^{-1} using the standard procedure described in the text.

Spin coating was used to fabricate AgNW networks for transparent electrodes because of its simplicity and easy access in the laboratory. However the alignment of nanowires is a problem as the anisotropy makes the number of nanowires needed for electrical percolation to increase,[2] and affects the electrical and optical properties of the network. In addition, spin coating is hardly able to scale-up, especially for flexible substrates for which a large platform is needed to avoid the substrate to fold during the rotation. To overcome these limitations, a spray deposition setup has been conceived and built in the laboratory in the framework of the present thesis. The setup is using an ultrasonic spray head that is described in the next section.

2.1.3.ii Spray coating procedure

The objectives that were meant to be fulfilled by using spray coating deposition instead of spin coating were the creation of networks without preferential orientation of the nanowires, a limitation of lost solution (by ejection) and the ability to coat large surfaces. The design of the spray setup built at the LMGP is presented in Figure 2-4a. The principle of the setup is the following: the solution enters a spray head thanks to a syringe-pusher, and is then transformed into microscopic droplets thanks to an oscillating piezoelectric ceramic. The droplets are then propelled out of the spray head (vertically) with the help of a carrier gas, and coats the sample. The spray head was mounted on a XY table allowing deposition on large samples through several sweeping patterns that can be programed. An example of pattern is presented in Figure 2-4b. The substrate is heated during deposition in order to evaporate the solvent instantaneously when the droplets are deposited, and avoid agglomeration due to the

formation of bigger drops on the surface. Such drops would lead to the creation of "coffee stains", altering both transparency and electrical properties. For this setup, a ultrasonic spray head made by Lechler was used (see Figure 2-4c, red circle) and the carrier gas used was nitrogen. The whole setup is protected by a Plexiglas hood that protects the user from solvent vapors, nanoparticles and mechanical harm by the motors. An extractor allows the deposition chamber to be ventilated.

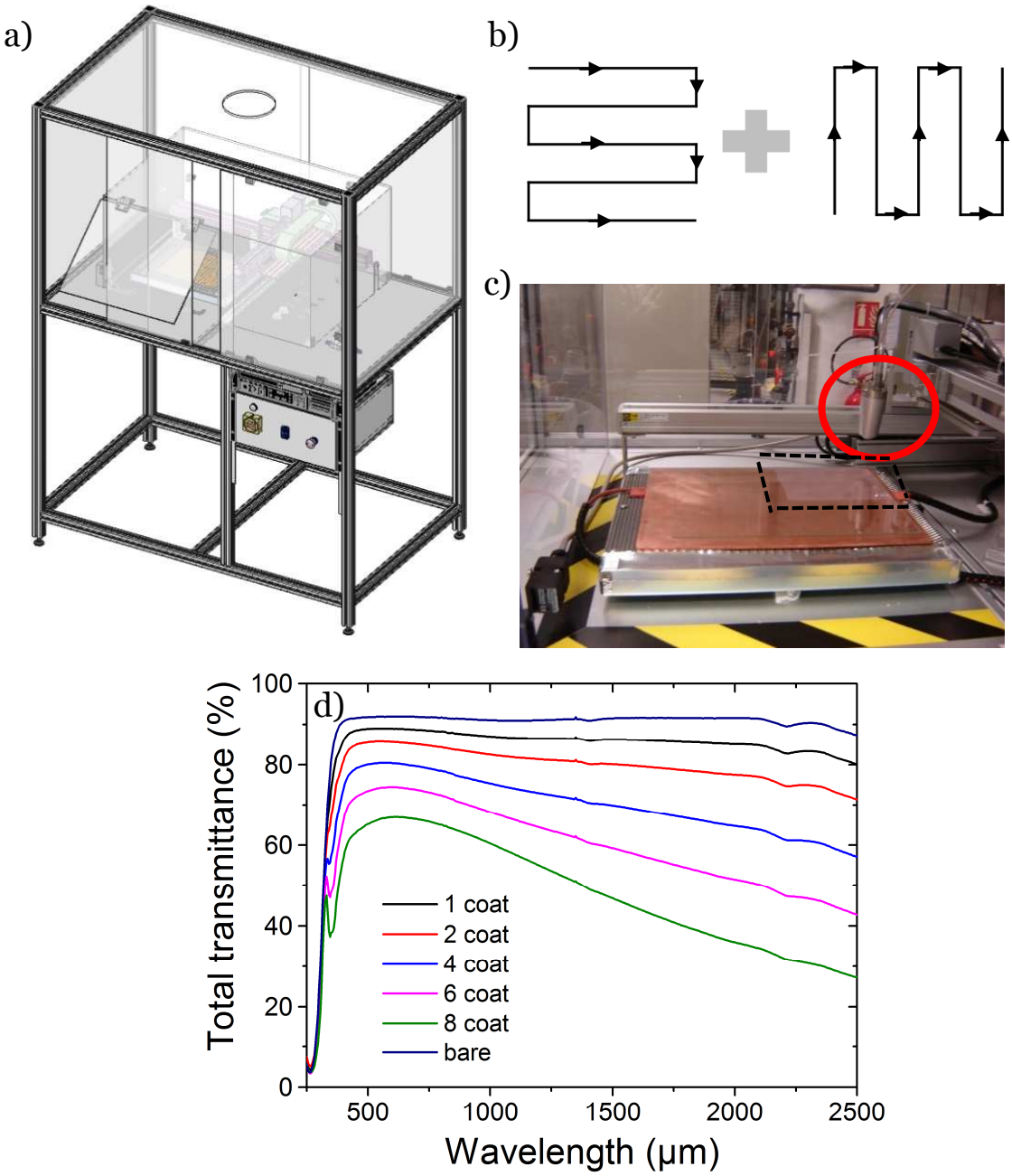

Figure 2-4: a) The spray setup built at the LMGP b) the standard coating pattern of the spray head c) photograph of the LMGP spray setup. The spray head is circled in red and the coated surface framed with black dash d) Transmittance of AgNW networks fabricated by spraying Ag45 nanowires, with different number of coats.

Several weeks have been devoted to the development and optimization of a standard procedure to deposit Ag45 nanowires by spray. The parameters leading to the best samples are the following: the spray head is placed at a height of 4.5 cm from the substrate, the solution concentration is around 0.5 $g.l^{-1}$, with a flow rate of 42.4 $ml.h^{-1}$. The concentration must be rather low to avoid the clogging of the provision line. The carrier gas has a flow rate of 7 $L.min^{-1}$ and the substrate is placed on a hot plate heated at 90°C, which is a high enough temperature to evaporate isopropanol efficiently and instantly. The spray coats the sample using motors that control the spray head: two times a combination of east-west + south-north sweeping, (see pattern in Figure 2-4b, and resulting coating framed in black dash in Figure 2-4c). The transmittance of Ag45 networks deposited by spray regarding the number of coats is presented in Figure 2-4d. The optimized deposition conditions allowing a good tradeoff between high transmittance and low resistance were found to be two coats, as just mentioned.

Advantages and drawbacks of spray coating

The resulting samples are very homogeneous and the nanowires randomly oriented. That can be seen by comparing Figure 2-5a with Figure 2-3b. The transmittance is uniform across the sample. We could fabricate homogeneous samples on large surfaces, up to 32*22 cm, with the spray setup (see Figure 2-5b). Such large specimen was necessary for performing experiments on electromagnetic shielding (see Chapter 5).

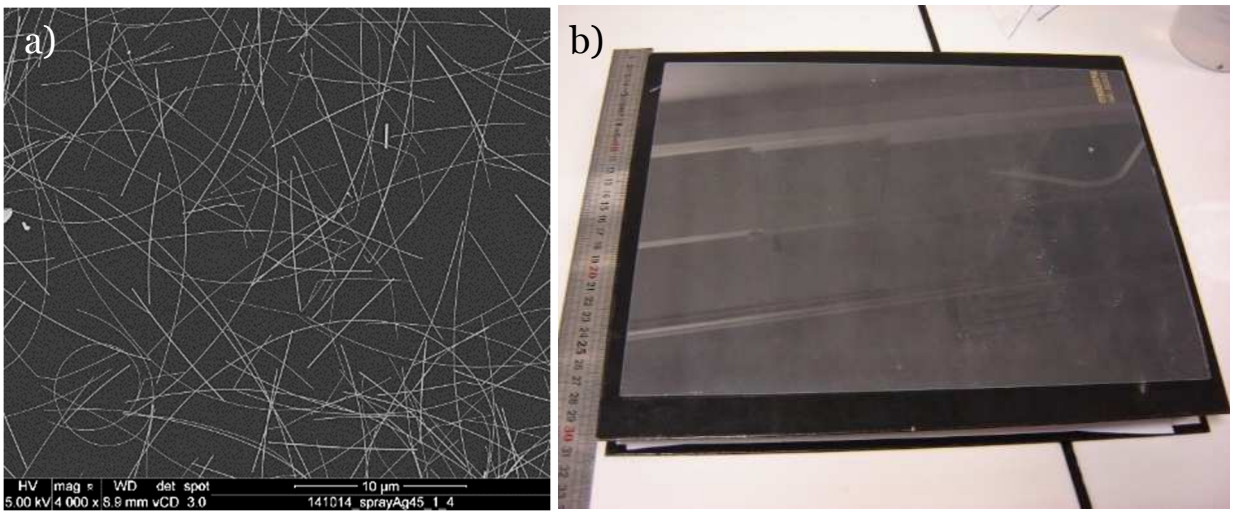

*Figure 2-5: a) SEM image of a Ag45 network sprayed with the standard spray procedure b) a large sample of size 32*22 cm of Ag45 nanowires sprayed on glass at the LMGP.*

The spray technique is very efficient to fabricate homogeneous networks but have a major drawback: long nanowires seem to be cut by the spray head. They appear shorter

compared to those coated by spin coating. This shortening is a problem regarding percolation, since the critical density is increasing when the length decreases, as discussed in Chapter 1. The relation between nanowire length and network electrical properties will be investigated experimentally in Chapter 3. The length reduction originates from the ultrasonic frequency of the piezoelectric ceramic oscillation in the spray head, allowing the formation of small droplets, but which tends to cut the nanowires by scission. The evolution of the nanowire length under ultrasonication has been studied using an ultrasonic bath Elmasonic Elma S15H, having an ultrasonic frequency of 37 kHz. The average length of Ag105 nanowires regarding ultrasonication time in this apparatus are presented in Figure 2-6. These results come from the measurement of nanowires lengths using the software Image J (~50 nanowires) on optical images of samples drop casted with solutions sonicated for different durations. The decrease in length is visible as well as the decrease of the standard deviation, even if the frequency is lower than the sprays (100 kHz). This is of great interest considering that we usually sonicate the nanowire solutions before their deposition (either by spin or spray coating) in order to homogenize them and prevent aggregates during deposition. The results reported in Figure 2-6 show that the nanowire length doesn't decrease significantly after few seconds in the ultrasonic bath. Therefore we ultrasonicated our solutions during 30 to 60 s before deposition, which was found to be long enough to disperse the nanowires without inducing too much degradation. This duration seems very low compared to the low length decrease rate shown in Figure 2-6. However the solutions were sometimes sonicated several times and therefore we chose to keep sonication duration as short as possible to avoid nanowires scission.

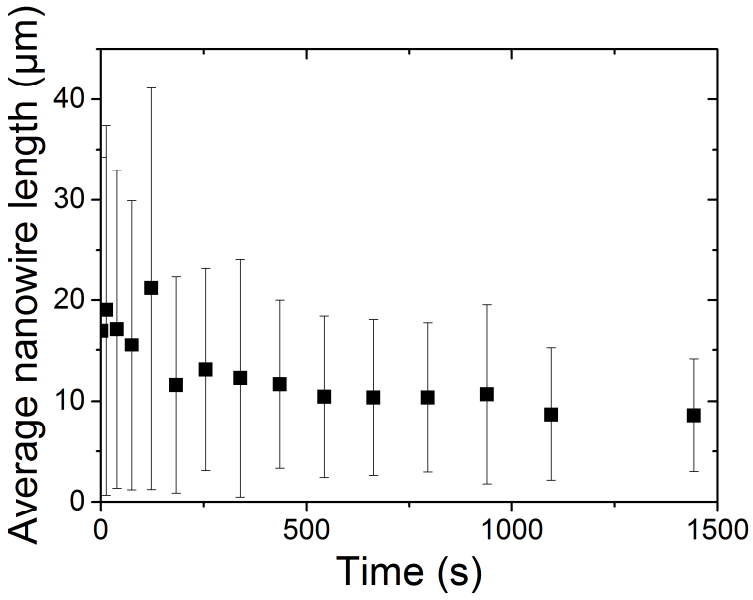

Figure 2-6: Length dependence with ultrasonication duration of Ag105 nanowires.

Networks with thinner nanowires such as Ag26, Ag55 and Ag45 seem to be less damaged than Ag105, Ag117 and Ag138 by the spray head, probably because they are also shorter. Therefore the effects of the length decrease is less significant on the networks properties than for the long nanowires which change size more radically. Long nanowires must have more probabilities to have weak points. The difference in length between spin coated and sprayed nanowires looks stronger on Ag117, as they are the longest, and it has more impact on their networks electrical properties. Therefore the nanowire types with lengths lower than 32 µm were used in priority for making sprayed samples (Ag45 mainly).

2.1.3.iii Mass density calculation

An estimation of the AgNW network areal mass density (*amd*) to create efficient transparent electrodes is primary to know. We established a method to determine the nanowire amd deposited on the samples by a SEM image analysis, using the software Image J. The nanowire density of each sample was calculated from 10 SEM images like the one reported in Figure 2-7a. The idea is to estimate the coverage fraction of the nanowires by making the image binary (Figure 2-7b) using Image J. Then the software allows to measure the area occupied by the nanowires (in white) from the non-occupied area (in black) and delimits them (Figure 2-7c). By dividing the value of the occupied area by the average diameter of the type of nanowires used (see Table 2-1), an equivalent length of the nanowires, as if they were abutted on the sample, can be extracted. To calculate the number of nanowires per unit area, we just need to divide this equivalent length by the nanowire average length (Table 2-1).

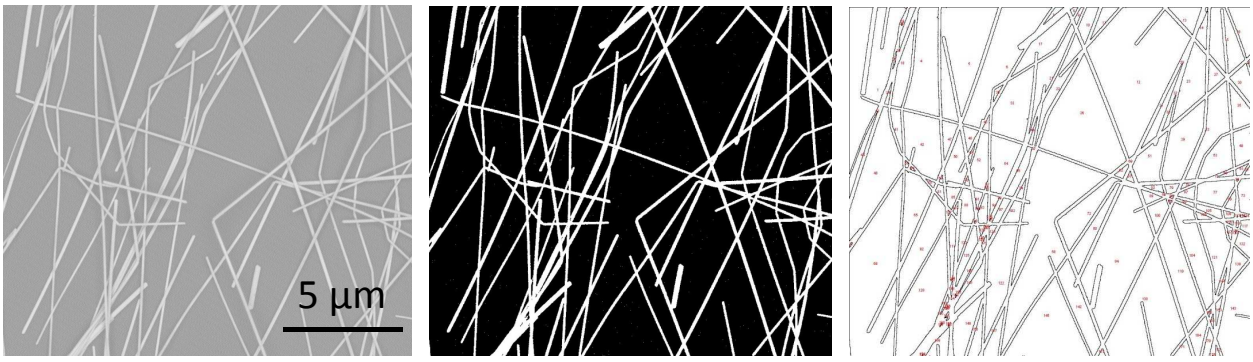

Figure 2-7: Different stages of the mass density calculation: a) initial SEM image b) binary image c) outline of the element that have been delimited by the software image J for the coverage fraction calculation.

The areal mass density *amd*, compared to the number of nanowires, illustrates more the amount of material present on the surface, independently of the nanowires type and dimensions. Every sample will be comparable and directly related to raw material cost. To

determine the *amd*, the volume of the nanowires present on the surface needs to be calculated. AgNWs have pentagonal cross-section[3] of area

$$A_{pentagon} = \frac{5a^2}{4}\cot 36 \qquad (2\text{-}1)$$

a is the side length, represented in Figure 2-8a which can be noted as

$$a = \frac{D_{NW}}{2 \cdot sin54} \qquad (2\text{-}2)$$

D_{NW} corresponds to the largest distance between two corners of the pentagone and can be associated with the nanowire diameter, because it is the distance that is observable from the top, for example when using SEM. Then the AgNW cross-section can be calculated from the diameter and Equation 2-1 using

$$A_{pentagon} = \frac{5 \cdot {D_{NW}}^2}{16 \cdot sin^2 54 \cdot \tan 36} \qquad (2\text{-}3)$$

From the Image J analysis of binary images, we determined the equivalent length corresponding to the amount of nanowires present on the surface. By multiplying it with $A_{pentagon}$ we have access to the equivalent volume of nanowires on the image. The total nanowire mass is then directly calculated from this volume knowing the bulk silver density is equals to 1.049 10^{-8} mg.µm^{-3}. By extrapolating the mass of silver present on the image to the whole sample, the amd can be deducted from this mass by dividing it by the image size. We expressed *amd* in mg.m^{-2}.

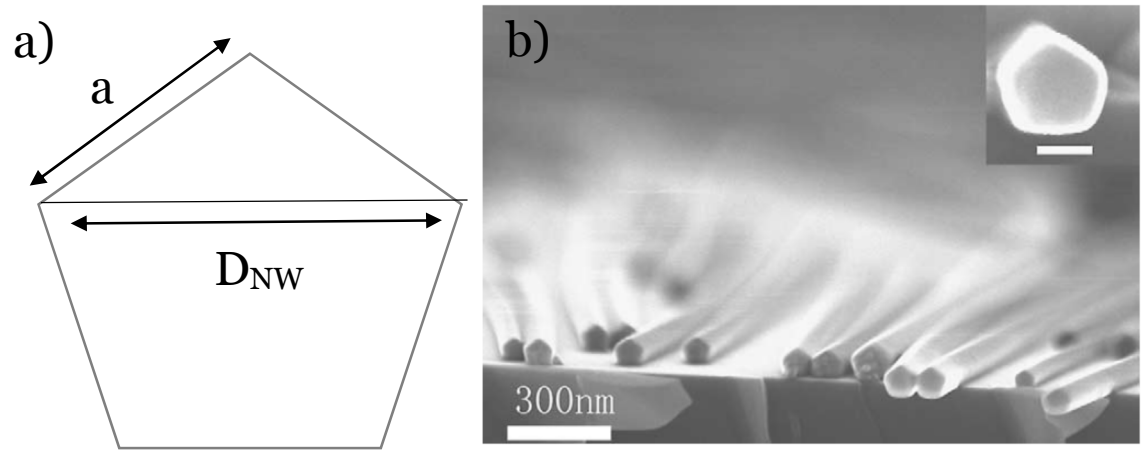

Figure 2-8: a) Diagram of the pentagonal cross-section of a AgNW b) SEM image from Gao et al.[3] showing the pentagonal cross-section of AgNW grown by polyol process. The scale bar in the inset is 60 nm.

This method has one major drawback: it is a "shadow" method of calculation. Therefore when two nanowires cross each other, the amount of silver present at the junction is counted only once, while it should be counted twice considering that in such configuration one

nanowire hides the other. This drawback is not taken into account in this study, since we are interested in rather low density samples, but leads to some uncertainty increasing with the network density considering that the mean number of contact per nanowire is highly dependent on the network density.[4] Therefore the *amd* calculated from high density networks has to be taken with precaution.

2.2 Methods of sample characterization

In order to evaluate the performance of the fabricated AgNW networks, several methods were used to characterize their physical properties. The first parameter that interest us is the nanowire morphology. We need to know the nanowires dimensions, as well as their morphology changes with temperature during the studies about thermal treatment. Then the main requirements of a TCM being high transparency and high conductivity, we were interested in studying the optical and electrical properties of the networks. The experimental methods used are detailed in the following sections.

2.2.1 Morphological and structural methods of characterization

2.2.1.i Scanning electron microscopy

Scanning electron microscopy (SEM) aimed at characterizing the samples morphology and estimating the networks mass density as discussed in the previous part. The SEM apparatus used for imaging was a FEI Quanta FEG 250 (environmental) with a field emission electron source (Schottky cathode). This SEM has a spatial resolution typically between 1.2 nm at 30 kV and 3 nm at 1kV.

The AgNW samples were observed using a working distance around 10 mm, and, depending on the density, with acceleration voltages between 3 and 10 kV. The samples used for electrical measurement (*i.e.* almost every sample) were deposited on glass, or, more generally, on insulating substrates. Therefore the acceleration voltage had to be low in order to avoid the charges of the electron beam to be trapped on the sample and then deviate the electron beam. This charging effect leads to distorted images that need to be avoided. The voltage acceleration had also to be low enough to enable the observation of the surface of the thin nanowires.

Electrons have different interactions with materials: elastic and inelastic interactions and lead to different ways of imaging. Those which interest us for the study of AgNW networks are secondary electron (SE) imaging (inelastic) and backscattered electrons (BSE) imaging (elastic). SE imaging was used for topographical studies. For mass density calculation purpose, we needed images with high contrast between the nanowires and the substrate. Using SE detector leads to images where charging effect occurs rapidly and therefore some bright zones

appear on the substrate image which would be inconvenient for the binarization of the images. Therefore, for mass density calculation, BSE images were used. This technique differentiates materials with different atomic numbers. Silver atomic number (47) is very high compare to the substrates, and so the nanowire contrast on the images was high, facilitating the image binarization.

2.2.1.ii Transmission electron microscopy

Transmission electron microscopy (TEM) was used to observe the AgNW shape, crystallinity and, mainly, the PVP evolution around the nanowires at different stages of thermal annealing. The apparatus used was a Jeol 2010, and the studies were performed using an acceleration voltage of 100 kV. Normally TEM images are made through thin samples but the AgNW could be deposited from isopropanol solution on copper grids filled with an amorphous carbon matrix. The grids could then be heated *ex situ* and the evolution of junctions or PVP was observed with the TEM.

The imaging was performed by Laetitia Rapenne (LMGP).

2.2.1.iii Raman spectroscopy

Raman spectroscopy is a non-destructive technique allowing to give structural and chemical information on a sample composition. The principle of Raman spectroscopy is based on inelastic scattering of a monochromatic light (from a laser) passing through a material. The laser photons, absorbed by the material and then reemitted, have their frequency shifted up or down in comparison with the initial laser frequency, which provides information on vibrational, rotational or low frequency transitions in molecules.

The apparatus used at the LMGP, Horiba/Jobin Yvon LabRam, has an argon laser emitting at a wavelength of 514 nm (spot size ~ 1 μm), and can be used under different conditions. *In situ* measurements can be performed at high temperature (up to 1500°C), at high pressure (up to 80 GPa) and under controlled atmosphere (air, oxygen, nitrogen etc…). Raman spectroscopy was used in the framework of this thesis in order to investigate the evolution of PVP on a sample at different temperatures. *In situ* or *ex situ* heating were undergone by the samples and then the Raman spectra were compared to interpret the different mechanisms, evolution or degradation of PVP that could occur during such thermal treatments. One has to be careful that the laser exposure tends to transform the PVP. Therefore the use of filters and short measuring durations are mandatory for the study of AgNW networks with this technique.

The measurements were performed with Dr Odette Chaix (LMGP).

2.2.2 UV-Visible-IR spectrophotometer for optical characterization

Transmittance and optical properties in general such as haziness or reflectance are very important in the field of TCM. They could be evaluated on AgNW networks using a UV-Visible-IR spectrophotometer. A spectrophotometer allows to illuminate a sample using a monochromatic beam at a normal incidence. It can then measure the percentage of light that is transmitted, reflected, or absorbed by the studied material. The total transmittance T_{tot} is therefore defined as the ratio between the light intensity transmitted by the sample I_t and the intensity of incident light I_0.

$$T_{tot} = \frac{I_t}{I_0} \qquad (2\text{-}4)$$

The total light transmitted by the material has two components: one direct, also called specular transmittance, and one diffused. They are related by the following formula:

$$T_{tot} = T_{direct} + T_{diffuse} \qquad (2\text{-}5)$$

To measure the sample transmittances and reflectance, a Perkin Elmer Lambda 950 UV-Visible-Near IR spectrophotometer equipped with an integrating sphere was used. The mentioned sphere allows the measurement of the transmittance and reflectance total components as it allows light collection in a semi-space, as shown in the diagram in Figure 2-9. The material covering the internal part of the sphere, Spectralon®, is highly reflective and therefore allows all the light transmitted by the studied material to reach the detectors. Light is produced thanks to a deuterium lamp (UV) or halogen lamp (visible and IR) allowing a wavelength range of measurement between 250 and 2500 nm. The light then passes through monochromators and then through a beam chopper that directs the light beam alternatively towards the detector, or towards the sample. Light either transmitted or reflected is then detected by a photomultiplier (UV-Visible) or an InGaAs sensor (IR).

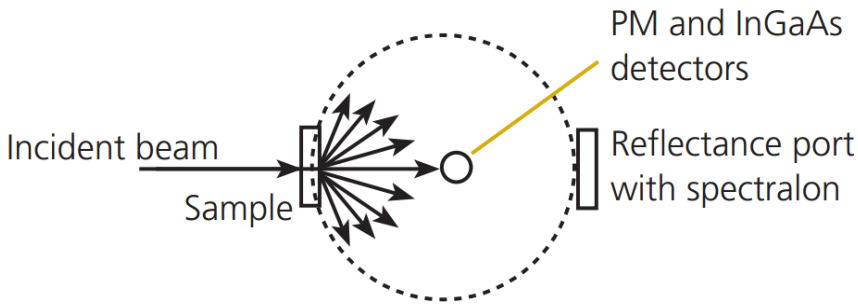

Figure 2-9: Configuration diagram of total transmittance measurement using an integrating sphere, from http://www.perkinelmer.com.

For each AgNW networks samples, measurements were performed on different locations (generally two) and results were averaged. The measurement spot area was 1.35 cm² for total transmittance, and 0.44cm² for direct transmittance.

2.2.3 Electrical measurements

2.2.3.i Two points electrical measurement

For two-point resistance measurement on a defined surface, two metallic electrodes must be fabricated on the sample, on opposite edges. We chose to fabricate them in the form of lines in order to access to a measure of the resistance of the whole network. To ensure a reproducible spacing between electrodes, the contacts on 1.25*1.25 cm² samples were made using a stamp soaked with silver paint, or by silver evaporation, using a mask. The evaporated silver was made using an evaporator Edwards Auto 306 and a mask allowing to fabricate silver electrodes spaced of 0.7 cm on glass slides of size 7.5*2.5 cm². A photograph of the mask is displayed as Figure 2-10. For bigger samples, the contacts for electrical measurements have been made on the samples using silver paint, deposited by hand.

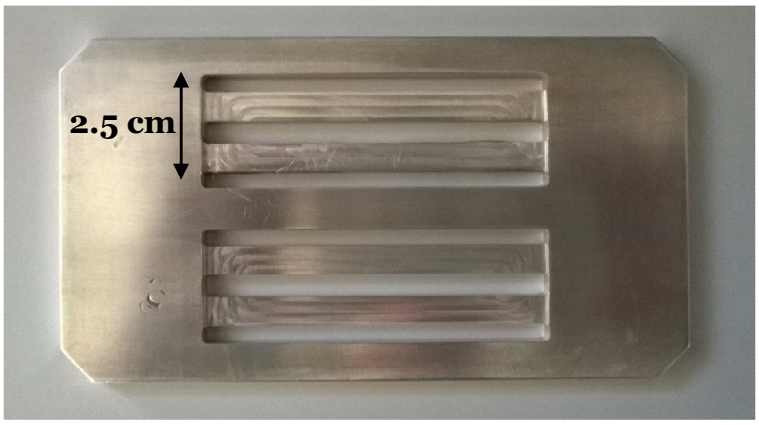

*Figure 2-10: Mask used for fabricating electrodes of silver by evaporation. The hollowed sites are dedicated to two glass slides of size 7.5*2.5 cm².*

2.2.3.ii Four point probes

Four point probes setup enables to measure the sheet resistance of the samples, which is of high importance as it is a major property in TCMs. Unlike two points measurement, four point probes allows to eliminate most of the resistances coming from the connectors. As a recall from Chapter 1, the sheet resistance can be written as: $R_s = \frac{\rho}{t}$. Therefore the measure of R_s leads to the value of either the sample thickness when the resistivity is known, or inversely, of the sample resistivity when the thickness is known. In the case of AgNW networks, these

deductions are however compromised by the fact that the AgNW networks are not homogeneous in thickness, considering the large amount of free space between the nanowires.

Sheet resistance measurement of the samples was performed with a four point probe Lucas Labo, pro4 apparatus. The device head is composed of in-line mounted tungsten probe pins, separated of 1 mm, with a pin radius of 40 µm. The standard 4pp measure is presented in Figure 2-11. The measurement is made by placing the probes in contact with the sample by mechanical pressure, and then by applying a current between the two outer probes, while the voltage between the two inner probes is measured. A Keithley 2400 sourcemeter is used to apply the current and measure the voltage.

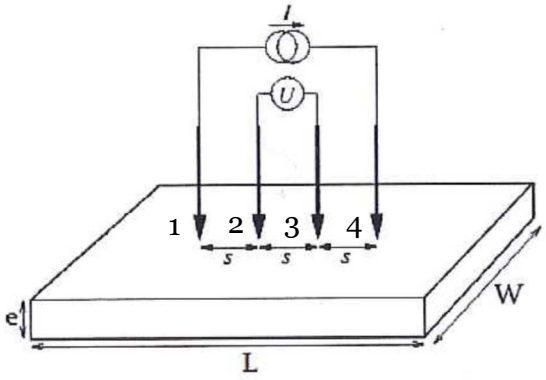

Figure 2-11: Diagram of a four point probes measurement.[5]

The sheet resistance is calculated from the measurements of V and I as follows:

$$R_s = k \cdot \frac{V}{I} \qquad (2\text{-}6)$$

k is a correction factor which, for a film considered as infinite compared to the probes spacing, equals approximately 4.53 (*i.e.* $\frac{\pi}{ln2}$),[6] and has no dimensions. This correction factor takes into account the sample geometry, as well as its thickness and the probes position. When the samples are small and can't be considered as infinite regarding the probes spacing, which is the case here, the dual configuration mode is preferably used. This mode is highly recommended for measurement at a distance from the sample edge lower than 10 times the pins space (in our case, 1 cm) and is accurate up to an edge proximity of 4 times the probes spacing (4 mm). It also helps eliminating errors introduced by imperfections in probes contact. In this mode, $\frac{V}{I}$ is measured twice, in two different configurations and R_s is calculated based on the two measurements.[7] The first configuration (A) is the standard one, *i.e.* current applied to probe 1 and out in probe 4, and voltage measured between probes 2 and 3. The second configuration (B) is with current into probe 1 and out probe 3, while the voltage is measured between probes 2 and 4. In dual configuration, sheet resistance is then given as:[8]

$$R_s = -14.696 + 25.173 \cdot \frac{R_A}{R_B} - 7.872 \cdot \left(\frac{R_A}{R_B}\right)^2 \qquad (2\text{-}7)$$

All the sheet resistance presented in this document were measured using the dual configuration.

2.3 Experimental setups

In order to study the physical properties of AgNW networks, several home-made setups were built at the LMGP to perform *in situ* studies. The properties studied were first the networks electrical behavior under thermal annealing, then the electrical and thermal behavior of the network under electrical stress. These setups also allowed to investigate the electrical and thermal stabilities of the samples. Another setup was built to study the electrical behavior of flexible substrates under mechanical stress. These three setups are presented in this section.

2.3.1 *In situ* resistance measurement setup

This setup was built in order to investigate the impact of a thermal annealing on the electrical properties of the networks. It enables the *in situ* measurement of the network resistance during heating with a sourcemeter Keithley 2500. As two sourcemeters are mounted on the setup, it is possible to study two samples at the same time, as shown in Figure 2-12a. Samples made of different nanowires types at various densities were investigated and compared. The samples contact electrodes were made from silver paint or evaporated silver as explained in section 2.2.3.i, and the electrical contact from the Keithley to the sample was made by using metallic probes.

The setup is quite versatile and enables to use different types of heating, thanks to a manual temperature controller, allowing testing the networks kinetics of resistance variation during heating, or their thermal stability. It was for instance possible to constantly increase the temperature at a defined ramp rate (Figure 2-12b), heat the samples at a constant temperature for a chosen duration (Figure 2-12c), or make a "stepped annealing" by subsequent plateaus at various temperatures (Figure 2-12d) *etc*. The *in situ* resistance and temperature were recorded and displayed on a computer thanks to a Labview program. This program allowed to choose the voltage used for the resistance measurement, but it was always set at 1V in the studies presented in this document. The number of measurement as well as their frequency could be also chosen. Typically during the thermal annealing experiments, we measured the resistance every second.

The setup could be confined thanks to a glass lid, allowing to perform experiments either under vacuum or under gas flow. When not specified, experiments have been performed in air without the presence of the glass lid.

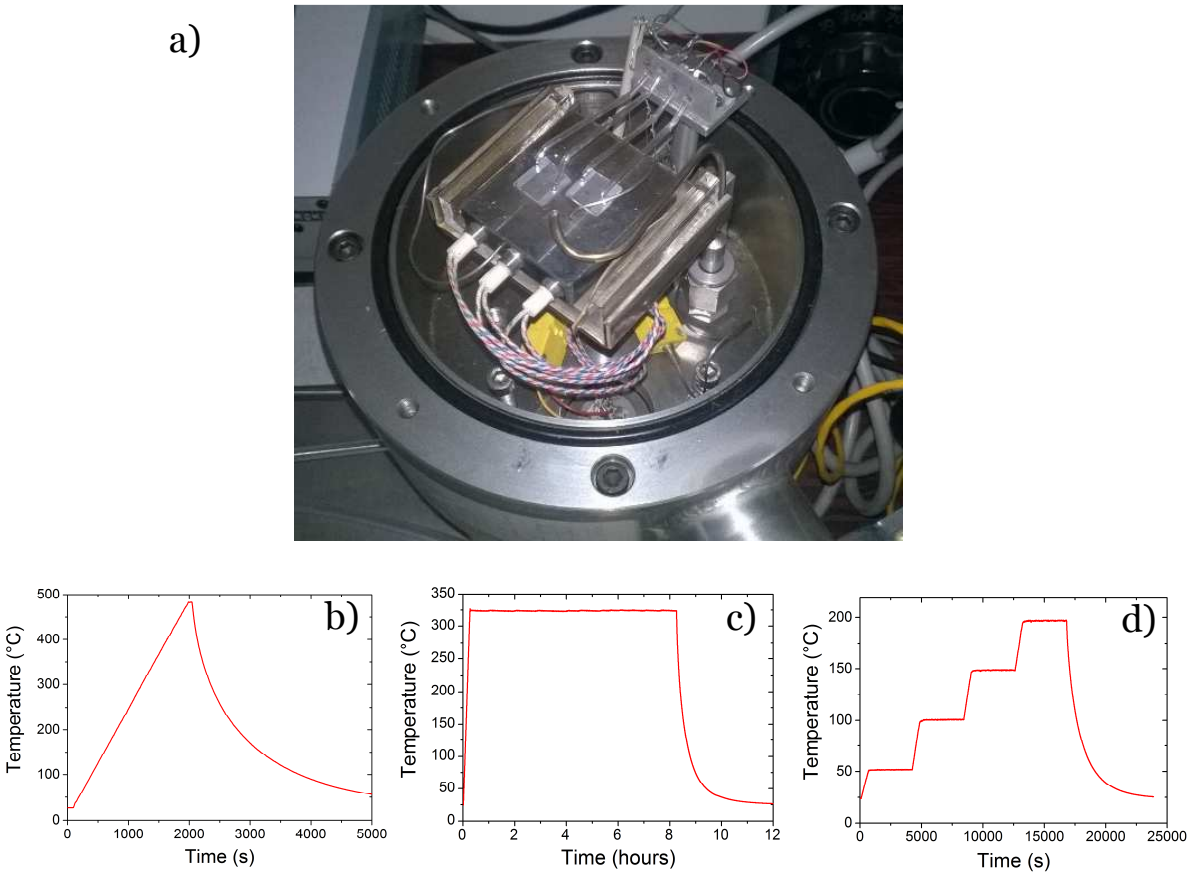

Figure 2-12: a) Thermal annealing setup with two samples contacted with two probes each, on a heating plate b) an example of ramp annealing up to 500°C c) an example of a long term annealing at 325°C d) an example of stepped annealing.

2.3.2 Electrical stability and transparent heaters setup

In order to investigate the performance of AgNW networks used as transparent heaters, a setup allowing to apply a current to the samples while measuring their temperature elevation caused by Joule heating was built at the LMGP, for the purpose of this thesis. It was possible either to apply a current to the sample, or a voltage. All the results presented in this document were obtained from a voltage application, because we were interested in obtaining efficient heating performances at low voltage, therefore this parameter had to be controlled. This setup was also used to investigate the limits of the networks in terms of electrical stability, electrical failure in particular due to electromigration.

The samples were contacted using silver paint stripes on two opposite edges (two points measurement) and were connected to a Keithley sourcemeter using silver electrical wires. The Keithley was controlled by a computer with a Labview program, quite similar to the one detailed in section 2.3.1. Instead of playing with temperature, different electrical stresses were possible. For example a voltage ramp, a voltage plateau, or a stepped voltage. Therefore we were able to collect information on the *in situ* electrical behavior of the networks, as well as on their self-heating performances. Such setup also allowed us to investigate the electrical stability

of the networks. The temperature elevation by Joule heating was measured using a RTD temperature sensor placed underneath the samples. It was composed of a 120 µm thick PEN with a surface area around 6 cm^2, rather close to the specimen area, allowing a good thermal contact while having a low thermal inertia.

In order to limit significantly the heat losses by conduction, the samples were mounted on a device, within the setup, that limits them. Instead of resting on a flat solid surface, the samples as well as the temperature sensor were laid on a set of parallel sewing threads, which is a poor thermal conductor. Another thread set was placed on top of the sample, in order to enable an efficient thermal contact between the sample and the thermal sensor (see Figure 2-13a and b) without inducing a large amount of heat losses by conduction. The thermal conductivity of sewing thread is low (around 0.04 $W.mK^{-1}$), the thread section small (around 0.3 mm) and they are spaced of 0.5 cm. Therefore the heat losses by conduction through the sets of sewing thread are very limited.

This setup could also be used under vacuum. That way it was possible to study the thermal behavior of the networks while cancelling the heat losses by convection.

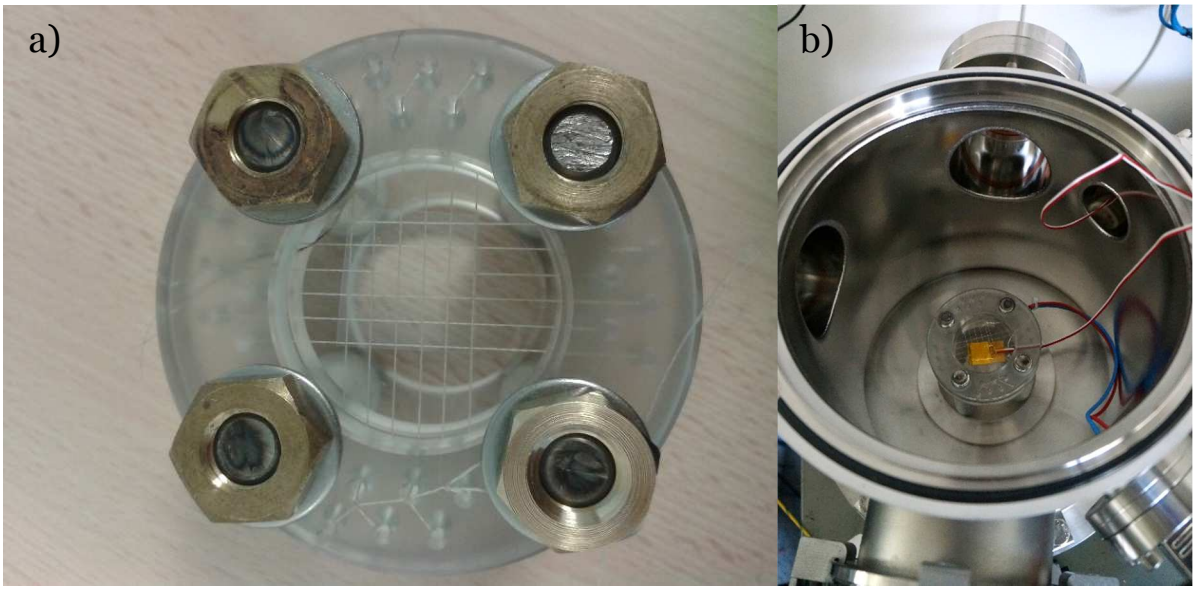

Figure 2-13: Transparent heaters setup a) top-view of the device used to limit heat losses by conduction, with the two sets of parallel sewing thread b) the device coupled with the temperature sensor in the vacuum chamber.

2.3.3 Mechanical stability setup

The last homemade setup presented in this section aimed at studying the mechanical stability of flexible AgNW networks (deposited on either transparent Kapton or PEN). A mechanical bench was mounted, as can be seen in Figure 2-14, with one element moving closer or farther from one fixed element. Copper plates were used to fix one edge of the sample on the

fixed element and the other on the moving one. When the setup was working, the mounted sample was subsequently flat or bent, the frequency and distance could be defined by a Labview program. Radius of curvature as small as 5 mm of the flexible samples could be obtained with this setup.

Electrical contact was ensured by silver paint lines drawn on the sample prior to its integration in the setup. Electrical wires were then connected to the copper plates to relate electrically the sample to a Keithley sourcemeter, related itself to the Labview program. The latter was used to measure the sample resistance *in situ*, like for the thermal annealing setup (section 2.3.1) or to apply different voltages like the transparent heaters setup (section 2.3.2). This setup was used to test the influence of bending on the samples resistance, as well as the influence of a combination of bending and voltage application.

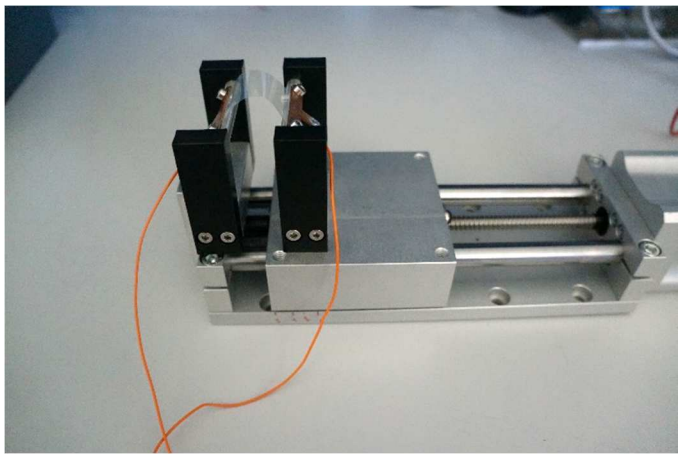

Figure 2-14: Mechanical bench with an AgNW network sample mounted and bent.

References

[1] Gao Y, Jiang P, Song L, Liu L, Yan X, Zhou Z, Liu D, Wang J, Yuan H, Zhang Z, Zhao X, Dou X, Zhou W, Wang G and Xie S 2005 Growth mechanism of silver nanowires synthesized by polyvinylpyrrolidone-assisted polyol reduction *J. Phys. Appl. Phys.* **38** 1061–7

[2] Balberg I and Binenbaum N 1983 Computer study of the percolation threshold in a two-dimensional anisotropic system of conducting sticks *Phys. Rev. B* **28** 3799–812

[3] Gao Y, Jiang P, Liu D ., Yuan H ., Yan X ., Zhou Z ., Wang J ., Song L, Liu L ., Zhou W ., Wang G, Wang C . and Xie S . 2003 Synthesis, characterization and self-assembly of silver nanowires *Chem. Phys. Lett.* **380** 146–9

[4] Heitz J, Leroy Y, Hébrard L and Lallement C 2011 Theoretical characterization of the topology of connected carbon nanotubes in random networks *Nanotechnology* **22** 345703

[5] Céline Mayousse 2014 *Elaboration d'électrodes transparentes souples à base de nanofils métalliques* (PhD thesis: Université de Grenoble)

[6] Smits F M 1958 Measurement of Sheet Resistivities with the Four-Point Probe *Bell Syst. Tech. J.* **37** 711–8

[7] Petersen D H, Lin R, Hansen T M, Rosseel E, Vandervorst W, Markvardsen C, Kjær D and Nielsen P F 2008 Comparative study of size dependent four-point probe sheet resistance measurement on laser annealed ultra-shallow junctions *J. Vac. Sci. Technol. B* **26** 362–7

[8] Schroder D K 2006 *Semiconductor Material and Device Characterization* (John Wiley & Sons)

Chapter 3 : Optimization of AgNW-based electrodes: effects of thermal annealing and comparison with different methods

When deposited into networks, the resistance of AgNW networks can be high because of the non-efficient contacts between nanowires which generally exhibit higher resistance than individual stick after deposition. Therefore several techniques used to decrease the junction electrical resistance have been developed in literature, such as thermal annealing,[1,2] mechanical pressing,[3] chemical treatments[4] or laser annealing.[5] Thermal annealing has been shown to reduce significantly the resistance of AgNW networks. The present chapter is dedicated to the experimental study of the influence of thermal annealing on the networks electrical properties, in particular the mechanisms of electrical resistance reduction and of morphological instability. At the end of the chapter, preliminary results from studies about other techniques used to improve AgNW networks electrical properties will be presented within the framework of an international collaboration.

3.1 Effects of thermal treatments on AgNW networks electrical resistance

Thermal annealing has been shown in the literature to improve significantly metallic nanowire-based transparent electrodes through a decrease of the contact resistance between nanowires.[3,6] The different mechanisms inducing resistance reduction but also thermal instability have however not been studied thoroughly. This section therefore aims at shedding light on the different thermally-induced mechanisms responsible for the improvement of networks electrical properties by using different thermal approaches. A study based on several results presented here has been published in 2014 by our team in the form of an article.[2] In the end, some solutions will also be proposed and discussed to overcome the problem of thermal instability.

3.1.1 Thermal ramps

A first way to analyze the different mechanisms occurring at different temperatures during thermal annealing is to gradually increase the temperature of the network while measuring its electrical resistance. Several thermal ramp rates were used in order to investigate the kinetics of the mechanisms involved. This section aims at identifying the various mechanisms occurring during ramped annealing, the effects of kinetics on the process as well as the study of thermal instability.

3.1.1.i Different stages of the TE resistance during thermal annealing

In Figure 3-1 is represented the resistance behavior of a sample fabricated with Ag117 nanowires by spin coating (1 $g.l^{-1}$ with the standard routine discussed in Chapter 2), during a thermal ramp at a rate of 2°C.min^{-1} until 500°C. Several stages of resistance changes are identifiable on the figure and will be discussed now. The following description and associated temperatures of the phenomena are particular to this sample but a similar general behavior has been observed for specimen associated with different network densities or different nanowire dimensions. The discussion of nanowire size and density effects on thermal annealing is reported in Chapter 4.

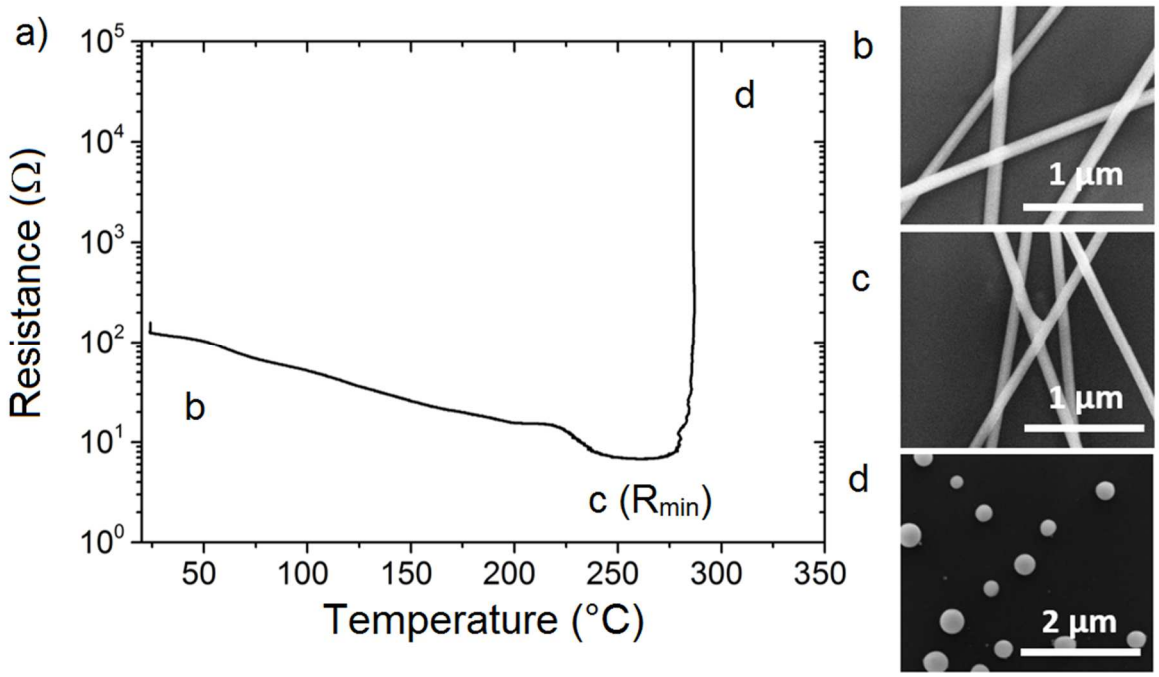

Figure 3-1: a) Electrical resistance of a Ag117 network during a thermal annealing at a ramp rate of 2°C.min^{-1}, with SEM images showing the morphology of the nanowires at different stages: b) as deposited, at room temperature, c) at minimum resistance, at 255°C, d) after spheroidization, at 500°C.

First, in the low temperature area (below 200°C), there is a strong electrical resistance decrease of at least one order of magnitude. This temperature range is associated with the thermal desorption of organic residues which are present around the AgNWs and at their junctions. These organic compounds might mainly be residual left from the isopropanol used to disperse the nanowires, as the deposition was performed at room temperature. Isopropanol acts as an insulating layer when it is trapped between two nanowires by capillarity, therefore its removal leads to a better electrical contact between nanowires at their junction. Another component surrounding the nanowires and acting like an insulating layer is the PVP. As seen

in Chapter 1, PVP is a polymer used as a capping agent during the nanowire synthesis.[7] PVP glass transition temperature is between 150°C-180°C therefore PVP might soften and/or move slightly from the junctions starting around 150°C, allowing a more intimate contact between AgNWs and thus a better electrical conduction of the network.

A second stage of resistance reduction at higher temperature is visible in Figure 3-1a that induces a morphological change in the network. During this stage the electrical resistance decreases further and achieves a minimum at a temperature around 255°C. The SEM picture in Figure 3-1c shows the nanowires morphology after a thermal ramp stopped at the temperature associated to the minimum resistance (255°C for this sample). This image shows a clear change in morphology of the nanowire junctions, which now look welded when compared to as deposited nanowires displayed in Figure 3-1b. This second drop in resistance is ascribed to a local sintering at the nanowire junctions thanks to a thermally induced surface atomic diffusion. This phenomenon is driven by the reduction of surface energy of the nanowires. Once again the contact between nanowires is even more efficient as the atoms from neighbor nanowires diffuse to form a sintered junction. The minimum resistance is achieved when the welded junctions led to the creation of enough efficient percolating pathways across the network to dominate the resistance behavior.

Eventually, above 275°C, the network electrical resistance goes to infinity within an increase of a few degrees. SEM image from Figure 3-1d shows that the morphology of the nanowires has entirely changed after heated up to 500°C, as they transformed into droplets: they spheroidized. Therefore the conducting pathways are completely destroyed and the electrode is not percolating anymore. Heating has led to the instability of the nanowires, once again caused by surface diffusion driven by surface energy reduction. When the temperature is high enough, the AgNWs tend to decrease their surface energy by adopting the morphology associated to the lowest one, *i.e.* a spherical shape. This phenomenon called Plateau-Rayleigh instability has been observed for other types of nanowires, for example gold nanowires by Karim *et al.*[8] (see thermal stability in Chapter 1). The nanowires dimensions (especially diameter) have a strong impact on this phenomenon of instability, as will be discussed in Chapter 4.

3.1.1.ii The role of PVP in AgNW network electrical improvement

PVP is known to be insulating and therefore to increase the electrical resistance between nanowires at junctions. However its role and evolution during thermal annealing seems complex and is still the object of discrepancy. Several characterization techniques have been used in this thesis work to investigate the evolution of PVP during thermal annealing: TEM, Raman spectroscopy and thermogravimetric analysis (TGA).

Transmission electron microscopy

TEM study shows that before annealing, the nanowires have an amorphous layer of PVP surrounding them, visible in Figure 3-2a, coming from the nanowire synthesis where PVP allows them to grow anisotropically. After annealing at 180°C for 1h, TEM images show that PVP remains on the nanowire walls. However, as shown in Figure 3-2b, the PVP is not placed between the nanowires but seems either to have disappeared or to have moved from the junctions and to remain only on the nanowire walls. The silver atoms might also have diffused through the PVP layer during the thermally-induced local sintering. Figure 3-2c and d show a zoom on a junction (the PVP layers are better visible in the electronic version of this document). The junction before annealing is made of nanowires on top of each other, each of them having their own PVP layer. After annealing, the junction is welded and the PVP layer appears now to surround the junction at the external surface of the nanowires but not anymore at the contact point between nanowires. Therefore as suggested in the last section, the PVP is not present anymore at the junctions, which enables a better electrical contact, but is still present on the sample at this temperature, allowing some protection of the nanowires from corrosion or thermal perturbation.

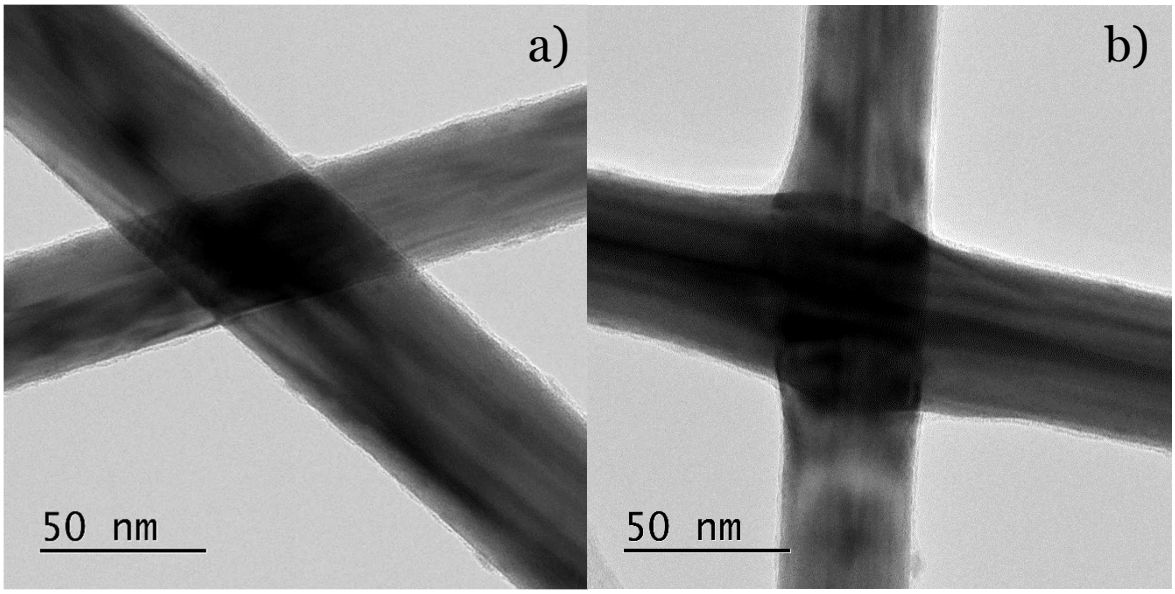

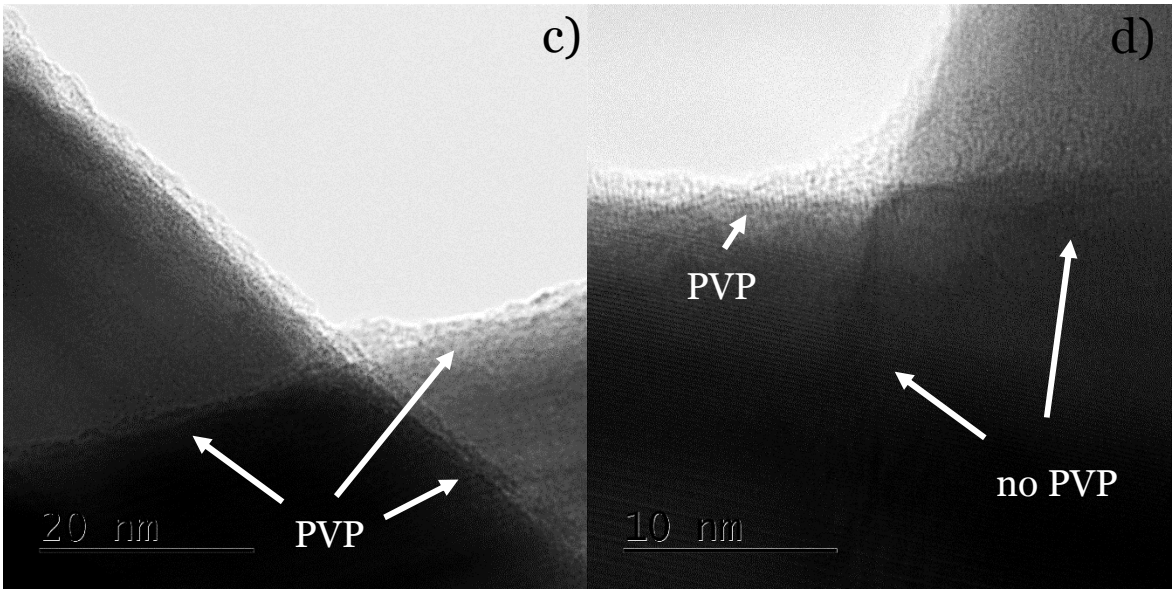

Figure 3-2: TEM images showing the evolution of PVP at a junction of two AgNWs a) and c) as deposited, b) and d) after annealing at 180°C for 1h.

Thermogravimetric analysis

Thermogravimetric analysis studies on AgNW have been performed at the LMGP by heating a significant mass of AgNW (~16 mg) at a thermal ramp rate of 2°C.min^{-1}. This technique would allow to see phase transitions or desorption that can occur during the treatment. However one has to be aware that for this study, the AgNW were not in the form of a network, but put in a crucible, with an initial mass of around 16 mg. The results of the TGA measurement are presented in Figure 3-3. From the black curve, a slight change in the sample mass is visible around 250°C as well as a change in the heat flow in the range 200-285°C, illustrating an exothermic reaction. This reaction can be ascribed to a phase transition, most probably of PVP, considering the range of temperatures. The mass loss within this temperature range is estimated from the curve to be around 12 µg. This is quite small compared to the proportion of PVP mass that should be present in the sample, estimated to be around 170 µg (by considering a PVP density of 1.2 g.cm^{-3}) for the amount of material used for the TGA experiment (16 mg). Therefore the PVP mass hasn't completely disappeared, but this exothermic reaction could be due to its combustion or graphitization.[9]

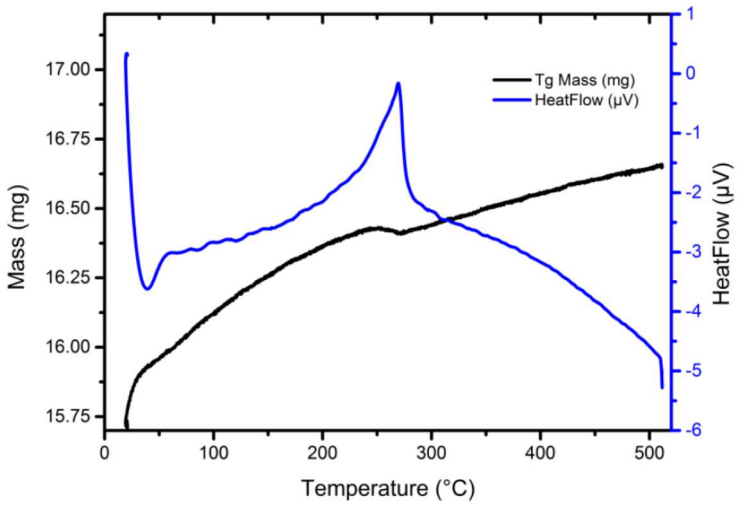

Figure 3-3: Results of TGA analysis of Ag105 during a thermal ramp rate of 2°C.min^{-1}, performed at the LMGP. The figure is extracted from Daniel Langley thesis.[10]

Raman spectroscopy

Raman spectroscopy studies have been also performed in order to investigate the evolution of PVP after different thermal treatments, *ex situ* and *in situ*. Two wavenumber ranges were considered since PVP seems to have characteristic peaks in these ranges: 200-1700 cm^{-1} and 2200-3500 cm^{-1}. In Figure 3-4 are presented Raman spectra of as deposited samples (black). Three parts of the spectra are characteristic of PVP: first there is a peak centered around 230 cm^{-1} which was ascribed to a Ag-O coordination by Gao *et al.*[7] which they suggested to be characteristic of the absorption of a monolayer of PVP on the surface of the nanowires, through this coordination. The second region is between 1100 and 1700 cm^{-1} which was difficult to ascribe to specific bonds but can be associated to carbon compounds. The last region of interest is the peak centered around 2940 cm^{-1} which is characteristic of C-H stretching vibrations in the PVP.[11] The first Raman study presented in Figure 3-4a and b was performed *ex situ*. AgNW networks of Ag117 were deposited on glass substrates using spin coating, and were then heated on a hot plate at the temperatures and duration used in the study of pre-annealing (that will be presented in section 3.1.2): 100°C for 8h, 150°C for 6h and 200°C for 2h. The spectra of each sample were then compared to those of an as deposited sample.

A first observation can be made on the Ag-O peak (close to 230 cm^{-1}). It seems to have decreased after every annealing studied here although it is still present. In the carbonaceous compounds area (1100-1700 cm^{-1}), it seems that there is an evolution at 200°C since the intensity of this region has increase. A modification is also visible in the peak around 2940 cm^{-1}, a bell-shape signal centered on the peak has appeared progressively from 150°C, until the peak is not visible anymore (at 200°C). This kind of bell shape signal usually stems for fluorescence and hides the Raman signal.

To obtain more information, Raman spectra were recorded *in situ* at various temperatures were the PVP could start changing: 175°C, 200°C and 250°C. The resulting spectra are presented in Figure 3-4c and d. This time the Ag-O peak have disappeared at every temperature. The signal between 1200 and 1700 cm^{-1} seems smoother than before and more intense after heating 60 minutes at 175°C. Two large peaks seem to emerge. They can potentially be ascribed to the evolution of PVP into carbonaceous compound such as graphite or amorphous carbon. These large peaks are present when heating at 175°C for 1h or 200°C for 50 min. However, they seem to disappear at 200°C after 2h. They are not present either for samples heated at 250°C. In the range 2200-3500 cm^{-1}, the characteristic peak related to PVP disappears at 175°C, 200°C or 250°C. However a bell shape is present at 175°C 1h and 200°C 50 min, but then decreases in intensity for 200°C 2h.

Ex situ

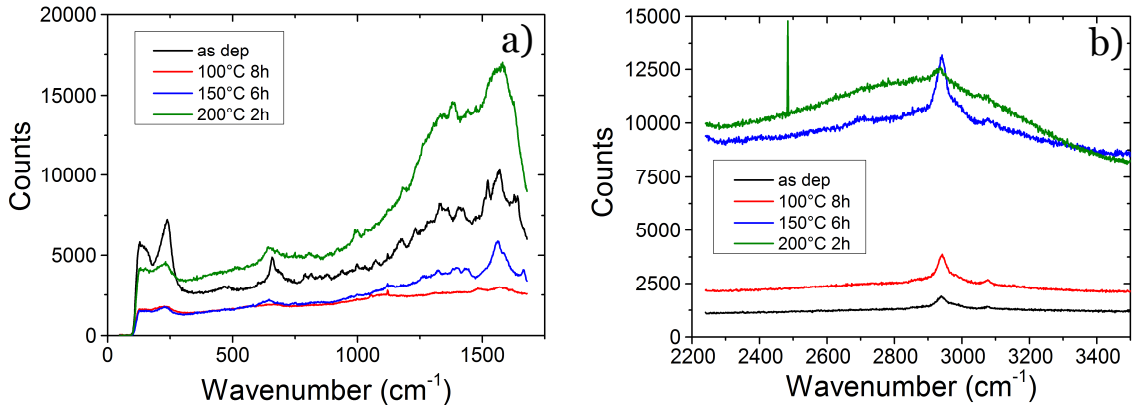

In situ

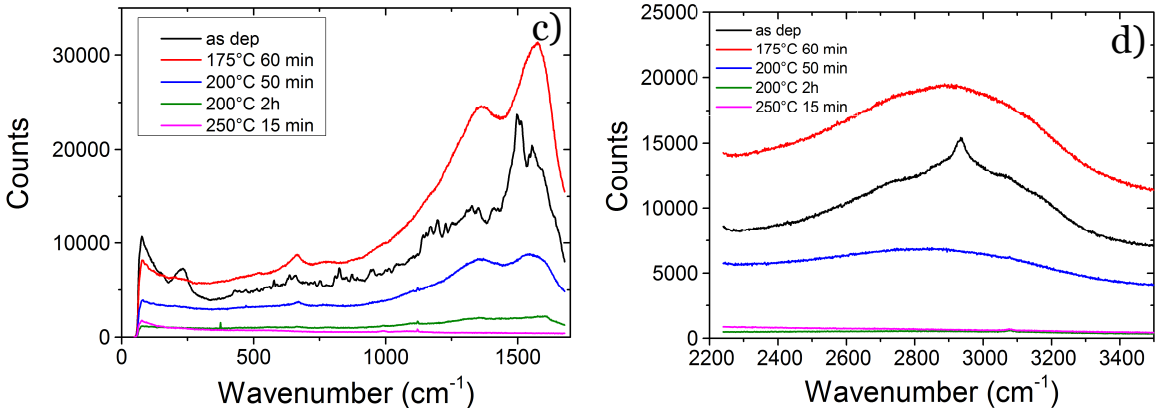

Figure 3-4: Raman spectra of PVP evolution in air a) and b) heating ex situ *at 100°C for 8h, 150°C for 6h and 200°C for 2h c) and d)* in situ *at 175°C, 200°C and 250°C at different times of annealing.*

All these information could lead to this interpretation of the PVP evolution when heating in air: below 175°C, the PVP doesn't evolve much. At 175°C, it starts to change and probably evolve into a carbonaceous component. This is in accordance with Borodko *et al.* who

stated that PVP degrade to form amorphous carbon under oxidizing conditions.[12] At 200°C, PVP also seems to transform into carbon but after 2h of heating the carbon seems to degrade as well. The Raman spectra taken at 250°C after 15 min heating don't show any PVP peaks either. Therefore it shows the faster kinetics of PVP degradation at 250°C compared to 175°C or 200°C. There seems to be a difference in kinetics between *ex situ* and *in situ* experiments (see 200°C 2h). It could be ascribed to the fact that the experiment *in situ* is made in a closed cell with flowing air. Therefore the air in contact with the sample always changes, and brings more oxygen that might increase the PVP degradation kinetics.

After the *in situ* experiments, the samples were cooled back to room temperature and measured again. The results are displayed in Figure 3-5. The graph shows that after 1h of heating at 175°C, the carbonaceous compounds area is enhanced, probably by a degradation of PVP into amorphous carbon or graphite, but after 15 min at 250°C, the carbon compounds have disappeared. But a new peak have appeared at 995 cm^{-1}, that can be ascribed to silver sulfite Ag_2SO_3.[13] This peak is quite impressive and shows the high sensitivity of silver to sulfur.

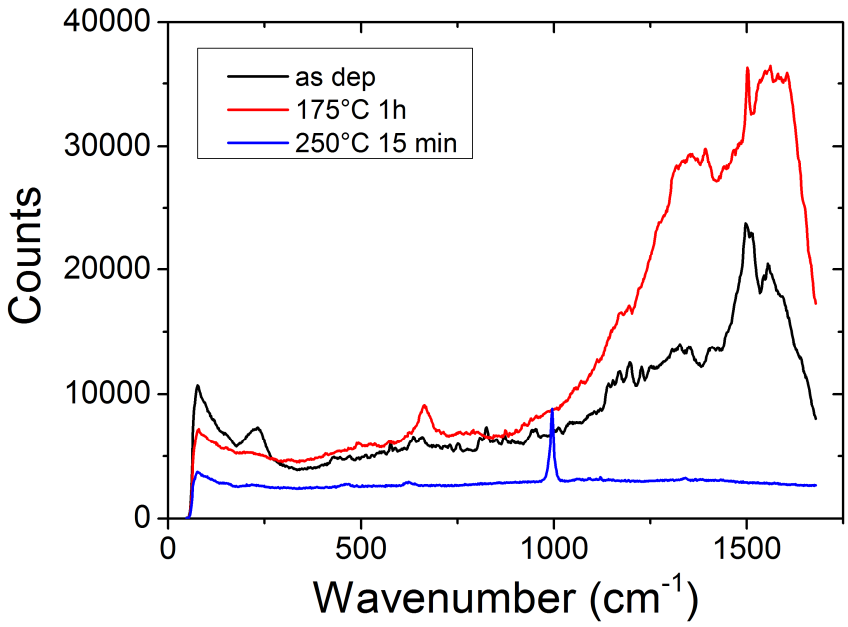

Figure 3-5: Raman spectra after the in situ *experiments at 175°C (total heating duration: 1h) and 250°C (total heating duration: 15 min). These spectra were recorded after the sample cool down back to room temperature.*

The conclusions on the evolution of PVP during thermal annealing from these different characterization techniques are not straightforward. The range of temperature at which PVP changes is estimated to be between 150°C and 175°C (Raman). According to TEM studies, it seems that PVP doesn't prevent the surface diffusion of silver atoms from one nanowire to the

other, which allows to improve electrical contact. Then from TGA it seems that there is a transformation occurring around 200°C (matching approximately the 150°C-175°C range found with Raman spectroscopy) which doesn't last after 285°C, but during this transformation the initial mass of PVP has not entirely been removed. That can be ascribed to a graphitization or the formation of amorphous carbon. However Raman studies showed that after heating at 250°C for 15 min, the carbon compounds have significantly decreased. The range 200°C-250°C corresponds to the temperatures at which thermal instability starts to become dominant for the AgNW. This might be related to the transformation or removal of the PVP. Besides, from Raman studies we identified an acceleration of kinetics with the amount of air (probably of oxygen) present during the experiment, PVP degradation being probably enhanced by oxygen. This was validated by performing *in situ* Raman spectroscopy under different controlled atmospheres: nitrogen and oxygen. At 200°C, the carbonaceous compounds signal (1100-1700 cm^{-1}) disappear completely under oxygen atmosphere while it is still present under nitrogen atmosphere.

These studies still give interesting information about the role of PVP during thermal annealing. This capping layer doesn't prevent nanowire from sintering and helps to protect the nanowires from corrosion and thermal instability (up to ~200°C-250°C). Although the understanding of the PVP behavior during thermal annealing is not straightforward, it however doesn't appear to be a real problem for AgNW networks TE optimization.

3.1.1.iii Kinetics

This section will now return on the study of the resistance behavior of AgNW networks during thermal ramp heating.

In order to study the kinetics of ramped thermal annealing process, especially of the thermal stability, heating rates were varied from 0.2 °C.min^{-1} to 24 °C.min^{-1} and applied to similar standard Ag117 spin coated samples. The resulting *in situ* measured resistances of the different samples are displayed in Figure 3-6a. This experiment shows an increase of the instability temperature of more than 100 °C when the rate is increased from 0.2 °C.min^{-1} to 24 °C.min^{-1}. This can be explained by the fact that samples heated at low ramp rates remain much longer within a temperature range and are then damaged at lower temperature. Figure 3-6b shows the evolution of the temperature of instability as well as the evolution of the temperature at which the minimum resistance is achieved, versus the thermal ramp rate. Both temperature follow the same trend of increasing with the ramp rate and the difference between T_{sph} and T_{Rmin} increases with the ramp rate. The markers represent an average over two samples for each ramp rate, the error bars correspond to one standard deviation of the two results.

The resistance of metals depends on the temperature. As will be explained in the following section, it is however possible to extrapolate the minimum resistance achieved by

each curve (at a specific temperature) at its value at room temperature (see Equation 3-1 in the next section). By doing this extrapolation from the data presented in Figure 3-6a, the minimum resistance at room temperature for the ramp rates considered is approximately the same, around 3 Ω. This is of great interest as it shows that the same resistance can be achieved more rapidly using a high ramp rate. Or, on the contrary, this low resistance can be achieved with a limitation in temperature (but with a higher process duration) when the ramp rate is low. The use of low temperature is of interest when the substrate is a polymer for instance, or sensitive to high temperatures (sensitive devices such as organic solar cells) in order to avoid its degradation.

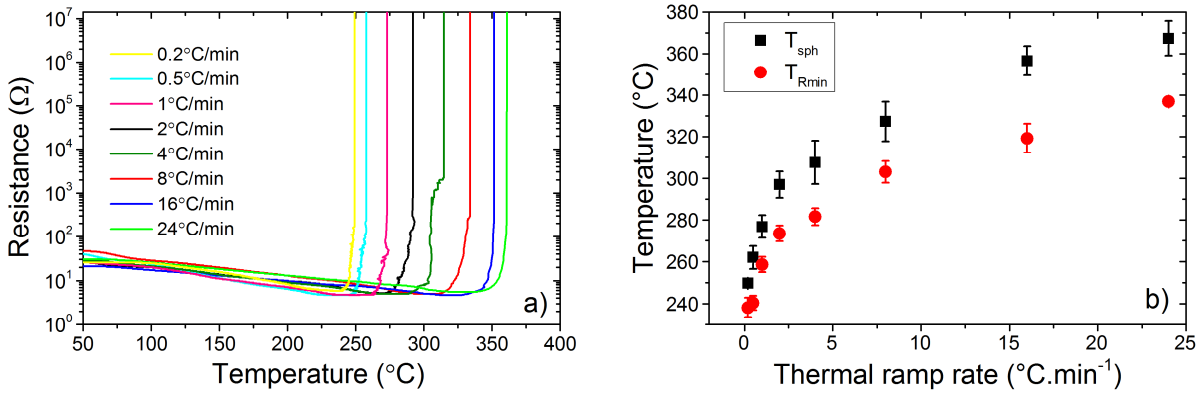

Figure 3-6: a) Resistance behavior of AgNW networks during thermal annealing at various ramp rates, b) Temperatures of instability and of minimum resistance versus heating ramp rate.

3.1.1.iv Network electrical optimization by stopped heating ramp

In order to reduce the electrical resistance of AgNW networks, one simple way is to stop the heating during a thermal ramped annealing, at the exact time when the minimum resistance is achieved *in situ*. To test this process, a sample was fabricated and then cut into four equal parts. On the first quarter, a thermal annealing was performed at a ramp rate of 2°C.min^{-1}, up to 500°C, so the sample undergoes all the mechanisms of resistance reduction and then thermal instability. This experiment enabled to find experimentally the temperature at which the minimum resistance is achieved for this specific sample. The second part of the sample was used for optimizing the network by stopping the thermal ramped annealing. The heating was stopped at the optimum temperature defined by the first experiment and the samples resistance was still measured during the cooling of the hot plate. The resistance behavior of the second sample is very similar to the first one before the ramp is stopped, as can be seen in Figure 3-7a. That first illustrates the reproducibility of thermal annealing on identical samples (same nanowire type and density). Another interesting observation is the linear behavior of the resistance during the cooling, in focus in Figure 3-7b. This will be discussed now.

The deep resistance changes of AgNW networks caused by junction sintering and organic residues desorption that happen during thermal annealing are irreversible. But in metals, another phenomenon, reversible, relates resistance and temperature: phonon-induced scattering. This phenomenon is well known and the resistivity ρ of a metal at a temperature $T_0 + \Delta T$ can be modeled by the linear approximation:[14]

$$\rho(T_0 + \Delta T) = \rho_0(T_0) \cdot (1 + \beta_R \cdot \Delta T) \qquad (3\text{-}1)$$

The resistance response to an increase of temperature in a metal is indeed linear at a temperature higher than 0.2 x T_d,[14] T_d being the Debye temperature (equals to 215 K for silver). The cooling resistance behavior shown in Figure 3-7 can be modeled with Equation 3-1. β_R is the temperature coefficient of resistivity and is equal to 3.8 x 10^{-3} K^{-1} for bulk silver.[15] Bid *et al.*[16] observed a similar value for individual and very pure AgNW. In the present work, $\beta_R$was found from the slope in Figure 3-7 to be around (2.2 ± 0.1) x 10^{-3} K^{-1}. The difference between the value of β_R for a single AgNW (and bulk silver) and for a AgNW network might arise from the presence of junctions between AgNWs which behave differently in terms of resistance, as well as defects such as grain boundaries that can be present in commercial AgNWs.

After cooling, the samples are very conducting, the sheet resistance can be measured and is generally found to be very uniform across the samples. This method of stopped thermal ramp is an original and efficient way to minimize the electrical resistance of AgNW networks.

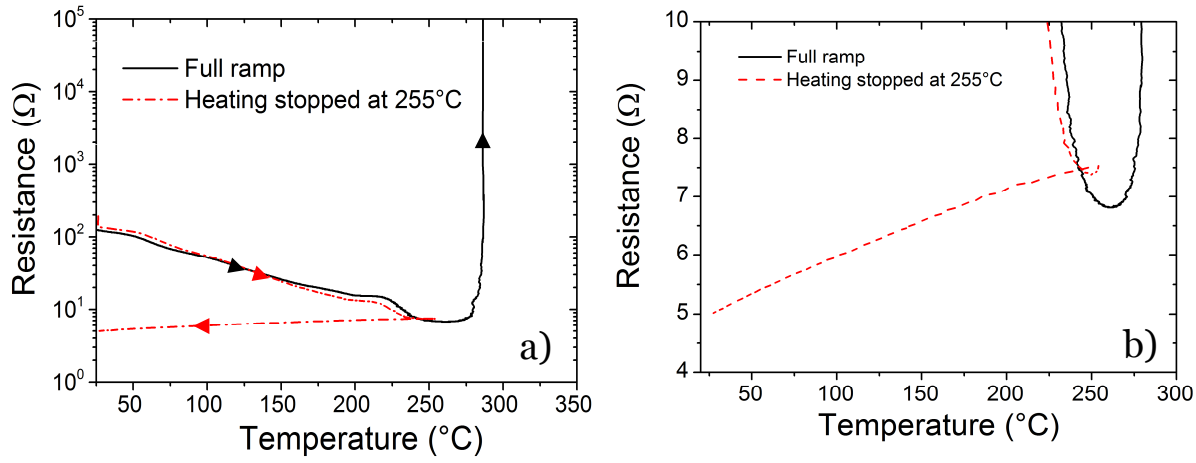

Figure 3-7: a) Electrical resistance behavior during a thermal ramp annealing at a rate of 2°C.min^{-1} performed on a sample of spin coated Ag117, until 500°C (black), and a ramp stopped at 255°C on a similar sample (dashed red) b) zoom of the same experiments in linear scale.

3.1.2 Pre-annealing treatment

Various *ex situ* annealing temperatures and times were tested to optimize the electrical resistance of AgNW networks. A sample made of Ag105 nanowires by spin coating was cut into

four equal parts in order to perform several experiments on comparable samples. The different parts were annealed at 100, 150 and 200°C, for durations of 8, 6 and 2h respectively. These duration were chosen as they allowed the sample resistance to relatively stabilize at these temperatures. We called this procedure pre-annealing.

After the pre-annealing treatment, an annealing at a ramp rate of 15°C.min^{-1} up to 500°C was performed on these samples, as well as the last quarter which didn't undergo any pre-annealing. The resistance behaviors resulting from these experiments are displayed in Figure 3-8a. It is clear that the samples heated at 100 and 150°C were further optimized by the ramped annealing even after several hours of pre-annealing, considering that their resistance decreases in the range of temperatures 150°C to 325°C. The organic residues having probably been entirely evaporated during pre-annealing, the decrease starting at 150°C might be induced by local sintering through the PVP layer. The pre-annealing at 100°C and 150°C were not high enough in temperature to induce all the mechanisms of resistance reduction. However the sample heated at 200°C has its resistance linearly increasing from room temperature to 200°C, in accordance with Equation 3-1. There is no decrease of the resistance except a slight one after 200°C but less significant compared to the two other samples. This indicates that heating the sample at 200°C for 2h is a good compromise in terms of temperature and time of annealing versus resistance optimization. An additional observation can be made in Figure 3-8a on the resistance behavior of the samples at temperatures higher than the pre-annealing treatment. Around 300°C, all curves seem to have the same behavior. The minimum resistance is approximately reached at the same time and the thermal instability occurs at the same temperature. Therefore the pre-annealing treatment doesn't impact the kinetics of the thermal process, at least when performed at such low temperatures.

This thermal optimization process at 200°C was tested on samples with various densities and the resulting sheet resistances measured *ex situ* after annealing at 200°C at different times are displayed in Figure 3-8b. The figure shows a stabilization of the sheet resistance after 2 h, confirming the results obtained in the pre-annealing study. It also shows that the sheet resistance is significantly reduced in the first minutes of annealing at 200°C (the initial resistances were between 1000 and 100 Ω/□ depending on the density and went rapidly under 10 Ω/□). These annealing conditions of 200°C for 2h were therefore often used during this thesis work to rapidly optimize the samples *ex situ*, when needed.

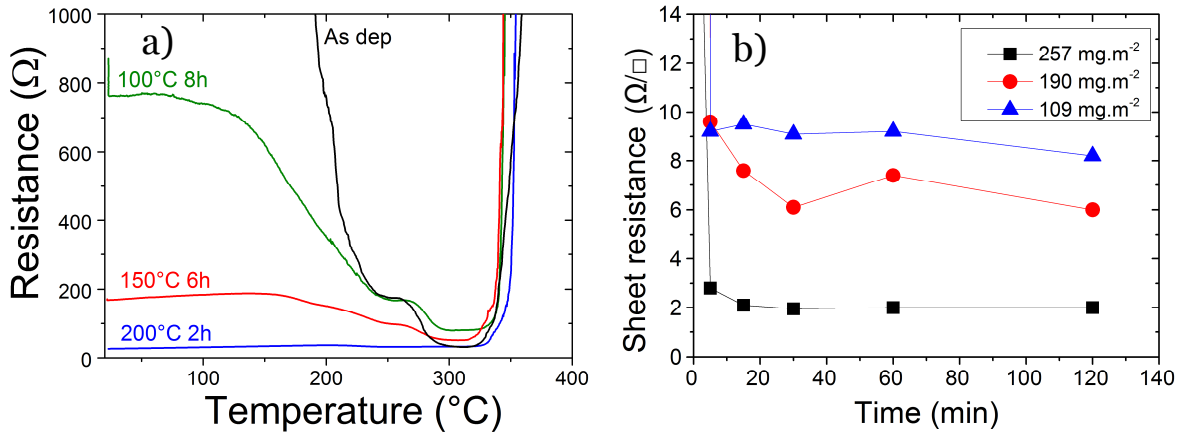

Figure 3-8 : a) Resistance behavior of the as deposited and pre-annealed samples during a thermal ramp at a rate of 15°C.min⁻¹ up to 500°C b) Sheet resistance of samples with different densities during thermal annealing at 200°C measured ex situ *at different durations (initial resistances above 100 Ω/□).*

3.1.3 Isothermal annealing

Long term annealing at a given temperature constitutes another way to go further in the understanding of the network evolution in terms of electrical optimization, and of thermal stability. The different thermally-induced mechanisms detailed in section 3.1.1.i seem to have different activation temperatures. Isothermal treatments could help to distinguish them. When the temperature is increased constantly, the network is first improved and then damaged at rather high temperature, depending on the ramp as seen in the previous section. However, knowing the behavior of such samples at constant temperature will give hints to figure out what temperature and duration combination is the best to optimize the samples without degrading them. Also it gives information on the thermal stability of the networks and on the kinetics of the mechanisms of resistance reduction.

3.1.3.i In situ resistance behavior

Thermal instability

Long term annealing at constant temperatures give additional insight regarding the thermal stability of silver nanowires. Therefore some similar samples made of Ag105 were pre-annealed *ex situ* at 150°C for 6h to stabilize their resistance and then underwent a long term annealing of 24h at 100, 150, 200, 225, 250 or 275°C during which the resistance was measured *in situ*. The resistance behaviors of the different samples during this treatment are displayed in Figure 3-9. The samples heated at 100°C and 150°C were stable even after 24h. For the other samples, the time at which instability occurs decreases with increasing temperature. Therefore at 200°C, the network resistance starts slowly to increase but only after several hours of heating. At higher temperatures, the instability occurs very rapidly, in less than 1h for the samples heated at 250°C or 275°C.

In Figure 3-9, the sample resistances don't start from the same point. This is due to the fact that the samples were fabricated by spin coating and the *ex situ* annealing was made at low temperature (150°C). This induces a variability in the initial resistances due to the nanowire junctions which have different advancement in term of optimization. Some of them would need an annealing at higher temperature to be efficient electrically. However this study still allows to see the impact of temperature on thermal instability and gives information on the duration before failure of a network at each temperature. An increase of the resistance can be seen in the beginning of each experiment presented in Figure 3-9. This, because the samples are at room temperature when the experiment is started. The increase or resistance therefore corresponds to the increase of the hotplate temperature to achieve the stabilized temperature defined for each sample (Equation 3-1).

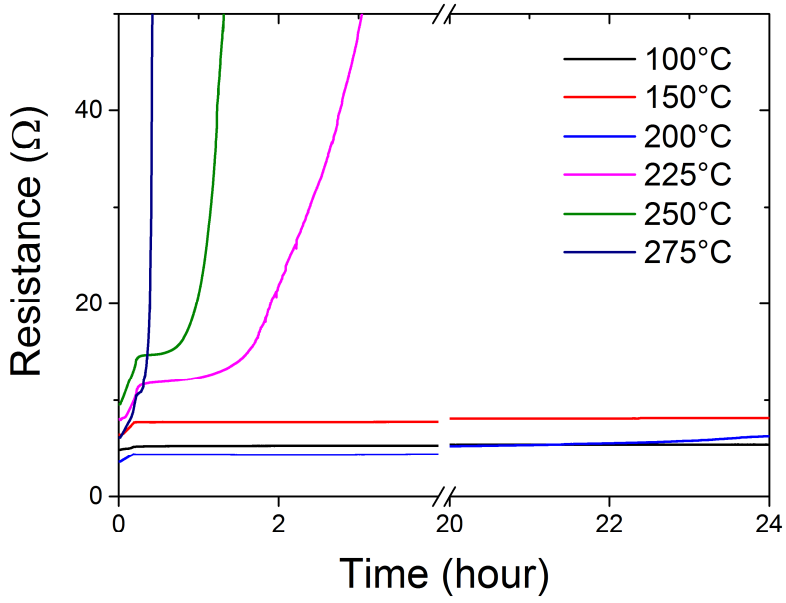

Figure 3-9: Comparison of the resistance behavior of spin coated Ag105 samples under isothermal heating in air for 24h at different temperatures, after a pre-annealing treatment at 150°C for 6 hours.

The experiment just described was made to identify the duration before instability at different temperatures. However it doesn't give any hints on the kinetics of the network resistance improvement during thermal annealing by the different thermally-induced mechanisms presented in section 3.1.1.i. Therefore, another experiment was performed without pre-annealing the samples to answer these questions, and is discussed hereafter.

Kinetics of the mechanisms

First, several networks of Ag45 nanowires were fabricated with identical density by spray coating. The samples were made on Corning glass, and the contact electrodes with

evaporated Ag. A long-term annealing of 10h has been performed on these samples at a given temperature and the resistance was measured *in situ* during the process. The process was repeated for different temperatures on similar samples. The temperature chosen were between 100°C and 400°C with 50°C spacing, except between 150°C and 250°C where the spacing was 25°C because this range of temperature is of interest for studying the mechanisms: close to the PVP transformation and sintering occurrence. The samples were initially placed on a cold hotplate which was then meant to be heated the temperatures mentioned above. The aim was to achieve the steady temperature as early as possible, so the hotplate heating ramp was set to 20°C.min^{-1}.

The behavior of the electrical resistance under these various heating processes is shown in Figure 3-10a. The first observation is that the minimum resistance achieved during the process varies with the temperature of annealing in the range of duration presented in the figure (*i.e.* ~ 2h45). Up to 200°C, the lower the temperature, the higher the minimum resistance. The samples heated at the highest temperatures in Figure 3-10a (250°C and 225°C) achieved the lowest resistance values, but these temperatures however are high enough to then induce instability rapidly, pictured by the slight resistance increase after 1100 and 5000 seconds respectively. This behavior is due again to surface diffusion driven by surface energy minimization which, after inducing a lower junction resistance through local sintering, starts to induce Rayleigh instability. The t_{Rmin}, plotted in Figure 3-10c, can therefore be seen as the time needed to optimize the junctions (and achieve R_{min}, also displayed in the figure) by sintering but also as the point at which they start to be degraded. The phenomena of local sintering and thermal instability being driven by the reduction of surface energy inducing surface diffusion, they should be controlled by the diffusion scaling law, which is solution of the two law of Fick about diffusion, *i.e.*

$$L \propto \sqrt{Dt} \qquad (3\text{-}2)$$

with L the diffusion path of the atoms, t the time and D the diffusion coefficient which has a temperature dependency that can be written as follows:

$$D = D_0 e^{-\frac{E_A}{kT}} \qquad (3\text{-}3)$$

where D_0 is constant and depends on the material studied, E_A is the activation energy, k the Boltzmann constant and T the temperature. Each physical mechanism, efficient local sintering leading to low junction resistance or Rayleigh instability occurrence, can be associated to a given value of L, characteristic of the phenomenon. Let's call this value L_C and the associated time t_C. Equations 3-2 and 3-3 would lead to a linear dependence between the logarithm of the time and the inverse of the temperature (in Kelvins).

$$\ln t_C = \frac{E_A}{kT} + \ln\left(\frac{{L_C}^2}{D_0}\right) + cste \qquad (3\text{-}4)$$

Experimentally, when the time needed to reach the minimum resistance (t_{Rmin}) is plotted versus the inverse of the temperature of annealing, two linear behaviors are observed, as displayed in Figure 3-10d where the data were taken from Figure 3-10c. The samples heated at temperature lower than 200°C have not achieved their minimum resistance (they didn't start to degrade during the process) and therefore can't be taken into account in this figure. By considering the data points in Figure 3-10d and fitting them with Equation 3-4, the activation energy E_A is found to be equal to 1 eV at low temperature (blue dashed curve), and 0.15 eV at high temperature (red dashed curve). These two values of activation energy might correspond to different mechanisms of resistance reduction. At high temperature ($E_A \approx 0.15$ eV) it could be ascribed to surface diffusion that leads to the sintering of the nanowires. At low temperature, ($E_A \approx 1$ eV) it could be ascribed to organic residue desorption. Another assumption can be that PVP is still present on the nanowires walls and can slow down the silver atoms diffusion from one nanowire to the other. They have therefore to cross the PVP barrier, and this could increase the activation energy needed for atomic diffusion at these temperatures. The temperature transition between the two phenomena is situated around 250°C, in accordance with the previous experiments (TGA, Raman).

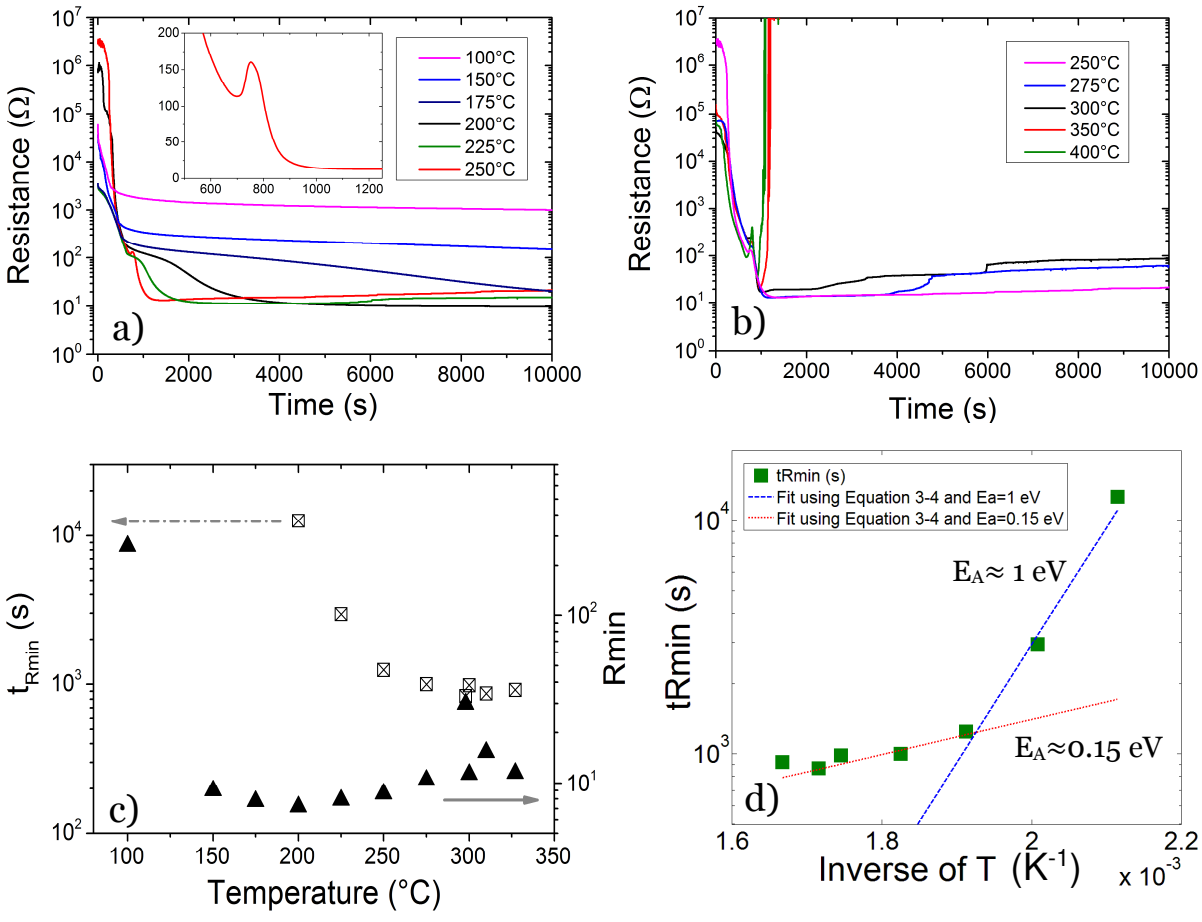

Figure 3-10: Isothermal annealing of sprayed Ag45 networks at various temperatures for 10h (the first 2h45 are displayed on the figures) for a) low and b) high temperatures; c) minimum resistance

(extrapolated at ambient temperature using Equation 3-1) and time to reach it plotted versus the temperature of long-term annealing d) time to reach R_{min} versus the inverse of the annealing temperature. The fits are associated to Equation 3-4.

For samples heated at 200°C or above, a drop of the resistance is visible early (around 2000 s for the sample heated at 200°C, around 1000s for the one at 225°C), which looks like the one observed during ramped annealing that leads to minimum resistance. For the sample heated at 175°C, we start to see it as well around 5000 s but the kinetic is slower. We can even see it at 150°C, but way later (it is not visible on the figure). This decrease might come from the silver atomic diffusion, and the process is faster for higher temperatures. At high temperatures, the process is so fast that instability occurs even before the network is fully optimized by local sintering.

The insert in Figure 3-10a displays a zoom of the 250°C curve. It shows that the resistance achieves a minimum, then increases and then decreases again. This behavior has also been observed for the samples heated at temperatures higher than 250°C, which are visible in Figure 3-10b. This phenomenon occurs when the hotplate temperature stabilizes. As previously said, the hotplate temperature first increase at a ramp rate of 20°C.min^{-1}, and then stabilizes at the defined temperature of annealing. This little resistance peak illustrates the competition between the irreversible reduction of resistance induced by local sintering, and the increase of resistance due to phonon scattering, when the temperature is elevated. It can be interpreted as follows: the resistance drops during the increase of temperature is due to chemical desorption and then local sintering. However the increase of temperature induces phonon scattering that increase the sample resistance, but the mechanisms of resistance reduction still dominate during the heating ramp. When the hotplate temperature stabilizes, the kinetics of surface energy reduction (sintering) might stabilize (at least stops to increase) and the phonon scattering starts to dominate the resistance behavior for a short time: therefore the resistance increases. Then, the temperature is well stabilized, the population of phonons doesn't increase anymore and sintering becomes dominant again.

Returning the focus on Figure 3-10c, the minimum resistance tendency shows that the optimum temperature to achieve the lower resistance stands around 200°C. The minimum resistances measured during annealing were extrapolated to room temperature using Equation 3-1. At temperature lower than 200°C, the sintering is not efficient enough, while at higher temperatures thermal instability tends to dominate the process too early. 200°C seems therefore to be the temperature allowing the lowest resistance and so the best tradeoff between efficient sintering and (low) thermal degradation. Figure 3-10c can be seen as a guideline to optimize the networks electrical properties by thermal annealing. 200°C is the best temperature in order to achieve the minimum resistance but if one wants to lower the time of annealing, one could choose a higher temperature without having a significantly higher

resistance or *vice versa* if one wants to reduce the annealing temperature (for example in order to use polymeric substrates for flexible applications).

3.1.3.ii Networks morphology evolution at different temperatures

The samples used for the isothermal study in Figure 3-10 were observed with SEM to determine the effect of the thermal treatment on the AgNW morphology. In Figure 3-11 are displayed the various morphologies obtained after 10h of annealing at 150°C, 200°C, 250°C, 300°C, 350°C and 400°C, respectively. The networks morphologies don't seem to have changed at 150°C or 200°C, although junction sintering has started. Instability starts to be observable at 250°C, where some nanowires have been broken by surface energy reduction. The thinner nanowires seem to be unstable first while the nanowires with large diameter have still, in majority, their initial shape. The nanowire junctions are visibly well sintered and most of the nanowire damaging seems to occur at these strategic locations. Surface energy reduction is enhanced close to junctions, allowing local sintering that decreases the sample resistance but then leads to the nanowire breakdown at these locations. As the temperature of thermal treatment increases, more damage is observed and the nanowires tend to transform into droplets to minimize their surface energy. The SEM image of the network heated at 350°C is very interesting: some nanowires are still cylindrical while some other are fully spheroidized, probably the thinnest. The sheet resistance of the different samples was measured using four point probes after annealing and those heated at 300°C or below are still conducting. However the resistance of the sample heated at 300°C measured between two points is above the Keithley detection limit ($> 10^7$ Ω). Therefore the sample is still conducting at some locations but the major percolating pathways between the two contact electrodes have been damaged. After 10h annealing at 350°C and 400°C, the samples sheet resistance was above the detection limit: this can be associated with the strongly damaged morphology of these samples observable in Figure 3-11.

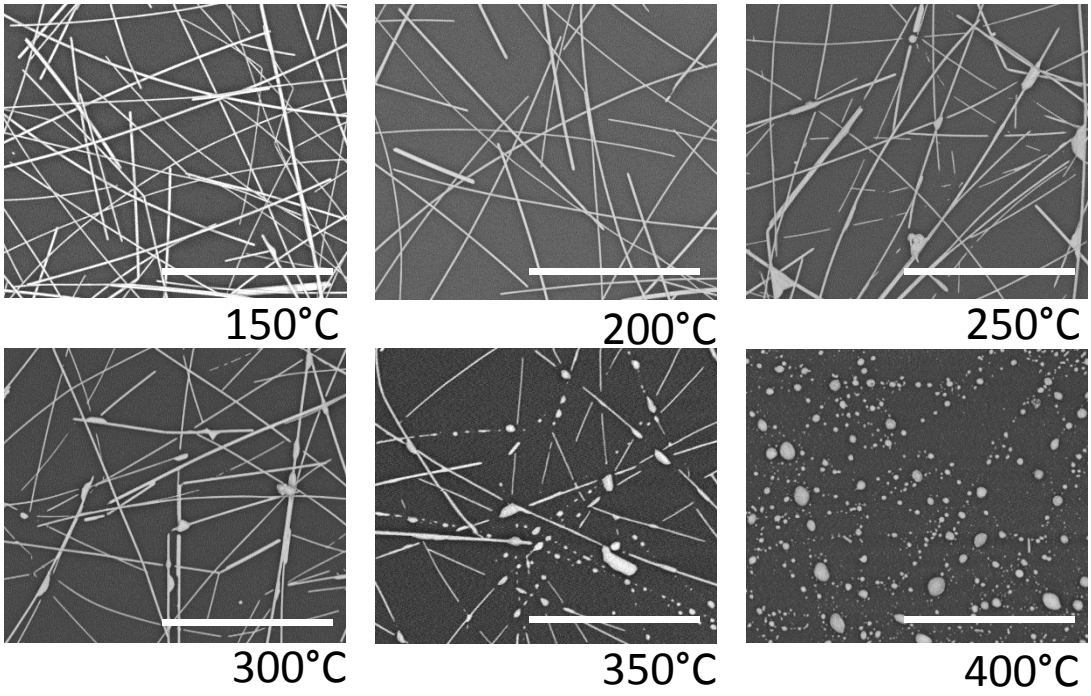

Figure 3-11: SEM observations of the morphology of sprayed Ag45 networks after different isothermal treatments. Each sample was heated for 10h at the different temperatures inscribed below each image. All scales are 4 µm.

3.1.3.iii Effects of density

As the process of instability seems to start at the junctions, a comparison of samples with different network densities might be interesting, considering that the number of junctions increases with density. Long term annealing between 200°C and 300°C was performed on samples with two different densities (around 50 and 150 mg.m^{-2}) during 24h.

At 250°C, the samples with different densities don't exhibit the same behavior. Some samples undergo instability, some don't. In accordance to the previous experiments (Raman, TGA), 250°C is a transitional temperature in the process of thermal annealing, between sintering and thermal instability. Statistics induce a non-reproducibility in the instability observation at this temperature: some networks are less sintered and don't spheroidize while others are in an advanced stage of surface energy reduction, starting to degrade the junctions. Regarding the minimum resistances achieved by the samples during heating above 200°C, displayed in Figure 3-12a, R_{min} increases with annealing temperature, in accordance with results displayed in Figure 3-10c. This is especially visible for low density networks (red markers in Figure 3-12a) while for dense networks the increase is smaller.

Figure 3-12b presents the time to achieve R_{min} and the time to achieve thermal instability (resistance > 100 000 Ω) during the different annealing performed on both network densities. While the time to achieve R_{min} is not greatly affected by density, it seems that the high density networks are stable slightly longer at high temperatures compared to low density

networks. They probably have more chance to have efficient percolating pathways over the network at high temperature. Equation 3-4 was also used to fit the time to reach R_{min} (t_{Rmin}) in this experiment, but also the time needed to be unstable (t_{Sph}) regarding temperature. In Figure 3-12c, which displays t_{Rmin}, two linear fits can be identified, similarly to the previous experiment shown in Figure 3-10d. The corresponding activation energies appear to be close to 1eV at low temperature and about 0.3 eV at high temperature. Once again these activation energies can be related to different mechanisms: chemical desorption, atomic diffusion through PVP, and surface diffusion. The transitional temperature is situated again around 250°C. Regarding the time of instability presented in Figure 3-12d, the fit of the experimental results using Equation 3-4 implies an activation energy around 1 eV. This activation energy might be related to mechanisms of surface energy reduction, coupled with the separation of atoms due to spheroidization, in accordance with our understanding of the mechanisms induced by thermal annealing.

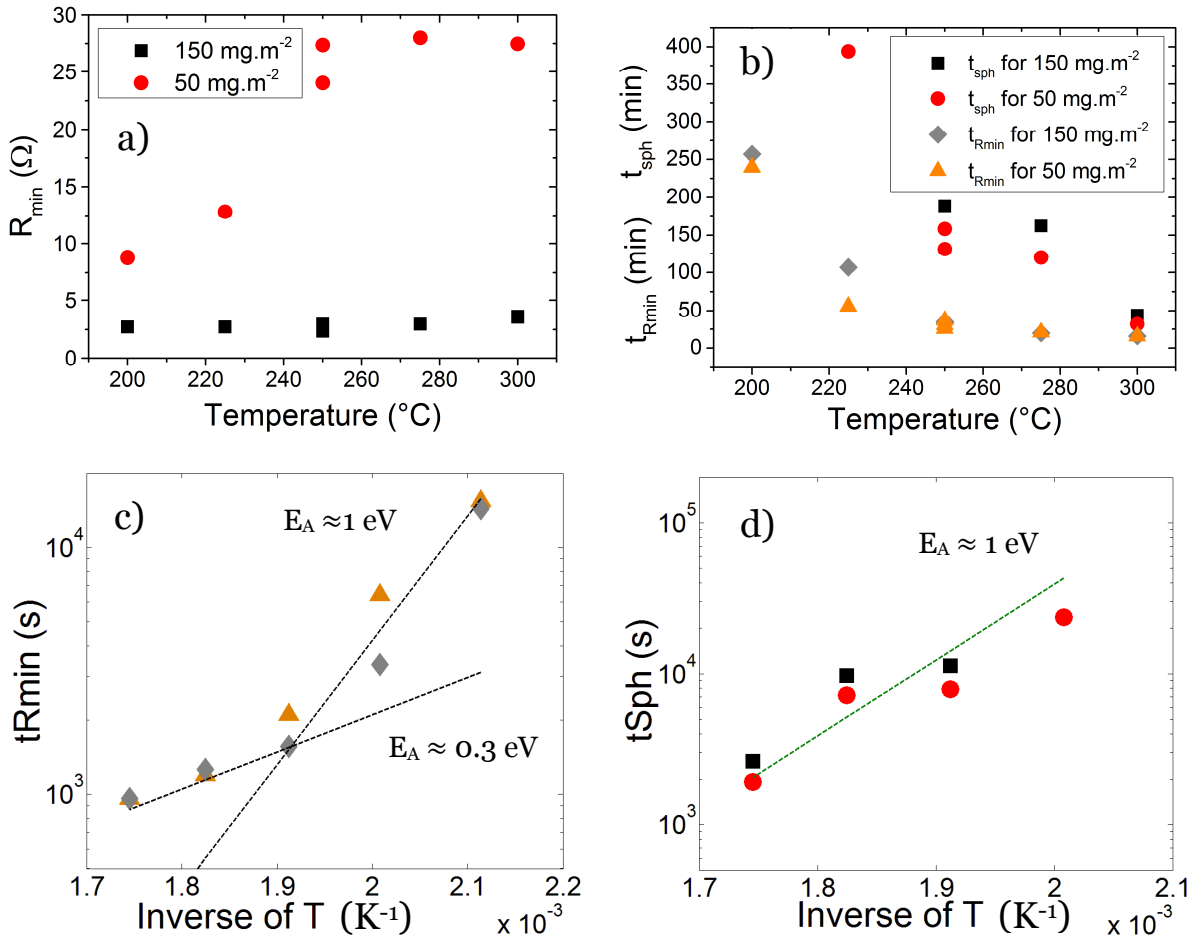

Figure 3-12: Effect of density on isothermal annealing at different temperatures a) Rmin value achieved during isothermal annealing regarding temperature for two different network densities b) Times to achieve R_{min} (t_{Rmin}) and to become instable (t_{sph}) at various temperatures for high and low density networks c) fitting of t_{Rmin} values using Equation 3-4 d) fitting of t_{Sph} values using Equation 3-4.

3.1.4 Thermal instability

Thermal instability is a serious issue for silver nanowire networks considering that the widely used method for optimizing their electrical properties is thermal treatment. Moreover AgNW networks are required to conduct electrical current that should increase their temperature by Joule heating, therefore they need to be resistant to heat. In addition their use as transparent heaters can be limited by thermal instability. Thermal instability has been seen to be dependent on the thermal ramp rate in section 3.1.1.iii and we'll see in Chapter 4 that it also depends on the nanowire diameter. The present section is dedicated to the understanding of thermal instability and on the various ways to prevent it.

3.1.4.i Thermal annealing under vacuum

In order to directly observe the nanowire thermal instability, studies of temperature effects on AgNW networks have been performed *in situ* in a SEM, therefore under vacuum. A sample was heated up to 700°C and no morphology change was observed up to this temperature, as can be seen in Figure 3-13a to c. The nanowires seemed to disappear after 700°C but didn't spheroidize. This behavior have been observed as well by Mayoral et al.[9] who heated nanowires above 650°C *in situ* in a STEM without seeing spheroidization but they observed a carbonaceous shell left on the substrate (probably graphitized PVP and/or amorphous carbon left from the nanowire synthesis).

We then performed thermal treatments under vacuum while measuring the resistance *in situ* to see if vacuum prevents the mechanisms of resistance reduction. Figure 3-13d presents an annealing at 280°C of a Ag105 network under vacuum for 60 min. The resistance is reduced by more than one order of magnitude under vacuum and then starts increasing after few minutes, before decreasing again during the cooling. The network was observed under SEM after annealing, and a modification of the nanowire morphology is clearly visible, as if the sample had been annealed in air (see Figure 3-13e). Therefore morphology modifications do occur under vacuum as it does in air, but the nanowire instability is different depending on the environment, and spheroidization doesn't occur under vacuum. It could be explained by the fact that, during thermal annealing, silver atom diffusion occurs at nanowire junctions even through the PVP layer, but the latter stays on the nanowires walls, as seen in 3.1.1.ii. Under vacuum the PVP might evolve into graphite when heated and create a protecting shell around the nanowires, preventing them from spheroidization, as suggested by Mayoral et al.,[9] while in air PVP can decompose due to the presence of oxygen.

Morphological changes due to thermal instability couldn't be observed *in situ* under SEM.

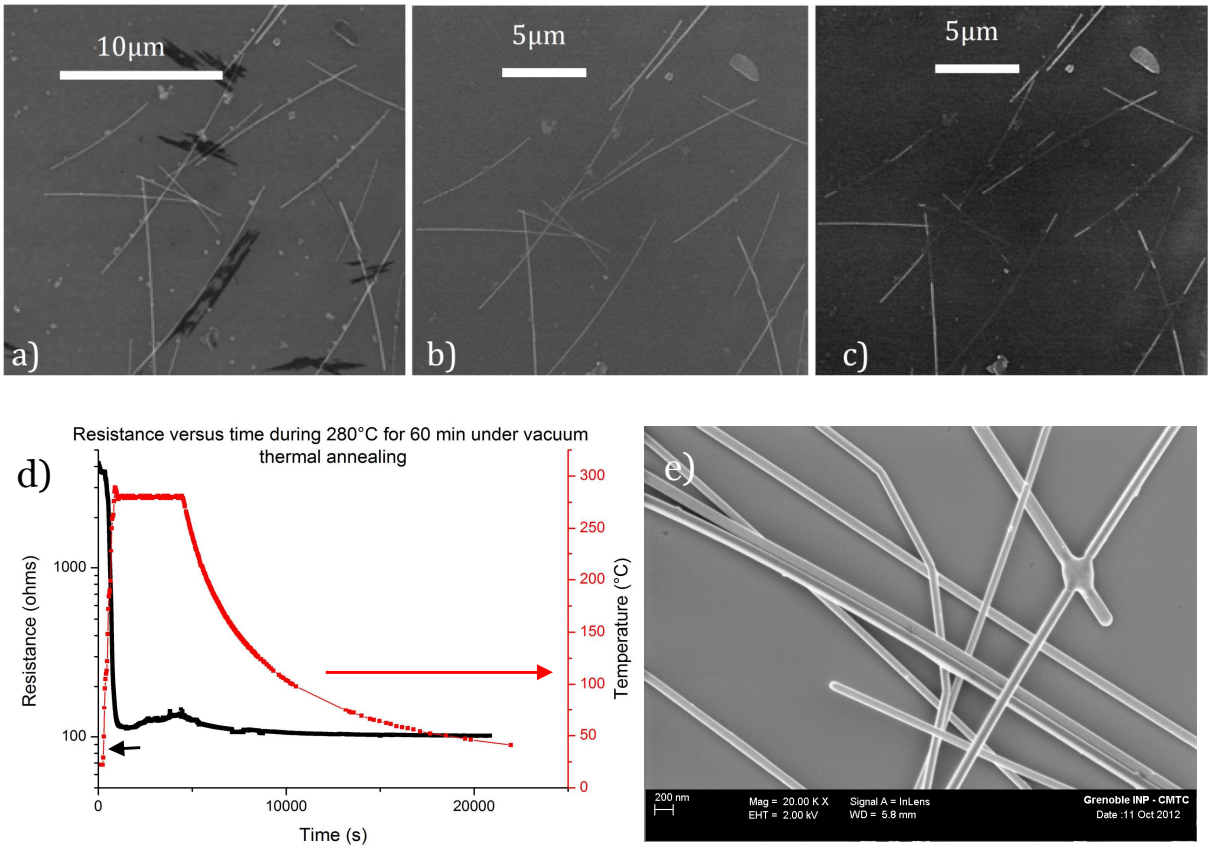

Figure 3-13: SEM images during an in situ *annealing. Images were taken at a) 30°C, b) 620°C and c) 717°C, published in reference [17] d) electrical resistance evolution of a Ag105 network annealed at 280°C under vacuum for 60 min and e) SEM image of the same sample morphology after annealing (*ex situ*), with a visibly sintered junction.*

One interesting study would be to perform a high temperature annealing under vacuum, in order to create the mentioned carbon shell. Then by doing another annealing at air, we could see if the graphitized shell created under vacuum would remain around the nanowires and protect them from thermal-induced degradation.

3.1.4.ii ZnO thermal protection

In order to increase silver nanowires thermal stability, a metal oxide under the form of a thin layer or of nanoparticles[18] can be deposited on the network, which will limit thermal-induced surface diffusion. Some spin coated AgNW networks were therefore coated with a zinc oxide (ZnO) layer to create a shell around the nanowires to improve their thermal stability. The coats were deposited by dip coating following a protocol which was developed with the help of Sophie Guillemin (LMGP), who developed similar seed layers, aimed for ZnO nanowire growth.[19] The protocol is the following: first, a solution of zinc acetate with monoethanolamine (MEA) is made in ethanol, with a concentration of 0.375 M. For 250 ml of final solution, we used 5.6 ml of MEA and 20.6 g of dihydrate zinc acetate. The solution was then heated at 60°C and stirred for 12h. The AgNW samples were then coated with this zinc

acetate solution using dip coating. Two heating stages, one of 10 min at 300°C and another of 20 min at 450°C were performed to obtain a crystallized layer of ZnO.

Networks of Ag105 were coated with a ZnO layer of thickness around 60 nm. Compared to bare glass, ZnO induced a reduction of total transmittance around 5.3% and around 7% for direct transmittance. Regarding the sheet resistance, the coated networks had resistances between 25 and 70 Ω/□ whereas the uncoated sample were at the limit of percolation. This difference comes from the heating steps mandatory for the ZnO film growth (see protocol) which probably induce some local sintering at nanowire junctions. Both bare and coated samples were then heated at 500°C for 2h on a hot plate, to test the protecting capability of ZnO. Figure 3-14 shows SEM images of the uncoated and coated with ZnO networks after this thermal treatment. The uncoated sample is entirely spheroidized, as expected, but the coated sample still presents unchanged nanowires. Therefore ZnO protects silver nanowires at temperatures as high as 500°C, and also enables to stabilize the nanowires on the substrate surface: the nanowire adherence is improved since the hybrid sample can pass the tape test without being removed.

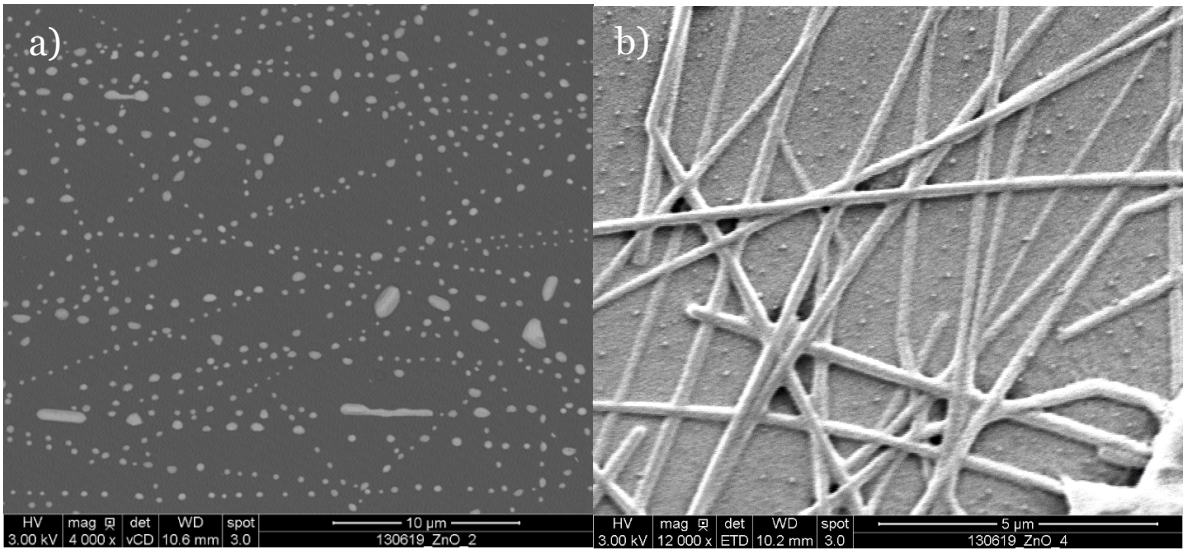

Figure 3-14: a) Morphology of an as deposited network after an annealing at 500°C for 2h, and b) Morphology of a network coated with 60 nm of ZnO after annealing at 500°C for 2h.

Another batch of coated samples was made with Ag105 to test reproducibility. However this time the networks spheroidized after an annealing of 2h at 500°C. One coated and one uncoated sample from the second batch were annealed with a thermal ramp at a rate of 15 °C.min^{-1}, the resulting curves are displayed in Figure 3-15. Even if the samples are not stable at 500°C, the figure clearly shows that ZnO increases the networks temperature of instability of slightly more than 100°C. However the minimum resistance achieved by the coated sample is higher than the one reached by the uncoated one. This can be explained by the deposition of

ZnO layer on the sample which requires high temperatures: 300°C for 10 minutes and then 450°C for 20 minutes, for ZnO crystallization. This process might damage the AgNW, inducing an irreversible increase of the network electrical resistance.

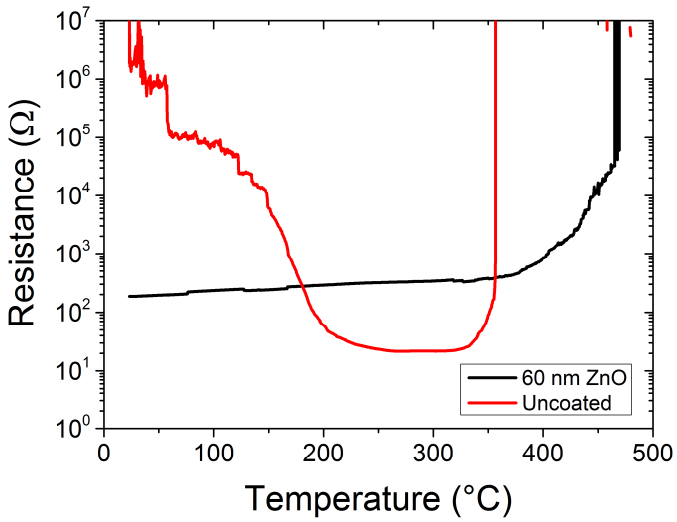

Figure 3-15: Electrical resistance behavior of a network of spin coated Ag105 coated with 60 nm of ZnO and of an uncoated sample during a thermal annealing with ramp rate of 15°C.min^{-1}.

ZnO has been proven to have potential in both thermal stabilization of AgNW and adherence improvement. However the results presented here are not perfectly reproducible and the sample transmittance is strongly impacted by the ZnO layer, as well as the electrical resistance. These problems probably come from the method of ZnO deposition which might be non-reproducible in thickness and uses high temperatures. Reproducibility is highly dependent on the method of deposition and on the freshness of the solution used for the dip coating, as well as on the age of the precursors. Besides, deposition of less material and at lower temperature would be required to limit the impact of ZnO on the optical transmittance.

Compared to dip coating, atomic layer deposition (ALD) technique should give more reproducible results in terms of thermal stability improvement of AgNW networks. An ALD setup has been recently developed at the LMGP by Jean-Luc Deschanvres and Hubert Renevier, allowing to deposit thin layers of ZnO at low temperature. It would be helpful to fabricate reproducible sample coated with ZnO allowing a more thorough study of the AgNW protecting capacity of this material.

3.1.4.iii TiO_2 thermal protection

Different other metal oxides can be used to create a protecting shell around the AgNW to thermally stabilize them. Among them, TiO_2 has been proven by Ramasamy *et al.*[20] to be efficient as a thermal stabilizer up to 750°C. However they studied the core-shell nanowires in

a TEM under high vacuum so it is interesting to also test the protecting layers in air considering the stabilization effect of vacuum on nanowires explained earlier. An ALD setup allowing to deposit TiO_2 was used in a platform nearby the LMGP: the PTA (Up-line Technological Platform), in Grenoble in collaboration with Dr David Muñoz-Rojas (LMGP). The main advantage of ALD is a conformal coating of a thin layer that can be performed at low temperature, which prevents AgNW instability during the deposition process.

The deposition was made at 250°C and the deposition rate corresponding to the recipe we used is estimated by the PTA to be around 0.40 Å by cycle. Each cycle has a pulse of water (unheated) for 0.06s, and then a purge time of 5s, then a $Ti(NMe_2)_4$ precursor (heated at 75°C) pulse of 0.10s followed by another purge time of 5s. The number of cycles used was 65, therefore the TiO_2 layer thickness considering the time of deposition was estimated to be 2.5 nm. TEM imaging of the nanowires was performed to validate this thickness, but the TiO_2 layer was found to be more close to 5 nm, as shown in Figure 3-16a. The TEM images also showed that the TiO_2 layer was mainly amorphous after deposition but after 1h annealing at 300°C, it became crystalline (see Figure 3-16b).

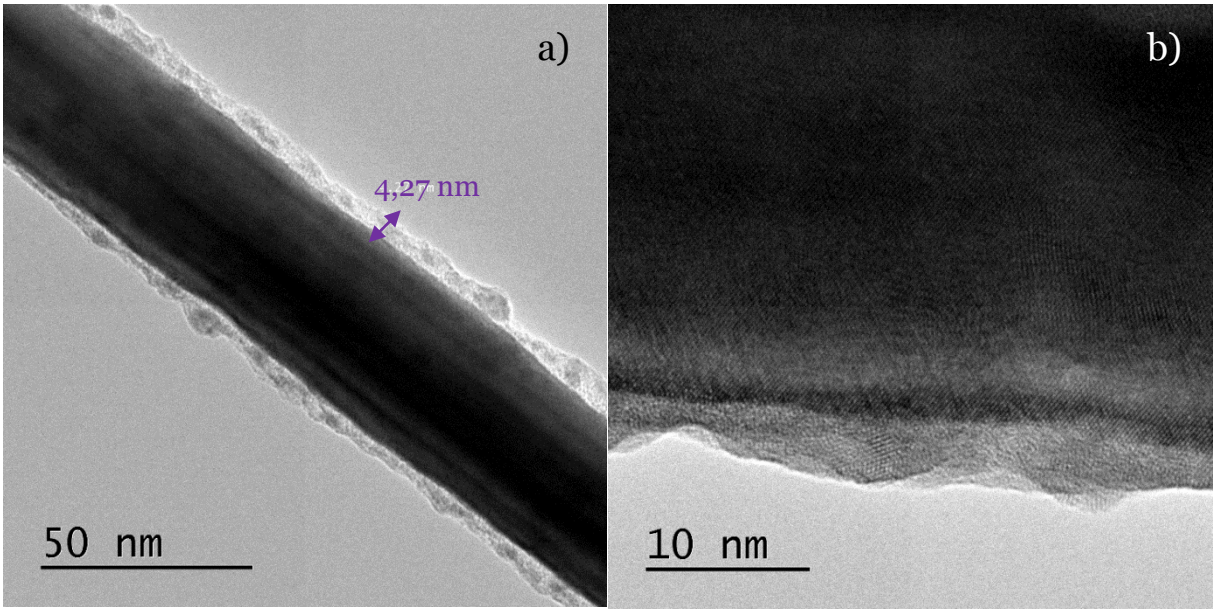

Figure 3-16: a) TEM image of the amorphous TiO_2 layer deposited by ALD on a Ag45 nanowire b) TEM image of a TiO_2 coated Ag45 nanowire after annealing 1h at 300°C: the TiO_2 layer is crystallized.

The TiO_2 layer didn't impact much the transmittance especially in the visible range, as seen in Figure 3-17a. As deposited samples had a transmittance at 550 nm around 87.7% and those coated with TiO_2 were around 87.1%. Regarding light diffusion, the haze factor of the different samples didn't vary much either and stands between 3.4% and 4% at 550 nm. As the sample temperature was elevated up to 250°C during the ALD deposition, the sample

resistance decreased during the TiO_2 deposition process and the nanowire junctions were well sintered (Figure 3-17e). The coated sample had a sheet resistances of 1800 Ω/□ after TiO_2 deposition while the initial resistance of the bare network was above 10^7 Ω/□. During ALD deposition, the sample is heated at rather low temperature (250°C) so the nanowires are not thermally damaged during the process. This is even beneficial as it acts as a thermal annealing process (promoting local sintering) and reduces the sample electrical resistance.

Coated and uncoated samples were then heated at a ramp rate of 2°C.min^{-1} up to 500°C and then cooled back to room temperature. TiO_2 played well its role of thermal stabilizer by shell action as can be seen in Figure 3-17b where the divergence of the resistance never occurs for the coated sample, even if the TiO_2 layer thickness is as low as 5 nm. A slight increase of the resistance occurs, which might be caused by the deterioration of some junctions that could be badly or partly coated, but at higher temperature compared to as deposited sample. One must be aware that some coated samples actually have their resistance increasing more significantly around 420°C, but not all of them. These disparities in electrical behavior might come from the very low thickness of the TiO_2 shells. Therefore they protect the nanowires but are still fragile and could fail to protect the nanowires at some locations in the network, not in a necessarily reproducible way. However for every sample the networks electrical resistance starts to slightly increase around 300°C, like in Figure 3-17b but the value of the resistance increase is not reproducible. Returning to the thermal ramp annealing, at the end of the process the sample is still conducting, the nanowires are still cylindrical even if some parts of the network are slightly damaged (at the junctions in particular), like in Figure 3-17f.

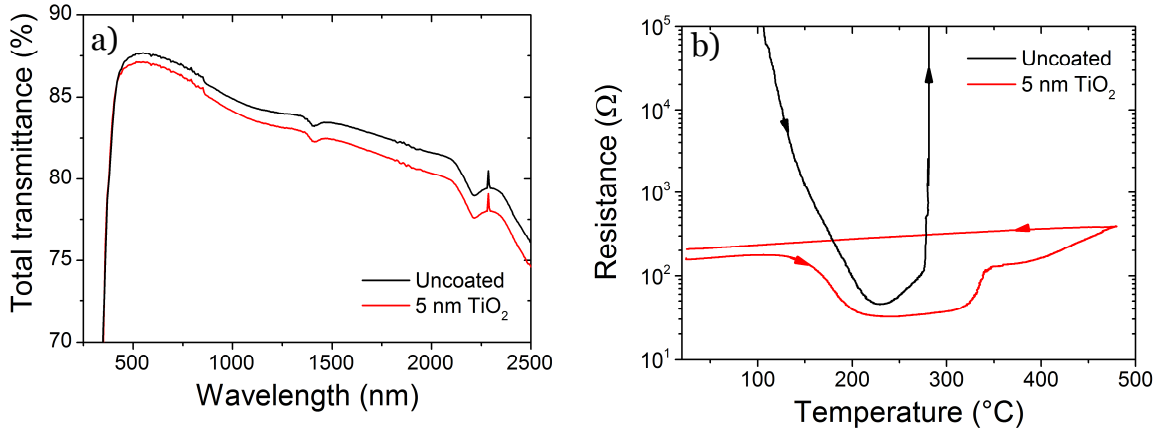

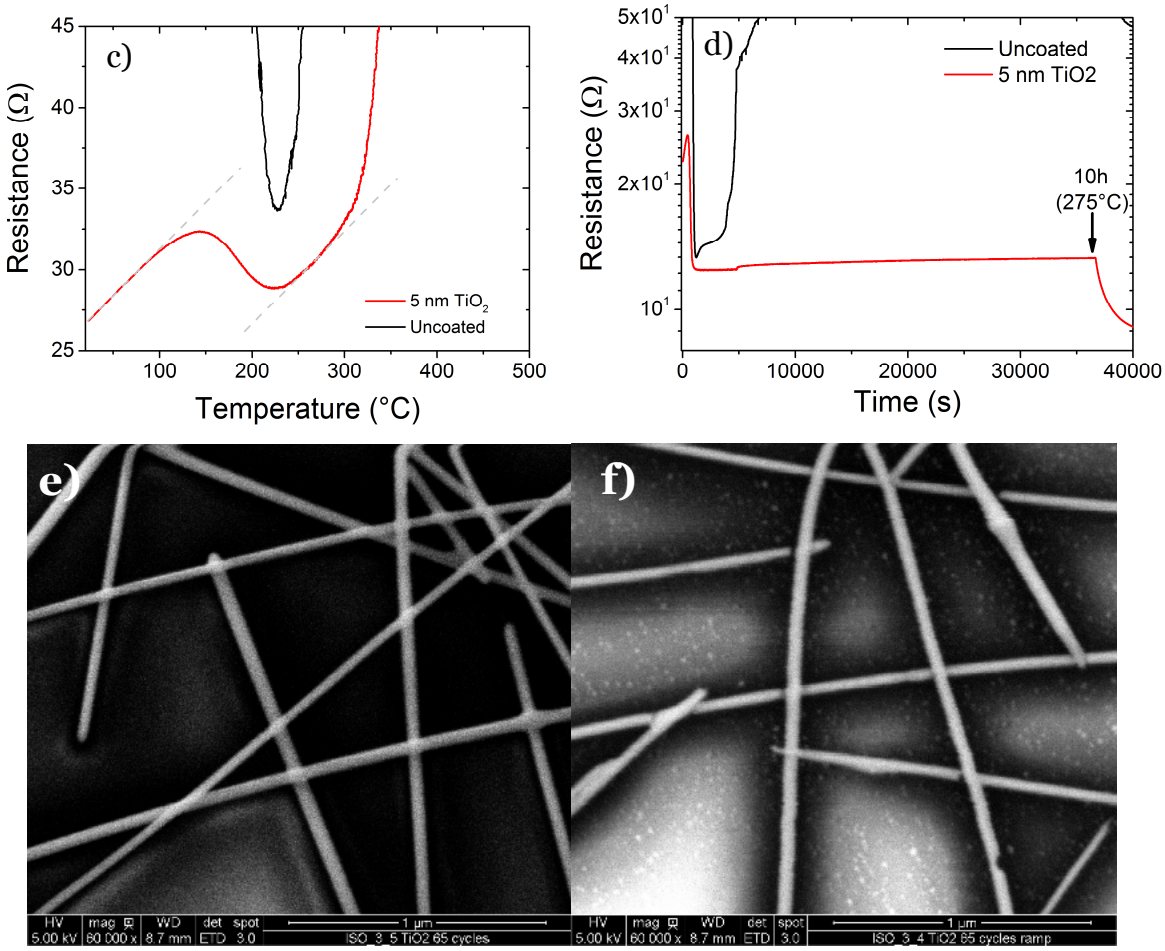

Figure 3-17: a) Influence of an ALD deposited TiO_2 layer of 5 nm on a AgNW network total transmittance (on a Corning glass substrate) b) Influence of a 5 nm thick TiO_2 layer on a AgNW network electrical resistance behavior during a thermal ramp at a rate of 2°C.min^{-1} c) zoom showing the different thermal mechanisms influencing the network electrical resistance: phonons scattering, sintering and instability d) Influence of a TiO_2 layer of 5 nm on the sample thermal stability during a long term annealing at 275°C e) SEM image of a Ag45 network coated with 5 nm of $TiO_2$by ALD f) the same coated sample after a thermal ramp at a rate of 2°C.min^{-1} up to 500°C.

Two other samples (one coated with 5 nm TiO_2 and one uncoated) underwent the same thermal ramp annealing (2°C.min^{-1}). A zoom on the critical point of the electrical resistance curves, where the minimum resistance is achieved, followed by the start of the instability dominance, is displayed in linear scale in Figure 3-17c. This figure illustrates very well the different phenomena which have an impact on the samples electrical resistance. At the beginning of the process, the electrical resistance of the coated sample is linearly increasing with temperature, as for bulk metals, due to phonon scattering (Equation 3-1). The uncoated sample, on the contrary, has its resistance decreasing due to organic residues desorption that are still present around the nanowires and then local sintering. These mechanisms already occurred (at least partly) for the coated sample during ALD deposition performed at 250°C. Then the resistance deviates from this linear behavior and decreases. This can be interpreted as a continuation of local sintering at some junctions that were not fully sintered during ALD

deposition. After the completion of sintering, the resistance increases linearly again, with the same slope than initially. Therefore this increase can be interpreted again by phonon scattering (with tendency is illustrated by the dotted lines). But shortly afterward the resistance deviates again from this linearity and increases more rapidly. This increase can be ascribed this time to a dominance of the Rayleigh instability which has detrimental effects on the resistance, in comparison to the phonon scattering effects.

TiO_2 capacity to improve thermal stability has also been demonstrated during a long term annealing. One coated and one uncoated sample were heated at 275°C for 10h, as shown in Figure 3-17d. While the uncoated sample became instable after less than 2h, the coated sample was conducting until the end of the process, the resistance having increased by less than 1 Ω.

Some TiO_2 coated samples with a higher thickness (15 nm) were heated up to 600°C, and their resistance has been seen to increase sharply, rendering the sample non-conducting just before 500°C because of thermal instability, see Figure 3-18a. Their morphology after annealing was investigated under SEM. The sample was found to have empty TiO_2 shells at some locations, as can be observed from SE and BSE SEM images shown in Figure 3-18b and c. This time the thickness is high enough for preventing the nanowire to be degraded everywhere. TiO_2 prevented silver spheroidization: the nanostructures are still cylindrical, but silver moved anyway and went out the TiO_2shells, causing the loss of electrical conductance. These coated samples with 15 nm of TiO_2 were resistant until 465°C, against 300°C with 5 nm. However the 15 nmTiO_2 shells are so thick that they seem to "break" as can be seen in the red circle in Figure 3-18b, which might be a problem for flexible applications.

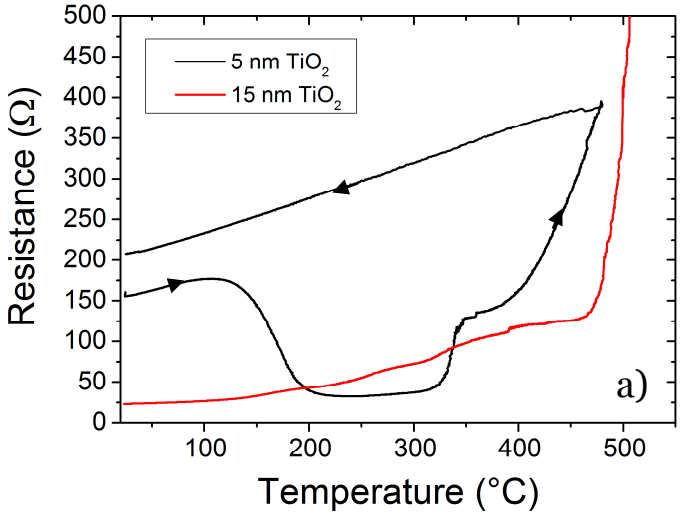

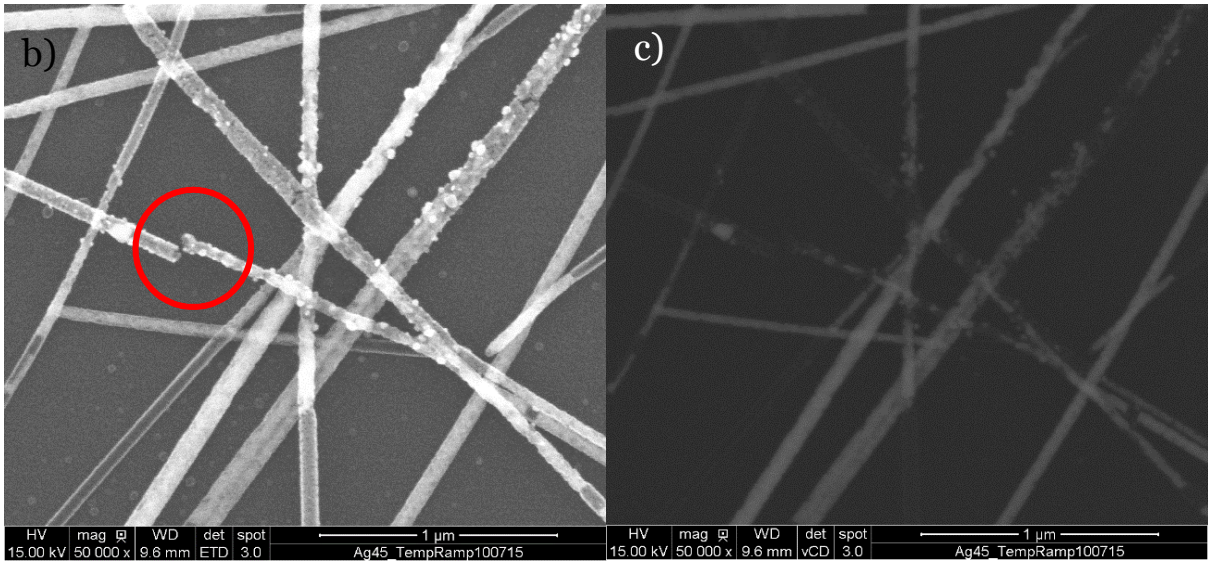

Figure 3-18: Resistance behavior of Ag45 networks coated with 5 nm and 15 nm of TiO_2 during a thermal ramp annealing at a rate of 2°C.min^{-1}, b) SE SEM image of the network morphology after annealing (15 nm TiO_2) and c) BSE SEM image of the same location.

The TiO_2 protection shell also improves the electrical stability of AgNW networks, in addition to the thermal stability, as will be addressed in Chapter 5.

3.1.4.iv SALD at the LMGP

A spatial ALD (SALD) setup is being developed at the LMGP by David Muñoz-Rojas. This setup performs the different injections of precursor and purges, normally sequenced during such process, at the same time constantly while the sample moves.[21] This technique is much faster than temporal ALD, can be operated in ambient conditions and is relevant for depositing on large surfaces.[21] This setup would allow to deposit different metal oxides on the AgNW, with reproducible thicknesses, and then to observe their protecting properties.

3.2 Effects of thermal treatments on optical properties

Considering that thermal treatments have a strong impact on AgNW networks morphology and on their electrical properties, the question we address now is to know whether the optical properties of the samples are also modified by such treatment. To answer this question, the transmittance of several initially identical samples made by spray coating on Corning glass is measured at different stages of a thermal ramp, like the one presented in Figure 3-1. As deposited samples were optically studied at each of the thermal process stages (the mentioned stages are noted b, c and d in Figure 3-1) as well as samples coated with TiO_2 (~ 5 nm thick). The corresponding *in situ* measurements of the resistance of the different samples during the annealing at a ramp rate of 2°C.min^{-1} is displayed in Figure 3-19. For the thermal stage corresponding to the minimum resistance achievement, the heating was stopped at 270°C and

the sample was cooled back down to room temperature before the transmittance measurements were performed (green and red curves in Figure 3-19).

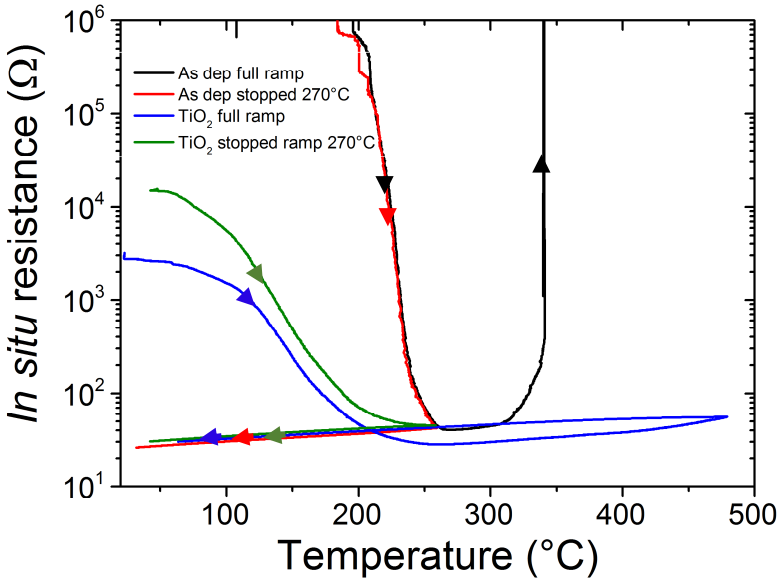

Figure 3-19: Resistance behavior during a 2°C.min^{-1} thermal ramp of Ag45 samples: full ramp and ramp stopped at 270°C, and the same experiment on samples coated with TiO_2. The samples were then used for an optical study of the thermal annealing effects.

After thermal annealing, the samples had different morphologies, depending on the temperature achieved, which are presented in Figure 3-20. The as deposited samples present expected morphologies that have already been observed in previous experiments. The junctions are welded at 270°C, explaining the networks low resistance, and the network is entirely spheroidized at 500°C. Regarding TiO_2 coated samples, their morphologies are different from the as deposited sample. As discussed above, the ALD performed at 250°C acts like a thermal annealing on the networks and the nanowire junctions are well welded before the thermal ramp is performed. Then the annealing stopped at 270°C has not a strong impact on the network morphology, the junctions are still welded and the nanowires still stable. While spheroidization has totally destroy the as deposited network at 500°C, the TiO_2 shell appears to have protected efficiently the nanowires: even at high temperature, the coated nanowires seem to be rather stable, even if some of them started to break at junction, mainly the thinnest.

a) As deposited Ag45

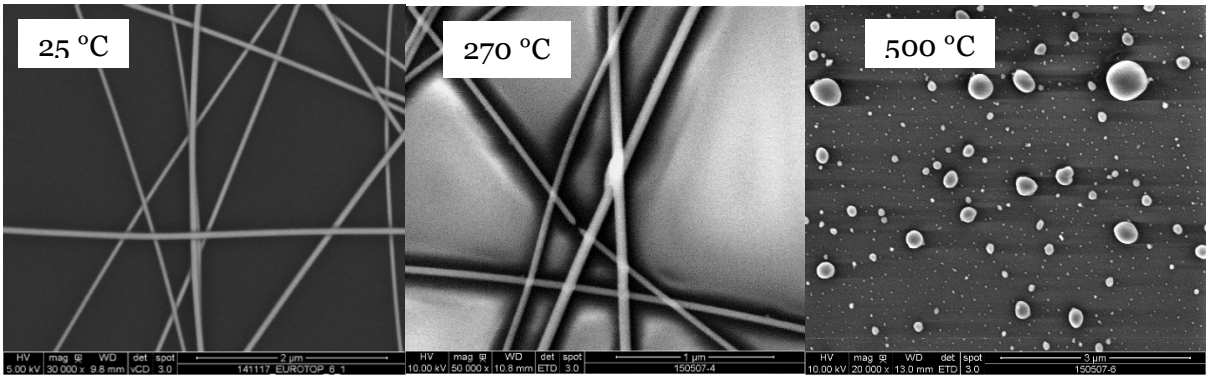

b) Ag45 coated with TiO_2

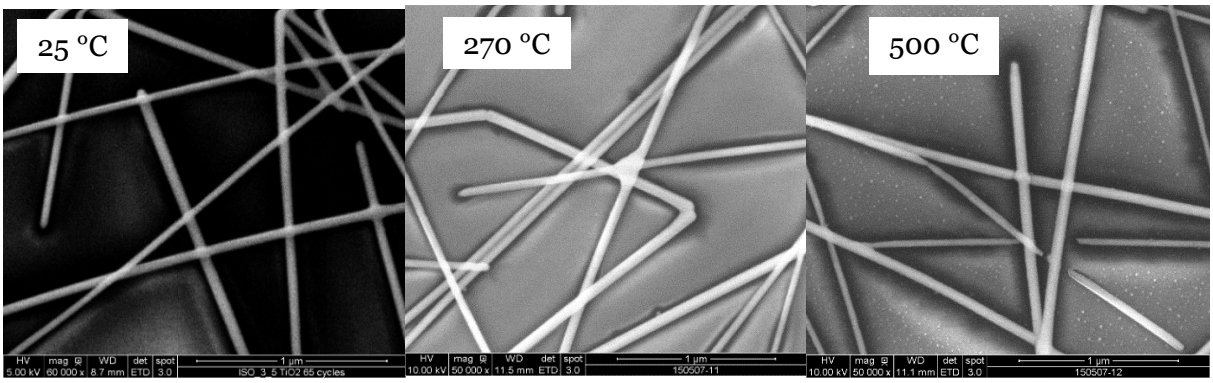

Figure 3-20: Morphology of Ag45 networks during a thermal annealing at a ramp rate of 2°C.min^{-1} up to the temperature inscribed in each image a) AgNW as deposited b) AgNW coated with a TiO_2 layer of 5 nm deposited by ALD.

Now that the resistance behavior as well as the network morphological changes have been recalled in this small summary, the focus is turned towards the network optical properties to see if these changes have impacted them.

3.2.1 Optical properties at the stage of junction optimization

Four samples in total underwent an optimum annealing *i.e.* a ramp stopped when R = R_{min} (*i.e.* 270°C in this case): two coated and two uncoated samples. Each uncoated sample had their transmittance and reflectance measured before and after annealing, the results are displayed in Figure 3-21a with the calculated haze factor and the same data from the bare substrate. A zoom on reflectance and haze factor is displayed in Figure 3-21b. The thermal ramp stopped at 270°C, doesn't induce any visible significant change in any of these optical properties. Only a slight increase of the total transmittance as well as a slight decrease of the reflectance is visible. One should be aware that these differences however stands in the spectrometer uncertainty and therefore could stem from the measure accuracy.

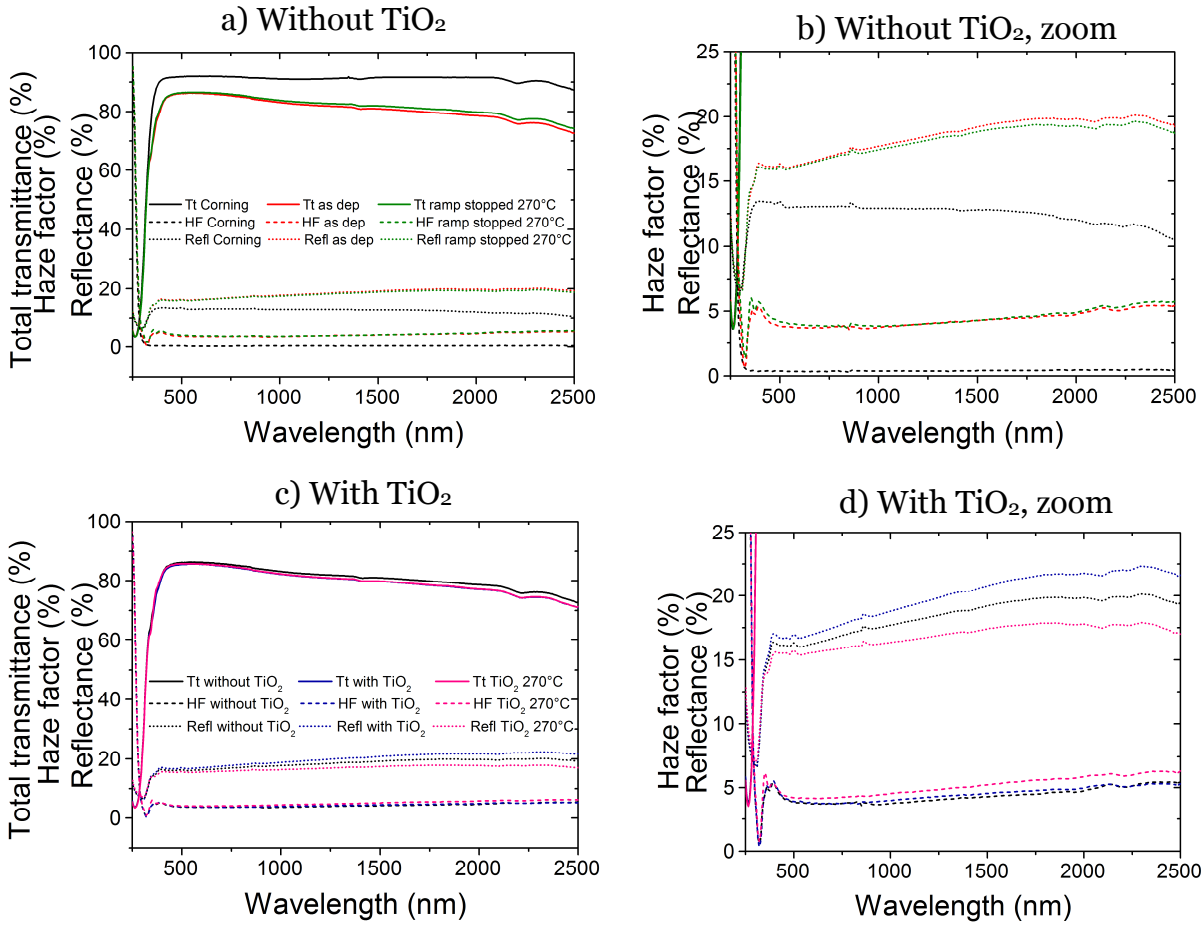

Figure 3-21: a) Total transmittance spectra, haze factor and reflectance before and after ramp annealing 2°C.min^{-1} up to 270°C of a sample made with Ag45 and of the substrate b) zoom on reflectance and haze factor c) Total transmittance spectra, haze factor and reflectance before and after ramp annealing 2°C.min^{-1} at 270°C of a sample made with Ag45 coated with 5 nm of TiO_2 and the same spectra of an uncoated sample before annealing d) zoom on reflectance and haze factor.

The same spectra were performed on the samples coated with TiO_2 and are displayed in Figure 3-21c and d. Compared to uncoated samples, the total transmittance of coated samples is slightly lower, especially in the range of large wavelengths. The haze factor is not strongly impacted by TiO_2 coating either. However the as deposited networks reflectance is lower than the coated network reflectance before annealing. The increase of thickness due to the TiO_2 layer as well as the coating of the sample part between the nanowires which normally are bare might have increase the total reflectance of the sample.

After annealing with a ramp rate of 2°C.min^{-1} stopped at 270°C, the transmittance of coated samples hasn't changed (the corresponding blue and pink curves in Figure 3-21c are superposed). But surprisingly, reflectance reduced after annealing and became even lower than the as deposited networks, while this annealing had no impact on non-coated samples. Also the haze factor increased, mostly in the IR range. The increase of haziness might come from the crystallization of TiO_2 that might occur in this temperature range, as seen previously. The reduction of reflectance remains however quite unclear and requires further investigation.

3.2.2 Optical properties after heating up to 500°C

Other uncoated samples similar to those used in the last section underwent a full thermal ramp up to 500°C. Once again their transmittances were measured before and after annealing. The resulting optical properties displayed in Figure 3-22a and b show a strong difference between as deposited and annealed samples. After 500°C, a drop in transmittance appears centered around 520 nm. A peak is also appearing in reflectance and haze factor, centered around 580 nm. These changes are probably caused by the complete change of morphology of the networks: after being heated up to 500°C, the nanowires become nanoparticles and therefore change the optical properties of the sample.

Regarding TiO_2 coated samples, no significant feature is visible in haze factor or reflectance, only a slight decrease of both after annealing. But a drop is also present in the total transmittance, this time centered around 550 nm, and the transmittance is higher in IR range compared to non-annealed as deposited or non-annealed coated samples, although less significantly than the uncoated sample heated at 500°C. Except from the drop in transmittance at 550 nm, the optical properties of annealed samples coated with TiO_2 haven't changed much. Therefore while the peaks occurring in haze factor and reflectance in Figure 3-22b might be caused by the transformation of nanowires into spheres, causing exalted haze and reflectance in a specific range of wavelength, the drop in transmittance is still a mystery: it appears even on coated samples, although they still have a cylindrical morphology after heating up to 500°C, as depicted by Figure 3-20b. Therefore this drop in transmittance could be due to the appearance of a new substance on the network at a certain temperature between 270°C and 500°C: maybe graphite or silver sulfite, considering the previous results on PVP evolution during thermal annealing.

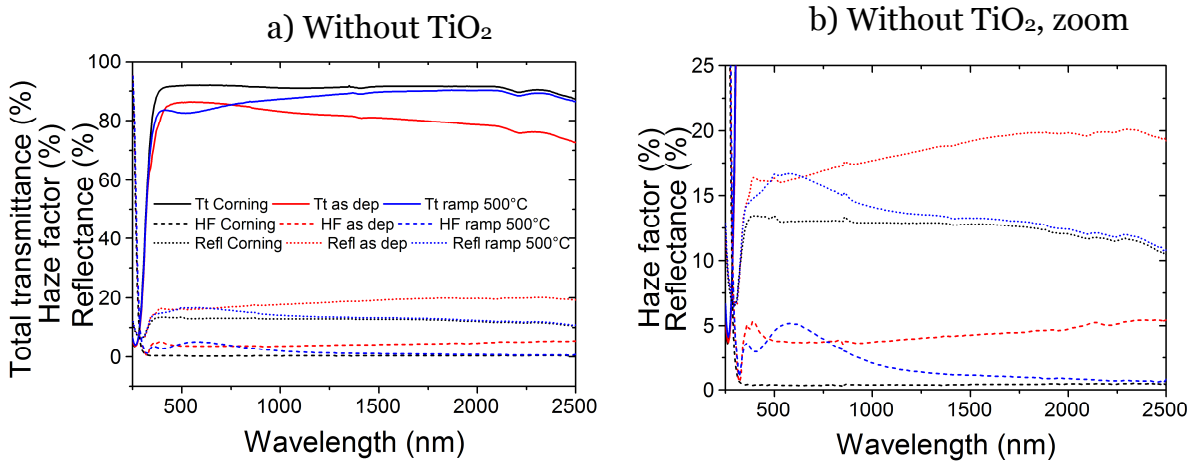

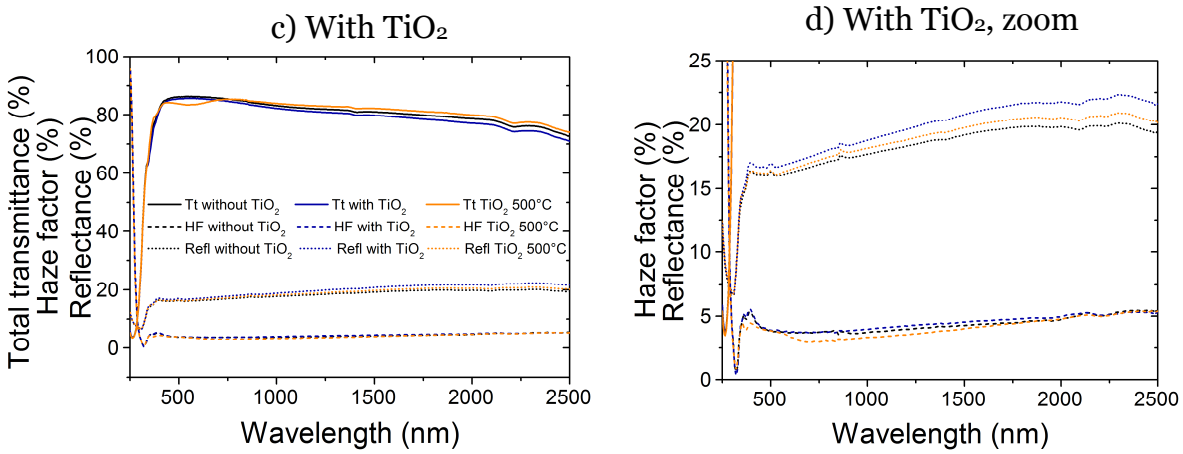

Figure 3-22: Total transmittance spectra, haze factor and reflectance before and after ramp annealing 2°C.min^{-1} up to 500°C of a sample made with Ag45 and of the substrate b) zoom on haze factor and reflectance c) Total transmittance spectra, haze factor and reflectance before and after ramp annealing 2°C.min^{-1} up to 500°C of a sample made with Ag45 coated with 5 nm of TiO_2, and the same spectra or an unannealed uncoated sample d) zoom on haze factor and reflectance.

The small peak present around 855 nm, especially visible on the reflectance spectra, is an artefact from the spectrometer. At this wavelength, there is a change of detector that induces this perturbation.

3.2.3 Summary on optical properties of AgNW network during thermal annealing

In order to observe more closely the effects of these different thermal annealing on AgNW networks transmittance, the relative transmittances between the different processes have been plotted in Figure 3-23. To construct the figure, the transmittance data of each annealing stage were divided by as deposited samples (with or without TiO_2, depending on the samples series) or the substrate (black curve). This figure was displayed in order to reveal the effects of each thermal step on the samples transmittance. The black curve, representing the transmittance of an as deposited unannealed sample divided by the transmittance of the substrate shows approximately the transmittance of the network alone. Below 500 nm, peaks and drops appear probably caused by plasmonic effects within the nanowires. The transmittance of the uncoated sample heated up to 270°C (red curve) divided by the unannealed sample shows an almost constant behavior close to 1, illustrating almost no change caused by the thermal process, in accordance with what was shown before. However the drop in transmittance occurring after heating up to 500°C is clearly visible on the blue solid curve, as well as the strong increase at high wavelength occurring as the nanowires have changed into nanoparticles. Also below 500 nm, the transmittance fluctuations are exactly inversed compared to the black curve (transmittance of the network alone), which might indicate that the plasmonic effects plays a fewer role in the spheroidized morphology. Regarding AgNW

networks coated with TiO_2, the transmittance of the sample heated up to 270°C (dashed red curve) doesn't change much relatively to the unannealed sample, as stated before. After heating the coated samples up to 500°C, the drop around 550 nm appears (blue dashed curve) relatively to unannealed sample, even if the sample hasn't a nanoparticle morphology like the 500°C-heated uncoated sample (blue curve). At high wavelength, the transmittance doesn't increase like the blue curve, because of the presence of the TiO_2 layer and the nanowire morphology that remained cylindrical.

As previously said, the drop occurring after heating up to 500°C is still unclear and might be related to an absorption by a compound formed at this temperature (maybe transformation of PVP into sulfite or graphite). The drop for the sample coated with TiO_2 is slightly shifted compared to the uncoated sample, which might mean that TiO_2 has an impact on the composition of the appearing compound. Further studies have to be conducted to find the nature of this compound.

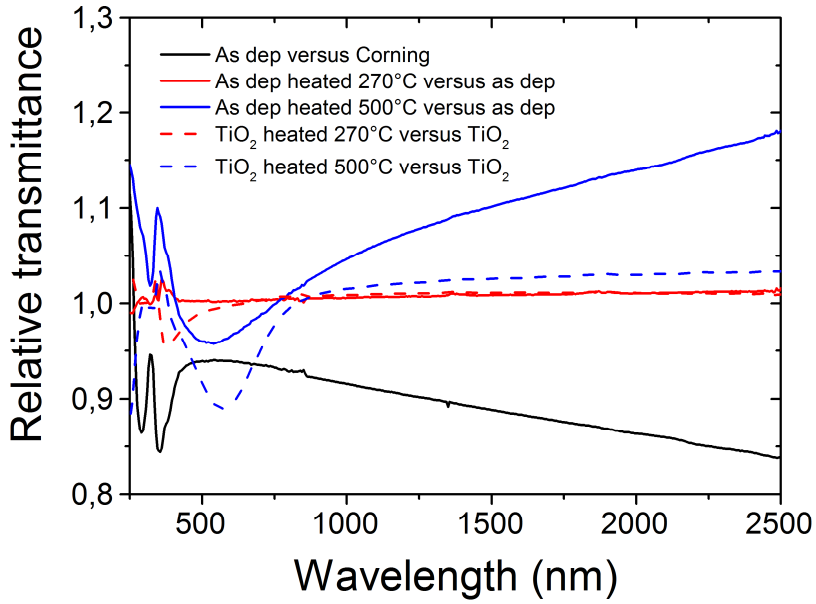

Figure 3-23: Relative transmittance (ratio between the transmittance of annealed samples with transmittances of unannealed samples) showing the effects of different thermal treatments on AgNW and on AgNW coated with a 5 nm layer of TiO_2.

Thermal annealing effects on morphological, electrical and optical properties have been thoroughly investigated. However other methods of AgNW networks optimization exist and will be discussed now.

3.3 Different methods to improve AgNW networks performance (preliminary results)

Post-deposition treatments play a key role in the improvement of TE properties. During this thesis work, we decided to investigate the effects of thermal annealing in details, which is an easily accessible technique. However some other processes of electrodes optimization exist, and for the purpose of comparing different techniques, a non-formal international collaboration initiated at the LMGP was created with CEA Liten (Grenoble), University of Konstanz and University of Catania. At University of Konstanz, the team of Prof. Lukas Schmidt-Mende performed some mechanical pressing on our AgNW-based TE. The team of Dr. Jean-Pierre Simonato at CEA Liten developed an acid treatment to reduce electrode resistance and tested it on our samples. The team of Prof. Antonio Terrasi at University of Catania has been working on laser annealing and preliminary tests of this process on our electrodes are developed here.

This section is dedicated to a discussion and comparison of these methods of AgNW networks optimization through resistance reduction.

3.3.1 Sample fabrication

To enable a comparison between the different methods of optimization cited above, several identical samples were fabricated and sent to each teams. A batch of 10 Corning glass slides, with size 7.5*2.5 cm^2 was deposited with Ag45 using the standard routine of spray coating. The initial sheet resistance of the samples was very high, above the limits of the 4 points probe setup ($> 10^7$ Ω/□), which is common for samples sprayed at LMGP before post-deposition treatment. The networks indeed seem to present much more organic residues trapped by capillarity between the nanowires, compared to those deposited by the spin coating technique. The transmittance was measured at various locations on two samples and was found to be 84.3 ± 0.1% at 550 nm, substrate included. The samples were sent to the different universities for electrical optimization, without any preliminary annealing. Two samples were sent to Stefano Boscarino, PhD student at University of Catania for laser annealing, two samples were sent to Julian Reindl, PhD student at University of Konstanz for mechanical pressing, four were given to Thomas Sannicolo, PhD student at the LMGP and CEA-Liten for acid treatment, and two samples remained at the LMGP for thermal treatment experiments.

3.3.2 Optimization by mechanical pressing

3.3.2.i Introduction to mechanical pressing and experimental methods

Mechanical pressing is a post-deposition optimization technique allowing to optimize nanowires junction resistance at room temperature[3]. The contacts between the nanowires

are improved as they are pressed against each other, as shown in Figure 3-24. The atoms from one nanowire are directly in contact with those of another one, which ameliorates the electrical conduction at junctions. Non-sintered junctions being the locations where resistance is the highest, this method allows to significantly decrease the electrical resistance of the whole network, as well as its surface roughness.

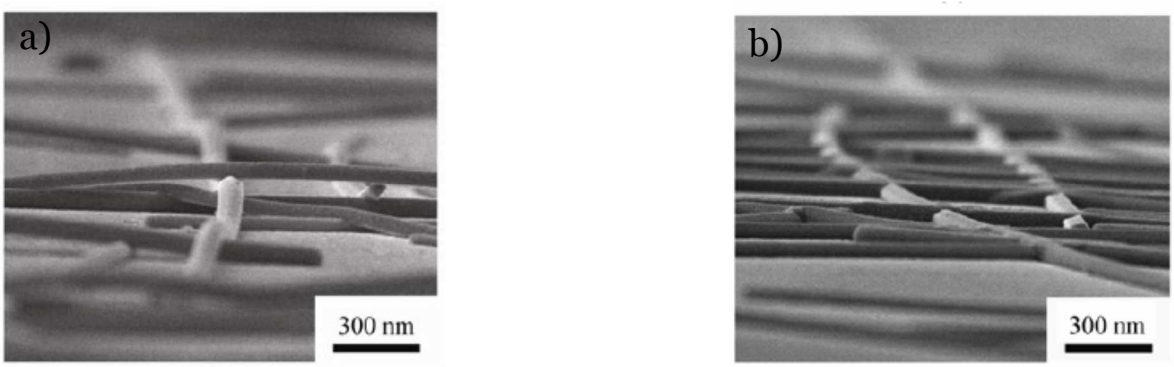

Figure 3-24: Mechanical pressing effects on network morphology by Tokuno et al.*[3] a) as deposited nanowires b) after mechanical pressing at 25 MPa for 5 s.*

The samples were received in Konstanz, and then were placed on a PDMS layer, placed itself on a copper plate. The PDMS was used to ensure a uniform pressing on the whole sample and prevent glass from breaking at high pressures. Then a silanized silicon stamp was put on the top, and pressed on the sample within in a press. The stamp has a low surface roughness in order to optimize the pressing treatment. A pressure of 17 MPa or 12.5 MPa was applied for 2 minutes. After the treatment, the sheet resistance and transmittance of the samples were measured at the LMGP and compared with as deposited samples, as described hereafter.

3.3.2.ii Optical and electrical properties after mechanical treatment

The first observation made on the treated samples was unfortunately the non-homogeneity of the sheet resistance. A specific part (one corner) of each sample had high resistances, especially for the samples pressed at 12.5 MPa, while the rest of the sample presented low values. Typically, the sample pressed at 17 MPa has a sheet resistance after treatment of 11.2 ± 10.6 Ω/□, which is quite scattered compared to what was obtained from thermal annealing at the LMGP. The sample pressed at 12.5 MPa has a sheet resistance across the sample averaged at 4517 ± 9085 Ω/□ but if the corner with high resistance is not taken into account, the sheet resistance is more close to 7 Ω/□. According to Julian, this non-uniformity was caused by the presence of bubbles in one corner of the PDMS layer. Therefore the pressing was different at this location, inducing the sheet resistance non-homogeneity. Mechanical pressing is well adapted for TE electrical improvement since the sheet resistance decreased of

several order of magnitude, especially for high pressures like 17 MPa. However one has to be careful that the pressure is homogenized on the whole sample to avoid high resistance points.

Regarding optical properties, transmittance changed during the treatment and is now at 82.7 % for 17 MPa and 83.2% for 12.5 MPa: it decreased of 1% to 1.5% at 550nm, as can be seen in Figure 3-25. This can be explained by the flattening of the nanowires induced by the process, causing a slight increase of the nanowire surface which decreases the transmittance.

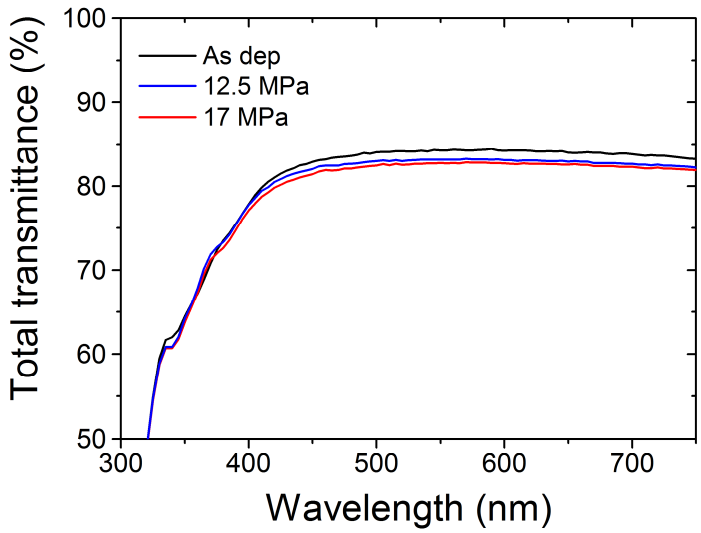

Figure 3-25: Total transmittance of samples before and after mechanical pressing

3.3.2.iii Validation of the mechanical pressing method efficiency

In order to validate the full optimization of the samples by mechanical treatment, a thermal annealing was additionally performed on the samples to verify if the resistance could be improved further by a heating process. A ramp of 2°C.min^{-1} was performed on the two pressed samples, and the samples resistances measured *in situ* are displayed in Figure 3-26a. The pressed samples have their electrical resistance starting at a low value around 10 Ω which doesn't decrease further before going to infinity after 310°C. Therefore no significant resistance decrease due to thermal annealing has been observed after the mechanical treatment. The latter can therefore be considered as complete.

Stopped thermal ramp has previously been seen to be very efficient for AgNW networks resistance optimization. Therefore other similar samples underwent a ramp annealing at 2°C.min^{-1}, stopped at 266°C, which was the temperature just before the mechanically pressed samples started to undergo instability during the thermal ramp. The stopped ramp didn't induce a decrease in the samples resistance, as shown in Figure 3-26b. However the sheet resistances of the two samples could be measured after annealing and were found to be 11.0 ± 6.5 Ω/□ and 8.5 ± 3.2 Ω/□ for the sample pressed at 17 MPa and the one pressed at 12.5 MPa respectively. The values are less scattered than before, and the sheet resistance of the 12.5 MPa

sample has significantly decreased, even if it wasn't visible on the two points measurement of the resistance *in situ* during the thermal ramp. Therefore some efficient percolating pathways already existed in the mechanically pressed samples, efficient enough to be insensitive to thermal annealing optimization. But thermal annealing could improve junctions that were not optimized and therefore enabled a better homogeneity of sheet resistance across the samples.

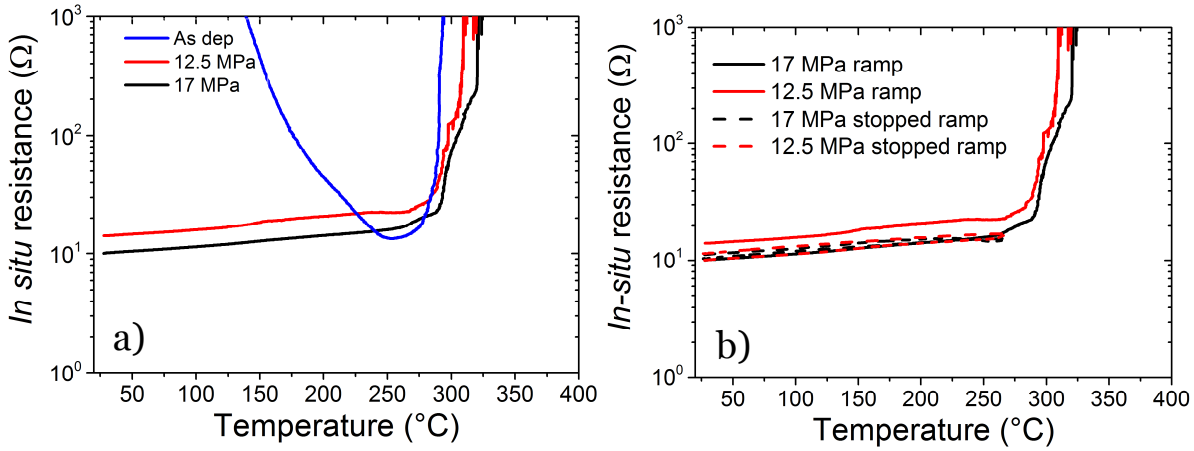

Figure 3-26: a) Thermal annealing at a ramp rate of 2°C.min^{-1} up to 500°C on as deposited and mechanically pressed sample b) thermal ramp stopped at 266°C compared with ramp up to 500°C of mechanically pressed samples.

Figure 3-27 show the morphology of pressed networks before (b) and after thermal ramp stopped when the minimum resistance is achieved (c), as compared to an as deposited sample (a). One can observe the creation of well sintered junctions after mechanical pressing, and after thermal annealing, guaranteeing efficient electrical conduction.

To conclude on this technique, mechanical pressing is very efficient to decrease sample resistance. But an additional thermal heating could help to make the resistance more uniform across the whole sample area. One possible next axis of research would be to press and heat the AgNW networks at the same time to improve the treatment efficiency. Another point is that, according to Tokuno *et al.*,[3] mechanical pressing can reduce the surface roughness of AgNW networks to one third of the initial value. This could be of great interest for the application of these networks in organic solar cells, to prevent short circuits, or in RF antennas where surface roughness is a key parameter in the antenna efficiency.[22]

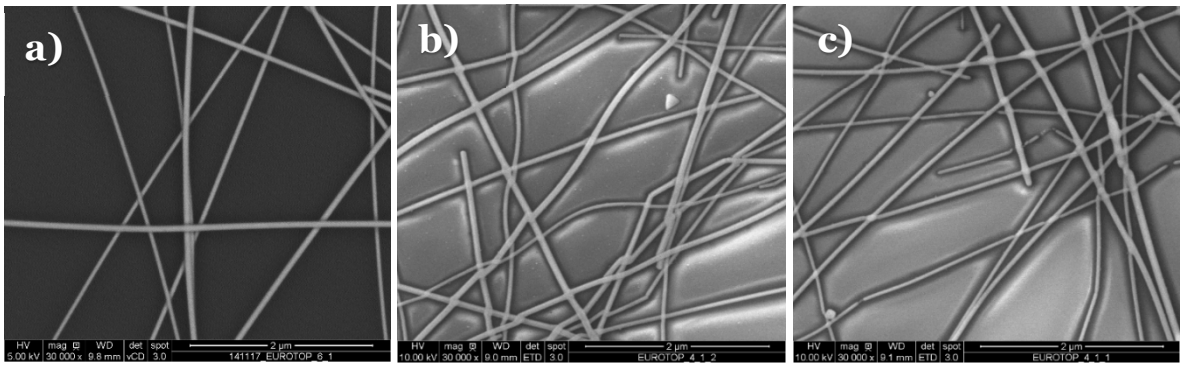

Figure 3-27: SEM images of the network morphology a) As deposited b) After mechanical pressing at 17 MPa and c) after mechanical pressing at 17 MPa and thermal annealing of 2°C.min^{-1} stopped at 266°C.

3.3.3 Acid treatment

3.3.3.i Experimental methods and results

Acid treatments were performed by Thomas Sannicolo at the CEA Liten. The principle is to use a solution of nitric acid concentrated at 5%, either as a washing step of the nanowires in solution before deposition, or as a network post-deposition treatment,[4] where the sample is dipped into the solution for 15 minutes. In this section are displayed results by using the second method. The samples were dipped in nitric acid and then rinsed with ethanol.

Regarding the two samples studied, their sheet resistances were greatly improved. One samples resistance decreased from above 10^7 Ω/□ to 6.7 ± 1.0 Ω/□. The second sample underwent also a significant resistance decrease but was not as optimized as the first sample. The final sheet resistance was 29.8 ± 8.8 Ω/□, and one corner of the sample (not included in the average) was more resistive with a sheet resistance of 84 Ω/□. The treatment seemed to increase slightly the transmittance of the samples, but less than 0.7 %, which stands within the range of incertitude of the spectrophotometer. Therefore it is difficult to know if the treatment is truly at the origin of this small increase.

To explain the decrease of resistance due to acid treatment, the CEA team suggested that the nitric acid might induce PVP dewetting from the NW walls and allows to improve the contacts between nanowires.[4] To test this hypothesis, some Corning glass substrates were coated only with PVP by Thomas Sannicolo and then dipped into the same nitric acid solution. SEM and AFM observations confirmed that the PVP formed droplets on the surface instead of a uniform thin film after acid treatment. However, acid-treated nanowires were observed with TEM and the PVP doesn't seem to have dewetted and still forms a continuous layer on the nanowires walls. Therefore the reason of resistance reduction using this technique remains unclear.

3.3.3.ii Validation of acid treatment efficiency

The treated samples were thermally annealed to verify the quality of the treatment in term of electrical optimization. A thermal annealing with ramp rate of 2°C.min^{-1} up to 500°C was performed on as deposited and acid treated samples. Then similar treated samples were heated again at the same ramp rate but stopped at 180°C which was the temperature before the treated sample started to undergo instability during the ramp up to 500°C, see Figure 3-28a. The resistance curves during annealing corresponding to the sample well optimized mentioned in the last section are presented in Figure 3-28a, and the one not optimized in Figure 3-28b. The first observation is that the stopped annealing didn't improve the resistance much, as for mechanical pressing. However on the full ramp curve of the sample with higher resistance, there is actually a decrease between room temperature and 200°C, indicating that some organic residues were still present between the nanowires after the acid treatment and desorbs from the network at low temperature, or some junctions might undergo some sintering.

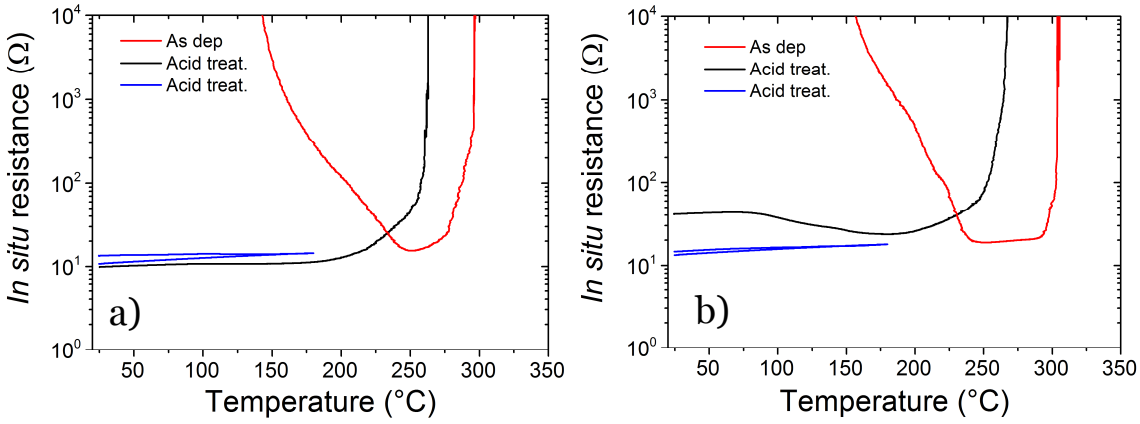

Figure 3-28 : Thermal ramp (2°C.min^{-1}) and stopped annealing on acid treated samples a) sample with sheet resistance 6.7 ± 1.0 Ω/□ b) sample with sheet resistance 29.8 ± 8.8 Ω/□.

The most remarkable effect of the acid treatment concerns the network instability, occurring at much lower temperature for treated samples. For as deposited samples the instability occurs around 300 ± 5 °C during these experiments, but occurrs at 264 ± 2 °C for the acid treated samples. This surprising result could be explained by a decrease of the nanowires diameter due to the acid treatment, considering that nitric acid dissolves silver. In Chapter 4, a relation between nanowire diameter and temperature of instability will be presented. According to this relation, the nanowire diameter should have decreased during the acid treatment from approximately 50 to 35 nm to lead to such low temperature of instability. However an analysis of nanowire diameters before and after treatment was made with SEM images and showed almost no change. Diameter of 53 ± 12 nm before and 51 ± 12 nm after

treatment were found. This difference is not significant enough to have induced such decrease of thermal instability temperature simply through a diameter decrease.

The reduction of AgNW networks resistance by acid treatment has been seen to be efficient, however the impact of the method on the nanowires remains not completely understood. We observed that the morphological instability following acid treatment appears at lower temperature during a thermal ramp, compared to non-treated samples. Further studies need to be performed in order to bring a full understanding of this technique.

3.3.4 Laser annealing and other optimization treatments

Several other techniques to improve the electrodes electrical properties have been investigated: UV and IR treatment at the CEA and laser annealing at University of Catania. These processes however are not yet well understood and the results are less significant than those obtained from the other techniques.

However, laser annealing results seem promising. Stefano used a Nd:YAG laser (523 nm), with pulses of 10 ns. The laser power was set to 50 mW and 500 pulses were performed on each location. In total, an area of 1.5 cm*1.5 cm was irradiated. The process allowed to decrease the resistance of the networks of around 3 order of magnitude, without inducing any morphological change.

Additional studies will be conducted on these techniques of resistance reduction, especially in the frame of Thomas Sannicolo's thesis (2014-2017).

3.4 Closing remarks and future work

Thermal annealing has been proven to be an efficient method of AgNW networks electrical properties improvement. The mechanisms of resistance reduction have been understood and a method of stopped ramp has been proposed as an efficient way to optimize the networks. The different mechanisms that impact the samples electrical resistance during thermal annealing have temperature-dependent kinetics, and can have either a reversible nature (phonon scattering) or be irreversible such as organic desorption, local sintering and morphological instability. Optical properties don't seem to be impacted at low temperatures during the thermal annealing, even when the minimum resistance is reached. Higher temperature however might induce the creation of a compound that leads to a small absorption of light in the visible range, but also thermal instability leading to the loss of the network electrical conductance through spheroidization. Several solutions have been studied to prevent this thermal instability, especially by using a metal oxide coating. The use of ALD deposited TiO_2 for this purpose has been seen to be efficient as the resulting layers don't induce a significant decrease of the sample transmittance and doesn't significantly increase the haze factor (at least before the layer crystallization). Other metal oxides (such as ZnO) could be also studied as

protecting layers using this deposition technique and could facilitate the integration of AgNW networks into devices.

Regarding the other post-deposition methods of resistance reduction, the collaboration with the different universities has been interestingly rewarding. Mechanical pressing and acid post-deposition treatment have been seen to reduce significantly the samples resistance while being rapid techniques that can be performed in ambient conditions. However they both suffer from non-homogeneity in terms of sheet resistance that could yet be reduced by thermal annealing. Therefore new experiments will be held on performing mechanical pressing while heating the sample at the same time, and more studies will be focused on the understanding of the resistance decrease induced by nitric acid. Nitric acid treatment in solution seems to be more efficient than the post-deposition acid treatment we discussed here, because it doesn't lead to homogeneity issues, according to the team at CEA. Laser annealing preliminary results are promising, and this method will also be further investigated and optimized.

References

[1] Coskun S, Selen Ates E and Emrah Unalan H 2013 Optimization of silver nanowire networks for polymer light emitting diode electrodes *Nanotechnology* **24** 125202

[2] Langley D P, Lagrange M, Giusti G, Jiménez C, Bréchet Y, Nguyen N D and Bellet D 2014 Metallic nanowire networks: effects of thermal annealing on electrical resistance *Nanoscale* **6** 13535–43

[3] Tokuno T, Nogi M, Karakawa M, Jiu J, Nge T T, Aso Y and Suganuma K 2011 Fabrication of silver nanowire transparent electrodes at room temperature *Nano Res.* **4** 1215–22

[4] Céline Mayousse 2014 *Elaboration d'électrodes transparentes souples à base de nanofils métalliques* (PhD thesis: Université de Grenoble)

[5] Lee J, Lee P, Lee H, Lee D, Lee S S and Ko S H 2012 Very long Ag nanowire synthesis and its application in a highly transparent, conductive and flexible metal electrode touch panel *Nanoscale* **4** 6408–14

[6] Lee J-Y, Connor S T, Cui Y and Peumans P 2008 Solution-Processed Metal Nanowire Mesh Transparent Electrodes *Nano Lett* **8** 689–92

[7] Gao Y, Jiang P, Liu D F, Yuan H J, Yan X Q, Zhou Z P, Wang J X, Song L, Liu L F, Zhou W Y, Wang G, Wang C Y, Xie S S, Zhang J M and Shen D Y 2004 Evidence for the Monolayer Assembly of Poly(vinylpyrrolidone) on the Surfaces of Silver Nanowires *J. Phys. Chem. B* **108** 12877–81

[8] Karim S, Toimil-Molares M E, Balogh A G, Ensinger W, Cornelius T W, Khan E U and Neumann R 2006 Morphological evolution of Au nanowires controlled by Rayleigh instability *Nanotechnology* **17** 5954–9

[9] Mayoral A, Allard L F, Ferrer D, Esparza R and Jose-Yacaman M 2010 On the behavior of Ag nanowires under high temperature: in situ characterization by aberration-corrected STEM *J Mater Chem* **21** 893–8

[10] Daniel Langley 2014 *Silver nanowire networks: Effects of percolation and thermal annealing on physical properties* (PhD thesis: Université de Grenoble, Université de Liège)

[11] Phoka S, Laokul P, Swatsitang E, Promarak V, Seraphin S and Maensiri S 2009 Synthesis, structural and optical properties of CeO2 nanoparticles synthesized by a simple polyvinyl pyrrolidone (PVP) solution route *Mater. Chem. Phys.* **115** 423–8

[12] Borodko Y, Habas S E, Koebel M, Yang P, Frei H and Somorjai G A 2006 Probing the Interaction of Poly(vinylpyrrolidone) with Platinum Nanocrystals by UV–Raman and FTIR *J. Phys. Chem. B* **110** 23052–9

[13] Martina I, Wiesinger R, Jembrih-Simbürger D and Schreiner M 2012 Micro-Raman characterization of silver corrosion products: Instrumental set up and reference database *Raman Spectrosc.* **9** 1–8

[14] J-P. Baïlon, J.-M. Dorlot 2000 *Des matériaux* (Presses internationales Polytechnique)

[15] D.R. Lide 2004 *CRC Handbook of chemistry and physics 2004-2005: A ready-reference book of chemical and physical data* (CRC press)

[16] Bid A, Bora A and Raychaudhuri A K 2006 Temperature dependence of the resistance of metallic nanowires of diameter ⩾15nm: Applicability of Bloch-Grüneisen theorem *Phys. Rev. B* **74** 035426–035426 – 8

[17] Guisti G, Langley D P, Lagrange M, Collins R, Jiménez C, Bréchet Y and Bellet D 2014 Thermal annealing effects on silver nanowire networks *Int. J. Nanotechnol.* **11** 785–95

[18] Morgenstern F S F, Kabra D, Massip S, Brenner T J K, Lyons P E, Coleman J N and Friend R H 2011 Ag-nanowire films coated with ZnO nanoparticles as a transparent electrode for solar cells *Appl. Phys. Lett.* **4** 183307–183307 – 3

[19] Guillemin S, Consonni V, Appert E, Puyoo E, Rapenne L and Roussel H 2012 Critical Nucleation Effects on the Structural Relationship Between ZnO Seed Layer and Nanowires *J. Phys. Chem. C* **116** 25106–11

[20] Ramasamy P, Seo D-M, Kim S-H and Kim J 2012 Effects of TiO2 shells on optical and thermal properties of silver nanowires *J. Mater. Chem.* **22** 11651–7

[21] Muñoz-Rojas D and MacManus-Driscoll J 2014 Spatial atmospheric atomic layer deposition: a new laboratory and industrial tool for low-cost photovoltaics *Mater. Horiz.* **1** 314

[22] Song L, Myers A C, Adams J J and Zhu Y 2014 Stretchable and Reversibly Deformable Radio Frequency Antennas Based on Silver Nanowires *ACS Appl. Mater. Interfaces* **6** 4248–53

Chapter 4 : AgNW dimensions and network density effects on AgNW networks physical properties

In Chapter 1, percolation theory has been introduced, which relates the number of nanowires per unit area and their length to electrical conduction. In the present chapter, we aim at relating the network mass density and nanowire dimensions (length and diameter) to the networks main physical properties: mostly electrical resistance and optical transparency, through an experimental approach coupled with simple physical modeling. A variety of AgNW networks, with varying density and fabricated with nanowire having different dimensions are experimentally studied and the comparison with simple models is discussed in this chapter. The dimensions of the nanowires used are displayed in Chapter 2 (Table 2-1). By determining simple models for these physical properties, it is possible to create a guideline to know which dimensions and density to choose to reach different properties requirements which depend on the intended application. The results presented in this chapter concerning the effects of density, nanowire dimensions and thermal annealing on AgNW-based TE have been published recently in the form of an article entitled "Optimization of silver nanowire-based transparent electrodes: effects of density, size and thermal annealing".[1]

4.1 Samples fabrication

Series of samples made from nanowires with various dimensions and at different network densities were fabricated by spin coating on 2.5 cm*2.5 cm Corning glass slides. The samples were deposited from nanowire solutions of various concentrations using the standard procedure (see Chapter 2). The samples total and direct optical transmittances were measured on each sample, on two different locations. Averages for the experimental direct and total transmittances were calculated, as well as the haze factor. Each initial sample was then cut into four square parts. One was kept as a control sample and another for SEM imaging and density calculation. The network density of each sample was calculated from 10 SEM images taken at different locations on each as deposited sample, with the method explained in Chapter 2. Typically the ranges of network densities considered for this study were within 0.4 and 15-20 times the theoretical critical density n_c, calculated from Equation 1-3 (Chapter 1). Higher densities were studied for Ag26 (up to 74 times n_c), and Ag117 (up to 36 times n_c). SEM images show the networks morphologies depending on density, for samples made of Ag117, in Figure 4-1.

Two silver paint contacts in the form of strips were placed upon opposing edges of the third quarter of the samples which was then heated in air at a constant ramp rate of 2°C.min^{-1} from room temperature to 500°C. The resistance was measured *in situ* by using the annealing

setup presented in Chapter 2. The size of the AgNW network electrodes being investigated was maintained constant for comparison purpose of the different samples, with a 7 mm gap between the silver paint electrodes, leading to a measured electrode of surface 1.25 cm by 0.7 cm. The last quarter of the samples made from the Ag117 series were annealed at 200°C for 2h in order to reach their minimum resistance, and then their sheet resistance was then measured.

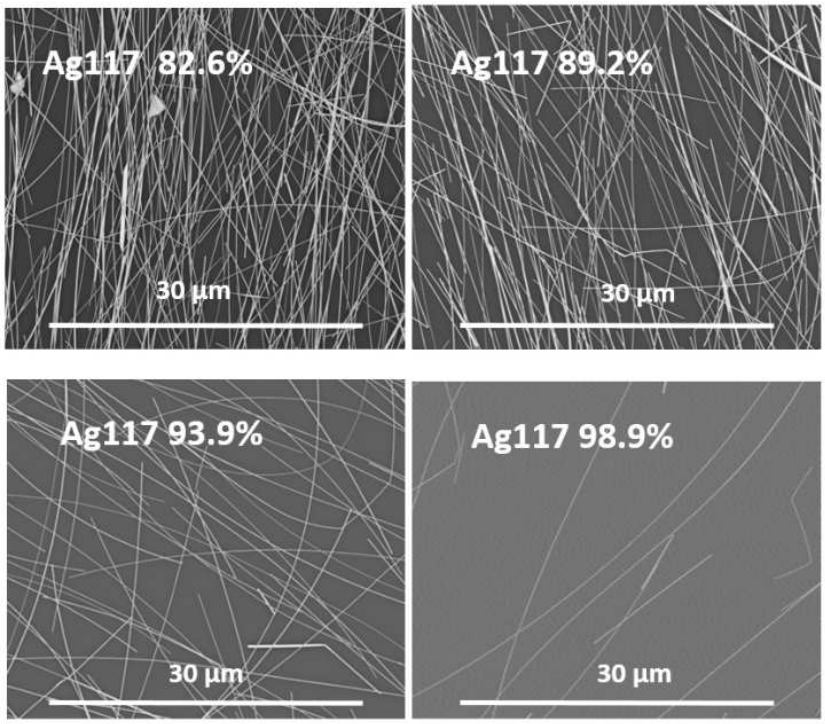

Figure 4-1: SEM images of Ag117 networks deposited by spin coating and associated to various densities. Their corresponding total transmittance (without substrate contribution) are written in each image.

4.2 Density and size effects during thermal annealing

Thermal annealing mechanisms have been investigated in Chapter 3. The different tendencies in terms of morphological change, resistance reduction and thermal instability were studied in a general way without taking into account the nanowire dimensions or the network density. Therefore the influence of these parameters on thermal annealing effects will be addressed now.

4.2.1 *In situ* resistance behavior with AgNW networks of different densities during a ramped annealing

In order to investigate the effects of network density and nanowire dimensions on ramped thermal annealing, the samples described in section 4.1 with different densities and nanowires types underwent thermal ramps at a heating rate of 2°C.min^{-1} in air. The resulting

in situ resistance evolution of the networks composed of Ag26, Ag45, Ag55, Ag117 and Ag138 are displayed in Figure 4-2. The network densities presented in this figure correspond to samples with optical transmittances at 550 nm close to 78-82% (black curves), 86-89% (red curves), 91-92% (blue curves), 93-94% (green curves) and 96% (magenta curves), once the substrate contribution to the transmittance is removed.

Figure 4-2 shows that the impact of thermal annealing on electrical resistance is significant, especially on low density networks, as resistances can decrease by 3 orders of magnitude or even more. For example the sample with T_{550}=90.9% of Ag55 and the one with T_{550}=92.6% of Ag138 resistance (blue and green curves respectively) decreased from 10^4 to 13.9 Ω and from 2.10^4 to 17.8 Ω, respectively. Some samples with low network density (for instance sample with T_{550}=96.5% of Ag45, magenta curve) seem not to percolate at the beginning of the treatment ($R > 10^7$ Ω) because of their high junction resistance, but then the resistance starts decreasing as efficient electrical pathways are created due to the isopropanol desorption, PVP removal and local sintering.[2] For less transparent samples, the resistance at low temperature seem quite stable, and then a resistance decrease above 120°C is visible, as for the samples T_{550}=89.2% of Ag117 (red curve) and T_{550}=80.3% of Ag26 (black curve). It can be explained by considering that, as these samples are associated with high AgNW densities, there are statistically more chances to find efficient conducting pathways on the sample before annealing, even if all the junctions are not yet fully optimized.

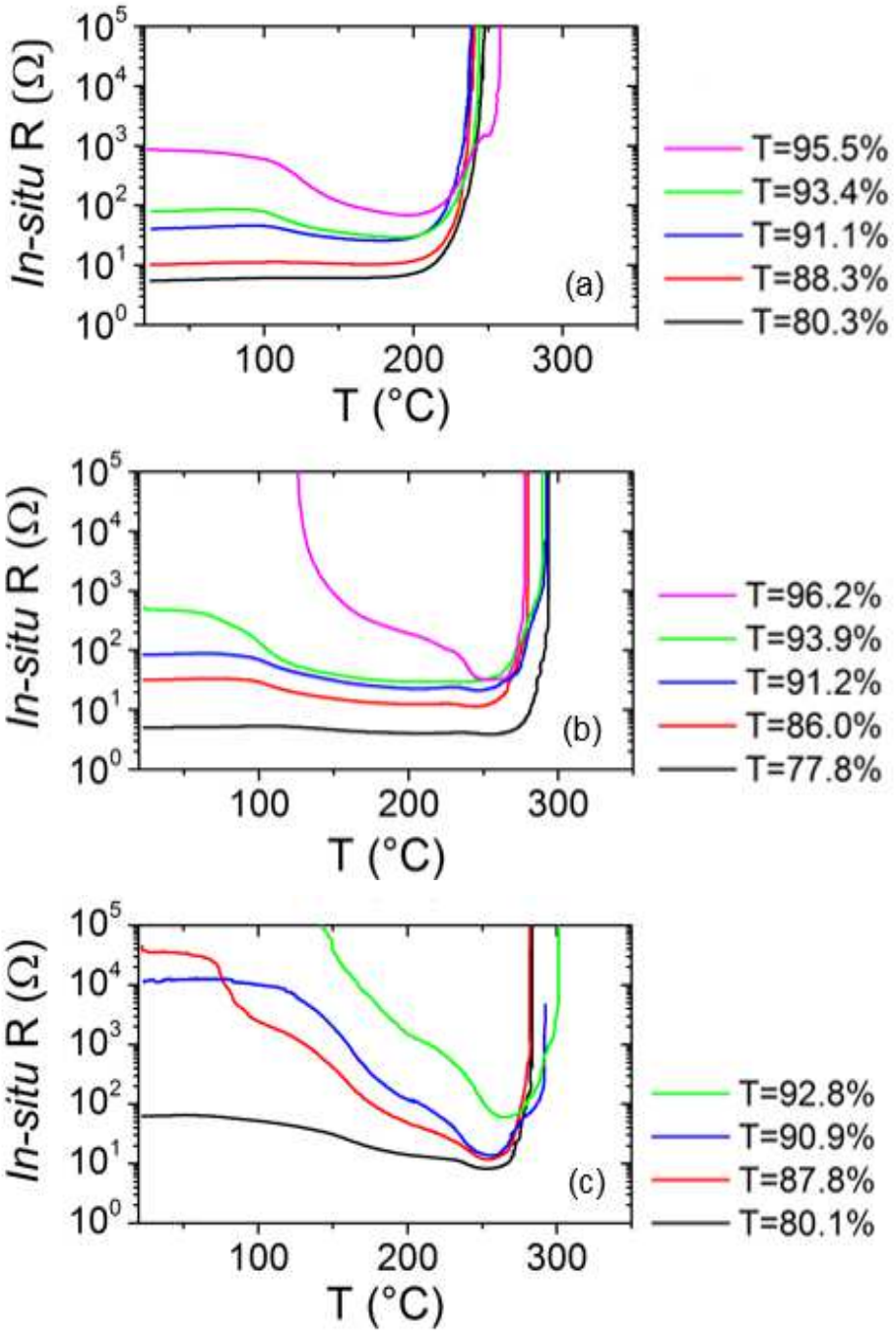
In-situ R (Ω)
T (°C)
(a)
T=95.5%
T=93.4%
T=91.1%
T=88.3%
T=80.3%
(b)
T=96.2%
T=93.9%
T=91.2%
T=86.0%
T=77.8%
(c)
T=92.8%
T=90.9%
T=87.8%
T=80.1%

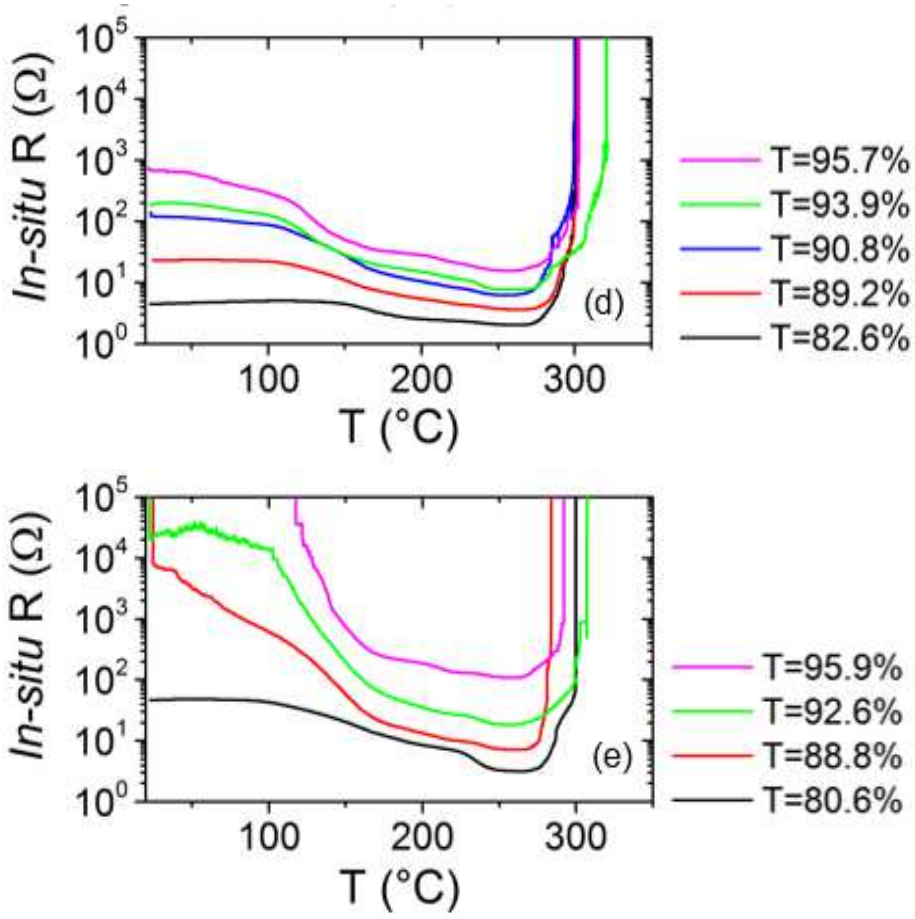

Figure 4-2: Electrical resistance behavior of networks made of various nanowire types, at different densities during thermal annealing in air at a ramp rate of 2°C.min^{-1} of a) Ag26, b) Ag45, c) Ag55, d) Ag117, e) Ag138.

4.2.2 Thermal instability relation with diameter

Figure 4-2 shows that the *in situ* electrical resistance behavior of AgNW networks is slightly different depending on the dimensions of the nanowires used. Both the spheroidization temperature (T_{sph}) and the temperature at which minimum resistance is observed for each sample (T_{Rmin}) increase with nanowire diameter, as can be seen in Figure 4-3a. T_{sph} was considered to occur when the network resistance was above 10^6 Ω, after the minimum resistance was achieved. The tendency of these characteristic temperatures, T_{sph} and T_{Rmin}, regarding the nanowire type is more visible by comparing them directly with the nanowire average diameter, as displayed in Figure 4-3b. Note that the experimental T_{Rmin} and T_{sph} reported in Figure 4-3b are taken from data shown in Figure 4-2 and averaged over the density series. The error bars represent one standard deviation of the experimental values (considering the different network densities used) for each type of AgNW. The observed trend in Figure 4-3, *i.e.* a lower temperature of both optimized resistance achievement and morphological instability with decreasing nanowire diameter, can be explained by surface effects enhancement which occurs for small AgNW diameters. In cluster physics, many physical or

chemical properties, for example one that we can call $G(r)$, vary with cluster size r, and generally follow the scaling law:

$$G(r) = G(\infty) \cdot (1 - \frac{l_c}{r}) \qquad (4\text{-}1)$$

where $G(\infty)$ is the value of the specific property G associated with large r values (*i.e.* bulk properties), and l_c is a characteristic length. The best known illustration of effects described by Equation 4-1 for nanoparticles or clusters is the dramatic deviation of melting point from bulk since the melting point change is inversely proportional to the particle radius r, leading to:

$$T_m(r) = T_m(\infty) \cdot \left(1 - \frac{2 \cdot V_m^S \cdot \gamma_s}{L \cdot r}\right) \qquad (4\text{-}2)$$

where, in the case of silver, V_m^S is the bulk Ag molar volume (10.3 $cm^3.mol^{-1}$), γ_s the free surface energy and L the molar latent heat of melting (11.3 $kJ.mol^{-1}$).[3]

Equation 4-2 is coherent with the fact that nanomaterials are able to undergo sintering at much lower temperatures compared to their bulk material[4] as also illustrated in the present work. Equation 4-1 can be used to describe the dependence of both T_{Rmin} and T_{sph} versus AgNW diameter as depicted in Figure 4-3b by the dashed lines. Physical estimation of l_c can be considered by comparing Equation 4-1 and Equation 4-2. Bulk silver γ_s value depends on crystallographic orientations and generally ranges between 1 and 1.5 $J.m^{-2}$.[5] This would lead to a value of l_c between 1.8 and 2.7 nm. However, nanomaterials physical values often differ from bulk. Indeed surface energy of (100) facets in silver nanowires has been found by Zhang *et al.*[6] to be 0.41 $eV.atom^{-1}$ (*i.e.* 0.78 $J.m^{-2}$), resulting in a theoretical value of l_c equals to 1.42 nm.

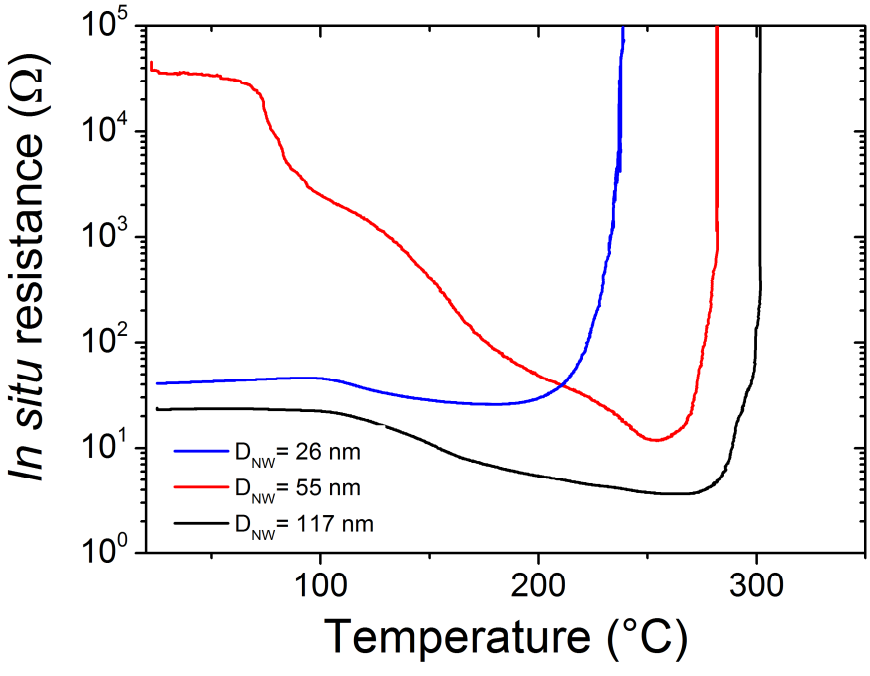

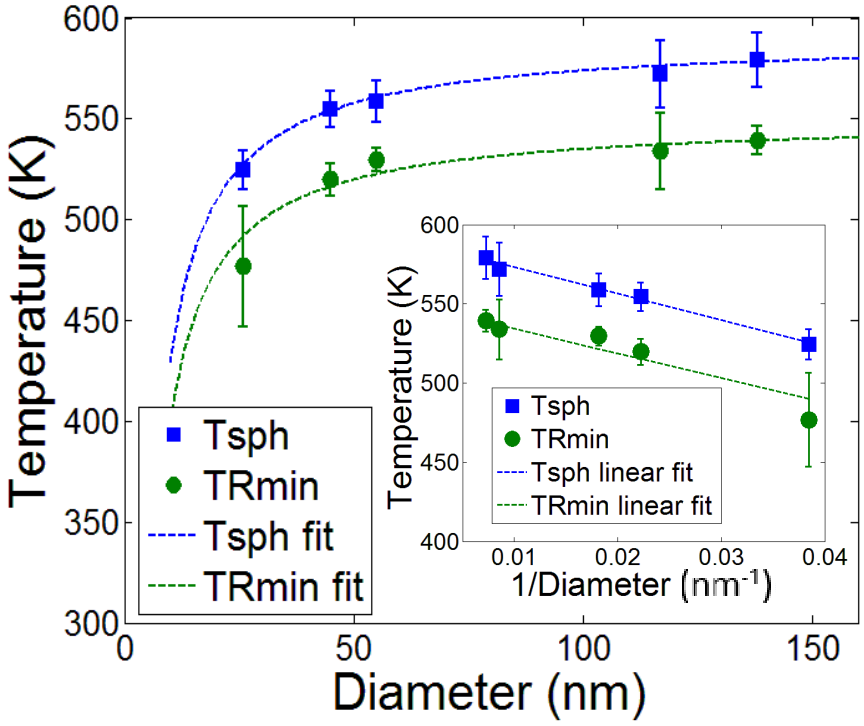

Figure 4-3: a) Resistance behavior during a 2°C.min^{-1} thermal ramp in air of samples made of AgNW with different diameters b) Temperature of instability T_{sph} and of R_{min} achievement, T_{Rmin} regarding nanowire diameter. The fits have been calculated from Equation 4-1 using l_c=1.42.

To validate the proposed model, the insert in Figure 4-3b shows the observed temperatures T_{sph} and T_{Rmin} as a function of the inverse of the nanowire diameter. A linear dependence is clearly observable, in accordance with Equation 4-2. Linear fitting of the data with the l_c value of 1.42 nm is well adapted and allows us to find $T_{sph}(\infty)$ = 590 K and $T_{Rmin}(\infty)$ = 550 K. These values, as well as l_c =1.42 nm have been used to fit the main graph in Figure 4-3b, showing good agreement between experimental and calculated values.

The comparison between the theoretical Equation 4-2 and the observed characteristic temperature dependence versus AgNW diameter exhibits very good agreement although the geometry of our system is different from the theoretical one: clusters are generally spherical while AgNW have a cylindrical shape. Moreover the interaction between AgNW and the substrate on one hand and the fivefold symmetry of the AgNW on the other hand complicates the interpretation since it has been observed that these features influence the thermal stability of metallic nanowires.[7] In conclusion although the detailed mechanisms governing the modifications of the physical properties of AgNW during thermal annealing are complex, a simple analysis based on the Gibbs-Thomson equation, leading to Equation 4-2, describes well the experimental observations.

It might appear questionable, in spite of the agreement obtained between Equation 4-2 and experimental data, that the same l_c value has been used for both T_{sph} and T_{Rmin}. However these processes, spheroidization and local sintering, are strongly dependent upon atomic

diffusion and have similar driving force: surface energy reduction, as discussed in Chapter 3. Equation 4-2 could then be used as a guideline for the purpose of finding the most suitable thermal process in terms of temperature to improve the sample conductivity without inducing instability.

4.2.3 Kinetics of ramp annealing

In addition to the dependence of the characteristic temperatures on AgNW dimensions, the general behavior of electrical resistance during thermal annealing can also be different depending on the type of nanowires. As explained in section 4.2.2, AgNW associated with low diameters become unstable at lower temperature. The different stages corresponding to the thermally activated mechanisms of resistance reduction at junctions, described in Chapter 3, are clearly visible for every AgNW types in Figure 4-2, except for Ag26. The second resistance reduction step corresponding to junction sintering is indeed not visible for this nanowire type. It has however been observed that when decreasing the heating ramp rate to 0.5°C.min^{-1}, the steps are then observable, as shown in Figure 4-4.

This change in behavior illustrates the influence of the diameter on the kinetics of the thermal process. In the case of nanowires with small diameter, the mechanisms occurring during heating have indeed faster kinetics since surface diffusion is exacerbated due to the increase of surface over volume ratio. With a ramp rate of 2°C.min^{-1}, the Ag26 samples did not exhibit all the thermal mechanisms allowing resistance reduction. Therefore they could not achieve the expected minimum resistance value for the ramp rate used because thermal instability already dominated the process at the temperature at which, normally, sintering occurs for samples made with larger-diameter nanowires. With a thermal ramp rate of 0.5°C.min^{-1}, the different stages described and pictured in Chapter 3 were observable for Ag26, and the minimum resistance was found to be lower (as in Figure 4-4). For example, Ag26 samples with transmittances equals to 95.5% and 97.3% had minimum resistances of 65 and 350 Ω, respectively, with a ramp rate of 2°C.min^{-1}, and minimum resistances of 36 and 127 Ω, respectively, with a 0.5°C.min^{-1} ramp rate.

During this experiment, the change of the ramp rate however didn't induce any change in the temperature of instability, contrary to the experiments of varying ramp rate presented in Chapter 3. It is probably due to the small diameter of Ag26. These nanowires therefore are unstable at lower temperature compared to Ag117. In order to see an effect on the temperature of instability of Ag26 nanowires, the ramp rate might be reduced further.

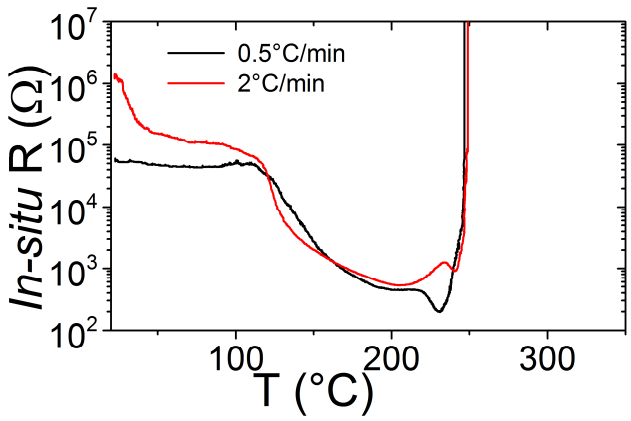

Figure 4-4: Resistance behavior during a thermal annealing with two different ramp rates: 0.5°C.min^{-1} (black) and 2°C.min^{-1} (red) of identical Ag26 networks.

4.3 Density and size effects on electrical properties

In percolation theory, the electrical properties of AgNW-based TE are tightly related to the network density, as mentioned in Chapter 1. The number of nanowires indeed instigates the number of percolating pathways across the network, when the sample is electrically optimized. The role of nanowire length on the percolation critical density has also be explained to be primary in chapter one. This section aims therefore at investigating and verify experimentally the influence of density and nanowire length on the AgNW networks electrical properties, but also to define new physical models that takes into account the diameter of the nanowires.

4.3.1 Experimental percolation threshold

Percolation theory was introduced in Chapter 1 and defined a relation between network resistance and density as follows:

$$R \propto (n - n_c)^{-\gamma} \qquad (4\text{-}3)$$

with

$$n_c \cdot {L_{NW}}^2 = 5.637\ 26 \pm 0.000\ 02 \qquad (4\text{-}4)$$

To analyze experimentally the validity of Equation 4-3 for percolating AgNW networks, it is necessary to compare the experimental and theoretical values of the critical density n_c, the theoretical one being calculated from Equation 4-4 for each nanowire type. To estimate the experimental n_c value, samples with densities close to the percolation threshold were considered. Instead of nanowire density (n), the areal mass density (amd) defined as the density n times the average mass of one single AgNW is investigated. The amd procedure of calculation from SEM image analysis was described in Chapter 2. amd is used instead of n

since it takes into account the AgNW experimental length and diameter distributions of each type of nanowires (also displayed in the Annexe). Then we have

$$R \propto (amd - amd_c)^{-\gamma} \qquad (4\text{-}5)$$

An example of minimum resistance analysis corresponding to Ag117 networks with different densities, close to amd_c, is displayed in Figure 4-5a. The open blue dots correspond to resistances values obtained from percolating samples while the open red rectangles correspond to non-percolating samples, with resistances above the Keithley detection limit, *i.e.* > 10^7 Ω. The experimental ranges of critical mass densities amd_c^{exp} presented in Figure 4-5b were obtained from data like those presented in Figure 4-5a, by considering the lowest density at which the samples start percolating (amd_2, blue dots), and the highest density at which the samples do not percolate (amd_1, red squares). The theoretical amd_c values were calculated by using Equation 4-4, considering the average length of the different AgNW used for the study (given by Seashell). The amd_1 and amd_2 values versus the theoretical amd_c are reported in Figure 4-5b, for each nanowire geometry. The error bars are due to the uncertainty related to the density calculation.

While we can observe a good agreement, especially for the three smallest values of amd_c, experimental results can deviate from theory. This deviation can be explained as follows. Firstly, in the simulated case from which Equation 4-4 was determined, all the nanowires have identical length, zero diameter and are also perfectly straight. In reality experimental wires have a distribution of both lengths and diameters and are also curved, as can be seen on SEM images displayed in Figure 4-1. Note that the types of nanowire which deviate the most from theory in this figure (Ag55 and Ag138) have the largest distribution of diameters among all the types of nanowire used (see the Annexe). Secondly, wires are placed with a completely uniform isotropic angular distribution in the simulations, whereas in the case of the samples studied here, deposited by spin coating, there is an angular anisotropy resulting from the radial alignment of AgNWs during deposition (observable in Figure 4-1). This anisotropy induces an increase of the critical density, as shown by Daniel Langley in his thesis thanks to Monte Carlo simulations of percolating stick network with different angular distributions.[8] Moreover some structural defects, such as grain boundaries, should also have a detrimental impact on the network electrical properties. These arguments suggest that the experimental n_c, and hence amd_c^{exp} values, should be larger than the theoretical ones, as observed in Figure 4-5. From a more fundamental point of view, the role of fluctuations near a critical point in any phase transition is important and is not considered by classical theory such as percolation theory described by Equation 4-3, and therefore only a qualitative agreement can be expected.

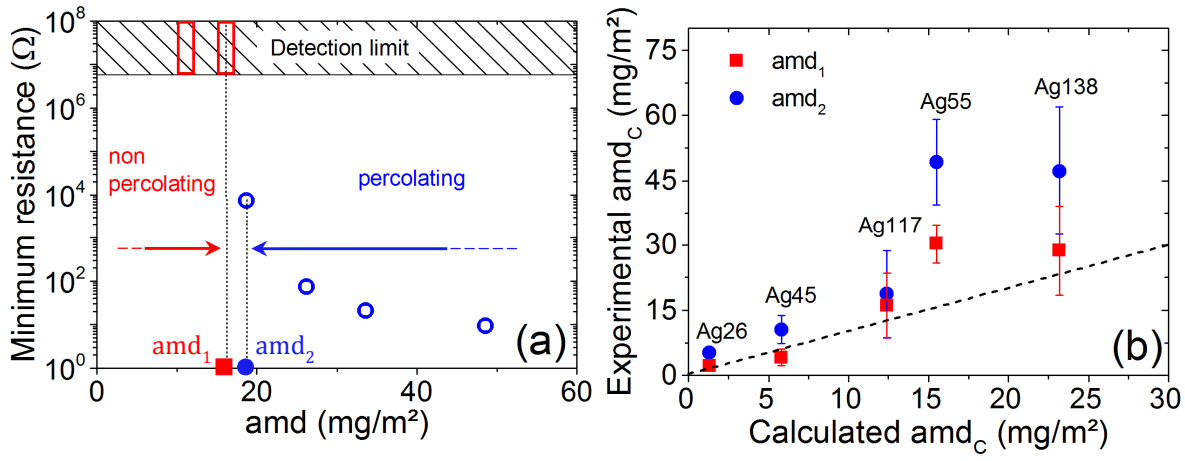

Figure 4-5 : a) Minimum resistances achieved during thermal annealing at a ramp rate of 2°C.min^{-1} for Ag117 networks with density close to the experimental critical density. The values amd$_1$ and amd$_2$ are respectively the highest network density where no percolation occurs and the lowest density at which it starts occuring b) amd$_1$ and amd$_2$ for each nanowire type plotted against the theoretical critical density calculated from Equation 4-4. The dashed line represents the theoretical critical density.

4.3.2 Network density and nanowire dimensions impact on AgNW networks minimum resistance

As shown by Equation 4-3 the network electrical resistance is dependent on network density n and n_c, the latter being determined from Equation 4-4. However Equation 4-4 only considers the nanowire length for the calculation of the critical density; in reality the nanowire diameter also plays a role regarding both transparency and conductivity. The impact of nanowire diameter on the network resistance is secondary to the formation of percolating pathways, meaning that the electrical behavior is dominated by the wire length except when wire diameter approaches the mean free path of electrons. In that case, the proportion of electrons undergoing surface scattering increases, leading to an increase of the AgNW resistivity[9]. However on the optical point of view, a low diameter is beneficial to increase the transmittance and to decrease the proportion of photons scattered by the nanowire.[10,11] These two features are considered hereafter in order to estimate quantitatively the effects of AgNW dimensions on both electrical and optical properties.

Equations 4-3 and 4-4 show that the network electrical resistance depends on nanowire density and on nanowire length. But there should also be a proportional dependence of R with the electrical resistivity of an individual AgNW, ρ_{NW}^{Ag}. Therefore, from Equation 4-3, one can deduce that the network electrical resistance R_{net} should follow this dependence:

$$R_{net} \propto \rho_{NW}^{Ag} \cdot (n - n_c)^{-\gamma} \qquad (4\text{-}6a)$$

which can also be written in terms of areal mass density

$$R_{net} \propto \rho_{NW}^{Ag} \cdot (amd - amd_c)^{-\gamma} \qquad (4\text{-}6b)$$

The electrical resistivity of individual AgNWs increases when their diameter decreases or comes closer to the electron mean free path, due to an increase of electron scattering on the nanowire walls. Bid *et al.* formulated a relation between the resistivity of a nanowire and its diameter which they confirmed experimentally.[9] It can be written as follows:

$$\rho_{NW}^{Ag} = \rho_{bulk}^{Ag} \cdot \left(1 + \frac{\Lambda}{2 \cdot D_{NW}}\right) \qquad (4\text{-}7)$$

with ρ_{bulk}^{Ag} the resistivity of bulk silver, D_{NW} the nanowire diameter and Λ the bulk silver mean free path. Equations 4-4, 4-6b and 4-7 can be used to write an expression of the network resistance depending on the nanowires diameter, length and network density. The network should be considered in series with an instrumental set-up resistance, R_0, which was determined experimentally by using a highly conductive silver thin layer. This leads to:

$$R(amd, D_{NW}, L_{NW}) = R_0 + C \cdot \rho_{bulk}^{Ag} \cdot \left(1 + \frac{\Lambda}{2 \cdot D_{NW}}\right) \cdot \left(amd - \frac{5.64 \cdot d_{bulk}^{Ag} \cdot \pi \cdot {D_{NW}}^2}{4 . L_{NW}}\right)^{-\gamma} \qquad (4\text{-}8)$$

where R_0 was measured experimentally to be 0.8 Ω, AgNW length is noted as L_{NW}, d_{bulk}^{Ag} is the mass density of bulk silver and *amd* is the sample areal mass density that can be expressed in mg.m^{-2}. C is unknown and is of the same order of magnitude for all the nanowires types. However it can vary slightly and should at least be dependent upon the network geometry but this was kept fixed for all experiments in the present work. It could also depend on the nanowires dimensions distribution, which varies with the nanowire type, and on the AgNW crystalline quality. Note that this model neglects the junction resistance and therefore is valid only when the minimum resistance is reached, *i.e.* when the contact area between adjacent nanowires is optimized (for instance after an optimized thermal annealing).

Experimental minimum resistances observed during the 2°C.min^{-1} thermal annealing for the different types of AgNW at various *amd* values have been measured from *in situ* resistance curves as those presented in Figure 4-2. These minimum resistance values, measured at the temperature T_{Rmin}, have been extrapolated to room temperature values by using Equation 3-1 (Chapter 3) and have then been plotted against *amd* for all samples in Figure 4-6a. All the data can be fitted with Equation 4-8 and those related to Ag117 and Ag138 networks are reported in Figure 4-6b as examples, with the fit represented by dashed lines. A fairly good agreement is observed by considering $\gamma = \frac{4}{3}$, that is the theoretical value of the percolation exponent for 2D infinite systems,[12] and C=7.10^{10} mg$^{4/3}$.m$^{-11/3}$ for Ag117 and C=11.10^{10} mg$^{4/3}$.m$^{-11/3}$ for Ag138. It is worth noticing that Equation 4-8 was used with only one fitting parameter, C, while all the other parameters can be experimentally measured (AgNW

diameter and length, network density and R_0) or are known (density or electron mean free path in bulk silver). The slight scattering of the experimental data arises from the probabilistic nature of sparse networks. As explained above, Equation 4-8 considers that AgNW networks are perfect while defects such as grain boundaries along AgNWs, diameter and length distributions or AgNW curvature, suggest that one should consider Equation 4-8 as a minimum limit for the network electrical resistance.

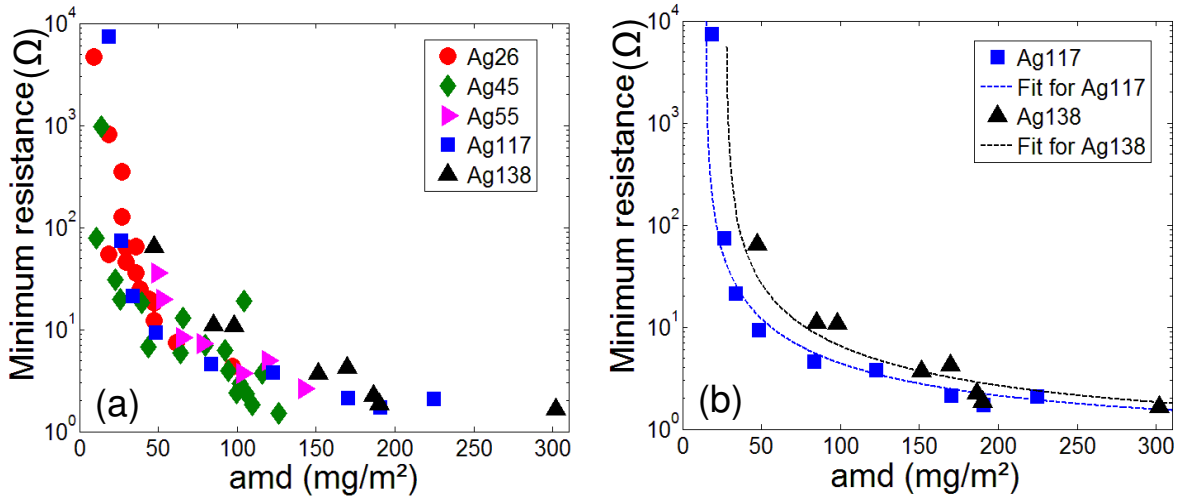

Figure 4-6: Electrical properties of samples a) with various network density and nanowire dimensions. b) Values for Ag117 and Ag138 fitted with Equation 3-5.

The R_{min}-R_0 data were then plotted against n-n_C in Figure 4-7. A linear tendency is observable when the axis are in logarithmic scale, with a slope corresponding to the value of $-\gamma$. The slopes were calculated for each nanowire type. For Ag117 and Ag138, γ is found to be 1.26 and 1.79, respectively, which is quite close to the theoretical value. However the other nanowire types deviate slightly from theory, with γ values of 2.33, 2.25 and 3.06 for Ag55, Ag45 and Ag26 respectively. Considering that these latter nanowire types are the thinnest, the deviation of γ from theory might come from the presence of defects that impact more thin nanowires than the others. In addition, we've seen in Figure 4-4 that the ramp of 2°C.min^{-1} was too rapid for Ag26 nanowires and that all the mechanisms of resistance reduction could not occur before instability. This might also be true, to a lesser extent, to the other thin nanowires Ag45 and Ag55. Therefore the resistance values presented in Figure 4-7 (and Figure 4-6) must be seen as an overestimation of the resistance that these networks could have with a suitable ramp rate, or by another annealing type.

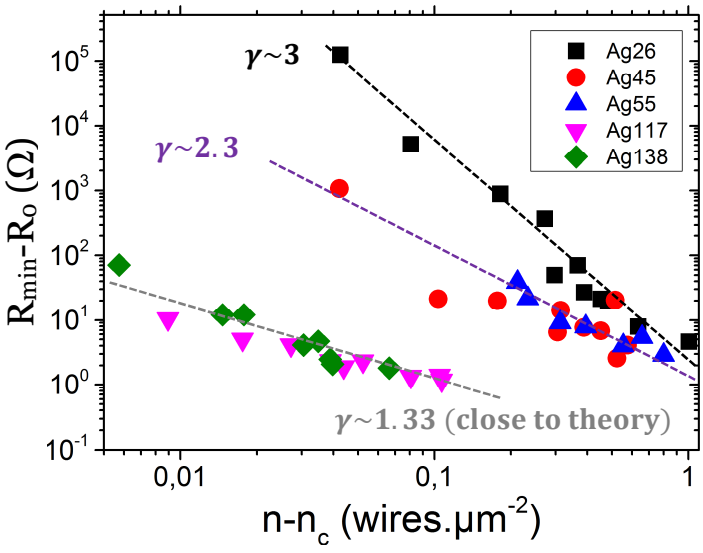

Figure 4-7: Representation of R_{min}-R_o of networks made from different nanowire types and at various densities in log-log scale.

4.3.3 Percolation and dimensions

To illustrate a different way the results mentioned in the two last sections, and verify the validity of Equation 4-4 for the different networks considered in this study, Figure 4-8 represents the various samples we studied, with their network density in y-axis versus the nanowire length. The red markers are related to non-percolating samples. Each green markers represent a sample with a marker size proportional to the R_{min} value it achieved during thermal annealing at a ramp rate of 2°C.min^{-1}. The dashed line corresponds to n_c calculated from Equation 4-4. Therefore it is expected that below this theoretical line, electrical percolation won't be observed. Figure 4-8 shows in a first approach, that experimental n_c meets theoretical n_c, as in Figure 4-5. But it also illustrates well percolation theory effects on electrical properties, as the resistance of the samples is increasing significantly when the density approaches the critical density. However some slight differences stand between experimental and theoretical values that might come from AgNW length distribution, curvature or defects. These differences are the subject of studies in progress at the LMGP. Monte Carlo simulations are being performed to shed light on this topic, in collaboration with Dr Daniel Langley (La Trobe University, Melbourne) and Pr Ngoc Duy Nguyen (University of Liège).

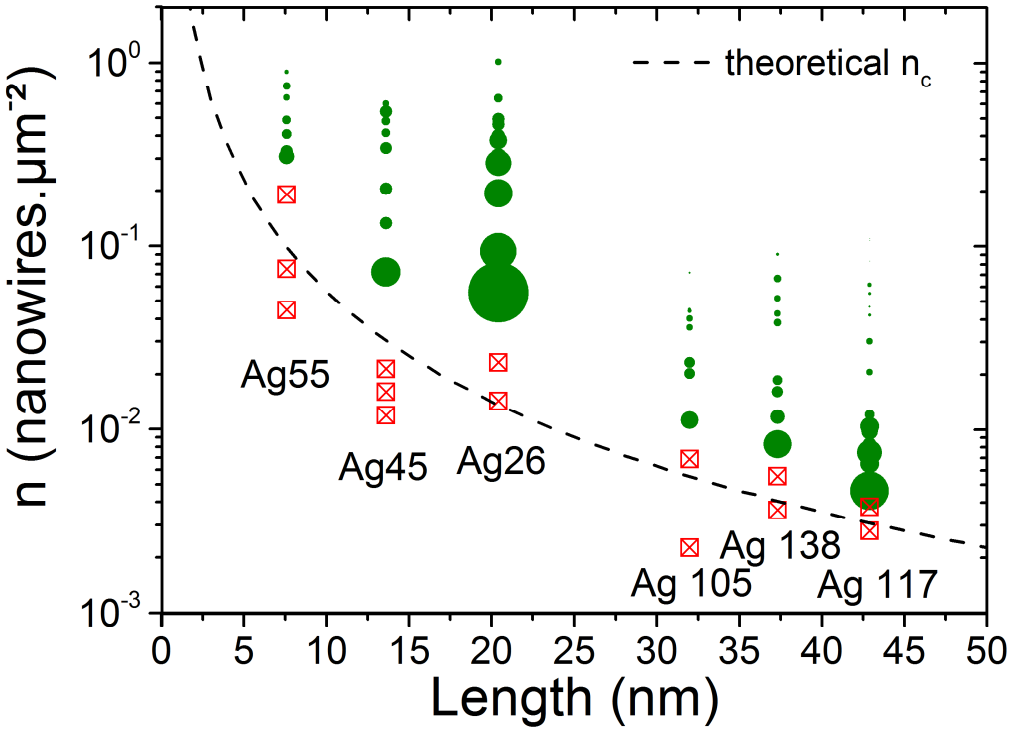

Figure 4-8: Illustration of the percolation theory and experimental critical density. Each marker is associated to one sample. The green circles markers represent percolating network, the circle size being proportional to the minimum achieved by the samples made at different densities (y axis) and with different nanowire types. The red square markers represent non-percolating networks. The dashed line is the theoretical critical density calculated at various length using Equation 4-4.

4.3.4 Geometrical "quantized" percolation

Individual creation of conducting pathways across the sample during thermal annealing can be observed on low density networks made from large-diameter nanowires. Figure 4-9 shows a zoom on a typical resistance behavior curve during thermal ramp annealing of such networks (from the sparsest networks in Figure 4-2e for Ag138). Some steep steps in resistance are identifiable at low temperature, *i.e.* between 100°C and 150°C. This phenomenon can be simply modeled by considering the creation of efficient conducting pathways, caused by local sintering at nanowire junctions or chemical desorption, as resistances in parallel, like in Figure 4-9b.[2] Since the mechanisms of resistance reduction are a local random process at such low temperatures, some junctions become efficient while others still exhibit very large resistance. When a new efficient percolating pathway is created across the sample, a sudden electrical resistance drop is observed. Later on during the annealing process, a state is achieved where the number of efficient junctions is large enough to then lead to a continuous decrease of the resistance. This phenomenon has been well detailed in the paper of Langley *et al.*[2] and in Daniel Langley thesis.[8]

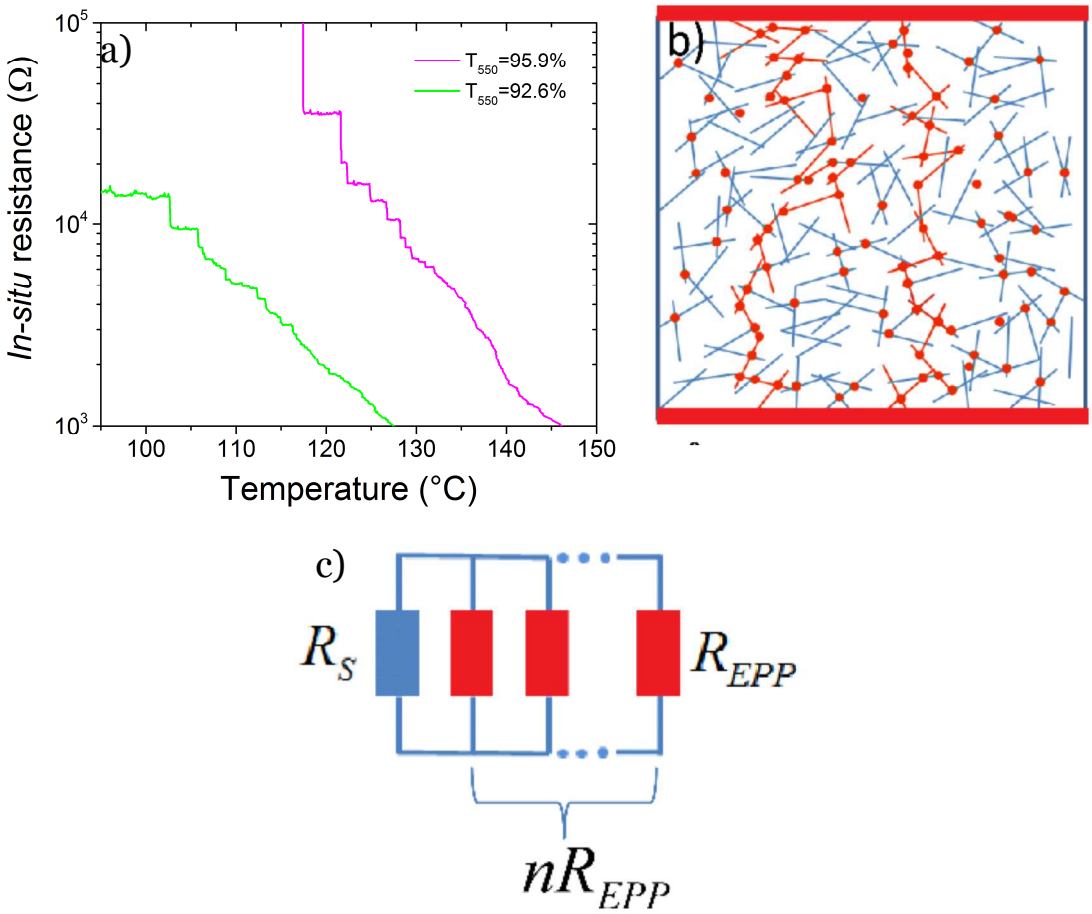

Figure 4-9: Experimental visualization of geometrical "quantized" percolation during a thermal annealing at a ramp rate of 2°C.min^{-1}, on two samples made from Ag138 with low densities b) diagram representing efficient percolating pathways (in red) across a nanowire network, c) diagram representing the efficient percolating pathways as n resistances (R_{EPP}) in parallel with the initial network resistance R_S.[2]

4.4 Density and size effects on optical properties

4.4.1 Total transmittance

The optical total transmittance of a homogeneous layer decreases as it becomes thicker, due to the increase of probability for a photon entering the material to be absorbed or reflected. This is also true for nanowire networks as the total transmittance decreases when the mass of material increases on the surface, as shown in Figure 4-10a. There is also a dependence of the transmittance with the nanowire diameter. In Figure 4-10b, we see that for sample made with nanowire with different diameters but with similar total transmittances at 550 nm, the transmittance behavior at large wavelength is different. The large wavelengths seem to be less transmitted when the diameter is small. Note that the spectra presented in Figure 4-10 have an artefact at 855 nm. This stems from the detector change that occurs at this wavelength. We

haven't identify the reason for this artefact, but we noticed that it become more significant when spin-coated samples are measured, especially high density samples. That makes us think that it might be related to the radial orientation of the nanowires induced by the spin coating technique. We believe that far from this wavelength (855 nm), we are still able to have a precise idea of the transmittance behavior, and especially of its value at 550 nm, which is the value we used to compare different networks and calculate figures of merit.

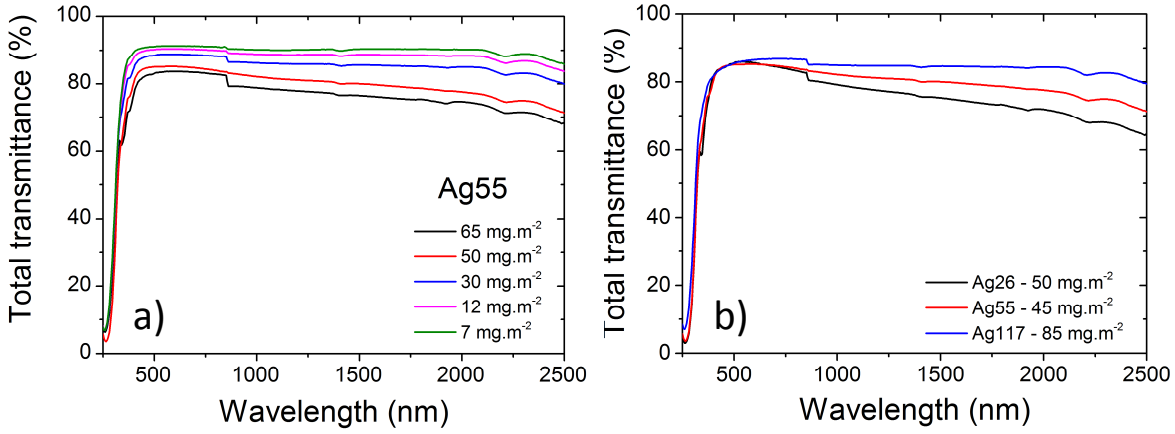

Figure 4-10: Dependence of total transmittance on a) network density and on b) nanowire dimensions, for samples with similar optical transmittance at a wavelength of 550 nm.

The total transmittances at 550 nm of the different samples, with different nanowire dimensions and network densities, are plotted in Figure 4-11, and a linear dependence with *amd* is observable. Simple considerations based on shadowing effects have already been reported in the literature where transparency was supposed to decrease linearly with the increase of the area covered by nanowires.[13,14] One can consider a slightly more sophisticated approach as follows. If one notes f_{NW} the fraction of the substrate surface covered by nanowires, the AgNW network total transmittance T_{opt} can then be written as the sum of the two following contributions associated to the covered and non-covered parts of the glass substrate:

$$T_{opt} = f_{NW} \cdot \left(1 - R_{opt}^{Sub}\right) \cdot T_{opt}^{Sub} \cdot \left(1 - R_{opt}^{AgNW}\right) \cdot T_{opt}^{AgNW} + (1 - f_{NW}) \cdot \left(1 - R_{opt}^{Sub}\right) \cdot T_{opt}^{Sub} \quad (4\text{-}9)$$

where R_{opt}^{AgNW} and T_{opt}^{AgNW} are the averaged optical reflection and transmittance, respectively, associated with a single AgNW, while R_{opt}^{Sub} and T_{opt}^{Sub} are the averaged optical reflection and transmittance, respectively, associated with the bare glass substrate. The average optical transmittance of a single AgNW, assumed to be a cylinder of diameter D_{NW}, can be estimated using the following integral:

$$T_{opt}^{AgNW} = \int_0^1 exp(-\alpha \cdot D_{NW} \cdot \sqrt{1-x^2}) \cdot dx \quad (4\text{-}10)$$

where α is the optical absorption coefficient associated with AgNW. Equation 4-9 leads to the following expression of T_{opt}:

$$T_{opt} = \left(1 - R_{opt}^{Sub}\right) \cdot T_{opt}^{Sub} \cdot \left[1 - \frac{4 \cdot amd}{\pi \cdot d^{Ag} \cdot D_{NW}} \cdot \left(1 - \left(1 - R_{opt}^{AgNW}\right) \cdot T_{opt}^{AgNW}\right)\right]$$

$$= T_{opt}^{0} \cdot (1 - \beta \cdot amd) \quad (4\text{-}11)$$

where amd is the network areal mass density (in mg.m^{-2}), d^{Ag} is the density of bulk silver, D_{NW} the AgNW diameter. T_{opt}^{0} refers to the optical transmittance of the substrate and is equal to:

$$T_{opt}^{0} = (1 - R_{opt}^{Sub}) \cdot T_{opt}^{Sub} \quad (4\text{-}12)$$

Therefore the transmittance of the network (equals to T_{opt}/T_{opt}^{0}) can be written as:

$$T_{opt}^{net} = 1 - \beta \cdot amd \quad (4\text{-}13)$$

Equation 3-10 then describes a linear dependence of T_{opt}^{net} measured at 550 nm versus amd in agreement with data reported in Figure 4-11. The slope β of the curve T_{opt}^{net} versus amd is equal to:

$$\beta = \frac{4}{\pi \cdot d^{Ag} \cdot D_{NW}} \cdot \left(1 - \left(1 - R_{opt}^{AgNW}\right) \cdot T_{opt}^{AgNW}\right) \quad (4\text{-}14)$$

Unfortunately, both absorption and reflection coefficients of AgNW are not known experimentally and might differ significantly from bulk silver values. For instance, De *et al.*[15] obtained AgNW networks optical conductivity lower by more than one order of magnitude when compared with a thin film of silver. There is so far no clear explanation for such observations. However, the term within the outer set of brackets in Equation 4-14 can be assumed to be rather close to unity since T_{opt}^{AgNW} is lower than unity and the reflection coefficient of a AgNW is probably (like bulk silver) rather close to unity. Therefore this is mainly the prefactor $\frac{4}{\pi \cdot d^{Ag} \cdot D_{NW}}$ which is supposed to dominate the β value. Accordingly, the slope values associated with large D_{NW} values (Ag117 and Ag138) are much smaller compared to small diameters (Ag26, Ag45 and Ag55). More quantitatively, the experimental slopes observed in Figure 4-11 span from 6.3.10^{-4} to 22.10^{-4} m^2.mg^{-1} while the calculated values of the prefactor (which corresponds to an over estimated value of the slope) are in the range from 8.8.10^{-4} to 47.10^{-4} m^2.mg^{-1} for the AgNW diameters considered here. In spite of the model's simplicity, this shows a rather good agreement. Thus, it allows a fair comparison with experimental data explaining the linear dependence of the relative network transmittance with amd. These experimental values are close to those predicted by the model and the associated slope tendency is to increase in magnitude for small AgNW diameter.

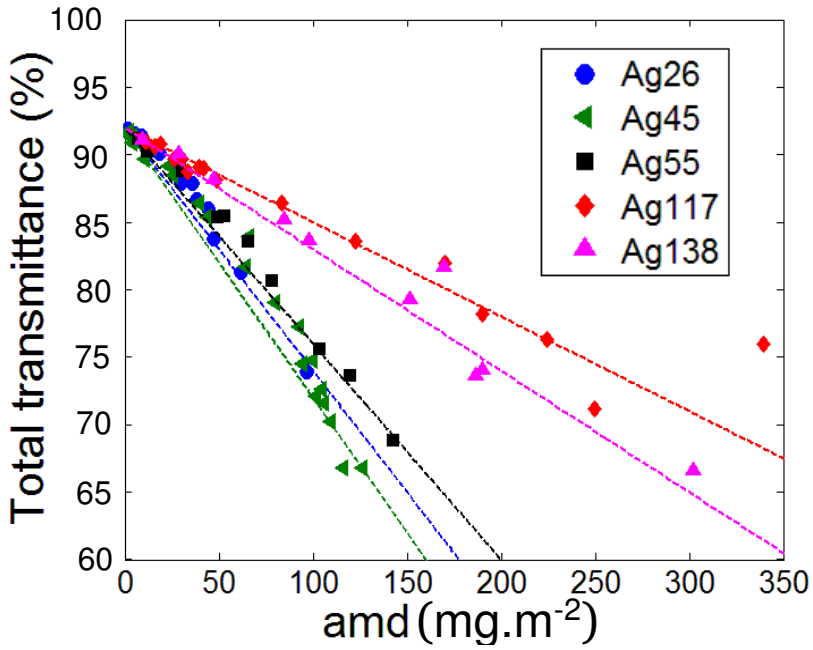

Figure 4-11: Transmittance at 550 nm of AgNW networks fabricated with nanowires of different dimensions, versus the networks mass density amd.

It is often a problem to retrieve the exact value of transmittance for a layer which is supported by a substrate since in general interferences between the media have to be taken into account. It is the case for transparent conductive oxide layers, for instance, which constitute a homogeneous layer. However, in the present case no clear interferences are present and a linear dependence of T_{opt} versus amd is observed, for the range of density considered. One can then, in a first approximation, suppose that the optical transmittance of the AgNW network can be obtained from T_{opt} divided by T_{opt}^{0}, the latter being the transmittance of the bare substrate. In the case of the study presented in this chapter, the total transmittance at 550 nm of the substrate, Corning glass, was 92%. Under this hypothesis, and except in Figure 4-11, all the transmittance data and fits presented in the rest of the chapter to assess and compare transparent electrodes composed of AgNW with different morphologies, are given without the substrate contribution.

4.4.2 Light scattering and haze factor

Scattering of light is another important feature for a transparent electrode.[10] The haze factor is a parameter that quantifies the amount of light scattered by a material and is defined as the ratio between diffuse transmitted light and total transmitted light. The needs regarding diffusion capabilities of transparent electrodes can be very different depending on the intended application. For example touch panels would need a low haze factor for comfortable visibility while solar cells performance would be enhanced by a high haze factor,[16] as discussed in the

previous chapters. This is why investigations have been lately focused on fabricating transparent electrodes with enhanced haziness.[17]

The haze factor of all the samples studied is plotted versus amd in Figure 4-12a. A linear trend is observed which is, in a first approximation, independent of the AgNW dimensions. However when the Haze factor values are plotted against the network total transmittance, like in Figure 4-12b, there is still a linear behavior, but this time the slope is dependent on the nanowire dimensions. This trend seems to be mainly dominated by the nanowire diameter. Figure 4-12b shows interestingly that the haziness can be tunable, at a specific transmittance value, by using nanowires of different types. This is of great interest considering that high performance TE sometimes needs high haze (solar cells) while sometimes low haze (screens). In order to optimize optical transmittance, electrical resistance and haziness for a specific application, one can also use a combination of different nanowires types.

Haze factor of AgNW networks has already been investigated in literature: for instance Araki *et al.*[10] showed that haze factor of AgNW networks can be decreased when using very long AgNW (20-100 µm), in agreement with Chang *et al.*[18] Preston *et al.*[11] also observed experimentally that AgNW with high diameters lead to higher haze factor compared to nanowires with low diameter.

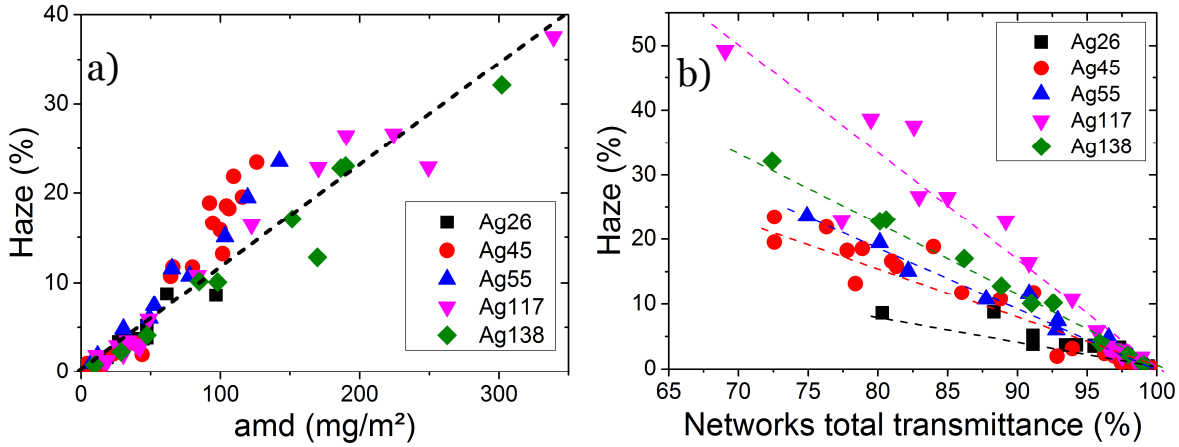

Figure 4-12: a) Haze factor dependence on mass density amd for networks fabricated from nanowires with different dimensions b) Haze factor dependence on the total transmittance of the networks.

4.5 Density and size effects on transparent electrode performance

4.5.1 Transmittance versus sheet resistance diagram

To compare the properties of different transparent electrodes, a transmittance versus sheet resistance diagram is generally used.[15] Such a diagram is illustrated for samples of various densities made from Ag117 in Figure 4-13. The samples sheet resistances were measured using the four point probe method after annealing the networks of various densities for 2h at 200°C, in order to obtain a resistance value close to the optimum. This thermal process was shown in a previous study to improve the electrical conductivity of samples with similarly shaped nanowires (see Chapter 3).[2] The region of interest in Figure 4-13 is situated at low resistance and high transmittance, *i.e.* top left region of the graph.

The model used to fit the experimental data in this figure is made from Equations 4-8 and 4-11. These equations relate the electrical resistance and the optical transmittance to amd. Replacing amd by one of these physical properties leads to a direct relation between R_{min} and T_{opt} which is then plotted as a continuous line in Figure 4-13. According to this fit (and the experimental data), there is a range in density allowing the networks to stand in the region of interest. The figure shows that the models proposed for the electrical resistance and the transmittance of the networks, including parameters such as the network density and the nanowire dimensions, agree well with experiments.

This type of diagram is used by De *et al.*[19] to separate the percolative regime from the bulk regime. In our case, the physical models used allow to fit the data of samples within the whole range of densities studied, which should in principle only be considered in the percolative regime. The fact that the relation between R_{min} and T_{opt} is still valid for rather dense networks is unexpected from a physical point of view since the number of percolating pathways within the network is sufficiently high to expect a thin film (bulk) behavior. However the fit shouldn't be valid for even denser networks.

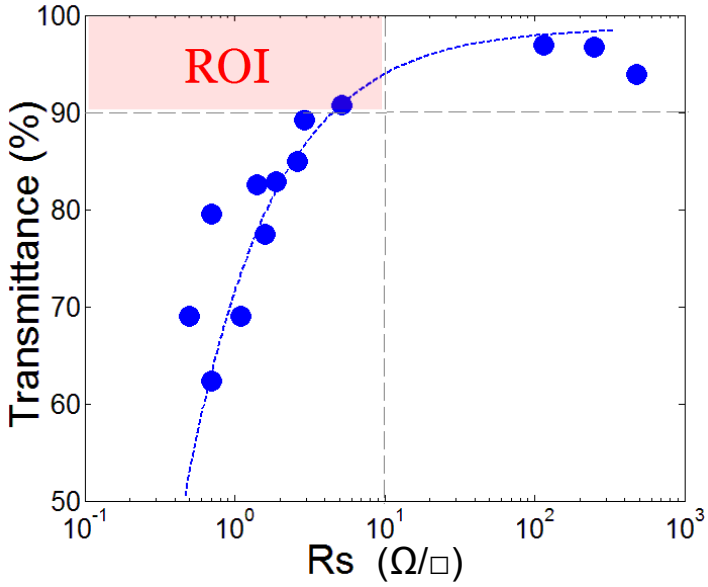

Figure 4-13: Transmittance versus sheet resistance diagram of networks made of Ag117 with various densities. The fit comes from the combination of equations 4-8 and 4-11. The region of interest (ROI) for applications is located at the top left of this diagram.

4.5.2 Haacke's figure of merit

A way to consider the performance of transparent conductive electrodes, and find the optimized density, is to calculate a figure of merit (FoM). In Chapter 2 we introduced the Haackes figure of merit[20], which we used for this density study in order to compare our different samples optical and electrical properties of thin films:

$$FoM_{Haacke} = \frac{T^{10}}{R_s} \qquad (4\text{-}15)$$

Haackes figure of merit is generally calculated with total transmittances T at 550 nm, which is standard for instance when solar cells applications are considered, and the sample sheet resistance R_s. In this study, instead of R_s, we used the minimum two points resistances R_{min} of each specimen, measured during the 2°C.min^{-1} thermal ramp, which are displayed in Figure 4-6a, to calculate the Haackes FoM. This approximation was considered reasonable since at high network density, when the resistance is lower than 5 Ω, the data exhibits a linear dependence between R and R_s values, as will be discussed now. Typically, we could calculate extrapolated sheet resistances $R_s^{Extrap.}$ values from room temperature resistances R_{min}^{RT} by using this equation, derived from Equation 1-6 in Chapter 1:

$$R_s^{Extrap.} = (R_{min}^{RT} - R_0) \cdot \frac{l}{d} \qquad (4\text{-}16)$$

where R_0 is the instrumental resistance (0.8 Ω) and $\frac{l}{d}$ the ratio between the length and width of the studied electrodes.

The experimental sheet resistance of Ag117 samples within the range 0 - 5 Ω measured by four point probe after an annealing at 200°C for 2h is plotted in Figure 4-14 against the

extrapolated sheet resistance that we just defined in Equation 4-16. The figure shows a clear agreement between calculated and experimental values by taking l =1.25 (cm) and d =0.7 (cm). As the optimum density for each type of nanowires leads to resistances in the 0-10 Ω range (see

Table 4-1, which will be introduced soon), the use of two points resistance instead of sheet resistance is valid for the purpose of finding the best density of the different series, and for the sake of comparison between different AgNW types.

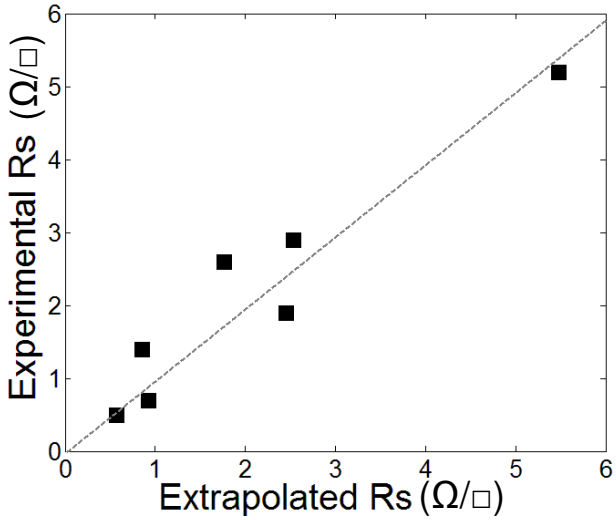

Figure 4-14: Comparison between experimental sheet resistance of Ag117 networks annealed at 200°C for 2h, and a sheet resistance extrapolated from in situ *minimum resistance measured of the same networks during a thermal annealing with ramp rate of 2°C.min^{-1}, using Equation 4-16.*

To evaluate the influence of both network density and AgNW dimensions on the TE performance, the Haackes FoM was calculated for samples made from various type of nanowires (see Table 2-1 in Chapter 2) with various densities. The FoM of samples made of Ag45, Ag55, Ag117 and Ag138 are plotted as an example against areal mass density in Figure 4-15. A bell shape is observed, defining the maximum FoM values indicating the range of optimum density. The experimental data can be fitted by using Equations 4-8, 4-11, and 4-15. A good agreement is observed with rather scattered values for large areal mass density which arise from the uncertainty associated with the method used to determine *amd* experimentally for dense networks.

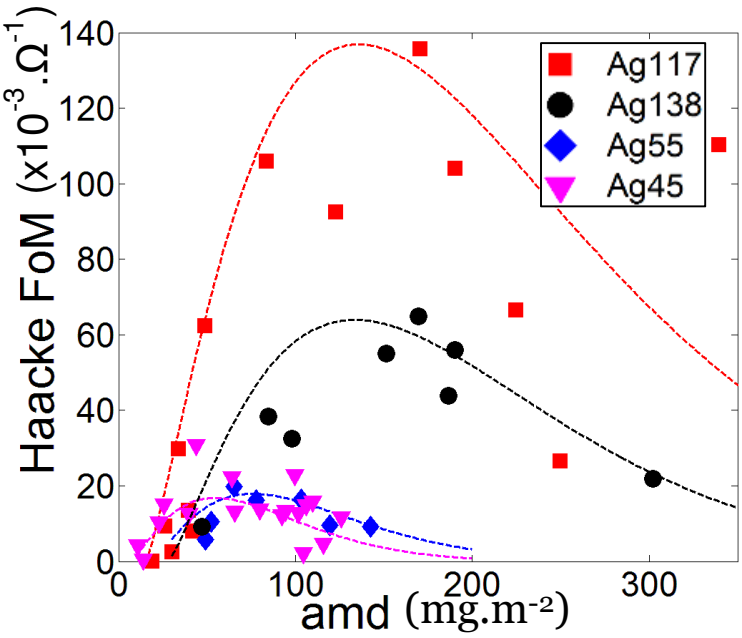

Figure 4-15 : Experimental values of FoM of different AgNW networks, fitted by a combination of Equation 4-8, 4-11 and 4-15, taking into account the networks density and the nanowire dimensions.

The bell shape comes from the formula of Haackes FoM. As discussed in Chapter 1, the transmittance contribution to the FoM is considered with the power 10 in order to have maximum values of FoM for a transmittance equals to 90%. In Figure 4-15, the sample close to the bell maximum have indeed transmittances close to 90%, and when samples transmittance is lower than 90%, the FoM decreases. When it is higher than 90%, *i.e.* for low density samples, the behavior of AgNW networks resistance within the percolative regime leads to very high resistance values that decrease the FoM as well. In other words, a too sparse network doesn't provide enough efficient percolating pathways, which is a limiting point. On the other extreme, a too dense network conducts efficiently but is too opaque. A trade-off between these two limits appears close to the top of the bell shape.

It was possible to extract the optimized density for each nanowire type thanks to the FoM calculation and fitting. The experimental characteristics (resistance, transmittance, *amd* and figure of merit) of each optimized sample have been displayed in

Table 4-1. Seeking the optimized density shows that networks cannot all achieve the same FoMs, the maximum value depends on the nanowire morphology. In Figure 4-15 there is a clear dominance of Ag117 on the other nanowire types. That might come from a better combination of the nanowires length and diameter. A high diameter allows to avoid too much electron scattering that normally increase the network resistance, and a high length leads to an improved sparseness of the nanowires, and so a higher transparency.

Table 4-1: Best samples characteristics from nanowires with different dimensions

	Ag26	Ag45	Ag55	Ag117	Ag138
Best sample Rmin calculated at 20°C (Ω) *	7.9	6.5	9.2	2.3	4.7
Best sample Transmittance (%)	88.3	88.8	90.9	89.2	88.8
Best sample FoM (x10^{-3} Ω^{-1})	37	47	42	135	65
Best sample amd (mg/m²)	62	64	65	170	170

* Note that the electrical resistances displayed in the table are two-point measured resistances and not sheet resistances (see text above and Figure 4-14 for discussion).

To go further in the comprehension of the influence of nanowire dimension on the TE performance, Figure 4-16 displays the maximum FoM achieved by samples versus the average length of their nanowires. This figure shows a clear increases of FoM with the nanowire length. However one point is diverging: Ag26. These nanowires are limited by their diameter which are below the mean free path of electrons (about 40 nm for bulk silver), unlike the others nanowire types, inducing much more surface scattering. Also it could be due to the fact that atomic surface diffusion effects in AgNW is exacerbated compared to bulk Ag due to the small diameter and so the thermal ramp at 2°C.min^{-1} was too rapid for Ag26. Therefore the resistance achieved by those samples could have been lower with a slower experimental thermal ramp rate.

The increase of nanowire length seems to be a positive way to improve the performance of AgNW-based TE. Nevertheless, the use of long nanowires leads to sparse networks, which is beneficial to improve the network transmittance, but can be a drawback when integrated into devices. For example in solar cells, the coverage of nanowires on the networks must be sufficiently high to optimize the collection of photo-generated carriers.

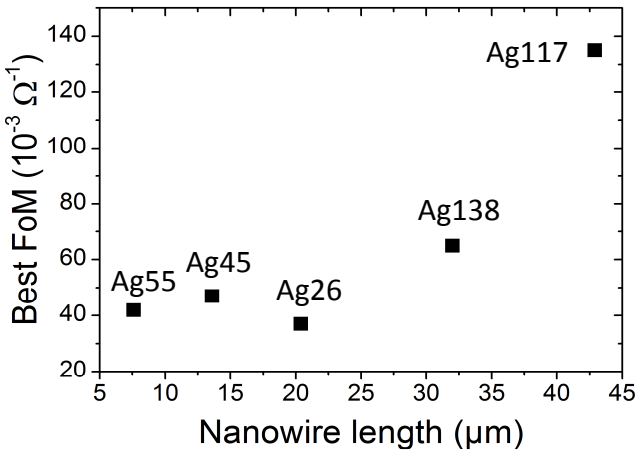

Figure 4-16: Best values of FoM of AgNW networks fabricated from different nanowire types, plotted against their nanowire length.

4.5.3 Length versus diameter diagram

Another way to compare networks made from different types of nanowires is shown in Figure 4-17. It exhibits a AgNW length-diameter phase diagram where each nanowire type is represented, plotted with a data disc size proportional to the maximum FoM value found at the experimental optimal density (red markers). Data for AgNW networks from the literature have also been plotted for comparison (green).[15,18,21–24] This shows that the method proposed in the present document: optimized density associated with appropriate thermal annealing, is an efficient way to optimize AgNW networks optical and electrical properties, and that these properties are enhanced in the area associated to large diameters coupled with large length. Especially, the largest length, Ag117, leads to a FoM much higher than the other nanowires. This is in good agreement with percolation equations and with the work of Bergin *et al.*[14] who showed experimentally that for nanowires with the same diameter, longer lengths led to better optical and electrical properties.

While Figure 4-17 shows that longer and wider AgNW give rise to better FoM, very likely other parameters should also be taken into account. Among them, defects are also expected to play an important role. Such defects concern for instance grain boundaries along AgNWs which can lead to thermal grooving,[25] increasing the electrical resistance along individual nanowires, and also decreasing the nanowires thermal and electrical stabilities. Furthermore, diameter and length distributions can influence the AgNW network behavior during thermal annealing, as well as the experimental conditions of network fabrication and of thermal treatment. Therefore, while Figure 4-17 reveals a tendency that long and wide AgNWs are interesting for optimizing the FoM, this may also stem from possible lower values of defect density or length and diameter distributions, clearly depending on chosen AgNW synthesis conditions.

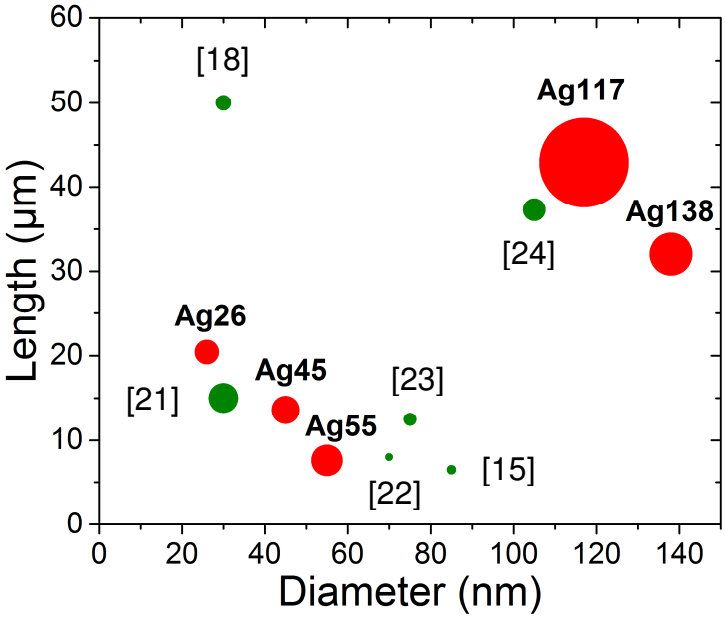

Figure 4-17: Length-diameter diagram comparing the best Haacke FoM values (displayed in table 4-1 for the red marker), which are proportional to the circles size, achieved by networks fabricated from nanowires with different dimensions. The red markers are from this work and the green are from the literature.[15,18,21–24]

4.5.4 Guideline for applications

Depending on dimensions and density, AgNW networks present a variability of electrical and optical properties. Optical transmittance and electrical resistance have been discussed, but another parameter is also very important for applications: the haze factor (HF). To take this parameter into account, and to illustrate the variability of electrical and optical properties of AgNW networks, the minimum resistance, the total transmittance and the corresponding Haacke FoM of Ag117 networks at various densities are plotted against the haze factor in Figure 4-18. This figure can be seen as a guideline to help finding the optimum network density for a specific application. For example, displays would need low HF while solar cells need the highest FoM coupled with a high value of HF. Let us note that Figure 4-18 can also be considered as a proposed guide for assessing networks composed of nanowires of different dimensions and/or of different metals.

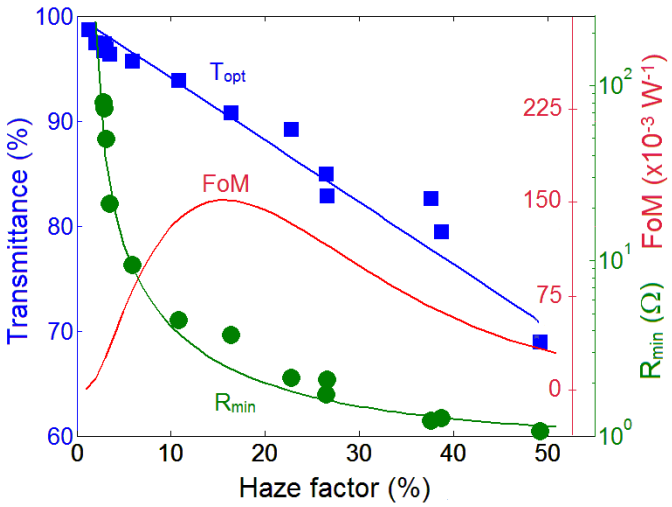

Figure 4-18: Total transmittance at 550 nm, minimum resistance and FoM fit versus haze factor of networks made from Ag117 with varying densities.

4.5.5 Comparison with an hypothetic metallic thin film containing the same amount of silver

The experimental optimum *amd* for Ag117 and Ag138 was found around 170 mg.m^{-2} (see Table 4-1). Such amount of silver would correspond to a homogeneous layer of 16 nm thick, illustrating well the very low amount of silver used. If one uses directly the Pouillet's law, *i.e.* $R = \frac{\rho \cdot L}{S}$ for a layer of length L, section S and electrical resistivity ρ, the resulting electrical resistance R of such 16 nm layer would then be equal to 0.55 Ω if the bulk silver value of ρ is considered (*i.e.* by neglecting any surface scattering). Added with the instrumental set-up resistance (R_0=0.8 Ω) the obtained value is very close to the observed R_{min} for the Ag117 optimized sample in this study (2.3 Ω, see Table 4-1). While this value is close to the one found for Ag117, the experimental resistance values of Ag138 samples are much larger. Ag138 nanowires are indeed shorter, which implies the nanowires to be more numerous on the sample to allow percolation. Therefore the number of junctions is higher and so is the electron scattering at these critical locations, inducing an increase of the resistance. That emphasizes the role of the nanowire length in the electrical properties of the sample. Although the diameter is very important, as it influences electron surface scattering, the scattering at junctions must not be neglected and is directly linked to the nanowire length.

This very simple calculation via Pouillet's law however shows that using a low amount of silver in the shape of NWs with diameter larger than the mean free path of the electrons instead of a very thin layer, where electron surface scattering would have too large effects, and with a sufficient AgNW length, constitutes a very efficient way to fabricate transparent electrodes.

4.5.6 AgNW networks comparison with other TCMs

For the sake of comparison of AgNW networks properties with those of transparent electrodes fabricated from other TCM, Figure 4-19 shows the characteristics (T versus R_s) of ITO,[15,22] single walled carbon nanotubes,[15,22,26] graphene,[22,27–29] copper[30–33] and silver nanowires,[22,23,34–36] and FTO,[17] the latter being fabricated at the LMGP. Samples made from Ag117 nanowires and Ag138 nanowires with densities close to optimum, and treated with thermal annealing exhibit excellent properties comparable with ITO. Good optical and electrical properties are of crucial importance for optimizing devices such as solar cells or efficient transparent heaters. It is also worth noting that AgNW network are flexible and can be easily integrated into flexible devices, unlike most TCOs owing to their brittleness.

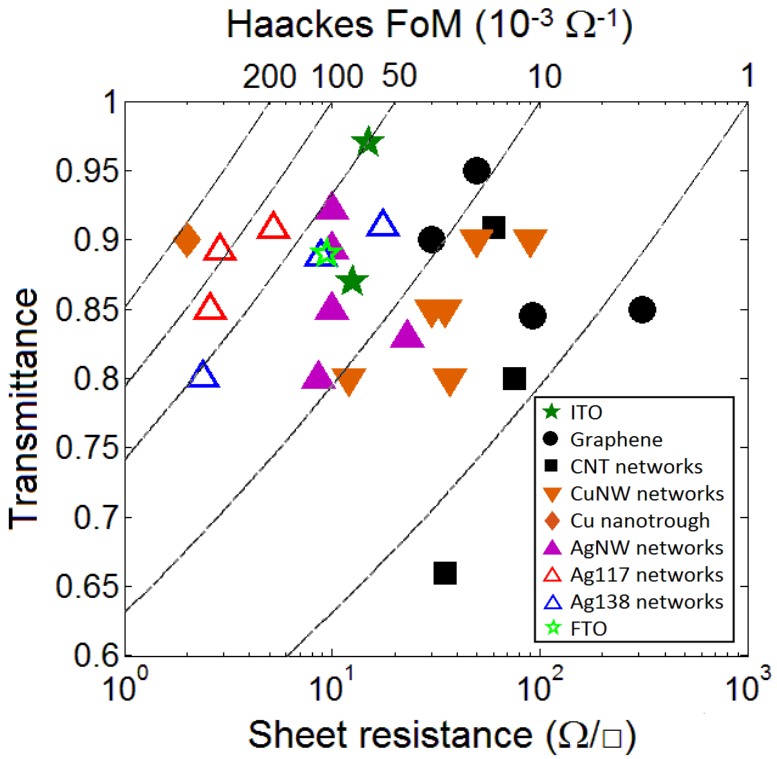

Figure 4-19: Transmittance versus sheet resistance diagram comparing the properties of different TCMs as well as the properties of the best samples obtained during this thesis work. See text for references.

4.6 Closing remarks

A thorough study has been performed on AgNW-based networks fabricated from nanowires with different dimensions (length and diameter). An optimum network density was found for each nanowire type with the help of Haackes FoM. The thermal stability of the samples was also investigated, and was shown to be strongly dependent on the nanowires diameter. This is of high interest to optimize parameters of thermal annealing, such as

temperature and duration, to fabricate efficient AgNW-based transparent electrodes. The study described in this chapter led to the fabrication of AgNW networks with high transmittance coupled with a low electrical resistance, and some of them stand in the requirements range of transmittance above 90% with sheet resistance below 10 Ω/□. These properties are very promising for a TCM as recently emerged as AgNW networks, are competing with those of ITO, while challenging other nanostructured TCM such as graphene and CNT networks. Simple models based on percolation theory and surface scattering linked the electrical resistance and optical transmittance to AgNW network density, nanowire length and diameter. Two different expressions were derived, one for the electrical resistance, the other for the optical transmittance, and both provide good agreement with the experimental observations. These models include bulk material physical quantities, and could, in theory, be applied to metallic nanowires with different nature (gold, copper for instance). The work presented in this chapter can therefore be used as a guideline to find the best density and nanowire dimensions to fulfill the requirements for a specific application.

Considering the good results obtained from spin-coated networks, we expect them to be even better with spray-coated samples. We successfully deposited the smallest nanowires using the spray (Ag26, Ag45 and Ag55) but couldn't achieve efficient samples with the bigger nanowires yet, due to the ultrasonic-induced scission addresses in Chapter 2.

References

[1] Lagrange M, Langley D P, Giusti G, Jiménez C, Bréchet Y and Bellet D 2015 Optimization of silver nanowire-based transparent electrodes: effects of density, size and thermal annealing *Nanoscale* **7** 17410–23

[2] Langley D P, Lagrange M, Giusti G, Jiménez C, Bréchet Y, Nguyen N D and Bellet D 2014 Metallic nanowire networks: effects of thermal annealing on electrical resistance *Nanoscale* **6** 13535–43

[3] D.R. Lide 2004 *CRC Handbook of chemistry and physics 2004-2005: A ready-reference book of chemical and physical data* (CRC press)

[4] G.L. Hornyak, H.F. Tibbals, J.Dutta, J.J. Moore 2009 *Introduction to Nanoscience&Nanotechnology* (CRC press Taylor&Francis)

[5] K.K Nanda, A. Maisels, F.E. Kruis, H. Fissan and S.Stappert 2003 Higher surface energy of free nanoparticles *Phys. Rev. Lett.* 106102

[6] Zhang W, Liu Y, Cao R, Li Z, Zhang Y, Tang Y and Fan K 2008 Synergy between Crystal Strain and Surface Energy in Morphological Evolution of Five-Fold-Twinned Silver Crystals *J. Am. Chem. Soc.* **130** 15581–8

[7] Klinger L and Rabkin E 2006 Thermal stability and creep of polycrystalline nanowires *Acta Mater.* **54** 305–11

[8] Daniel Langley 2014 *Silver nanowire networks: Effects of percolation and thermal annealing on physical properties* (PhD thesis: Université de Grenoble, Université de Liège)

[9] Bid A, Bora A and Raychaudhuri A K 2006 Temperature dependence of the resistance of metallic nanowires of diameter ⩾15nm: Applicability of Bloch-Grüneisen theorem *Phys. Rev. B* **74** 035426–035426 – 8

[10] Araki T, Jiu J, Nogi M, Koga H, Nagao S, Sugahara T and Suganuma K 2014 Low haze transparent electrodes and highly conducting air dried films with ultra-long silver nanowires synthesized by one-step polyol method *Nano Res.* **7** 236–45

[11] Preston C, Xu Y, Han X, Munday J N and Hu L 2013 Optical haze of transparent and conductive silver nanowire films *Nano Res.* **6** 461–8

[12] Aharony A and Stauffer D 1991 *Introduction To Percolation Theory* (Taylor & Francis)

[13] Zhu S, Gao Y, Hu B, Li J, Su J, Fan Z and Zhou J 2013 Transferable self-welding silver nanowire network as high performance transparent flexible electrode *Nanotechnology* **24** 335202

[14] Bergin S M, Chen Y-H, Rathmell A R, Charbonneau P, Li Z-Y and Wiley B J 2012 The effect of nanowire length and diameter on the properties of transparent, conducting nanowire films *Nanoscale* **4** 1996

[15] De S, Higgins T M, Lyons P E, Doherty E M, Nirmalraj P N, Blau W J, Boland J J and Coleman J N 2009 Silver Nanowire Networks as Flexible, Transparent, Conducting Films: Extremely High DC to Optical Conductivity Ratios *ACS Nano* **3** 1767–74

[16] Chih-Hung T, Sui-Ying H, Tsung-Wei H, Yu-Tang T, Yan-Fang C, Jhang Y H, Hsieh L, Chung-Chih W, Yen-Shan C, Chieh-Wei C and Chung-Chun L 2011 Influences of textures in fluorine-doped tin oxide on characteristics of dye-sensitized solar cells *Org. Electron.* **12** 2003–11

[17] Giusti G, Consonni V, Puyoo E and Bellet D 2014 High Performance ZnO-SnO2:F Nanocomposite Transparent Electrodes for Energy Applications *ACS Appl. Mater. Interfaces* **6** 14096–107

[18] Chang M-H, Cho H-A, Kim Y-S, Lee E-J and Kim J-Y 2014 Thin and long silver nanowires self-assembled in ionic liquids as a soft template: electrical and optical properties *Nanoscale Res. Lett.* **9** 330

[19] De S, King P J, Lyons P E, Khan U and Coleman J N 2010 Size Effects and the Problem with Percolation in Nanostructured Transparent Conductors *ACS Nano* **4** 7064–72

[20] Haacke G 1976 New figure of merit for transparent conductors *J. Appl. Phys.* **47** 4086–9

[21] Lee H, Lee D, Ahn Y, Lee E-W, Park L S and Lee Y 2014 Highly efficient and low voltage silver nanowire-based OLEDs employing a n-type hole injection layer *Nanoscale* **6** 8565–70

[22] Barnes T M, Reese M O, Bergeson J D, Larsen B A, Blackburn J L, Beard M C, Bult J and van de Lagemaat J 2012 Comparing the Fundamental Physics and Device Performance of Transparent, Conductive Nanostructured Networks with Conventional Transparent Conducting Oxides *Adv. Energy Mater.* **2** 353–60

[23] Madaria A, Kumar A, Ishikawa F and Zhou C 2010 Uniform, highly conductive, and patterned transparent films of a percolating silver nanowire network on rigid and flexible substrates using a dry transfer technique *Nano Res.* **3** 564–73

[24] Langley D P, Giusti G, Lagrange M, Collins R, Jiménez C, Bréchet Y and Bellet D 2014 Silver nanowire networks: Physical properties and potential integration in solar cells *Sol. Energy Mater. Sol. Cells* **125** 318–24

[25] Mullins W W 1957 Theory of Thermal Grooving *J. Appl. Phys.* **28** 333

[26] Hecht D S, Heintz A M, Lee R, Hu L, Moore B, Cucksey C and Risser S 2011 High conductivity transparent carbon nanotube films deposited from superacid *Nanotechnology* **22** 075201–075201 – 5

[27] Kim U, Kang J, Lee C, Kwon H Y, Hwang S, Moon H, Koo J C, Nam J-D, Hong B H, Choi J-B and Choi H R 2013 A transparent and stretchable graphene-based actuator for tactile display *Nanotechnology* **24** 145501

[28] Bae S, Kim H, Lee Y, Xu X, Park J-S, Zheng Y, Balakrishnan J, Lei T, Ri Kim H, Song Y I, Kim Y-J, Kim K S, Özyilmaz B, Ahn J-H, Hong B H and Iijima S 2010 Roll-to-roll production of 30-inch graphene films for transparent electrodes *Nat. Nanotechnol.* **5** 574–8

[29] Sun T, Wang Z L, Shi Z J, Ran G Z, Xu W J, Wang Z Y, Li Y Z, Dai L and Qin G G 2010 Multilayered graphene used as anode of organic light emitting devices *Appl. Phys. Lett.* **96** 133301–3

[30] Rathmell A R and Wiley B J 2011 The Synthesis and Coating of Long, Thin Copper Nanowires to Make Flexible, Transparent Conducting Films on Plastic Substrates *Adv. Mater.* **23** 4798–803

[31] Han S, Hong S, Ham J, Yeo J, Lee J, Kang B, Lee P, Kwon J, Lee S S, Yang M-Y and Ko S H 2014 Fast Plasmonic Laser Nanowelding for a Cu-Nanowire Percolation Network for Flexible Transparent Conductors and Stretchable Electronics *Adv. Mater.* **26** 5808–14

[32] Hu L, Wu H and Cui Y 2011 Metal nanogrids, nanowires, and nanofibers for transparent electrodes *MRS Bull.* **36** 760–5

[33] Zhang D, Wang R, Wen M, Weng D, Cui X, Sun J, Li H and Lu Y 2012 Synthesis of Ultralong Copper Nanowires for High-Performance Transparent Electrodes *J. Am. Chem. Soc.* **134** 14283–6

[34] Tokuno T, Nogi M, Karakawa M, Jiu J, Nge T T, Aso Y and Suganuma K 2011 Fabrication of silver nanowire transparent electrodes at room temperature *Nano Res.* **4** 1215–22

[35] Lee H, Lee D, Ahn Y, Lee E-W, Park L S and Lee Y 2014 Highly efficient and low voltage silver nanowire-based OLEDs employing a n-type hole injection layer *Nanoscale* **6** 8565–70

[36] Leem D-S, Edwards A, Faist M, Nelson J, Bradley D D C and de Mello J C 2011 Efficient Organic Solar Cells with Solution-Processed Silver Nanowire Electrodes *Adv. Mater.* **23** 4371–5

Chapter 5 : AgNW networks electrical stability and application for transparent heaters, electromagnetic shielding and RF antennas

Metallic nanowire networks have been proved in the previous chapters to be efficient as TE, with excellent transmittances coupled with high conductivity. Therefore their integration into optoelectronic devices seems promising. To prove AgNW network efficiency in various devices, studies were performed at LMGP in the field of different applications developed in this chapter: transparent film heaters (TH) mainly, as well as preliminary experiments on electromagnetic shielding and RF antennas. Each application is first defined and understood through a bibliographical study, and then tested with samples made at LMGP. The potential of AgNW networks used for the different applications is discussed in this chapter and the limiting features, such as electromigraton, are highlighted.

5.1 AgNW-based transparent heaters

Transparent heaters have been introduced in Chapter 1. They are transparent materials which need to be also conducting to heat by Joule effect. The Joule's law, experimentally demonstrated by J.P. Joule (1818-1889), states that when an electrical current I propagates along a metallic conductor with electrical resistance R, heat is released and its amount per unit time is equal to RI^2. TH can be used for defrosting or defogging transparent surfaces such as windscreens or helmet visors, outdoor panel displays, or more generally devices exposed to temperature variations. One of the first patents concerning TH suggested their application for aircraft windscreen deicing to allow them to flight at higher altitudes. [1]

Metallic nanowire networks are among the most promising materials for TH application, and especially silver nanowires (AgNW). To our knowledge, no other type of metallic NWs have been tested as TH yet, even if copper NW or cupronickel NW networks, for example, have been studied as transparent electrodes[2–4]. AgNW networks achieve satisfactory optical and electrical properties (typically R_s ~ 10 Ω/□ for transmittance ~ 90%), even with a low amount of material used – typically between 50 and 150 $mg.m^{-2}$ as presented in Chapter 4, corresponding to a silver amount lower than that of a homogeneous layer associated to a thickness 20 nm. Another advantage of AgNW networks for this application is their mechanical stability: they don't show any significant resistance change when bending[5]. Flexibility is a key criterion for TH applications considering that they can be used for surfaces with complex shapes (helmet visors, windscreens…) and geometries.

AgNW networks ability to increase their substrate temperature to several tens of degrees using an operation voltage lower than 12 V, which is convenient for most devices, will be displayed in this section, confirming their potential for such application.

5.1.1 AgNW-based transparent heaters operation and state of the art

The first report of AgNW networks used as transparent heaters was from Celle et al.[6] They investigated the temperature elevation of the films while applying different voltages, as displayed in Figure 5-1. The power dissipated in the material (V^2/R), is directly related to the achieved steady-state temperature through a balance between Joule effect and heat losses, which depends on temperature, conduction to the substrate, convection to the surrounding air and radiation from the hot surface.

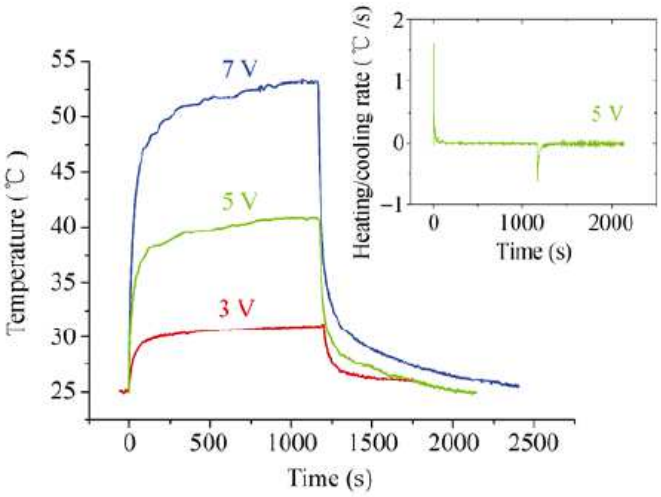

Figure 5-1: Temperature versus time achieved by a AgNW-based TH with sheet resistance R_s = 33 Ω/□ at various voltages. Insert: heating and cooling rates at 5 V.[6]

5.1.1.i Energy balance

Sorel *et al.*[7] gave a comprehensive and thorough description of the theory of Joule heating in a TH made with AgNWs. Considering the temperature is uniform across the sample, the energy balance can be written as follows (conduction losses to extern parts of the system are neglected):

$$I^2R = (m_1C_1 + m_2C_2)\frac{dT(t)}{dt} + A(h_1 + h_2)(T(t) - T_0) + \sigma A(\varepsilon_1 + \varepsilon_2)(T(t)^4 - {T_0}^4) \quad (5\text{-}1)$$

For each parameter, the indexes 1 and 2 correspond to the network and the substrate, respectively, $T(t)$ is the instantaneous sample temperature, and T_0 the ambient temperature. In Equation 5-1, the term on the left is the dissipated power input to the TH per time unit, with I the current and R the resistance. The first term on the right is the heat per unit of time brought to the network and substrate *via* conduction which is responsible for the temperature elevation

of the sample through the specific heat capacities C, m_1 and m_2 being the masses of the network and of the substrate, respectively. The second term represents the heat losses per unit of time by convection, with h_1 and h_2 the convective heat-transfer coefficients and A the area of the film, assumed to be equal to the substrate area. The third term illustrates the heat losses by radiation, with σ the Stefan-Boltzmann constant and ε_1 and ε_2 the emissivity of the network and of the substrate, respectively. This energy balance, if simplified by considering small temperature rises, allowing a linear expansion of Equation 5-1 (the non-linear term associated to radiation losses is neglected), and $m_1 \ll m_2$, which has the following analytical solution, demonstrated in Sorel's paper:

$$\mathrm{T(t)} \approx T_0 + \frac{1}{\alpha}\frac{I^2R}{A}\left[1 - \exp\left(-\frac{\alpha}{C_2 m_2/A}t\right)\right] \quad (5\text{-}2)$$

with α the heat transfer constant, which take into account the parameters of heat losses:

$$\alpha = (h_1 + h_2) + 4(\varepsilon_1 + \varepsilon_2)\sigma {T_0}^3 \quad (5\text{-}3)$$

Another characteristic parameter related to α is the time constant $\tau = \frac{m_2 C_2}{A\alpha}$. It is generally found to be around 60-100s for AgNW networks.[6–11] Equation (5-2) shows that there is a transitional state at small t, and then a steady-state temperature is achieved, which value depends on the voltage, after a certain time equals to a few τ. This approach is validated by the experimental results displayed in Figure 5-1. The steady-state temperature elevation is therefore directly proportional to the applied areal power density ($\frac{I^2R}{A}$), and equals to

$$T_{stab} - T_0 = \frac{1}{\alpha}\frac{I^2R}{A} \quad (5\text{-}4)$$

The key parameters in TH are therefore the steady-state temperature T_{stab}, and the response time, which needs to be as short as possible. Response time is considered as the time needed to achieve 90% of T_{stab}. T_{stab} depends on the network density and on the applied current.[7] The heater efficiency is better when a defined increase in temperature is obtained from an applied voltage as low as possible, typically below 12 V for standard use. Such low voltage enables to lower the damages induced by the current flow, such as electromigration which is addressed later in this chapter. The criteria limiting these key parameters are the heat losses by conduction, convection and radiation, illustrated by α. From Equation 5-4, the operating voltage V_{op} of a transparent heater can be related to the bulk film sheet resistance R_s and α by: [7]

$$V_{op} = \sqrt{\alpha \cdot \Delta T \cdot R_s \cdot l^2} \quad (5\text{-}5)$$

l is the inter-electrode spacing and ΔT the temperature elevation. To minimize the operation voltage, α needs to be low while the electrode figure of merit (related to R_s and the network transmittance) needs to be high.[7] Operation voltage, temperature elevation and heat losses depend strongly on the network density. First, for samples with transmittance below

80%, α increases with density. This can be explained by the increase of convection caused by a higher surface roughness and higher internal area induced by the increase of nanowire number. Convection as well as radiation are both significant ways of heat losses in AgNW networks. However, reducing the network density to reduce heat losses causes an increase of the sample resistance. According to Figure 5-2a, which shows the temperature elevation versus the current applied for samples with various sheet resistances, Joule heating seems to be enhanced by samples with high resistance. Also when samples in the percolating regime (high transparency but also higher resistance) are compared with bulk-like samples (low resistance but low transparency), the thermal behavior is clearly different: Figure 5-2b displays the temperature elevation, divided by the square of the electrical current, versus a function of the transmittance, showing *a priori* better thermal capacities for the percolating samples. However this is misleading. Low density networks haven't higher efficiency compared to high density samples since more power is required to drive a given current within these networks. The networks behaving within the percolative regime (therefore having a low network density), although having high transparencies, are less efficient compared to those that can be considered as bulk,[7] as they must be operated at higher voltage.

Sorel *et al.*[7] proposed a figure of merit for TCM used specifically as transparent heaters, to define the materials enable to reach high temperature with low applied voltage. These FoM are simply the FoM used for transparent electrodes in general, divided by the parameter dedicated to heat losses, α. According to this new FoM, Sorel *et al.* found AgNW to be the most promising TCM used as transparent heaters, among CNT and graphene.

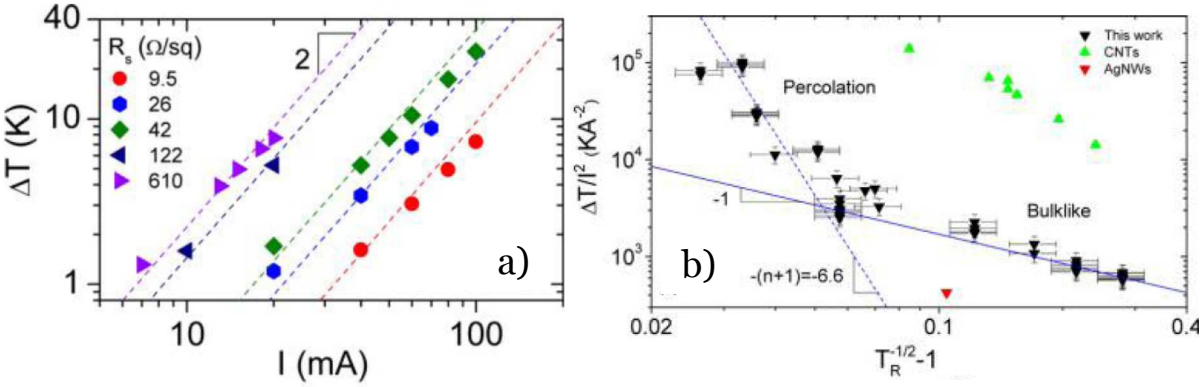

Figure 5-2: a) Temperature elevation of AgNW networks whith different sheet resistance versus the applied current b) AgNW temperature elevation divided by the square of the electrical current plotted versus a function of the sample transmittance to identify the percolative regime (dashed line) and the bulk like regime (solid line). [7]

5.1.1.ii Major limitations of AgNW-based TH

One of the major issues of metallic nanowires is their low adherence on substrates and their stability during TH operation *i.e.* thermal and/or electrical stability. Several studies can

be found in the literature that propose solutions to overcome these problems. As mentioned in Chapter 1, Kim *et al.*[8] have found one solution for the adhesion problem by using clay platelets and PET, but they used very thin nanowires and so the electrical and thermal stability might be still a critical problem. To address this issue, Li *et al.*[12] created a polymer composite resistant at temperatures as high as 230°C, while allowing adhesion that could pass the tape test. Also the samples were mechanically stable because bending cycles did not impact on the heating temperature. Ji *et al.*[13] coated AgNW networks with PEDOT:PSS for the same reasons of thermal stability and adhesion improvement, and Zhang *et al.* with graphene microsheets[10]. To finish, another drawback of metallic NW network for TH application is that they usually present high haze. This can be a problem for application in windows defrosting, where haze factor needs to be low for comfortable viewing. High haze could be limited by using long nanowires[14] to reduce the amount of material needed for the required conductivity.

5.1.2 Motivations

AgNW-based TE properties have been optimized during this thesis work, see Chapters 3 and 4, with the relevant choice of nanowire size, network density and thermal annealing. AgNW networks will now be applied as transparent heaters. An ANR project (FICHTRE, 2014-2017) is being funded around a collaboration with the CEA and other partners including two companies, aiming at creating transparent heaters that could be deposited on motorbike helmet visors for defogging purpose. Several requirements raised such as a low haze factor, typically below 3%, a response time around $1°C.s^{-1}$ and an operation voltage below the standard 12 V. In addition the use of fast fabrication processes and a low cost final product is of high interest. More fundamental issues concerning TH are addressed in this thesis, especially on the electrical, thermal and mechanical stability of AgNW networks during operation as TH. The different heat losses have been identified in the literature but studies haven't been conducted on the impact of each of them individually. This work presents studies carried on heat losses especially by switching on and off convection through experiments performed at air and under vacuum, respectively.

5.1.3 Samples fabrication

Experiments have been performed first on Corning glass and then on flexible substrates: PEN and transparent Kapton. The majority of the samples was made from Ag45 with the spray coating standard routine in order to have efficient samples (sheet resistance close to 20 Ω/□ after annealing 2h at 200°C and transmittance around 91 %, without substrate contribution). Otherwise, fabrication details will be given when needed. After nanowires

deposition, two silver paint lines were deposited on opposite sides of the samples for contacting purpose, except when indicated.

5.1.4 Standard response of a AgNW network with voltage application

As previously presented, an electrical current flowing in a conducting material induces a generation of heat by Joule effect, for example in AgNW-based transparent electrodes. Several effects of the current on the AgNW networks resistance were however identified: reversible and non-reversible effects. They are presented and discussed now.

5.1.4.i Irreversible effects

One would expect that, when a current is flowing in a material, electrons interact through inelastic collisions with the atoms of the material studied, inducing a temperature elevation. Therefore the resistance should increase with the voltage considering the variation of metals resistivity in function of temperature (see Chapter 3). This is not the case in Figure 5-3 where the resistance has even the opposite behavior and decreases as the voltage increases by steps of 1 V between 1 and 4 V. The sample presented in this figure was made with spin coated Ag117 (concentration 0.5 $g.l^{-1}$) on a PEN substrate with a studied surface of 2x2 cm^2. The sample was annealed at 150°C for 1h to decrease the initial resistance. This annealing is performed at low temperature compare to previous samples (200°C) since PEN becomes unstable at temperatures higher than 150°C. After annealing, the samples properties were a sheet resistance around 100 Ω/□ and a transmittance around 94%, without substrate contribution. The starting resistance in Figure 5-3a is however higher (almost 280 Ω), which can be due to a poor electrical contact between the setup and the network.

The resistance reduction seen in Figure 5-3a happens to be non-reversible and resembles the sintering effect on resistance induced by a thermal ramp annealing. The figure shows that for each step of voltage, the resistance tends to stabilize but a further increase of voltage makes it decrease again *etc*. This experiment can't help to distinguish the electrical effect on the resistance from the thermal effects induced by Joule effect. This question will be addressed in section 5.2.4. However when we look at the temperature profile, it seems that the maximum temperature achieved by the sample is 30°C. Even if we expect the temperature within the nanowires to be higher than the one measured, which is averaged over a larger scale of the whole substrate, substrate included, it is rather low and no temperature-induced sintering should occur yet. Therefore, the electrical current might have reduced the resistance by electromigration-driven junction sintering. Analogously to thermal annealing, where the temperature induces first a decrease of resistance at the junction, but then instability, a current flowing through the network induces sintering, as just mentioned, but then nanowire

instability through the same electromigration process, probably coupled with Joule effect induced temperature elevation (and so thermal instability). This will be discussed later.

After this stepped voltage induced resistance reduction, another experiment was subsequently performed on the same sample: the application of a higher voltage (6 V) for a long time (20 minutes). The results are displayed in Figure 5-3b, and show a resistance reduction as well. Once again the resistance, instead of increasing with voltage and stabilizing, is reduced by several tens ohms. An interesting fact is that the resistance actually first starts to increase with voltage, but then decreases when voltage goes above 4 V, which is the maximum voltage that was achieved in the last experiment presented in Figure 5-3a. The sample seems to have reversible behavior if it is operated at a lower voltage that the one it has been previously stabilized with.

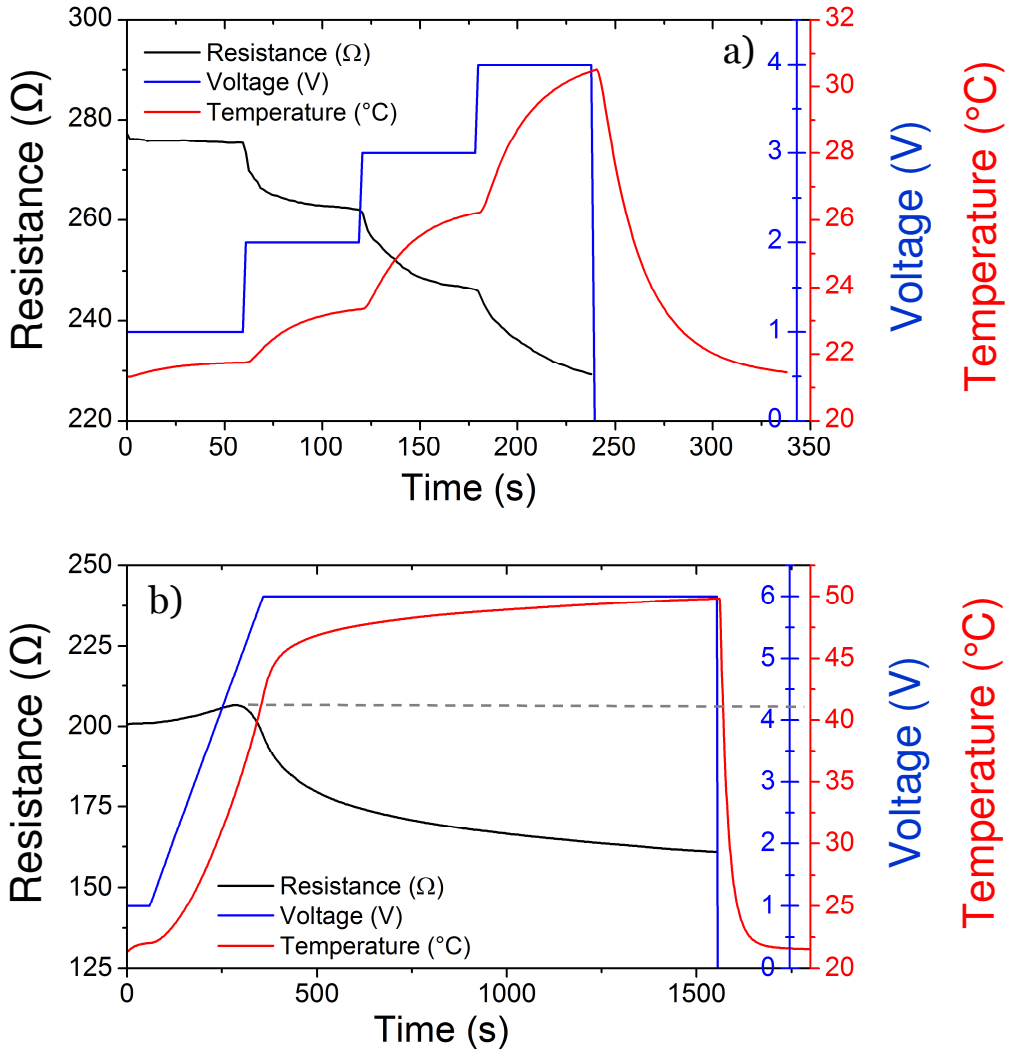

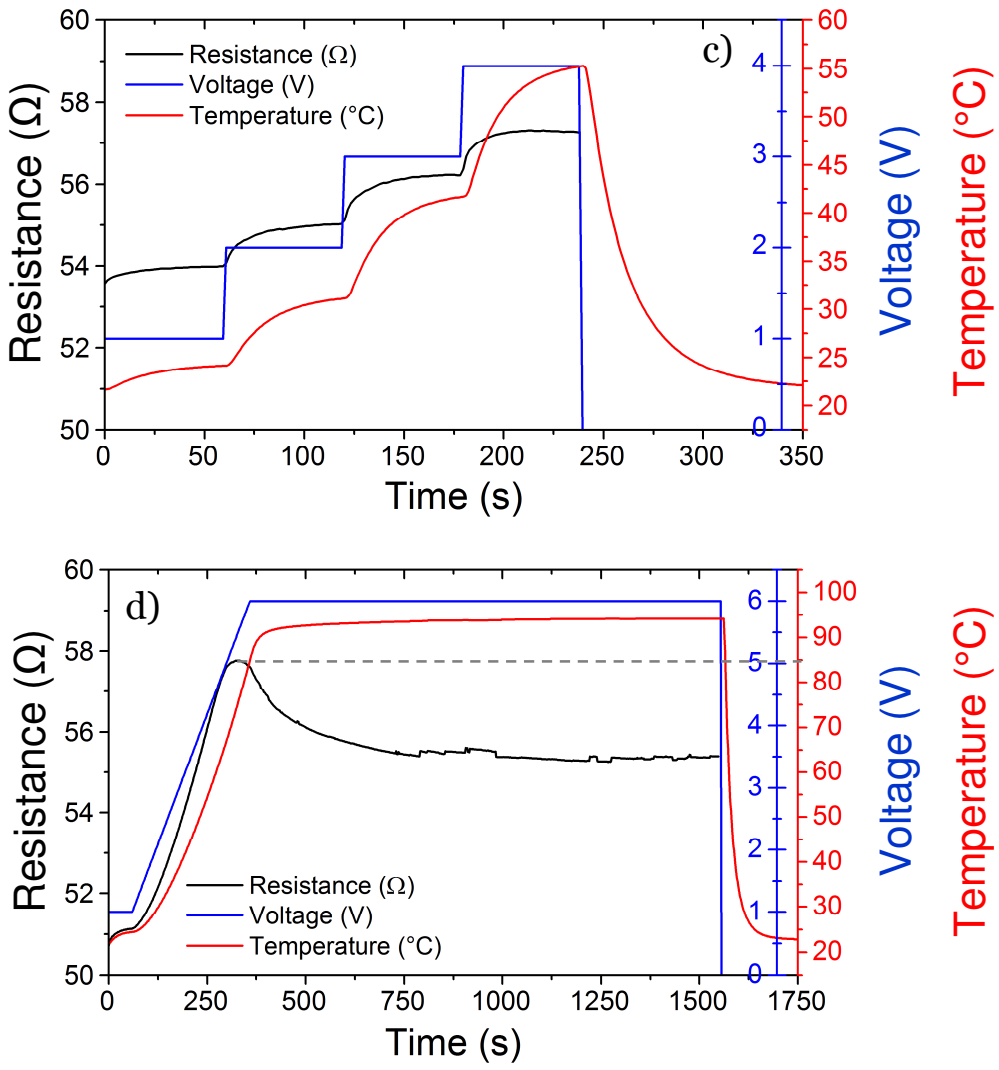

Figure 5-3: a) Irreversible effects of electrical current, through application of different voltages, on a AgNW network in air with initial sheet resistance around 100 Ω/□. Each plateau duration is 1 minute b) Irreversible effect on the sample resistance during a plateau at 6 V for 20 minutes c) Irreversible effects of electrical current, through application of different voltages, on a AgNW network in air with initial sheet resistance around 30 Ω/□. Each plateau duration is 1 minute d) Irreversible effect on the same sample resistance during a plateau at 6 V for 20 minutes.

Another sample fabricated exactly like the one presented in Figure 5-3a and b, with the same density, but having a lower initial resistance, 30 Ω/□, was investigated. This difference in resistance is induced by the pre-experimental thermal sintering performed at 150°C for 1 hour. This annealing, which is not optimum, led to different initial sheet resistance (30 and 100 Ω/□, respectively). The reason for choosing 150°C is because PEN is damaged at higher temperatures. This annealing temperature is not high enough to induce all the mechanisms of resistance reduction discussed in Chapter 3. Therefore due to the conditions of thermal annealing different from the optimized one, the samples have different resistances after annealing although the two samples have the same density. The last statement is confirmed by

the similar total optical transmittances (82.5 and 82.6 %) measured for each sample, and the identical conditions of deposition.

However a difference in resistance behavior is observable when an electrical current is applied, as can be seen in Figure 5-3c: the sample resistance increases well with the voltage, this time, although it tends to start to slightly decrease during the 4 V plateau. The plateau at 6 V for 20 min performed afterwards, with resulting resistance and temperature displayed in Figure 5-3d, shows a strong decrease of the resistance before it stabilizes. This time the temperature increased above 90°C so it is difficult to know whether it is a thermally-induced sintering by surface diffusion or sintering by electromigration, or a combination of both phenomena. The fact that resistance starts decreasing only at high voltage would mean that the sample heating, and/or electromigration are efficient enough to induce atomic diffusion responsible for junctions sintering.

Another irreversible effect that is going to be studied more thoroughly in section 5.2.2 is the network electrical instability. Instability occurs when the voltage is too high and might be driven by electromigration. For example a sample made with Ag45 (spray standard routine) on transparent Kapton, after annealing at 175°C for 30 minutes was first stabilized with different voltage plateaus and steps, and then underwent a voltage ramp of 0.1 $V.min^{-1}$. The resulting temperature and resistance behavior regarding voltage are displayed in Figure 5-4. Temperature increases with voltage, as expected, and the resistance increases slightly in accordance with the classic behavior of a TH. However between 7.5 and 8 V, the resistance diverges and the temperature goes back to room temperature. This instability might originate from a current density which is too high and induces electromigration followed by nanowire breakdown. Voids in the nanowires are formed due the current[15] and deteriorates the electrical percolating pathways.

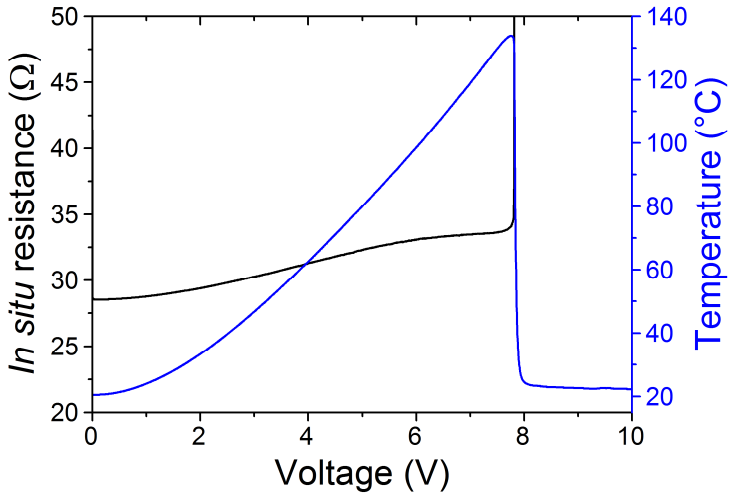

Figure 5-4: Electrical instability of a spray deposited Ag45-based AgNW network subjected to a voltage ramp of 0.1 $V.min^{-1}$.

One way to understand the data reported Figure 5-4 is to try to model the temperature elevation during a voltage ramp. One can follow a similar method reported by Sorel *et al.*, applied for a constant voltage, which results in the Equations 5-1 to 5-4. The differential Equation 5-1 could then be replaced by:

$$\frac{V^2}{R} = mC\,\frac{d\Delta T(t)}{dt} + \alpha\, A\, \Delta T(t) \qquad (5\text{-}6)$$

where V increases linearly with time, therefore: $V(t) = \dot{V} \cdot t$. Equation 5-6 can then be written as:

$$\frac{d\Delta T(t)}{dt} + \frac{\alpha\, A}{mC}\Delta T(t) = \frac{\dot{V}^2}{mCR}t^2 \qquad (5\text{-}7)$$

where mC replaces $m_1.C_1 + m_2.C_2$ to simplify the notations. This equation has an easy solution (knowing that $\Delta T(t = 0) = 0$) and can be written as:

$$\Delta T(t) = \frac{\dot{V}^2 m^2 C^2}{\alpha^3 A^3 R}\left\{\left(\frac{t}{\tau} - 1\right)^2 - 2e^{-\frac{t}{\tau}} + 1\right\} \qquad (5\text{-}8)$$

Equation 5-8 is obviously very different from Equation 5-2 since the applied electrical power is not constant anymore but increases with the square of time. It is worth keeping in mind that Equation 5-8 has been solved with the following hypotheses: the electrical resistance R is constant, and the radiative term has been linearized as previously supposed for a constant power. Indeed the following Figure reports a good agreement at least at low voltage before an increasing discrepancy. However the experimental behavior of the TH at low voltage combined with Equation 5-8 could be, generally speaking, of interest for instance when non constant voltage could be applied. One could as well go a bit further in the analysis by considering the dependence of the network resistance with voltage (as shown in Figure 5-4) and as well the first non-linear term in the development of the radiative term to get a fair agreement for a larger voltage range. More importantly a deeper detailed analysis in this direction should allow, from only the fitting of temperature versus voltage, to see when the network starts to be deteriorated in a non-reversible way.

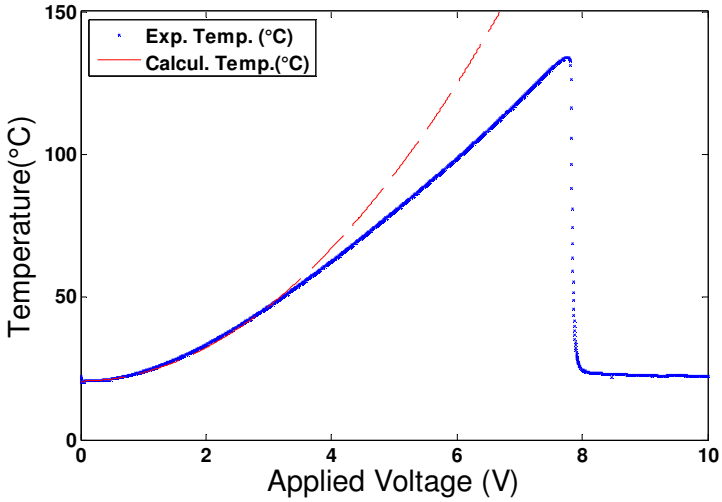

Figure 5-5: Experimental and modelled temperature behavior, using Equation 5-8, of a AgNW network during a voltage ramp of 0.1 V.min^{-1}.

5.1.4.ii Reversible effects and lifetime

Transparent heater is an application that should undergo a lot of ON and OFF situations. So, one has to verify that they have a sufficiently long lifetime and reproducible behavior during a sufficient number of cycles. For further studies of AgNW-based TH, especially for the study of reversible effects, it is important to have a resistance which is stabilized, to avoid the irreversible electrical effects on the resistance that were just discussed. For this purpose, the samples must be optimized thermally and then further stabilized with a voltage plateau at higher voltage than the one which will be used later on for their operation, if needed.

Voltage cycles were made on samples with same coverage but different resistances. The samples were the same that were presented in the last section, *i.e.* two identical samples made with spin coated Ag117 (c=0.5g.l^{-1}) on PEN substrates of size 2*2 cm², and then annealed at 150°C for 1 hour. As seen before, even with identical fabrication conditions, they however present different initial sheet resistances: 30 and 100 Ω/□. Before investigation of the reversible effects, a plateau at 6 V has been performed on the samples in order to stabilize the sample's resistance to be used at 5 V, as shown in Figure 5-3b and Figure 5-3d. Then a series of voltage plateaus has been performed on the sample, in order to sinter them and avoid irreversible effects on the resistance during the cycles.

Both samples have then been used to test TH reproducibility and lifetime with 8 cycles of 10 minutes at 5 V spaced with "resting time" at 1 V for 2 minutes. A zoom on 3 cycles showing the results for the temperature behavior are displayed in Figure 5-6a. Over 8 cycles at 5V for 10 minutes, the resistance or temperature achieved at each plateau was different of less than 0.3% for each sample. The influence of the sample resistance on TH operation is quite clear, as the temperature elevation at 5 V for the sample with sheet resistance equals to 30 Ω/□ is more

than twice larger compared to the one achieved by the 100 Ω/□ sample: 75 °C and 43°C respectively. Resistance has also an impact on the response time. As seen in Figure 5-6b, which displays the response time of the cycle experiment shown in Figure 5-6a by simply calculating dT/dt, the heating speed is higher for low resistance samples. This is not surprising considering that at a defined voltage, if the resistance is lower, the power input $\frac{V^2}{R}$ is larger. Therefore the temperature increases more, and more rapidly, as well as the heat exchanges.

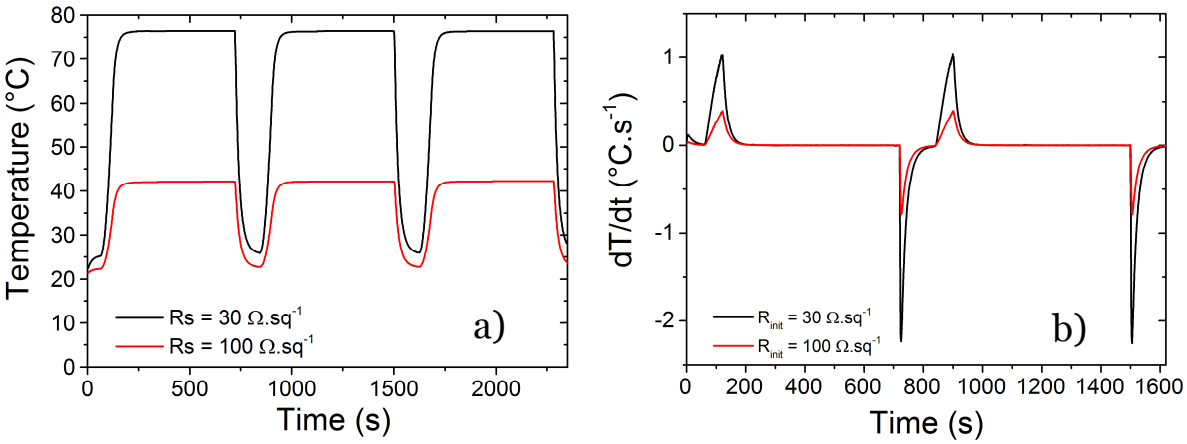

Figure 5-6: a) Temperature of spin coated AgNW network with similar nanowire density but different resistances during cycles of plateaus at 5 V of 10 minutes spaced by 2 minutes at 1 V b) Response time during the cycles experiments.

Another interesting observation in Figure 5-6a is that the temperature seems stable during a plateau, unlike what was observed in the previous section. Therefore we assume that the samples have been well optimized by thermal and electrical sintering before the experiment, or at least the voltage used (5 V) was not high enough at this stage to induce more sintering leading to irreversible effects on the sample resistance.

5.1.4.iii Influence of nanowire density

Optimized AgNW networks constituted of nanowires of the same type but having different resistances would imply that they have different network densities. This difference in the fraction of the sample covered by nanowires will definitively have an impact on the capacity of the sample to heat, and on the heat losses. Therefore, we started experiments to look at the influence of the network resistance without the impact of the coverage fraction by studying samples with same AgNW surface coverage but different resistances coming from a non-optimized thermal annealing. Once again, the samples studied in the last section, after all the treatment undergone explained above, were tested again with a voltage ramp of 0.1 $V.min^{-1}$ with increasing voltage up to instability. The temperature and resistance of the two samples

with same nanowire density but different resistances were recorded during the experiment and are displayed in Figure 5-7a.

Considering the resistance behavior, first an irreversible decrease of R occurs for the sample with the highest resistance, after 3500 s, corresponding to approximately 6 V, which was the highest voltage that the sample has undergone during all experiments. For the sample with lowest resistance, at this voltage of 6 V the resistance starts to increase significantly and eventually diverges, inducing the temperature stopping to increase and going back to room temperature. The other sample, however, has its resistance diverging slightly later, around 8 V, with the same effect on temperature. The steps in resistance after the first increase are not completely understood at the moment but might be influenced by the substrate. In addition, some parts of the sample might become less efficient, therefore leading to an increase of the specimen electrical resistance. This kind of steps was only observed for samples made on PEN, and the latter was observed to be degraded by the process and melted at high voltages (see SEM image in Figure 5-7c) parallel to the silver paint electrodes, all along the sample. The increase of the temperature of the sample with lowest resistance is more rapid but both sample undergo instability around the same temperature (~ 110°C). The latter observation might be biased by the local melting of the substrate which might enforce the electrical conduction failure at this temperature. To avoid this artefact, experiment were then made on transparent Kapton (like the one presented in Figure 5-4), much less temperature sensitive, for further electrical instability studies. In the experiment with PEN substrate presented in Figure 5-7, the interest is more focused on the behavior of the resistance and the temperature during the voltage ramp. Figure 5-7a shows that at a voltage V, a higher temperature is achieved when the sample resistance is lower. However the temperature achieved versus the power density $\frac{V^2}{R \cdot A}$, with A the sample surface, stands on the same linear slope for both samples as shown in Figure 5-7b. However two different slopes can be observed, one in the range 0-0.1 $W.cm^{-2}$, and the other at higher power densities. The reason for the presence of two slopes is not completely understood but could stem from the partial local melting of the substrate, as mentioned above. According to equation 5-4, the slopes in Figure 5-7b are approximately equal to the inverse of the heat transfer constant α, the latter is therefore around 19.8 $W.m^{-2}.K^{-1}$ between 0-0.1 $W.cm^{-2}$ and 25.8 $W.m^{-2}.K^{-1}$ at higher power density. These values are within the range found in the literature for AgNW: *i.e.* 15-123 $W.m^{-2}.K^{-1}$.[7]

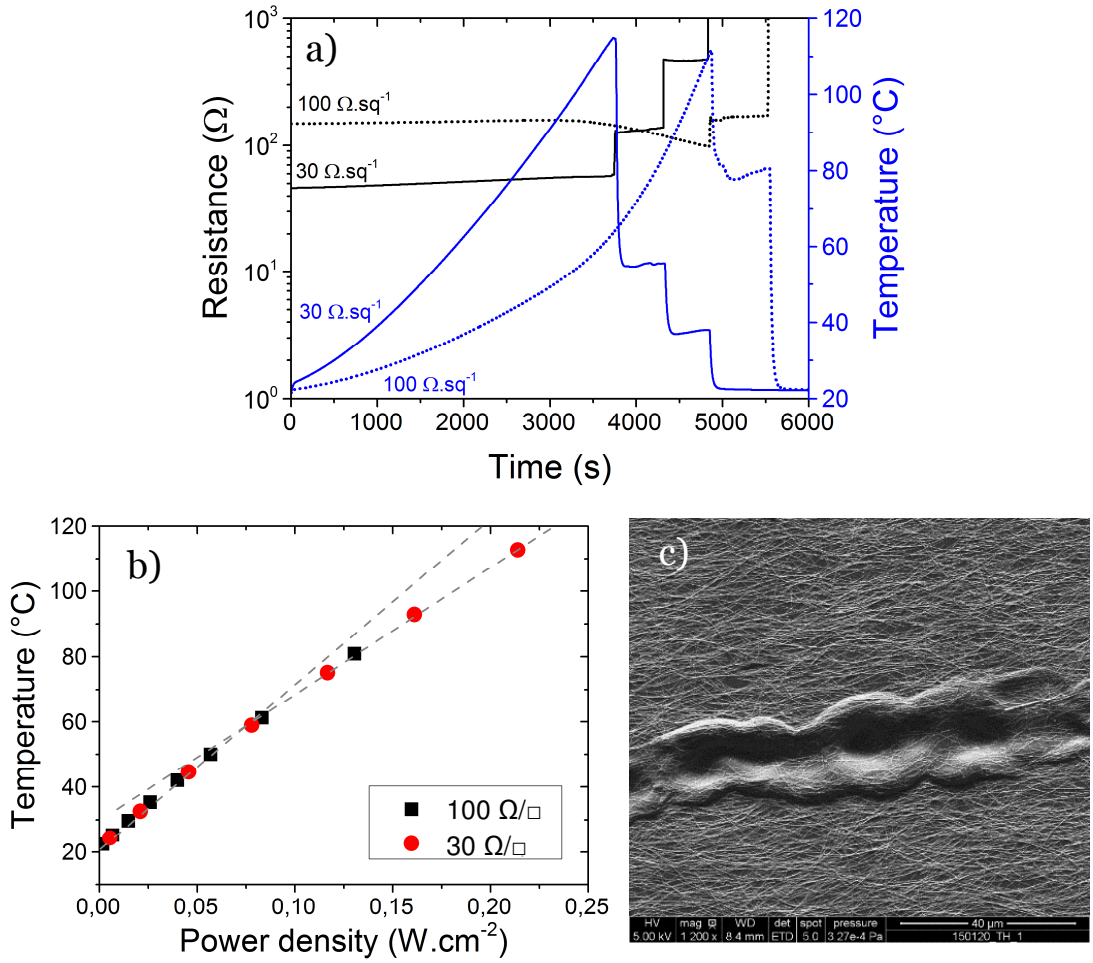

Figure 5-7: a) Influence of AgNW sheet resistance on the resistance and temperature behavior during a voltage ramp of 0.1 V.min⁻¹ b) Temperature achieved by the samples at different power densities leading to an estimation of the heat transfer constant α c) SEM image of a AgNW network deposited on PEN, after instability caused by electrical stress. It shows the degradation (partial local melting) of the substrate due to the high temperatures undergone by the sample.

During this thesis, several voltage ramps were performed on different samples. Therefore we were able to calculate α for each of them. Samples made from Ag117 (spin coating, c=0.5g.l^{-1}) had the lowest values: between 19 and 23 W.m^{-2}.K^{-1} (3 samples). Then, Ag45 spin coated (c=0.75 g.l^{-1}) with values between 23 and 25 W.m^{-2}.K^{-1} (2 samples), and then spray coated Ag45 (c=0.5g.l^{-1}) with values between 33 and 35 W.m^{-2}.K^{-1} (2 samples). These results are presented in Figure 5-8, which also gives information on the transmittance of the sample as well as its resistance (2 points) before the ramp. The fact that the heat transfer constants are similar for samples that were deposited with the same conditions (therefore they have similar nanowire density and coverage), even when having very different resistances, shows the dominance of network density on heat losses over the resistance. For this purpose the most impressive samples are those of Ag45 spray coated, having the same heat transfer constant even if one has a resistance of 27 Ω, and the other 434 Ω. Figure 5-8 seems to illustrate a tendency of an increase of α when the nanowire length decreases. Reducing the nanowire

length induces a need of a higher density of nanowires to obtain efficient networks (see the dependence of the critical density in percolation regime with the nanowire length). The dense networks might therefore induce more losses by convection or radiation, explaining the increase of α.

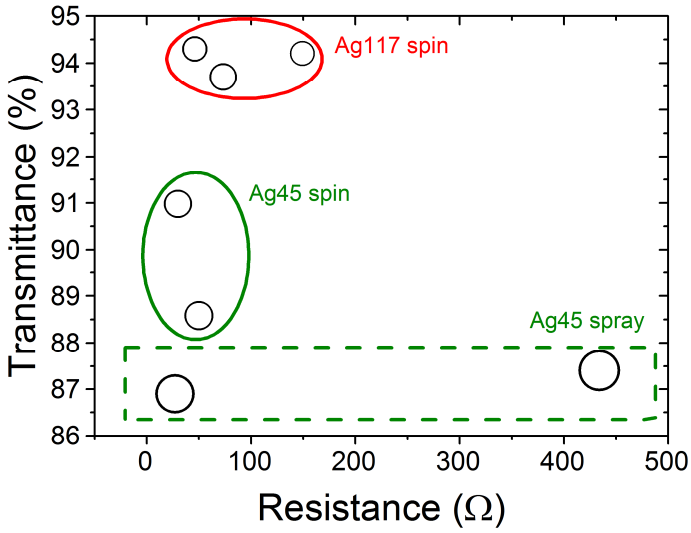

Figure 5-8: Heat transfert constant of AgNW network with various fabrication conditions. The ciircle size are proportional to α: between 19 and 23 W.m⁻².K⁻¹ for spin coated Ag117, between 23 and 25 W.m⁻².K⁻¹ for spin coated Ag45, and between 33 and 35 W.m⁻².K⁻¹ for sprayed Ag45.

One would expect from the results of the present section that to optimize a thermal heater and allow it to operate at low voltage, it is preferable to have a low nanowire density and to reduce the network resistance as much as possible. This can be made by thermal annealing or with the different methods presented in Chapter 3, and choose samples with the highest Haacke FoM.

5.1.5 Influence of convection

To have a quantitative estimation of the heat losses by convection, experiments on Joule effect within AgNW networks have been performed under vacuum or in air, and compared. A sample made of Ag45 by spray coating on transparent Kapton (2x2 cm²) using the standard routine has been fabricated for this purpose, and its resistance was reduced by thermal annealing (175°C for 30 min). After annealing the sheet resistance was around 20 Ω/□ and the transmittance 73.8% (86.9% without substrate). The initial resistance with 2 points was more around 28 Ω, probably due to the sample geometry and the setup contacts. Then the sample was optimized electrically by tension steps or ramp, but never exceeded 6V. That way, we could play with Joule effect (at tensions lower than 6 V) without inducing more irreversible effects on the resistance, and only the increase of resistance due to phonon-electron interactions could be observed.

Some stepped electrical annealing has been performed on the sample: steps of 5 minutes at tensions 1, 2, 3, 4 and 5 V, and then the same for descending tensions. This experiment allows to see the reversibility of resistance during the process and proves the observation of phonon-induced temperature increase only. This experiment has been performed in air and under vacuum. The resulting temperature variations, shown in Figure 5-9a, shows a clear higher increase of temperature during the experiment performed under vacuum, which is also observable on the resistance (not displayed). The response time during this experiment is displayed in Figure 5-9b.

Unlike the tendency discussed in the section 5.1.4.ii, the experiment allowing the highest stabilized temperature (here, under vacuum) have actually the longest response time (almost half of the one in air when a tension of 5 V is applied) which can be understand as follows. Equation 5-2 was used to fit the experimental data, in Figure 5-9c and d. As reported in Figure 5-9c, a fairly good agreement is observed, except for temperatures higher than 60°C. The disagreement at high temperature originates from the linearization of the radiation term which is only valid at low temperature, since:

$$\sigma(\Delta T + T_0)^4 - \sigma {T_0}^4 \cong 4\sigma {T_0}^3 \Delta T \left(1 + \frac{3}{2}\frac{\Delta T}{T_0}\right) \qquad (5\text{-}9)$$

The first nonlinear term is negligible (for instance < 0.2) as long as ΔT < 40°C. As well for high temperature range the conduction loss term (towards external parts of the system) should not be negligible anymore. A way to rewrite Equation 5-2 leads to:

$$\Delta T = \frac{P}{\alpha}\left(1 - e^{-t/\tau}\right) \qquad (5\text{-}10)$$

Where P is the areal power density and $\tau = \frac{mC}{A\alpha}$. Therefore the time derivative of ΔT(t) is:

$$\dot{\Delta T} = \frac{P}{mC} e^{-t/\tau} \qquad (5\text{-}11)$$

The decrease of temperature elevation rate can be associated to a characteristic time, $t_{1/2}$, for which the rate is half of its maximal value. $t_{1/2}$ can then be expressed as:

$$t_{1/2} = \ln 2 . \frac{mC}{\alpha A} \qquad (5\text{-}12)$$

The difference between the experiments in air and in vacuum originates from the presence or absence of the convection losses. From Equation 5-3, we can write:

$$\alpha^{air} = (h_1 + h_2) + 4(\varepsilon_1 + \varepsilon_2)\sigma {T_0}^3 \qquad (5\text{-}13a)$$

$$\alpha^{vacuum} = 4(\varepsilon_1 + \varepsilon_2)\sigma {T_0}^3 \qquad (5\text{-}13b)$$

So $\alpha^{air} > \alpha^{vacuum}$ and then, from Equation 5-12, ${t_{1/2}}^{air} < {t_{1/2}}^{vacuum}$, therefore the characteristic time is expected to be smaller in air than in vacuum. This is in good agreement with experimental data displayed in Figure 5-9b.

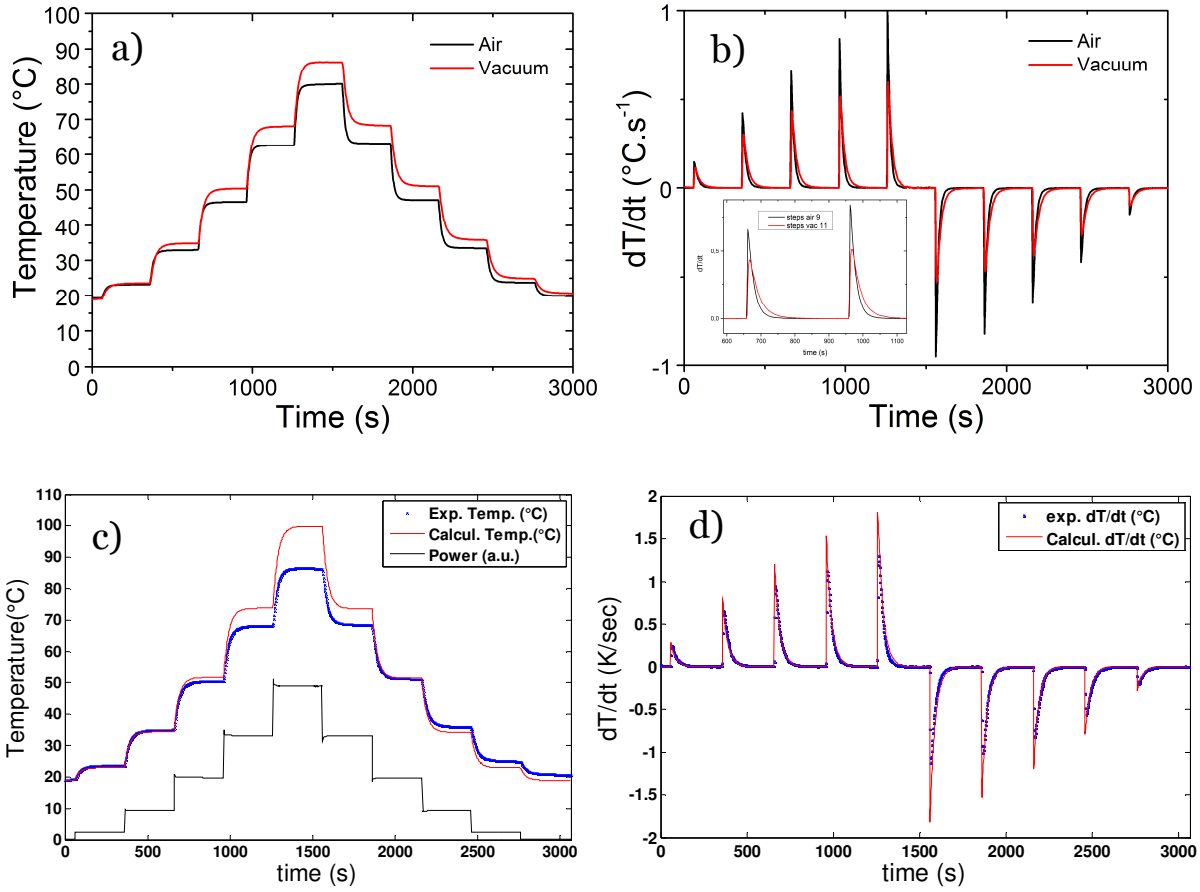

Figure 5-9 : a) Voltage steps of 1, 2, 3, 4, 5 V and reverse on the same sample at air and then under vacuum b) Corresponding dT/dt versus time c) experimental time variation of the temperature (blue curve, same data than Figure a, in vacuum) and applied power (black) related to AgNW network, with numerical fit adjusted at low temperatures using Equation 5-10 (red; the discrepancy at higher temperature is explained in the text) d) experimental and fit (using Equation 5-11) of the time derivative of the temperature during the experiment presented in Figure c.

Then, voltage ramps of 0.1 V.min^{-1} experiments were performed on the same sample in air and under vacuum, up to 5 V. The resulting temperatures are displayed in Figure 5-10a. Once again, the temperatures achieved under vacuum are higher for a specific voltage. After these experiments, a graph plotting the achieved temperature against the areal power density input to the sample was made and is displayed in Figure 5-10b. All the data from voltage ramps (0.1 V.min^{-1}) or steps are plotted and they are mingled into two lines: one for experiments under vacuum and the other in air. The first observation is therefore that the ramp rate is sufficiently slow to lead to the same temperature/resistance at a specific voltage that would have been achieved with a step at this voltage. Then, a clear difference in slopes is observed which illustrates the heat losses by convection. By calculating the slopes of each of these linear curves, the heat transfer constant α can be calculated. Therefore the heat losses by convection, canceled when experiments are performed in vacuum, can be extracted from the α difference between vacuum and air experiments. In Figure 5-10b, the slopes of the temperature dependence on the power density are well separated, and α was found to be 25 and 30.5 W.m^{-}

$^{-2}$.K^{-1} in vacuum and in air, respectively, which is consistent with values found in literature.[7] Therefore an estimation of the heat losses by convection could be calculated by subtraction, and, from Equation 5-3: $(h_1 + h_2) \approx 5.5$ W.m^{-2}.K^{-1} (convection losses). Therefore it seems that, although both radiative heat losses and convection heat losses are significant in the heat losses process of AgNW networks, it seems that radiative heat losses are dominant.

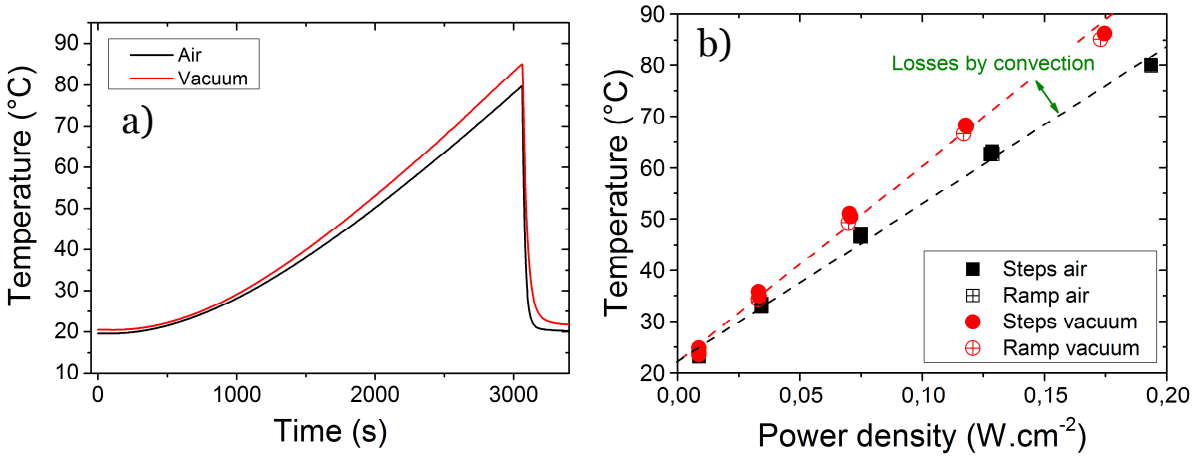

Figure 5-10: a) Voltage ramp of 0.1 V.min^{-1} on the same sample at air and then under vacuum. The ramps were stopped after a voltage of 5 V was reached b) areal power density dependence of the temperature during the experiments shown in the Figure 5-10a and Figure 5-9a.

To briefly summarized section 5.1, we have seen that AgNW networks can behave as efficient transparent heaters. Simple physical models (developed in more details in Sorel's paper [7]) show that the experimental temperature variations can be well understood and a comparison between experiments in air and vacuum enabled us to determine the convection contribution. However we have seen as well that non reversible features can be observed and this could be detrimental for device integration of AgNW networks if used as a transparent heater. The next section is addressing these non-reversible features and the electrical instability with an approach partially similar to the one presented in chapters related to thermal instability, dealing with both its physical origin and a way to prevent it.

5.2 Electromigration and electrical stability solutions

Applying a voltage to a AgNW network induces phenomena such as electromigration. The latter can cause a destruction of the materials used as electronic pathways, and is common in integrated circuits[16]. Electromigration can be defined as the motion of atoms induced by an electrical current and is driven by electron collisions (wind force) or electric field (direct force). This phenomenon is a key issue considering the size of interconnects in electronic devices and also for AgNW-based TE. It especially influences the device lifetime. Electromigration is

exacerbated for small size elements due to the increased current density forced by the material small cross section.

In this section, the effects of electromigration on AgNW are studied, and an efficient solution will be proposed to overcome this problem.

5.2.1 Few words on electromigration

Electromigration can be defined as the motion of atoms by a current flow, which induces what is called the "wind force" or an electric field, inducing the direct force[17]. It is a problem for small interconnects such as nanowires for which electrical breakdown is easier compared to bulk considering the low amount of atoms. Khaligh and Goldthorpe[18] estimated that AgNW would fail within few days when integrated as a TE in a solar cell. However they couldn't validate if the failure was due to thermal or electrical effect as atomic diffusion is enhanced at high temperature. Moreover the authors performed this investigation without using a method for preventing such failure (for example by coating with a metal oxide layer).

Wind force and direct force have opposite directions. The wind force leads to vacancy diffusion due to inelastic scattering between conduction electrons and atomic cores and induces a mass transport in the direction of the electron flow (cathode to anode). The direct force is caused by the electric field interacting with atoms that are not completely shielded by electrons, inducing a mass flow in the opposite direction (anode to cathode). Stahlmecke *et al.*[15] identified the formation of void at the anode and hillocks at the cathode when a voltage difference is applied at the extremities of a single nanowire (current around 20 mA, therefore a current density around $3 \cdot 10^{10}$ A.m^{-2} considering the nanowire dimension in Figure 5-11). They also observed that when the current direction is reverse, the void formation occurs on the other extremity.

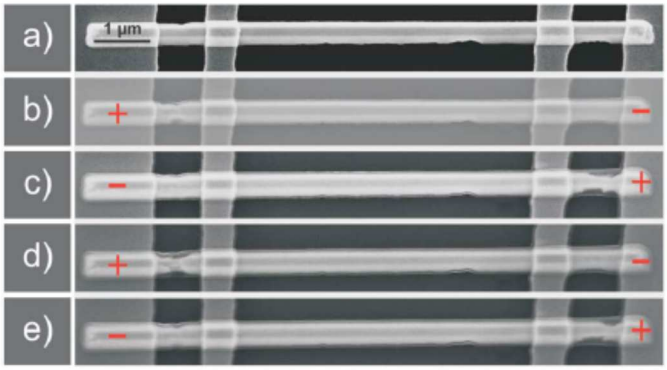

Figure 5-11: Void formation in single crystalline AgNW due to current flow.[15]

Kaspers *et al.*[17] could identify the dominance of each force depending on the material crystallinity. They observed a dominance of the wind force for polycrystalline silver, illustrated

by the dominance of grain boundary diffusion. For single crystalline silver, instead of grain boundary, surface diffusion is dominant. They could also prove that electromigration occurs in vacuum as well. Electromigration can also be beneficial to a sample conductivity. Song *et al.*[19] could prove that electrical sintering occurs at a single junction by electrical current treatment, and could decrease R from 10^{10} to 185 Ω, as illustrated in Figure 5-12. But once again, the sintering might be due to a local increase of temperature due to Joule heating. They assumed that the heat is localized at junctions since $R_{junction} >> R_{NW}$. That was experimentally shown by Maize *et al.*[20]

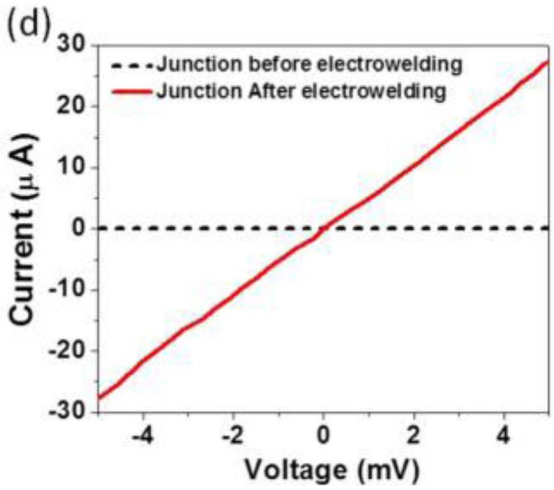

Figure 5-12: Electrosintering of a single AgNW junction by Song et al.[19]

5.2.2 Electrical instability of AgNW-based transparent electrodes

Similarly to thermal annealing, an electrical current can induce instability within AgNW networks and is a key issue considering the applications that need high current densities.[18] To investigate the failure voltage of our networks, we performed voltage ramps, typically 0.1 $V.min^{-1}$. The tested samples were made with Ag45 by the spray standard fabrication conditions on glass, (sample size 1.25*1.25 cm^2), and the electrodes were made by evaporated silver, spaced with 0.7 cm. The samples underwent a thermal annealing at 200°C for 2h in order to reduce their resistance and have different samples with the same initial resistance. The resistance behavior of the samples during these voltage ramps is displayed in Figure 5-13a. The failure voltage for these samples occurred typically between 6 and 8 V. The corresponding power densities were within the range 2.6 ± 0.8 $W.cm^{-2}$.

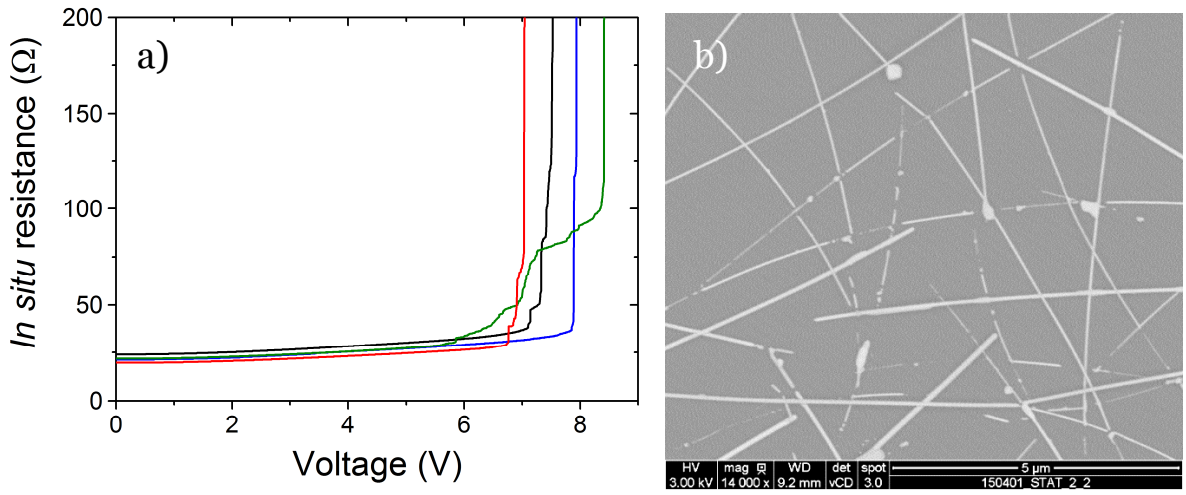

Figure 5-13: a) Electrical instability of similar sprayed Ag45 networks on glass with a voltage ramp of 0.1 V.min^{-1} b) SEM image of a Ag45 network after electrical failure.

A way to calculate the electrical current density at which failure is observed can be the following: Figure 5-14a exhibits a schematic of a random network composed of AgNW. For rather dense networks (*i.e.* associated with density much larger than critical density n_c), the equipotential, shown in Figure 5-14a as the dashed line, is in first approximation parallel to the external electrodes. The latter are separated by a distance W, between which a voltage V is applied. This equipotential is therefore perpendicular to the electric field $\vec{E}$. If the length between two junctions of a given AgNW is called L_n (as depicted in Figure 5-14b), and this AgNW is placed in an electrical field $\vec{E}$, with an angle θ_n, then the potential difference ΔV_n across this part of the AgNW can be written as:

$$\Delta V_n = E.L_n.\cos(\theta_n) \qquad (5\text{-}15)$$

Thanks to the randomness of both θ_n and L_n, the mean potential difference value $<\Delta V>$ can be calculated as:

$$< \Delta V >= E < L_n >< \cos\theta_n >= E < L_n > \frac{2}{\pi} \qquad (5\text{-}16)$$

The mean electrical current $< I >$ passing through an individual AgNW of conductivity σ ($=\frac{1}{\rho}$) in between two junctions can then be written as:

$$< I >= \frac{<\Delta V>}{R_{NW}} = \frac{<\Delta V>\cdot S}{\rho_{NW}\cdot<L_n>} = \frac{E}{\rho}\frac{2}{\pi}S \qquad (5\text{-}17)$$

And the mean electrical current density is given by:

$$< j >= \frac{2}{\pi}\sigma E = \frac{2}{\pi}\frac{V}{\rho_{NW}\cdot W} \qquad (5\text{-}18)$$

Equation 5-18 is simply the usual local Ohms law ($j = \sigma E$) except with a coefficient in front which is smaller than unity since not all AgNW are aligned with the electrical field E. This

prefactor, equal to $\frac{2}{\pi}$ for perfectly random networks, should be replaced by $< \cos\theta_n >$ for a non-isotropic network. For instance, for a spin coated sample or in the presence of coffee stains, local heating at some spots should occur since the prefactor could exhibit large non spatial homogeneities: a fact which could be rather detrimental for the specimen lifetime.

Applying Equation 5-18 for V = 8 V, W = 7 mm and $\rho^{Ag45} \sim 1.5\ \rho^{bulk}$ (see Chapter 4) then the theoretical value for the current electrical density at failure is $3.1 \cdot 10^{10}$ A.m^{-2}. This value is more close to the current density that induced electromigration (but not nanowire breakdown) in the paper from Stahlmecke *et al.*[15]. The diameter of the nanowire we used, 10 times thinner than the one presented in Figure 5-11, would however break at such high current density considering the stronger impact of electromigration when the surface to volume ratio increases.

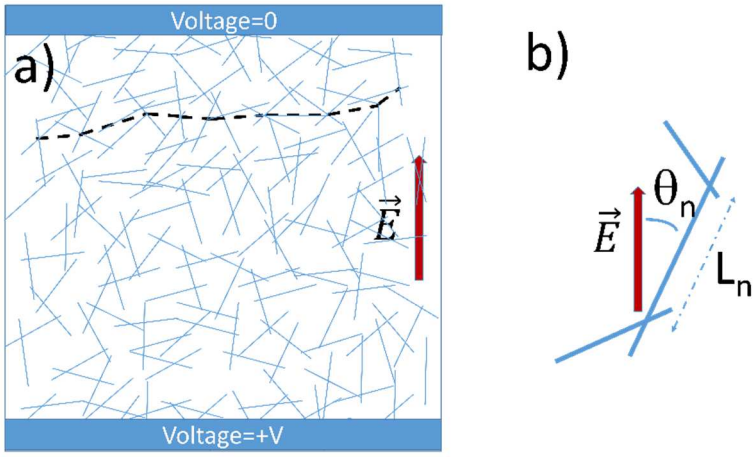

Figure 5-14 : a) Diagram showing an equipotential across a AgNW network submitted to an applied voltage V b) schematic of the angle formed by a nanowire with an electrical field $\vec{E}$.

5.2.3 TiO_2 protection against electrical failure

In order to limit the noxious effects of electromigration on AgNW networks electrical properties, they were coated with a thin layer of TiO_2 using ALD, with the same conditions explained in Chapter 3. The TiO_2 layer indeed showed really good results as AgNW thermal stabilizer and we will now test it against electrical failure. The resistance behavior during a voltage ramp performed at 0.1 V.min^{-1}, until electrical failure, of an AgNW network (sprayed Ag45) was compared with the resistance behavior of a similar network coated with TiO_2. The results are displayed in Figure 5-15. As can be seen in Figure 5-15, the voltage inducing electrical failure went from 7 to 13 V. TiO_2 coating therefore allowed to improve the electrical stability of the networks and doubled the failure voltage, without inducing a large change in transmittance (see Chapter 3). Equation 5-18 can be used to calculate the electrical current

density at failure for networks coated with TiO_2. The failure voltage is this time situated around 13 V, therefore the electrical current density at failure is around 5.0 10^{10} $A.m^{-2}$. Therefore the presence of TiO_2 seems to have increase the electrical stability of the networks to higher current densities (without TiO_2, the current density at failure was 3.1 10^{10} $A.m^{-2}$).

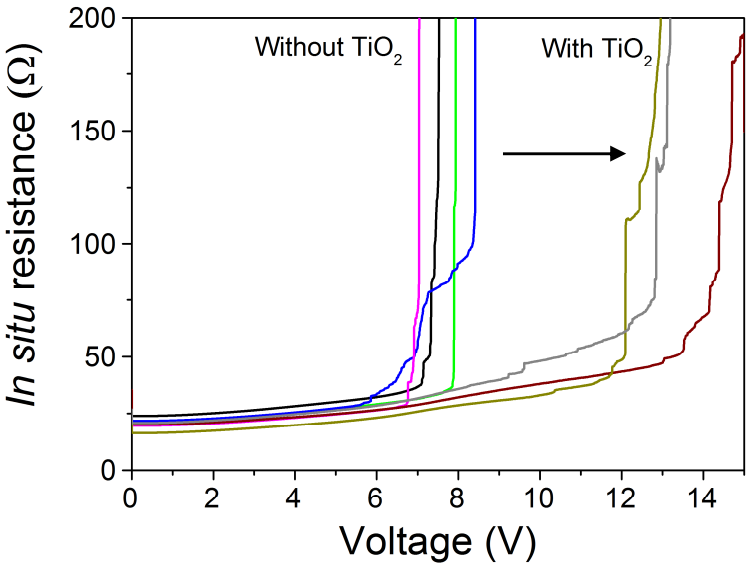

Figure 5-15: Electrical resistance of Ag45 networks submitted to a voltage ramp of 0.1 $V.min^{-1}$: comparison between uncoated samples, and samples coated with 5 nm of TiO_2 by ALD.

In order to validate the use of TiO_2 for applications as an electrical but also thermal stabilizer, it is important to know if it can be applied to flexible samples. Therefore Ag45 samples coated with TiO_2 were tested on the mechanical bending bench presented in Chapter 2 and which is depicted, in Figure 5-16a. Several experiments were made: first we tested the resistance stability *in situ* while bending for 2000 cycles with a radius of curvature around 1.4 cm. The resulting resistance, measured with a voltage V = 0.1 V, is shown in Figure 5-16b and attests the mechanical stability of the sample. After 2000 bending cycles (equivalent to approximately 1h40), the resistance increase was less than 0.5% of the initial resistance. Therefore the TiO_2 layer doesn't alters the mechanical stability of AgNW networks.

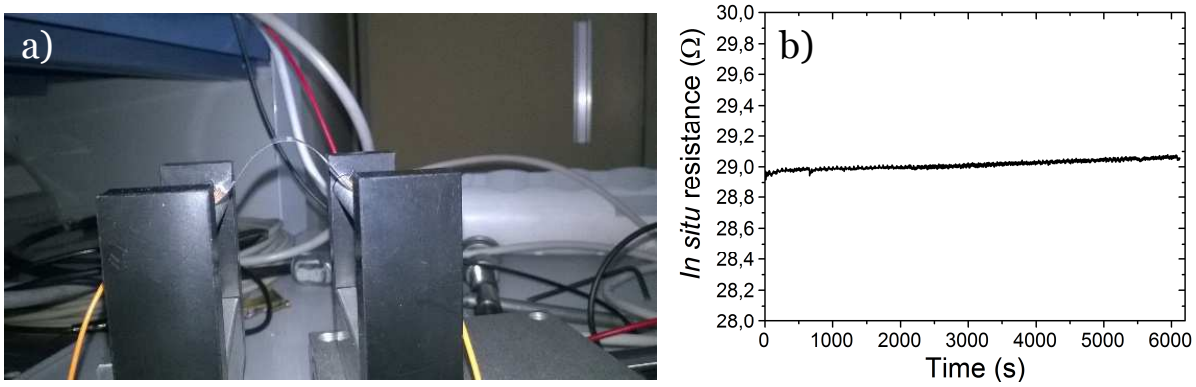

Figure 5-16: a) Mechanical bench to test bending stability of TiO_2-coated samples b) Resistance of the sample measured during 2000 bending cycles with radius of curvature of 1.4 cm.

Another test to validate TiO_2 use for transparent heaters application is to apply an operating voltage while bending. The results have been displayed in Figure 5-17a, where one experiment with voltage increase to 1 and 3 V and then back to 1 V on a flat sample is compared with the same experiment but on a sample mechanically bent with cycles of radius of curvature around 1.4 cm (one cycle every 3s, approximately). Once again the resistance stayed quite stable, even when the sample is bent. The temperature couldn't be measured during the experiment but considering the previous experiments on Joule effect in AgNW networks presented in this document, one would expect that a stable resistance induces a stable temperature. However a question that could be addressed is whether the temperature is uniform across the sample while bending.

The same sample has then been used for the same type of experiment but this time went up to 5 V. The "flat" (not bent) experiment was performed first, before the "cycled" one (*in situ* measurement during bending). Both are displayed in Figure 5-17b. One can observe the difference in resistance, the "flat" being higher than the "cycles". This can be explained by electrical sintering that certainly happened at 5 V during the first experiment ("flat"). Therefore for the second one ("cycles"), the resistance was lower at the beginning of the experiment. Although mechanical bending don't have an impact on the samples resistance, the voltage application can change it irreversibly, even with a TiO_2 protecting shell.

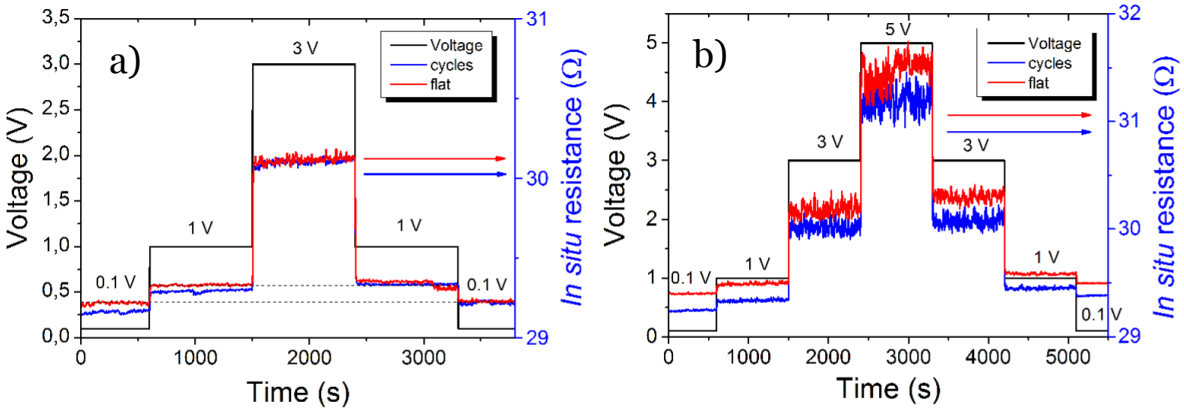

Figure 5-17: Mechanical flexibility of TiO_2 coated AgNW network and heating while bending a) Electrical resistance measured in situ *during voltage application at 1 and 3 V on a flat sample and on a bent sample, during bending cycles b) same experiment at 1, 3 and 5 V.*

5.2.4 Electrical versus thermal treatment

We just discussed that applying a current to a AgNW network can induce resistance reduction. It is difficult to separate the effects of electromigration and those, induced by Joule heating (associated to local sintering) on this phenomenon. In order to investigate the role of each mechanism, and look at the effects of electrical sintering only, the setup presented in Figure 5-18a, with a schematic view in Figure 5-18b was built to cool down the samples with ice during experiments, and therefore cancel any thermal effects on the sample.

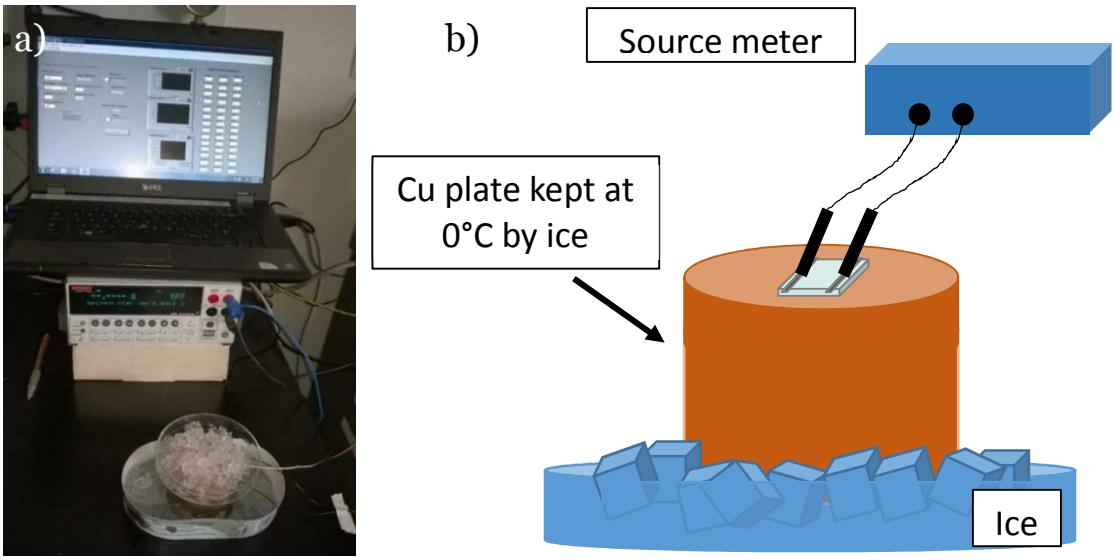

Figure 5-18: a) Photograph of the setup used to apply a voltage to a sample while cooling it with ice b) Diagram of the cooling system.

Various voltages were applied to a Ag117 sample made by spin coating (c = 1 $g.l^{-1}$) on Corning glass with size 3x2.5 cm^2. The resulting samples resistance during the process is displayed in Figure 5-19a. The experiment shows that the samples resistance can be reduced

only by voltage application, while the sample stays at a temperature below 5°C, and that increasing voltage induces further resistance decrease. The sample was then observed under SEM after the experiment and, while it looked normal in the center, as shown in Figure 5-19b, some surprising structures were visible close to the contact electrodes, as shown by the SEM images in Figure 5-19c and d. The presence of these structures hasn't been clarified yet.

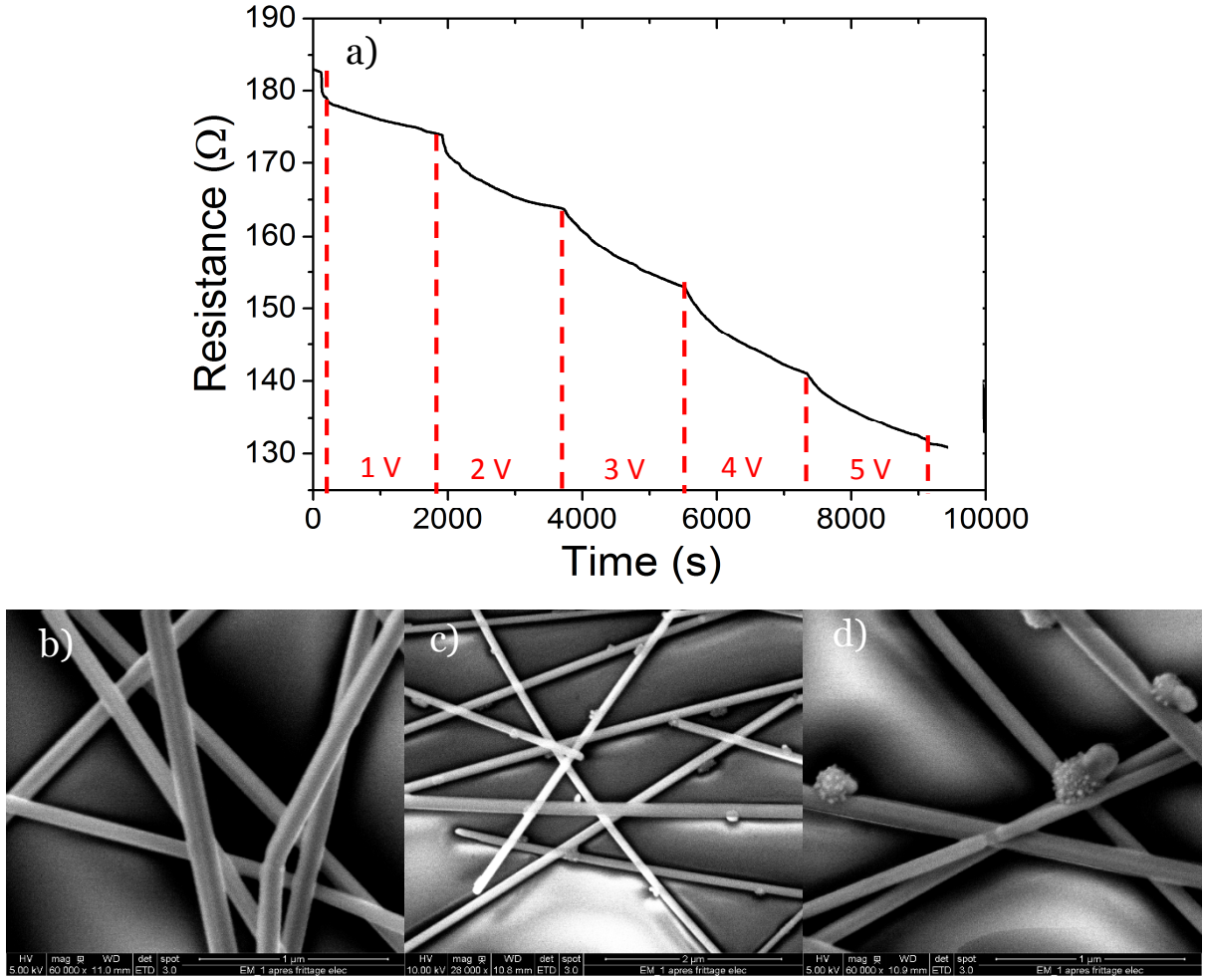

Figure 5-19: a) Resistance measured during application of different voltages on a sample while its temperature is kept close to 0°C by ice cooling b) SEM image of the nanowires at the center of the sample after treatment c) nanowires morphology close to the contact electrode after treatment d) zoom on structures grown during the treatment.

Further experiments have been performed with the cooling setup. One similar sample to those presented in section 5.2.2 was used in the same purpose of electrical failure study, *i.e.* applying a voltage increasing by 0.1 $V.min^{-1}$ until the sample electrically fails, but this time it was cooled close to 0°C. The resulting resistance, displayed in Figure 5-20, shows that the sample was stable at higher voltage and became unstable around similar voltage that the sample coated by TiO_2. This observation shows that ice is not sufficiently cold to protect the

sample at high voltage but could slow down the process of instability by thermal surface diffusion.

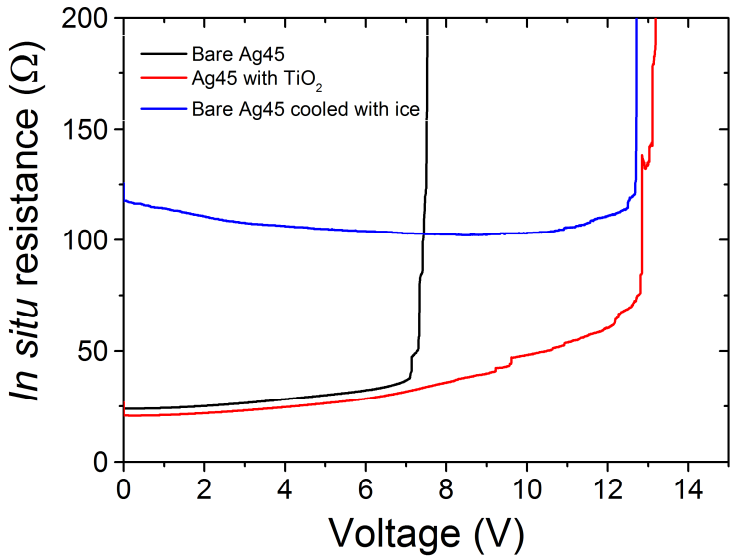

Figure 5-20: Electrical ramp of 0.1 V.min^{-1} applied on Ag45 samples: bare, cooled with ice and coated with TiO_2.

Some experiments were performed on uncoated samples in liquid nitrogen in order to cancel any thermal effect, and see only the electrical effects. Thermal ramps, steps, and long term annealing were performed, and the (as deposited) samples resistance was measured *in situ*. The resulting resistance behavior is displayed in Figure 5-21a. It shows that a large current (1 A) could be applied to the electrodes without damaging them. After the treatment, the morphology of the networks was observed under SEM. No significant change or deterioration is visible, as shown in Figure 5-21b, compared to a sample that underwent a voltage ramp of 0.1 V.min^{-1} performed at room temperature (Figure 5-21c). This experiment clearly shows that, at short term at least, the thermal effects plays a dominant role in the instability of the nanowires compared to the electrical effect: a current as high as 1A have never been sustained by the networks at room temperature.

It could be interesting, in future experiments on the topic, to set different temperatures by using ice, liquid nitrogen *etc*... to study the networks behavior while the thermal effects are controlled.

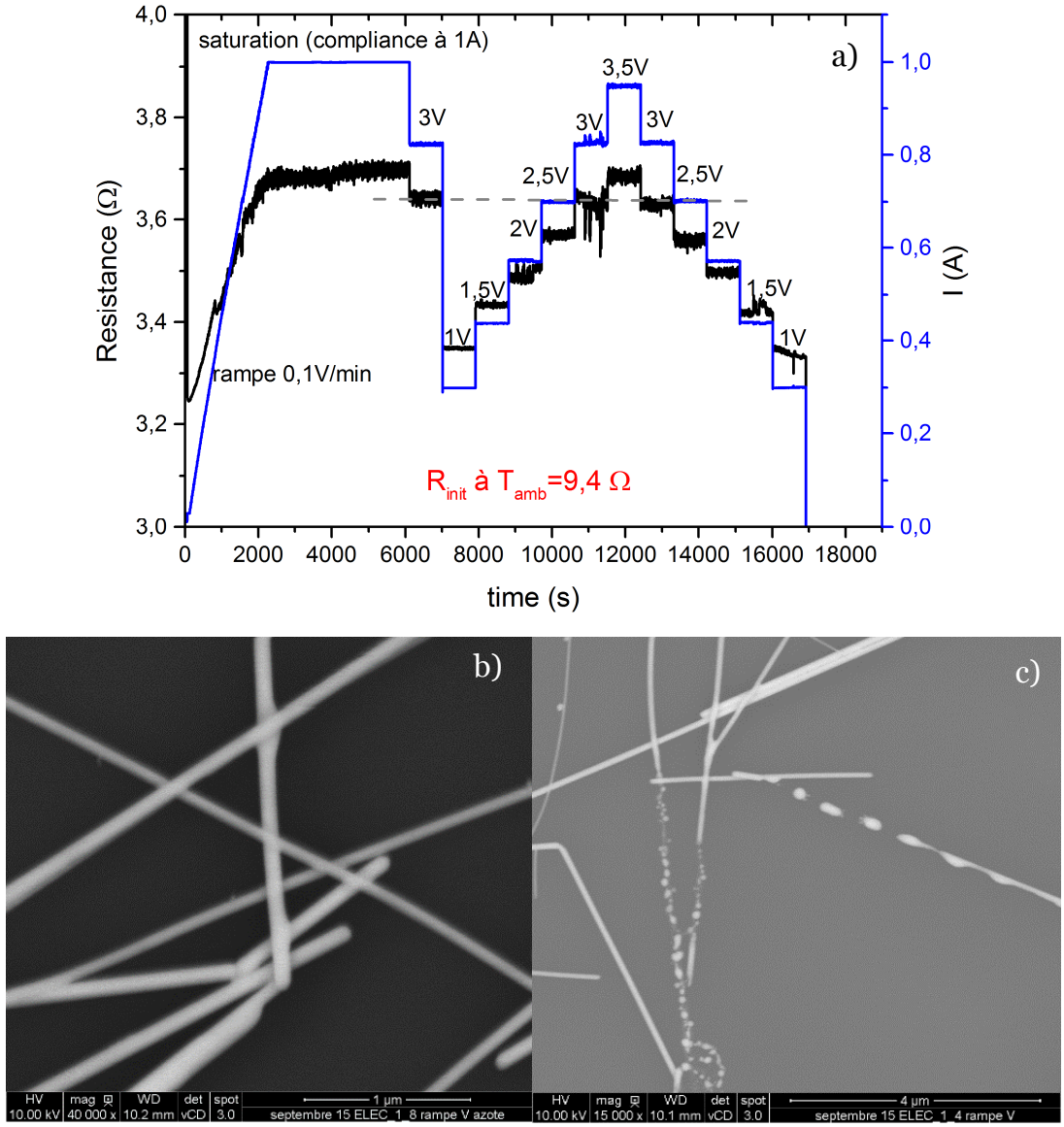

Figure 5-21: Electrical behavior of an Ag45 sample, uncoated, during different thermal annealing in liquid nitrogen. A current as high as 1 A was reached and sustained for more than 1 hour b) SEM image of the sample after these treatments: no damaging c) SEM image of an uncoated sample that underwent a voltage ramp of 0.1 V.min^{-1} at room temperature, for comparison.

5.3 AgNW networks for antennas and electromagnetic shielding

A recent collaboration between the LMGP and the Radio frequency and millimeter-waves team of IMEP-LaHC (Institute of Microelectronics, Electromagnetism, Photonics, and the Laboratory of Hyper-frequency and Characterization, Grenoble) has started in order to address the application of AgNW as RF antennas and electromagnetic shielding. The scientists involved in the collaboration are Prof. Tan-Phu Vuong, Prof. Philippe Ferrari and Alejandro Niembro (PhD student) from IMEP-LaHC, and also Thomas Sannicolo (LMGP - CEA Liten). The result of the experiments performed on this topic for the first time by the two laboratories, displayed

hereafter, should be considered as preliminary experiments which will be the subject of further investigations.

There are many potential applications concerned by such investigation. A non-exhaustive list concerns for instance defense and security, data protection, health, telecommunications, RFID identification/authentifications, which constitute large markets.

5.3.1 Electromagnetic shielding

5.3.1.i State of the art

As seen in Chapter 1, the use of AgNW for EM shielding was validated in the literature[22,23], as well as other materials such as CNT[24,25], graphene[26] and copper nanowires[27]. The scientific community works on transparent materials for EM shielding, for instance to allow the shielding of a complete room, windows included. All the works found in the literature, discussed in Chapter 1, are actually on opaque samples, except for Hu *et al.*[22], on silver nanowires. They obtained samples (PES/AgNW/PET) with transmittance at 76% coupled with a sheet resistance of 7.2 Ω/□, an EMI SE of -25, -30 dB between 8 and 12 GHz (see Figure 5-22). They also insisted on the attractiveness of nanomaterials with good conductivity and large surface area for EMI shielding considering the importance of the skin effect (electromagnetic radiation at high frequencies penetrates only the near surface of an electrical conductor) coupled with multiple reflections by the material on the shielding. They also discussed the fact that the sample resistance contributes more to the EMI SE compared to the density of NW on the sample, which opens the door for transparent materials, and to AgNW considering their good FoM regarding optical and electrical properties.

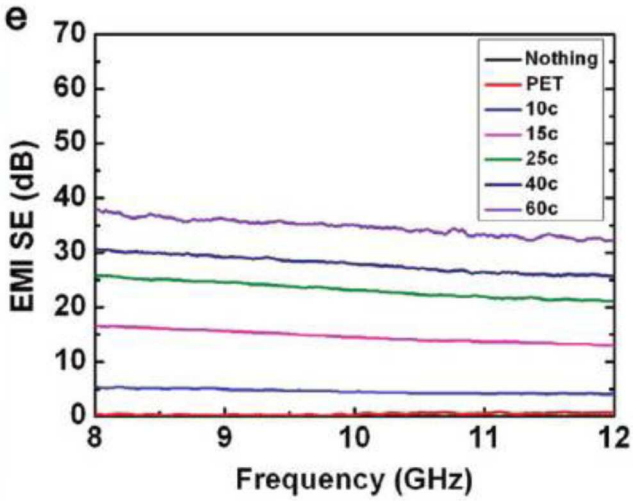

Figure 5-22 : EMI SE of AgNW network with various densities, from Hu et al.[22]

5.3.1.ii Motivations

The main axis of research on this topic was therefore to propose a material for electromagnetic shielding that could be transparent. Electromagnetic shielding is well known with non-transparent materials that can be used on walls, knowing that non-transparent material can be efficient and low cost for this purpose. Indeed IMEP (in collaboration with Paper Technical Center, CTP Grenoble) has worked on a lining that could filtrate some frequencies and could be used as a tapestry.[28] But what about windows? A transparent electromagnetic shielding would allow to isolate whole rooms from electromagnetic waves, without constraining electromagnetic waves-free places to rooms without windows.

5.3.1.iii Setup electromagnetic shielding and samples

In order to test the electromagnetic shielding capacity of different materials, a setup was developed by Alejandro Niembro in the anechoic chamber of IMEP-LaHC.[29] Two antennas, one receptor inside the chamber and one emitter outside, are spaced by 1 m, as shown in the diagram of Figure 5-23a. There is an empty window at mid-distance, in blue in Figure 5-23b where a sample with size A4 or A5 can be held to be studied. Then the difference between the power transmitted by the emitter antenna and the one received by the receptor is measured. The typical power transmitted was around 3 mW (5 dBm).

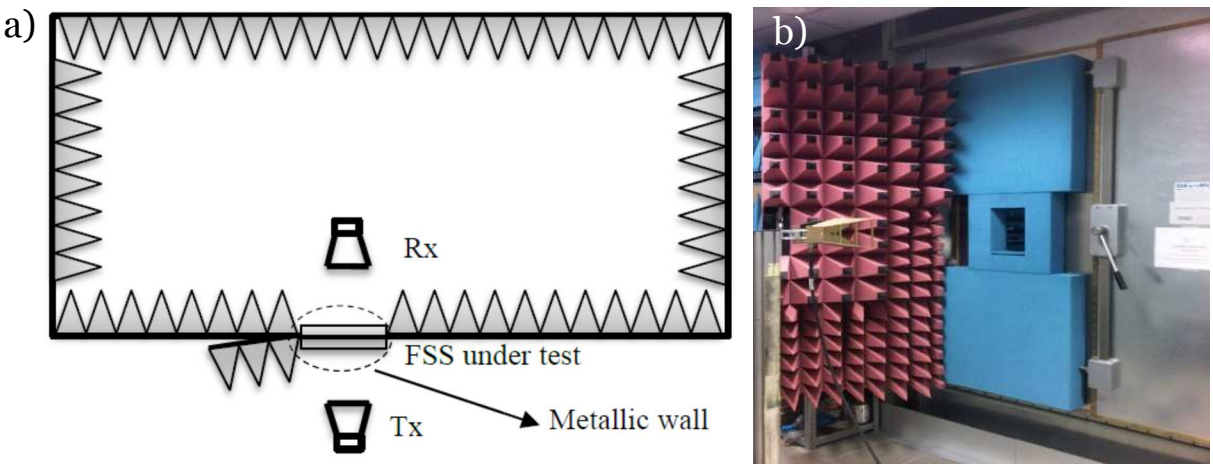

Figure 5-23: a) Schematic of the electromagnetic shielding setup at IMEP-LaHC b) Photograph of the setup, from outside the anechoic chamber. On the left of the image, the emitter can be seen, in blue the sample holder placed where normally stands the door of the anechoic chamber. The door can be seen with the red spikes on the left.

5.3.1.iv Results

For the study of AgNW, a large sample of size 22*32 cm² was deposited on glass by spray coating. We first tested a sample with 2 coats, after annealing at 200°C for 2h with a transmittance around 94%, network only (see Chapter 2 for the relation between number of

spray coats and transmittance for Ag45), considering that the sample was made with the spray standard routine with Ag45. But the resistance was too high (around 30 Ω/□), and the shielding not very efficient (see the red curve in Figure 5-24). Therefore 4 more coats of Ag45 were deposited on the sample to improve shielding by reducing the electrical resistance. The transmittance of the network alone is then estimated at around 81% and the resistance was measured to be around 10 Ω/□. The transmittance doesn't include the substrate which is 1 mm-thick, therefore thicker than the Corning glass we generally use. The resulting shielding was much more efficient, as can be seen in Figure 5-24 with values higher than 20 dB between 2 and 16 GHz. The sample seem to have a higher SE around 11 GHz, as could be also observed by Yu *et al.* [146] The presence of this peak however remains unclear and will be the subject of further investigations.

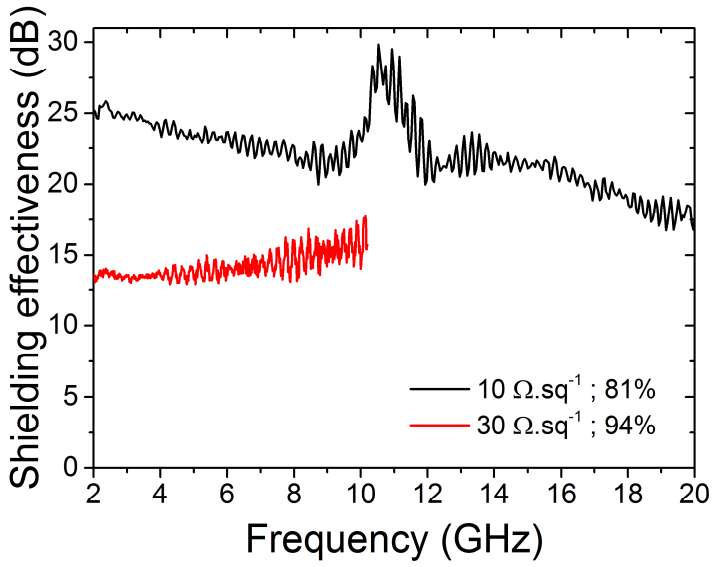

Figure 5-24: EM shielding efficiency of large sample made from sprayed Ag45 with two different densities.

5.3.2 Antennas

5.3.2.i State of the art

Transparent antennas have been studied at the beginning of the 21st century using ITO, FTO,[30] or TCOs in general,[31] metallic meshes,[32] AgHT (silver coated polyester film) or thin metallic films, with silver and gold being very promising.[33] The criterion of transparency was mainly introduced for aesthetics improvement but also for antenna integration into windows or optical displays and has been the subject of patents.[34] To our knowledge, transparent antennas made of AgNW haven't been reported in the literature. In Chapter 1, the interest of AgNW for antennas have been highlighted considering the change of resonant

frequency with tensile strain[35] or by folding.[36] In addition, AgNW are very attractive considering they are a light-weight material and present high transparency.

The use of 1D nanoparticules with high aspect ratio, and especially of AgNW for efficient antennas have been studied by Komoda *et al.*[37] They compared the capability of different materials to be used as antennas: AgNW, silver flakes, silver particles and etched copper foil. For printed lines such as the one presented in Figure 5-25a, they calculated the S_{11} parameter, called parameter of return loss, which indicates the loss of signal power caused by its reflection in a conductive line. They found that the return losses decrease with the decreasing material resistance but also that the aspect ratio of the material tends to decrease return losses. To illustrate this, Figure 5-25b shows that nanowires present the lower return losses even with a resistivity higher than copper foil, and Figure 5-25c shows the influence of the resistivity of AgNW printed lines: return losses decrease with resistance. The reason for these low losses seems to be related to surface roughness, AgNW having the lowest.

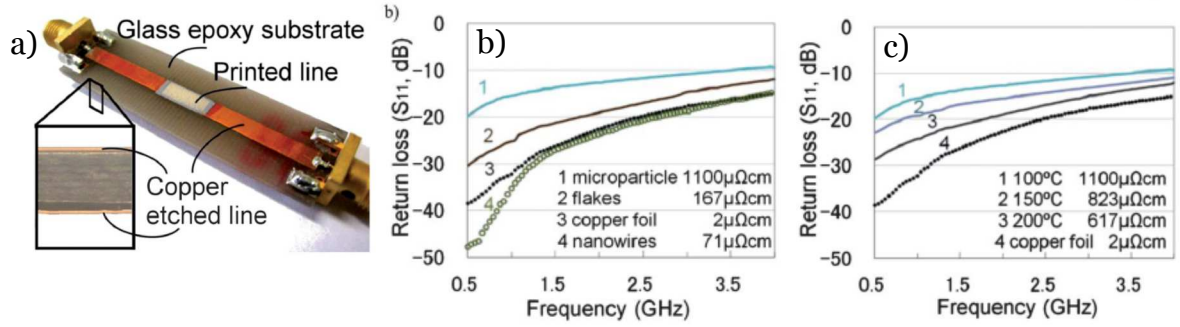

Figure 5-25: a) Example of a printed line b) Influence of the material type and their resistances on the S_{11} parameter c) Influence of AgNW network resistance on the S_{11} parameter and comparison with copper foil. [37]

Several quantities must be defined before going further in the antenna topic. First the radiation efficiency, which is the ratio of total power radiated by the antenna over the power that it accepted from the connected transmitter. Then the directivity is the maximum value of the power density radiated by the antenna in the direction of its strongest emission. Finally, the antenna gain can be seen as the product of the radiation efficiency with the antenna directivity. In a specific direction, the gain can be defined as the ratio of the radiation intensity in that direction to the mean radiation intensity of a perfectly efficient isotropic antenna. Radiation pattern can be made by plotting the gain as a function of the direction at a specific frequency, like those presented in Figure 5-26a and b, in the E-plane (plane containing the electric field vector, usually coinciding with the vertical plane) and the H-plane (magnetic field vector, usually coinciding with horizontal plane), respectively.

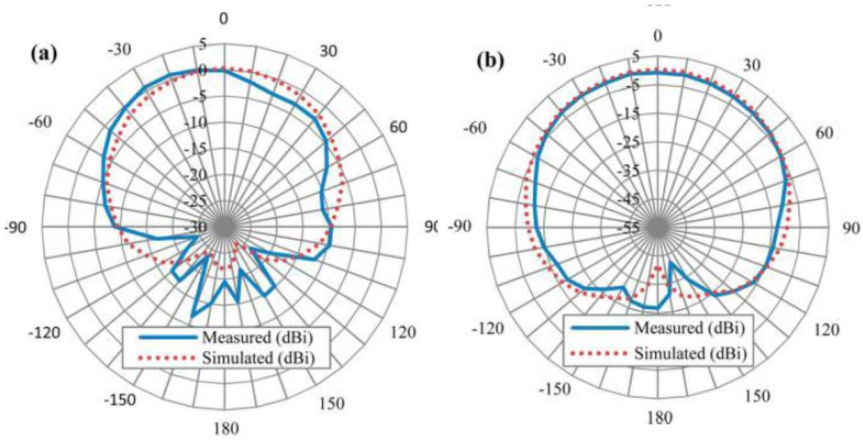

Figure 5-26: a) E-plane radiation pattern of a AgNW-based microstrip patch antenna at a frequency of 2.92 GHz b) H-plane measurement, from Song et al.[35]

5.3.2.ii Motivations

The collaboration between LMGP and IMEP-LaHC aims at building a project to fabricate efficient transparent antennas using AgNW networks. The project is for now very new but additional research axis will result from the preliminary studies presented below. To our knowledge, transparent antennas made from any metallic nanowire networks haven't been yet reported.

5.3.2.iii Sample fabrication

The samples were fabricated by depositing Ag45 by spray on glass. A copper stencil was used during spray deposition to obtain single patch shapes such as the one presented in Figure 5-27, with a transmission line coupled with a radiating element. The antenna was fabricated with 6 spray coats of Ag45 (transmittance 81% without substrate), and then annealed at 200°C for 2h to decrease the sheet resistance. The thermal annealing reduced the antenna sheet resistance to 3 Ω/□.

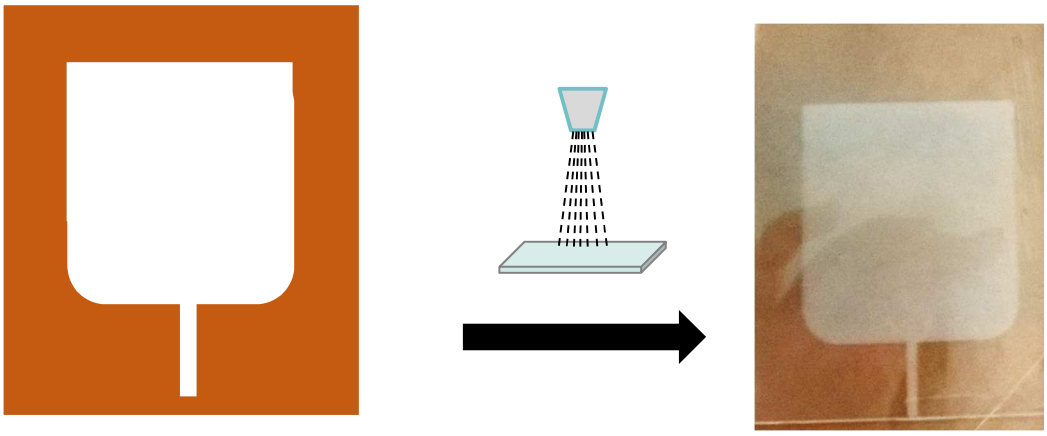

Figure 5-27: AgNW-based patch antenna fabrication

5.3.2.iv Antenna setup

First, the S_{11} parameter, *i.e.* the return losses, was determined at the IMEP-LaHC with the setup pictured in Figure 5-28a. It allows to know if a signal is transmitted or reflected by the antenna. If the signal is reflected (S_{11} is high), the signal won't be radiated by the antenna. The measurements also show the frequency at which the antenna is able to transmit the signal the most efficiently. Then the antenna's gain was measured in the anechoic chamber. The studied antenna was mounted as shown in Figure 5-28b (circled in red) across from a standard antennas, at a distance around 4 m. Then the gain is measured at various frequencies in the horizontal plane (0°) and in the vertical plane (90°). In addition, some simulations were made by Alejandro Niembro with a 3D electromagnetic simulator, CST Microwave studio, taking into account the antenna configuration, and in particular the network conductivity and the dielectric constant of the substrate, to fit with the experiments.

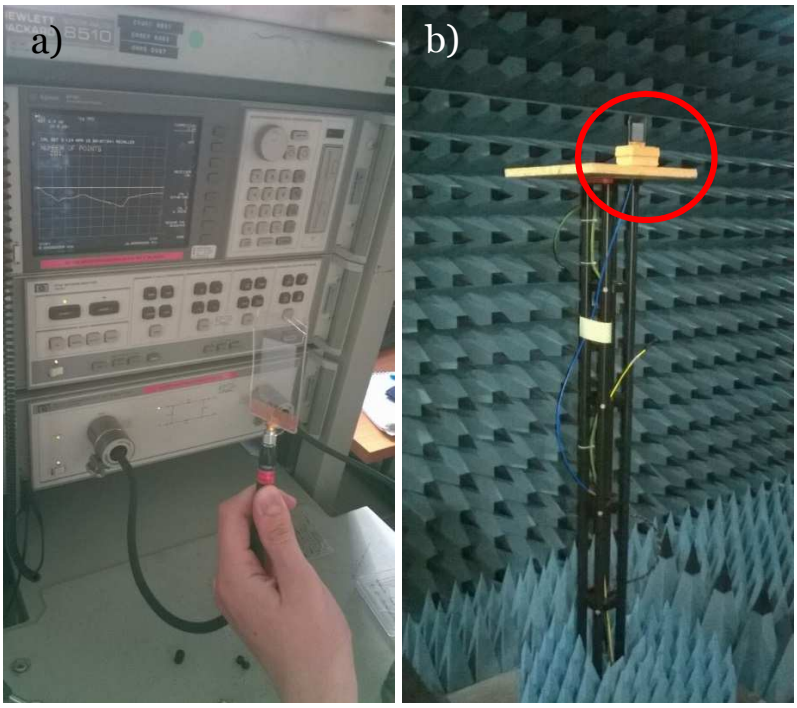

Figure 5-28: Antenna measurements of a) the return losses (S_{11} parameter) b) the gain.

5.3.3 Results and discussion

With the antenna described in section 5.3.2.iii, the results measured for the S_{11} parameter were very different from simulation. Only one resonant frequency was observed experimentally around 7 GHz while two were observed with the simulation at 2.2 and 7.5 GHz (data not shown). We thought that it might be due to the transmission line since the stencil was very narrow at this location, and we speculate that the density of nanowire that could be deposited there is lower compared to the one deposited on the radiating element. Therefore, in a second step, some silver paint was deposited on the place of the transmission line to allow

a maximum of signal to enter the antenna. With this change, the simulation fitted rather well, as can be seen in Figure 5-29a. Two resonant frequencies appear, the most demarcated one being close to 2 GHz (for the measured curve, and 2.2 GHz for the simulated one). Then the gain was measured in the anechoic chamber, and the results are displayed in Figure 5-29b. Unfortunately we couldn't achieve a positive gain, but the radiation diagram looks isotropic in the 0° plane, as expected by the simulation. Additional studies are needed to know how to improve the gain while keeping the antennas as transparent as possible.

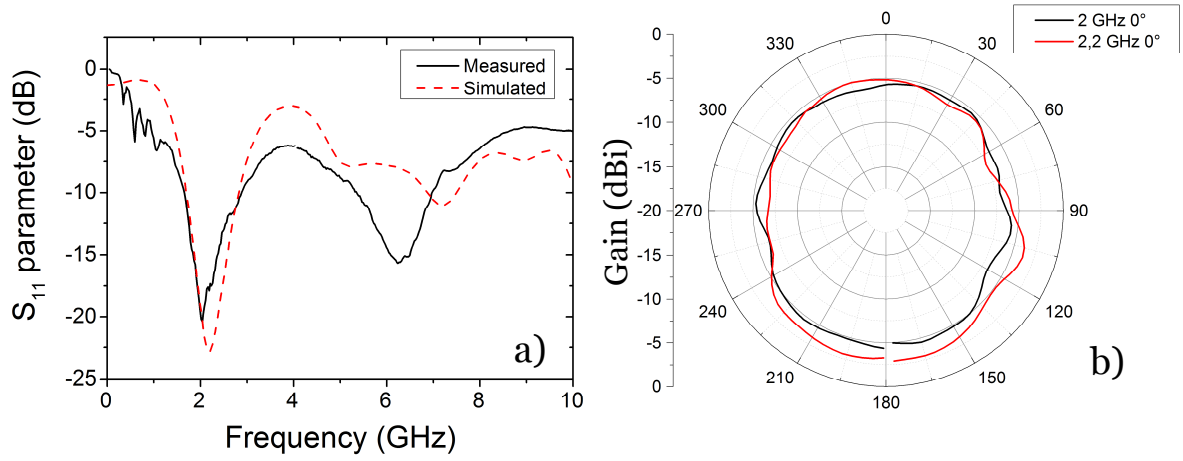

Figure 5-29: S11 parameter and gain of antenna with R_s ~ 3 Ω/□ with silver paint as transmission line

These first experimental results obtained close to the very end of this thesis work will be continued with Thomas Sannicolo, in the framework of a collaboration with specialists of antennas and electromagnetic shielding at IMEP-LAHC.

5.4 Closing remarks and future work

The results for AgNW networks applied as transparent heaters were very satisfactory, with reasonable response time and low operation voltages. Rather high temperatures (above 100°C) could be reached. The heat losses of AgNW networks fabricated with different methods of deposition and different nanowire sizes could be estimated through the heat transfer constant α. A slight decrease of this parameter was observed with the increasing length of the nanowires within the network. In addition, the network density was shown to play a greater role than the network resistance on heat losses. An original experiment performed both in air and in vacuum allowed to quantify the effect of convection on heat losses. Non-reversible effects of electrical stress (and Joule heating) on the AgNW networks were also observed and investigated. The role of electromigration and of thermal instability could be shown and separated. Thermal and electrical instability could be overcome (at least partially) by depositing a very thin TiO_2 layer by ALD on the nanowires. More studies should be conducted on the lifetime and

electromigration within the networks, which seems to be the main problems for this application.

The electromagnetic shielding measurements shown in this chapter are the preliminary results of studies that will be the subject of Thomas Sannicolo thesis (CEA Liten – LMGP, 2014-2017). The results are very promising, with a shielding effectiveness close to 30 dB with a network relatively transparent, with a transmittance of 81% at 550 nm. Most of the future work on this topic will be focused on the tradeoff between resistance and transmittance to allow efficient shielding. Some studies will also be performed with patterned samples in order to shield specific frequencies. Numerical simulations will be used and compared with experimental data allowing a better understanding of the system, as well as optimizing the devices.

Concerning antennas, preliminary results show some agreement with the simulated behavior of the S_{11} parameter. However more studies need to be performed to optimize the samples in order to obtain devices with positive gain. Axis of research will be focused in particular on the influence of surface roughness with the use of several coating such as TiO_2 or PEDOT:PSS, and on the antenna geometry.

References

[1] Harold A. Mcmaster 1947 Conductive coating for glass and method of application

[2] Rathmell A R, Nguyen M, Chi M and Wiley B J 2012 Synthesis of Oxidation-Resistant Cupronickel Nanowires for Transparent Conducting Nanowire Networks *Nano Lett* **12** 3193–9

[3] Rathmell A R and Wiley B J 2011 The Synthesis and Coating of Long, Thin Copper Nanowires to Make Flexible, Transparent Conducting Films on Plastic Substrates *Adv. Mater.* **23** 4798–803

[4] Rathmell A R, Bergin S M, Hua Y-L, Li Z-Y and Wiley B J 2010 The Growth Mechanism of Copper Nanowires and Their Properties in Flexible, Transparent Conducting Films *Adv. Mater.* **22** 3558–63

[5] Langley D, Giusti G, Mayousse C, Celle C, Bellet D and Simonato J-P 2013 Flexible transparent conductive materials based on silver nanowire networks: a review *Nanotechnology* **24** 452001

[6] Celle C, Mayousse C, Moreau E, Basti H, Carella A and Simonato J-P 2012 Highly flexible transparent film heaters based on random networks of silver nanowires *Nano Res.* **5** 427–33

[7] Sorel S, Bellet D and Coleman J N 2014 Relationship between Material Properties and Transparent Heater Performance for Both Bulk-like and Percolative Nanostructured Networks *ACS Nano* **8** 4805–14

[8] Kim T, Kim Y W, Lee H S, Kim H, Yang W S and Suh K S 2013 Uniformly Interconnected Silver-Nanowire Networks for Transparent Film Heaters *Adv. Funct. Mater.* **23** 1250–5

[9] Wang S, Zhang X and Zhao W 2013 Flexible, Transparent, and Conductive Film Based on Random Networks of Ag Nanowires *J Nanomater.* **2013**

[10] Zhang X, Yan X, Chen J and Zhao J 2014 Large-size graphene microsheets as a protective layer for transparent conductive silver nanowire film heaters *Carbon* **69** 437–43

[11] Kim D, Zhu L, Jeong D-J, Chun K, Bang Y-Y, Kim S-R, Kim J-H and Oh S-K 2013 Transparent flexible heater based on hybrid of carbon nanotubes and silver nanowires *Carbon* **63** 530–6

[12] Li J, Liang J, Jian X, Hu W, Li J and Pei Q 2014 A Flexible and Transparent Thin Film Heater Based on a Silver Nanowire/Heat-resistant Polymer Composite *Macromol. Mater. Eng.* **299** 1403–9

[13] Ji S, He W, Wang K, Ran Y and Ye C 2014 Thermal Response of Transparent Silver Nanowire/PEDOT:PSS Film Heaters *Small* **10** 4951–60

[14] Araki T, Jiu J, Nogi M, Koga H, Nagao S, Sugahara T and Suganuma K 2014 Low haze transparent electrodes and highly conducting air dried films with ultra-long silver nanowires synthesized by one-step polyol method *Nano Res.* **7** 236–45

[15] Stahlmecke B, Heringdorf F-J M zu, Chelaru L I, Hoegen M H, Dumpich G and Roos K R 2006 Electromigration in self-organized single-crystalline silver nanowires *Appl. Phys. Lett.* **88** 053122

[16] Tu K N 2003 Recent advances on electromigration in very-large-scale-integration of interconnects *J. Appl. Phys.* **94** 5451–73

[17] Kaspers M R, Bernhart A M, Heringdorf F-J M zu, Dumpich G and Möller R 2009 Electromigration and potentiometry measurements of single-crystalline Ag nanowires under UHV conditions *J. Phys. Condens. Matter* **21** 265601

[18] Khaligh H H and Goldthorpe I A 2013 Failure of silver nanowire transparent electrodes under current flow *Nanoscale Res. Lett.* **8** 1–6

[19] Song T-B, Chen Y, Chung C-H, Yang Y (Michael), Bob B, Duan H-S, Li G, Tu K-N, Huang Y and Yang Y 2014 Nanoscale Joule Heating and Electromigration Enhanced Ripening of Silver Nanowire Contacts *ACS Nano* **8** 2804–11

[20] Maize K, Das S R, Sadeque S, Mohammed A M S, Shakouri A, Janes D B and Alam M A 2015 Super-Joule heating in graphene and silver nanowire network *Appl. Phys. Lett.* **106** 143104

[21] Aherne D, Satti A and Fitzmaurice D 2007 Diameter-dependent evolution of failure current density of highly conducting DNA-templated gold nanowires *Nanotechnology* **18** 125205

[22] Hu M, Gao J, Dong Y, Li K, Shan G, Yang S and Li R K-Y 2012 Flexible Transparent PES/Silver Nanowires/PET Sandwich-Structured Film for High-Efficiency Electromagnetic Interference Shielding *Langmuir* **28** 7101–6

[23] Yang C, Gu H, Lin W, Yuen M M, Wong C P, Xiong M and Gao B 2011 Silver Nanowires: From Scalable Synthesis to Recyclable Foldable Electronics *Adv. Mater.* **23** 3052–6

[24] Huang Y, Li N, Ma Y, Du F, Li F, He X, Lin X, Gao H and Chen Y 2007 The influence of single-walled carbon nanotube structure on the electromagnetic interference shielding efficiency of its epoxy composites *Carbon* **45** 1614–21

[25] Xiang C, Pan Y and Guo J 2007 Electromagnetic interference shielding effectiveness of multiwalled carbon nanotube reinforced fused silica composites *Ceram. Int.* **33** 1293–7

[26] Song W-L, Cao M-S, Lu M-M, Bi S, Wang C-Y, Liu J, Yuan J and Fan L-Z 2014 Flexible graphene/polymer composite films in sandwich structures for effective electromagnetic interference shielding *Carbon* **66** 67–76

[27] Al-Saleh M H, Gelves G A and Sundararaj U 2011 Copper nanowire/polystyrene nanocomposites: Lower percolation threshold and higher EMI shielding *Compos. Part Appl. Sci. Manuf.* **42** 92–7

[28] De Barros F, Eymin-Petot-Tourtollet G, Lemaitre-Auger P and VUONG T-P 2011 Surface for filtering a plurality of frequency bands

[29] Niembro-Martin A, Pistono E, Lemaitre-Auger P, Vuong T-P and Tourtollet G E P 2014 Efficient setup for the measurement of transmission-coefficients with a single-room anechoic chamber *2014 IEEE Conference on Antenna Measurements Applications (CAMA)* 2014 IEEE Conference on Antenna Measurements Applications (CAMA) pp 1–3

[30] Song H J, Hsu T Y, Sievenpiper D F, Hsu H P, Schaffner J and Yasan E 2008 A Method for Improving the Efficiency of Transparent Film Antennas *IEEE Antennas Wirel. Propag. Lett.* **7** 753–6

[31] Saberin J R and Furse C 2012 Challenges with Optically Transparent Patch Antennas *IEEE Antennas Propag. Mag.* **54** 10–6

[32] Yasin T, Baktur R and Furse C 2011 A comparative study on two types of transparent patch antennas *General Assembly and Scientific Symposium, 2011 XXXth URSI* General Assembly and Scientific Symposium, 2011 XXXth URSI pp 1–4

[33] Mias C, Tsakonas C, Prountzos N, Koutsogeorgis D C, Liew S C, Oswald C, Ranson R, Cranton W M and Thomas C B 2000 Optically transparent microstrip antennas *2000/002), IEE Colloquium on Antennas for Automotives (Ref. No* 2000/002), IEE Colloquium on Antennas for Automotives (Ref. No pp 8/1–8/6

[34] Anon Vehicle window glass antenna using transparent conductive film

[35] Song L, Myers A C, Adams J J and Zhu Y 2014 Stretchable and Reversibly Deformable Radio Frequency Antennas Based on Silver Nanowires *ACS Appl. Mater. Interfaces* **6** 4248–53

[36] Nogi M, Komoda N, Otsuka K and Suganuma K 2013 Foldable nanopaper antennas for origami electronics *Nanoscale* **5** 4395–9

[37] Komoda N, Nogi M, Suganuma K, Kohno K, Akiyama Y and Otsuka K 2012 Printed silver nanowire antennas with low signal loss at high-frequency radio *Nanoscale* **4** 3148–53

Conclusions and future work

Silver nanowire networks constitute a promising alternative to indium tin oxide (ITO) as a transparent conductive material (TCM). The interest devoted to this material is increasingly growing and its integration into devices has diversified recently. AgNW based TE were initially developed mostly for solar cells or OLEDs but since the start of this thesis, three years ago, a lot of new applications have been considered, such as transparent heaters or RF antennas. Compared to other transparent conductive materials, silver nanowires are shown to be very promising candidates as transparent electrodes since, apart from their excellent optical and electrical properties, they present many other advantages such as flexibility and low cost fabrication, at rather low temperature. These advantages are very helpful for replacing ITO, in particular in flexible devices.

Simple and low cost methods were used to fabricate AgNW networks. The use of spin coating in a first approach allowed to rapidly obtain samples with excellent properties. A setup of spray deposition was however developed in the frame of this thesis in order to suppress some anistropic orientation effects present in electrodes fabricated by spin coating, and to deposit networks on large surfaces. Samples up to 32*22 cm^2 in size could be fabricated. A routine has been developed for the spray method in order to obtain reproducible samples with an optimum density allowing the best tradeoff between low electrical resistance and high optical transparency. Both methods of spin and spray coating however led to samples with relatively high resistances due to organic residues trapped between nanowires. Therefore an easy way to optimize the samples properties, especially to lower the resistance, was to perform a thermal annealing. This method has therefore been extensively studied in this document.

In situ resistance measurements were performed to shed light on the network electrical behavior during thermal annealing. An interpretation of the different mechanisms occurring has been proposed, and the study of the kinetics allowed to find the optimum thermal annealing parameters in terms of temperature and duration. The thermal process includes a first stage where all the organic residues from the deposition desorb from the nanowire junctions, so the electrical contact is improved. Then a local sintering of the nanowire junctions occurs which improves further the electrical contact. At this stage the polymeric capping agent used in the NW synthesis, PVP, is still present and protects the nanowires. It doesn't block the electrical sintering at junction, as silver atomic diffusion seem to occur through the PVP layer. This stage of fully sintered junctions corresponds to the lowest value of the network resistance. Therefore, interrupting the ramped thermal annealing at the temperature at which the resistance is the lowest has been shown to enable reaching the optimum sample conductivity in a reproducible way. This method was used on a variety of samples having different network densities and nanowire sizes. AgNW-based electrodes properties were then compared by using

the Haacke figure of merit in order to find the optimum density allowing the best tradeoff between transparency and conductivity for each type of nanowire. Haacke figures of merit were found to be up to 107.10^{-3} Ω^{-1} for a sample made with 170 $mg.m^{-2}$ of Ag117 nanowires, and with a sheet resistance of 2.9 Ω/□ and a transmittance of 89%.

The optimization of the networks during this density study was obtained solely by using the thermal annealing method. However other techniques of conductivity improvement exist. Few of them were studied in the framework of an international collaboration aiming at comparing them. In addition to thermal annealing, mechanical pressure, acid treatment and laser annealing were investigated. These techniques show promising results but should be further improved to lead to results as efficient and spatially homogeneous as those obtained from thermal annealing. Regarding mechanical pressing, a problem of homogeneity has been emphasized. It could be bypassed by a combination of mechanical pressing and thermal treatment performed at the same time. Acid treatment has been seen to lead to good results but the treatment was performed on different samples and the results were not completely reproducible. The treatment however has been seen by the CEA to be more efficient as a washing of the NW solution, instead of a post-deposition bath, therefore efforts should be focused in that direction. Pulsed laser annealing has been difficult to set to lead to good results but has shown to be promising and should be further improved.

Nanowire dimensions are at the core of this topic. The use of a nanomaterial instead of bulk allows to have a transparent layer which is conducting by electrical percolation. Percolation is very dependent on the nanowire size. Length is the dominant parameter impacting on the maximum network sparseness, and the diameter can detrimentally affect the electrical conduction when the size is low enough to induce electron surface scattering (typically below 40 nm). Simple models based on percolation theory and surface scattering have been proposed to relate the electrical resistance and optical transmittance of AgNW networks to their density, and to the nanowires length and diameter. The expressions derived, one for the electrical resistance and the other for the optical transmittance, provide good agreement with the experimental observations. These models can be seen as a guideline for the use of percolating metallic nanowires since they include bulk material physical quantities, and could, in theory, be applied to metallic nanowires of different nature (copper for instance, which is a more abundant material. Copper nanowire systems are also increasingly studied). AgNW networks possess many advantages as a TCM considering their high optical transparency and high electrical conductivity. But playing with the network density and the nanowires dimensions can lead to a variety of properties, which can improve the performance of optoelectronic devices. Other parameters are related to the network density or nanowire size. The haze factor for instance is of great interest to improve solar cells efficiency, and can be increased by increasing the network density, or by using NW with a larger diameter.

AgNW however suffer from several drawbacks in terms of stability, due in particular to their small size. Thermal annealing, which has been shown to be efficient for optimizing AgNW networks, can induce instability leading to a loss of the conductivity at high temperatures. Rayleigh instability, driven by surface energy reduction, has been considered and was shown to occur for AgNW at high temperatures. The thermal instability starts to occur at different temperatures, which have been shown to be dependent on the nanowires diameter. By performing similar experiments on networks composed of AgNW with different diameters, the diameter-dependence of the two characteristic temperatures (*i.e.* associated to the optimal electrical resistance and to the morphological instability occurrence) have been shown to follow fairly well a Gibbs-Thomson law. This thermal instability must be taken into account when a thermal process is envisaged on AgNW networks. Thermal annealing parameters (duration and temperature) must be carefully adapted to optimize the networks without degrading them. The role of junction in the process of nanowire instability has also been addressed. Junctions are critical locations where the mechanisms of resistance improvement occur, through local sintering, which is a great advantage of metallic nanowires over carbon nanotubes, for instance. The junction assembly in a AgNW network shouldn't be considered as a uniform population, but should exhibit a distribution of properties, such as electrical resistances, caused by the AgNW diameter and length distributions, as well as structural defects. In other words, any physical property of AgNW networks, for example electrical resistance, should be representative of a collection of statistical distributed junction resistances, and not as identical entities. Moreover, nanowire junctions which play a key role for the electrical resistance optimization can also become the weakness of the network since they are the first points to induce resistance increase, due to instability caused by surface energy reduction-driven surface atomic diffusion. This can be well illustrated by the SEM images hereafter.

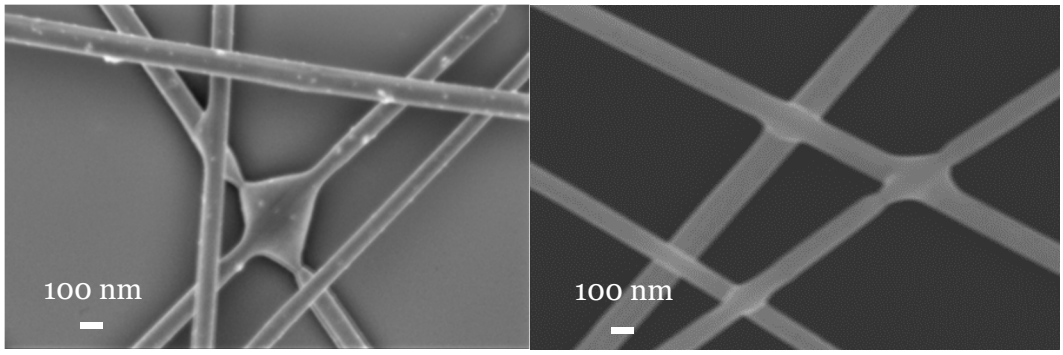

Figure 6-1: SEM images of nanowires instability starting to occur at a well sintered junctions after thermal annealing.

Coating the networks with TiO_2 uniform layers has been tested and validated to delay thermal instability to higher temperatures. The hybrid networks were still conducting after being heated up to 500°C. The nanowires encapsulation allows to limit atomic surface diffusion. It also has been seen to improve the networks electrical stability and prevents the nanowires degradation from atmospheric corrosion. The latter feature must however be further studied. Other metallic oxides can be envisaged for encapsulation, and could be soon deposited using an SALD setup which is currently being developed at the LMGP. In addition, ZnO can be presently deposited by temporal ALD at the LMGP, and also FTO by pyrolysis, so further studies will be conducted concerning encapsulation using these materials to improve AgNW stability.

To finish with, the use of AgNW networks as transparent electrodes in several applications has been validated in this document. AgNW-based transparent heaters have been investigated during the present thesis work, especially in terms of electrical and thermal response to an applied voltage. They have been shown to be promising in terms of performance, response time and lifetime, but still suffer from some instabilities, in particular coming from electromigration. This problem can however be limited by metal oxide encapsulation, like thermal instability. Studies will be further conducted on the stability improvement against electromigration. The heat losses due to Joule effect were also investigated, and losses by convection could in particular be evaluated from experiments in vacuum. Other less known applications of AgNW have been investigated in a less extent: electromagnetic shielding and RF antennas. Electromagnetic shielding has been shown to be efficient with shielding effectiveness values lower than 20 dB between 2 and 16 GHz for a sample having a sheet resistance around 10 Ω/□. Studies will be continued in order to define more precisely the role of network density and nanowire dimensions on the electromagnetic shielding effectiveness. Finally, some transparent antennas were fabricated. The experimental data show that the signal is well transmitted to the radiating material, and the resulting S_{11} parameter fits fairly well with simulation when the transmission line is made with bulk silver. More studies however need to be performed to improve the gain and determine the effects of network density and nanowire dimensions.

The properties of AgNW networks, improving progressively, are tunable with network density and nanowire size, which is a great advantage. Although the development of other TCM is of interest in order to fulfil some of the TE requirements, or lead to better tradeoffs between some properties, AgNW (and more generally metallic nanowires) networks have a bright future in this field. Considering the increasing number of publications on AgNW and the diversification of their applications, as transparent electrodes or other, like antennas, this material is at the heart of a dynamical research axis. It is worth noting that while silver possesses the great advantage of having the highest bulk electrical conductivity among all

materials at room temperature, other metals (or alloys) could replace silver inducing for instance cost reduction. Scientific investigations on AgNWs, such as the present thesis work, could serve as contributions on a model (and simple) material for then transposing its scientific content towards more complex nanowires composed of other metals such as Cu, Cu-Ni, or on hybrid TCM such as a combination between metallic nanowire and graphene.

Annexe: Seashell nanowires length and diameter distributions

Six different types of AgNW have been used during this thesis work. They were synthesized by Seashell Technology by the polyol process and have different diameters and lengths. An image analysis study was conducted in order to estimate the distribution of length and diameter of each nanowire type. The software Image J was used and the study was performed on 100 nanowires from SEM images.

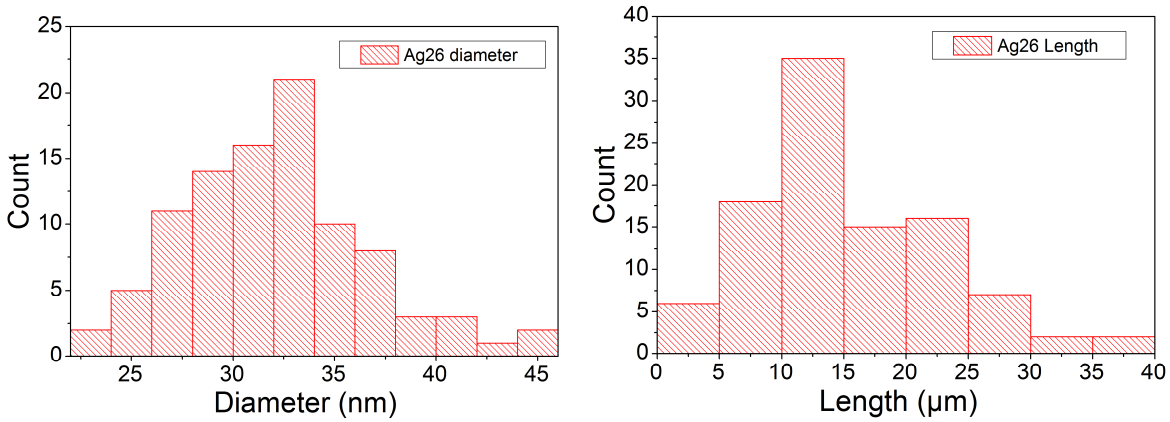

Figure A-1: a) Ag26 distribution of diameter on 100 nanowires b) Ag26 distribution of length on 100 nanowires.

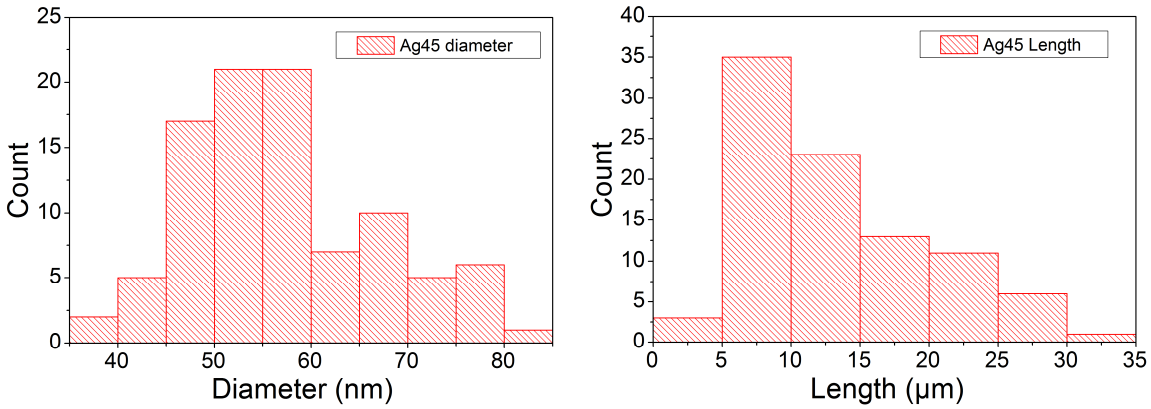

Figure A-2: Ag45 distribution of diameter on 100 nanowires b) Ag45 distribution of length on 100 nanowires.

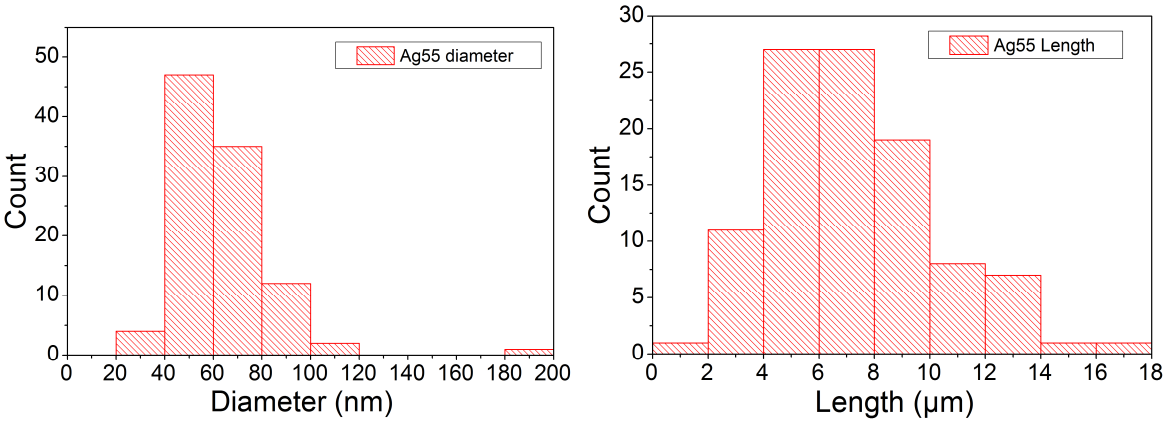

Figure A-3: Ag55 distribution of diameter on 100 nanowires b) Ag55 distribution of length on 100 nanowires.

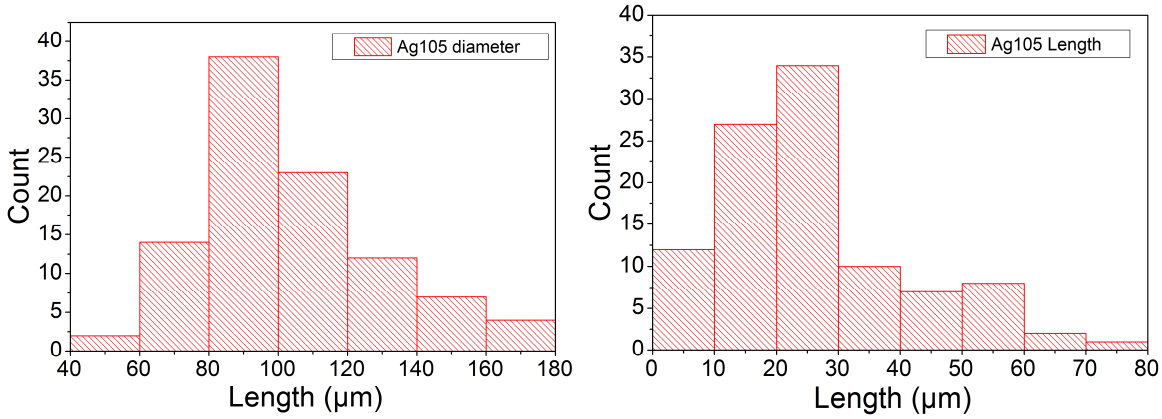

Figure A-4: Ag105 distribution of diameter on 100 nanowires b) Ag105 distribution of length on 100 nanowires.

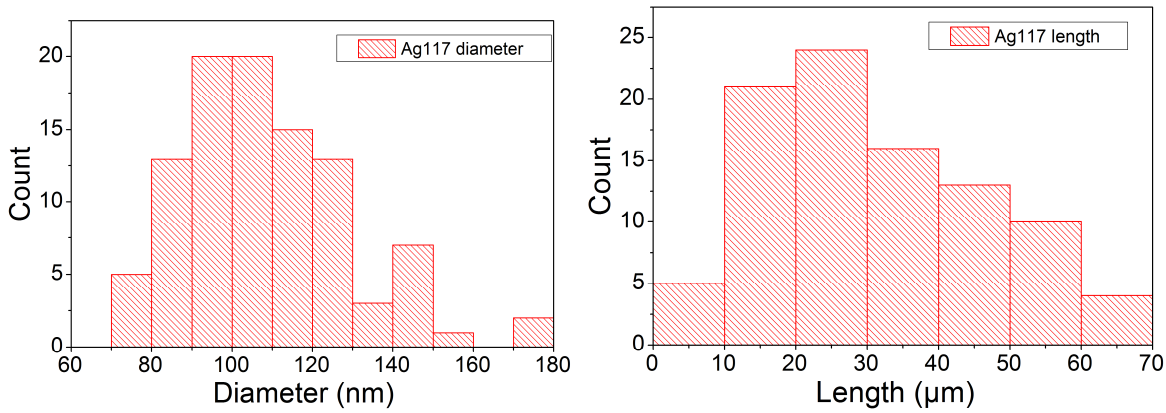

Figure A-5: Ag117 distribution of diameter on 100 nanowires b) Ag117 distribution of length on 100 nanowires.

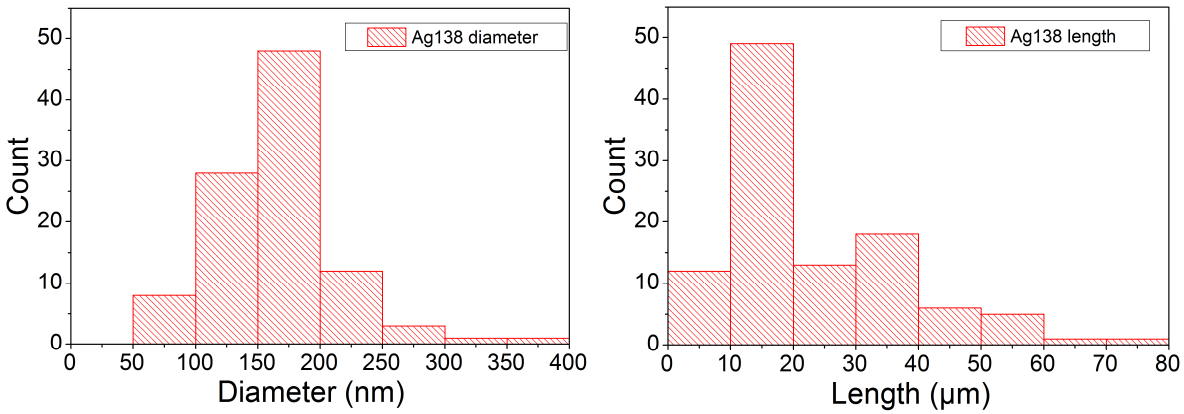

Figure A-6: Ag138 distribution of diameter on 100 nanowires b) Ag138 distribution of length on 100 nanowires.

Abstract

Transparent electrodes (TE) are used in a variety of optoelectrical devices. Among them, solar cells, flat panel displays, touch screens, OLEDs can be cited but also other applications such as transparent heaters. The physical properties of the TE influence the efficiency of these devices as a whole. Such electrodes are fabricated from transparent conducting materials (TCM) that have been undergoing development since the 1950s, initially from metallic oxides. Among these transparent conducting oxides (TCO), indium tin oxide (ITO) is the most commonly used in solar cells, and television or smartphone screens. However requirements such as cost reduction, flexibility and low cost/temperature fabrication techniques have oriented the researches toward emerging TCM, mostly using nanostructures. Among them, metallic nanowire networks, and in particular silver nanowires (AgNW), already present optical and electrical properties approaching those of ITO, *i.e.* a high electrical conductivity and a high transparency. These two properties are intrinsically linked to the network density, therefore a tradeoff has to be considered knowing that when conductivity increases, transparency decreases. Some post-deposition treatments do exist, allowing an increase of the TE electrical conductivity without changing the network density. Several of these optimization methods have been thoroughly studied during this thesis work, especially thermal annealing. This method have been investigated in details to understand the different thermally-induced mechanisms of conductivity improvement. In addition, the investigation of thermal effects raised the question of thermal instability of the nanowires, which is also addressed and discussed in this document. The key issue of density optimization, allowing the best tradeoff between transparency and conductivity, has been investigated for nanowires with different dimensions. Nanowire size has a strong impact on the network properties. Thus, electrical properties, within the framework of percolation theory, optical properties such as transmittance or haziness, and even thermal instability have been linked to the nanowires' dimensions and the network density by using simple physical models. Regarding the application of these emerging TE, studies were conducted on the application of AgNWs as transparent heaters, and the results are reported at the end of the document. Limitations arising from this application, like thermal and electrical stabilities, have also been addressed. To finish, preliminary studies conducted on new applications such as transparent antennas and transparent electromagnetic shielding using AgNW are presented.